STUDY ON ELECTRICAL AND OPTICAL PROPERTIES OF ZINC OXIDE SEMICONDUCTOR FOR GAS SENSOR APPLICATION

A THESIS SUBMITTED TO THE

CENTRAL DEPARTMENT OF PHYSICS

INSTITUTE OF SCIENCE AND TECHNOLOGY

TRIBHUVAN UNIVERSITY

NEPAL

FOR THE AWARD OF

DOCTOR OF PHILOSOPHY

IN PHYSICS

By

DINESH KUMAR CHAUDHARY

JANUARY 2023

STUDY ON ELECTRICAL AND OPTICAL PROPERTIES OF ZINC OXIDE SEMICONDUCTOR FOR GAS SENSOR APPLICATION

A THESIS SUBMITTED TO THE

CENTRAL DEPARTMENT OF PHYSICS

INSTITUTE OF SCIENCE AND TECHNOLOGY

TRIBHUVAN UNIVERSITY

NEPAL

FOR THE AWARD OF

DOCTOR OF PHILOSOPHY

IN PHYSICS

By

DINESH KUMAR CHAUDHARY

JANUARY 2023

TRIBHUVAN UNIVERSITY

Institute of Science and Technology

DEAN'S OFFICE

Kirtipur, Kathmandu, Nepal

Reference No.:

Institute of Science & Technology
Dean's Office
Kirtipur 2045

EXTERNAL EXAMINERS

The Title of Ph.D. Thesis: " Study on Electrical and Optical Properties of Zinc Oxide Semiconductor for Gas Sensor Application "

Name of Candidate: Mr. Dinesh Kumar Chaudhary

External Examiners:

(1) Prof. Dr. Tika Bahadur Katuwal
Tri-Chandra Multiple Campus
Tribhuvan University, NEPAL

(2) Prof. Dr. S.N. Pandey
Motilal Nehru National Institute of Technology
Allahabad, INDIA

(3) Prof. Dr. Mim Lal Nakarmi
Brooklyn College
City University of New York
Brooklyn, USA

July 13, 2023

(Dr. Surendra Kumar Gautam)
Asst. Dean

DECLARATION

Thesis entitled **"STUDY ON ELECTRICAL AND OPTICAL PROPERTIES OF ZINC OXIDE SEMICONDUCTOR FOR GAS SENSOR APPLICATION"** which is being submitted to the Central Department of Physics, Institute of Science and Technology (IOST), Tribhuvan University, Nepal for the award of the degree of Doctor of Philosophy (Ph.D.), is a research work carried out by me under the supervision of Prof. Dr. Leela Pradhan Joshi of Department of Physics, Amrit Campus, Tribhuvan University and co-supervised by Prof. Dr. Shankar Prasad Shrestha of Department of Physics, Patan Multiple Campus, Tribhuvan University.

This research is original and has not been submitted earlier in part or full in this or any other form to any university or institute, here or elsewhere, for the award of any degree.

.....

Dinesh Kumar Chaudhary

RECOMMENDATION

This is to recommend that **Mr. Dinesh Kumar Chaudhary** has carried out research entitled **"STUDY ON ELECTRICAL AND OPTICAL PROPERTIES OF ZINC OXIDE SEMICONDUCTOR FOR GAS SENSOR APPLICATION"** for the award of Doctor of Philosophy (Ph.D.) in **Physics** under our supervision. To our knowledge, this work has not been submitted for any other degree.

He has fulfilled all the requirements laid down by the Institute of Science and Technology (IoST), Tribhuvan University, Kirtipur for the submission of the thesis for the award of Ph.D. degree.

.....

Prof. Dr. Leela Pradhan Joshi
Supervisor
(Professor)
Department of Physics,
Amrit Campus, Tribhuvan University,
Kathmandu, Nepal

.....

Prof. Dr. Shankar Prasad Shrestha
Co-Supervisor
(Professor)
Department of Physics,
Patan Multiple Campus, Tribhuvan University,
Kathmandu, Nepal

Janaury 2023

TRIBHUVAN UNIVERSITY
CENTRAL DEPARTMENT OF PHYSICS
Kirtipur, Kathmandu, Nepal

☎ 4331054
www.tucdp.edu.np

Tribhuvan University Central Department of Physics Kirtipur

Ref. No.: (F.No .....) CDP .....

Date: 20 July, 2023

LETTER OF APPROVAL

Date: 08/01/2023

On the recommendation of **Prof. Dr. Leela Pradhan Joshi**, Department of Physics, Amrit Campus, Tribhuvan University, Nepal and **Prof. Dr. Shankar Prasad Shrestha**, Department of Physics, Patan Multiple Campus, Tribhuvan University, Nepal, this Ph.D. thesis submitted by **Mr. Dinesh Kumar Chaudhary**, entitled **"STUDY ON ELECTRICAL AND OPTICAL PROPERTIES OF ZINC OXIDE SEMICONDUCTOR FOR GAS SENSOR APPLICATION"** is forwarded by Central Department of Research Committee (CDRC) to the Dean, Institute of Science and Technology (IoST), Tribhuvan University.

O.P. Niraula

Dr. Om Prakash Niraula
(Professor)
Head,
Central Department of Physics,
Tribhuvan University, Kirtipur,
Kathmandu, Nepal

ACKNOWLEDGMENTS

The present thesis, entitled "STUDY ON ELECTRICAL AND OPTICAL PROPERTIES OF ZINC OXIDE SEMICONDUCTOR FOR GAS SENSOR APPLICATIONS," is being submitted in partial fulfillment of the requirement for the degree of Doctor of Philosophy (Science) of Tribhuvan University, Kirtipur, Nepal. I am delighted to feel that I have gained enough knowledge on the fundamentals of research in experimental physics on this topic. I am extremely grateful to my supervisors, Prof. Dr. Leela Pradhan Joshi, Department of Physics, Amrit Campus, Tribhuvan University, Nepal, and Prof. Dr. Shankar Prasad Shrestha, Patan Multiple Campus, Department of Physics, Tribhuvan University, Nepal, for providing valuable suggestions in every step of my Ph.D. thesis work.

I would like to express my indebtedness to Prof. Dr. Rajendra Parajuli, Prof. Dr. Shriram Sharma, and Assistant Prof. Pitambar Shrestha, Department of Physics, Amrit Campus, Tribhuvan University, for their help in completing this work. I am grateful to Prof. Dr. Binil Aryal, Dean, IoST, Prof. Dr. Om P. Niraula, Head of the Central Department of Physics, Prof. Dr. Lok N. Jha (Ex. Head, CDP), Prof. Dr. Jeevan Jyoti Nakarmi, Prof. Dr. Raju Khanal, Prof. Dr. Narayan P. Adhikari, Prof. Dr. Hari Lamichhane, Dr. Ishwor Koirala, Dr. Sanju Shrestha, Dr. Gopi Chandra Kaphle, Dr. Madhav Ghimire, Dr. Tikaram Lamichhane, Dr. Hari Shankar Mallik, Dr. Hom B. Baniya, Dr. Rishi Ram Ghimire and Dr. Bhushan Shakya for their great supports and encouragements during my hard times.

I would like to express my thanks to all the faculty members and administrative staff of the Central Department of Physics. I am thankful to the Department of Physics, Amrit Campus for providing a research laboratory and to the Institute of Science and Technology, T.U. for providing me with a study leave to carry out this research work.

I am very much thankful to the International Science Program (ISP), Uppsala University, Sweden for their partial financial support to purchase the necessary chemicals and equipment under the research grant ISP, NEP-01.

My special thanks go to my friends Dr. Manoj Kumar Chaudhary, Mr. Mohan Bahadur Kshetri, Mr. Bal Vikram Khatri, Mr. Shiv Prasad Baral, Mrs. Sumana Gyawali, Mr. Yogesh Maharjan, Dr. Hari Krishna Neupane, Mr. Devendra Raj Upadhyay, Mr. Roshan Chalise, Mr. Shiromani Gajurel, Dr. Suresh Basnet, Dr. Sharmila Amatya, Mr. Prakash Man Shrestha, Mrs. Usha Joshi, Dr. Surendra Maharjan, Mrs. Yamuna Paudel, Mrs. Sabita Sharma, Mr. Yaduram Panthi, Mr. Rajesh Shrestha, Mr. Tirtha Raj Acharya, and

Mr. Shyam Prasad Shrestha for their moral supports during this work. Last but not least, without the support and devotion of my family, especially my wife, I would never have reached my goal in the manner that I have. Her constant support, encouragement, and faith in me inspired me to complete my Ph.D. work.

.....

Dinesh Kumar Chaudhary
January 2023

ABSTRACT

Ammonia, ethanol, acetone, etc. are commonly found as toxic gases in most places. The real-time monitoring of these gases is essential because their excessive exposure may produce serious health problems. In recent times, several metal oxide semiconductors (MOS) have been exploited for gas detection. In this context, zinc oxide (ZnO) is considered one of the potential materials for its interesting properties such as non-toxicity, high thermal & chemical stability, and easy tunable electrical & optical behavior. High working temperature (>300 °C), poor selectivity, and low sensitivity are some of its shortcomings. The operation at high temperatures degrades the sensor's stability and consumes power. This study aims to enhance the sensing characteristics of ZnO-based sensors after utilizing strategies like metal and metal-metal doping into it. Herein, the ZnO and metal-doped films were prepared by using spin coating, spray pyrolysis, and doctor blade methods for an in-depth understanding of gas sensing. Its optical and structural characterizations were done by ultra violet visible (UV-Vis) spectrophotometer and X-ray diffraction (XRD) respectively. Surface morphology and elemental composition were studied using scanning electron microscopy (SEM) and energy-dispersive X-ray (EDX) analysis. The gas sensing performances of ZnO-based sensors were measured using a homemade gas sensor setup.

At first, spin-coated ZnO was tested for the detection of traces of ammonia, ethanol, acetone, methanol, and isopropanol at room temperature. Its XRD and SEM micrographs demonstrated the polycrystalline wurtzite phase with a grainy surface. The band gap was found to be 3.202 ± 0.023 eV. The sensitivity measurements revealed the highest response of 38.5 ± 0.6 with an exposure of 400 ppm of ammonia vapour, indicating its selectivity among the tested gases. The results of sensitivity measurements over multiple cycles showed the device's good stability. The sensing capability here was found to be better than other similar works. Hence, the results obtained here will be helpful in the development of a low-cost, effective room temperature MOS gas sensor with a lower detection limit of 20 ppm which is below the Occupational Safety and Health Administration's (OSHA) approved threshold.

For acetone sensing, ZnO deposited on an fluorine doped tin oxide (FTO) substrate prepared by doctor blade was used. XRD and fourier transform infrared (FTIR) spectroscopy were used for phase purity and optical characterization of ZnO nanoparticles (ZnONPs) prepared from the co-precipitation method prior to deposit on the FTO substrate. The sensing measurements demonstrated the maximum value of gas response of 25.697 ± 0.012 at an operating temperature of 285 ± 7 °C for exposure of 800 ppm of acetone

along with the rapid response and recovery. This operating temperature was found to be lower than the published values that were prepared by different methods. The response & recovery times were measured to be 39 sec and 79 sec, respectively.

Sequentially, in other sets of experiments, the undoped ZnO, Fe-doped ZnO (Fe-ZnO), and Sn-doped ZnO (Sn-ZnO) films were used to detect ethanol vapours in the temperature range of 100-300 °C. The sensitivity measurements for 2% Fe-ZnO film showed the highest response of 40.91 ± 0.23 at the exposure of 400 ppm of ethanol at 260 ± 7 °C. The comparison with similar reported values confirmed its goodness. And 2% Sn-ZnO film showed the highest response of only 17.659 ± 0.011 for 400 ppm exposure at 220 ± 5 °C. This working temperature was found to be slightly lower than the published value. Interestingly, this also reports that 2% Sn-ZnO film was able to detect as small as 0.5 ppm of ethanol. The spin-coated Fe-Al co-doped ZnO sensors were also tested to monitor ethanol in the temperature range of 120 − 360 °C. The 1%Fe-1%Al-ZnO sample showed a very high value of the response, 152.304 ± 0.003 at the exposure of 400 ppm at 290 ± 7 °C. It is due to an increase in specific surface area which occurs due to the reduction of grain size after Fe-Al co-doping. The observed values of response and recovery times were 33 sec and 201 sec respectively at an operating temperature of 290 ± 7 °C. Hence, metal-metal co-doping is found to be a good strategy to improve the sensitivity of ZnO-based gas sensors.

Finally, the effect of gate electrode potential on the ammonia sensing ability of ZnO at ambient temperature was also reported here. Required films were prepared by the spray pyrolysis method. The gas response of ZnO for 400 ppm of ammonia was increased from 30.292 ± 0.042 to 54.581 ± 0.062 on increasing the gate electrode potential from 0 to 24V. Hence, this will be a new finding to improve the gas response of future ZnO-based gas sensors.

LIST OF ACRONYMS AND ABBREVIATIONS

ATR	Attenuated Total Reflectance
Al-ZnO	Aluminum Doped Zinc Oxide
at. %	Atomic Percentage
CBM	Conduction Band Minimum
Co-ZnO	Cobalt Doped Zinc Oxide
CRT	Cathode Ray Tube
Cr-ZnO	Chromium Doped Zinc Oxide
DEA	Di-ethanolamine
EDX	Energy Dispersive X-Ray
ET	Evehart-Thornly
FE-SEM	Field Emission Scanning Electron Microscope
Fe-Al-ZnO	Iron-Aluminum Doped Zinc Oxide
Fe-ZnO	Iron Doped Zinc Oxide
FTIR	Fourier Transform Infra-Red
FTO	Fluorine Doped Tin Oxide
FWHM	Full Width at Half Maxima
GBs	Grain Boundaries
HCP	Hexagonally Close-Packed
In-ZnO	Indium Doped Zinc Oxide
IR	Infra-Red
JCPDS	Joint Committee on Powder Diffraction Standards
Li-ZnO	Lithium Doped Zinc Oxide
MEMS	Microelectromechanical System
Mn-ZnO	Manganese Doped Zinc Oxide
MOS	Metal Oxide Semiconductor
NCs	Nano Composites
OSHA	Occupational Safety and Health Administration
ppm	Parts Per Million
PL	Photoluminescence
RF	Radio-Frequency
RGO	Reduced Graphene Oxide
RPM	Revolutions Per Minute
RT	Room Temperature
SEM	Scanning Electron Microscope

Sn-ZnO	Sn Doped Zinc Oxide
TCO	Transparent Conducting Oxide
TEM	Transmission Electron Microscopy
UV-Vis	Ultra Violet Visible
VBM	Valance Band Maximum
W-H plot	Williamson-Hall Plot
wt.%	Weight Percentage
XRD	X-Ray Diffraction
ZnO	Zinc Oxide
ZnONPs	Zinc Oxide Nanoparticles

LIST OF SYMBOLS

Zn_i	Zinc Interstitials
$V_\circ$	Neutral Oxygen Vacancies
$V_\circ^-,\ V_\circ^{--}$	Charged Oxygen Vacancies
a, c	Lattice Parameters
Zn^{2+}	Zinc Ion
O^{2-}, O^-	Oxygen Ion or Species
O_i	Oxygen Interstitial
V_{Zn}	Zinc Vacancies
O_{Zn}	Oxygen Anti-Site
Zn_O	Zinc Anti-Site
I_0	Intensity of Incident Light
I	Intensity of Transmitted Light
t	Thickness of Film
α	Absorption Coefficient
T	Transmittance
E_g	Band Gap
ν_p	Frequency of Phonon
D	Crystallite Size
d	Lattice Spacing
2θ	Diffraction Angle
ε	Lattice Strain
E	Amplitude of Beam
$I_r(0)$	Flux Associated with Coherent Interference
$I_r(x)$	Flux Associated at Path Difference x
$R^{'}$	Molecule of Reductive Gas
R_a	Resistance of Sensing Element in Air
R_g	Resistance of Sensing Element in Gas
$R\ or S$	Gas Response or sensitivity

LIST OF TABLES

LIST OF FIGURES

TABLE OF CONTENTS

Page No.

CHAPTER 1

1. INTRODUCTION

In this chapter, a brief history of gas detection, improvement in the gas detection technology using nanostructured zinc oxide (ZnO) and the properties of ZnO will be discussed.

1.1 History of Gas Detection

Due to increasing worldwide industrialization, daily exposure to toxic gases such as methane, ethanol, ammonia, acetone, propanol, hydrogen sulfide, etc is increasing. For our own health security, it is important to monitor these toxic gases. Ever since people worked in coal mines, it has been imperative to monitor toxic gases. Around 2000 years ago, Lucretius, a poet, proposed a straightforward explanation for the sense of smell. He assumed that the "palate" had tiny pores of different sizes and forms. Every odor-producing material released tiny molecules of certain sizes and forms, and when these molecules entered the palate pores, the odor was detected. Each odor's identity depends on which pores the molecules filtered through (Amoore *et al.,* 1964).

The typical operating method, in the ancient time, was to send a recruit down into the coal mine with a torch and cover them with a damp blanket to identify any odorless gases, such as methane gas. Small air pockets would flare up, while large ones would require a fresh volunteer.

The well-known "canary in a coal mine" was the next development in gas detection technology. Raucous canaries were introduced into the mines by employees long before Sting began singing about them. If the birds stopped chirping, there was thought to be a leak. As the canneries began to rattle in their cages, signaling their last moments, miners started to evacuate the mine.

A "flame light" came next. Before miners entered the mine, a median level could be measured. They observed an oxygen-deficient environment if the flame crossed below the line and an oxygen-rich environment if it crossed above the line. Other gases were present if various hues were flickering.

In the 1920s, major advancements in gas detection were achieved. Dr. Riken, from Japan, in collaborative works with RKI Instrument in North America, a leading company, developed the first combustible toxic gas detector. A technique for identifying flammable gases was also developed by Standard Oil Company researchers using Platinum catalysts.

The next step in advancement in gas detection was accomplished in 1952 with the

evolution of the gas chromatography technique, introduced by Martin and James (Bartle & Myers, 2002). For use with gas chromatography equipment, a sensitive and stable detector was built on the basis of the unique ionization characteristics of argon. The detector can detect as few as 2–10–12 moles of the majority of organic compounds, and its response to various molecular species was remarkably consistent and linear with concentration over a broad range.

Based on the discovery that the mechanisms of gas adsorption and desorption modify the conductivity of metal oxide film, Seiyama, and their group invented a gas detection method utilizing a metal oxide semiconductor thin film in 1 962. They used ZnO films with a thickness range from 20 to 1000 Å that were deposited on borosilicate glass by vacuum evaporation of metallic zinc and then oxidization of the resulting residue in the air at 450 °C for 10 hours (Seiyama *et al.,* 1962; Seiyama & Kagawa, 1966). They were able to detect a variety of gases, including toluene, benzene, ethyl ether, ethyl alcohol, propane, carbon dioxide, etc. with just a slight change in conductivity. To the best of my knowledge, it was the first r eport o f a g as s ensor m ade o f Z nO. The experimental arrangement of the gas sensing device is shown in Figure 1. It consists of a borosilicate glass tube with an internal diameter of 8 mm. It is joined to the outlet of the gas chromatograph. Nitrogen gas was used as the carrier gas. The film was heated using the external heater. The sensing element was connected to the resistor (R_s) in series to convert the current into voltage. The voltage drop across the R_s was recorded without amplification before and during the flow of gas. In the past 60 years, gas detection using various metal oxide semiconductors has resulted in greater improvements in gas sensing technology (Lovelock, 1958).

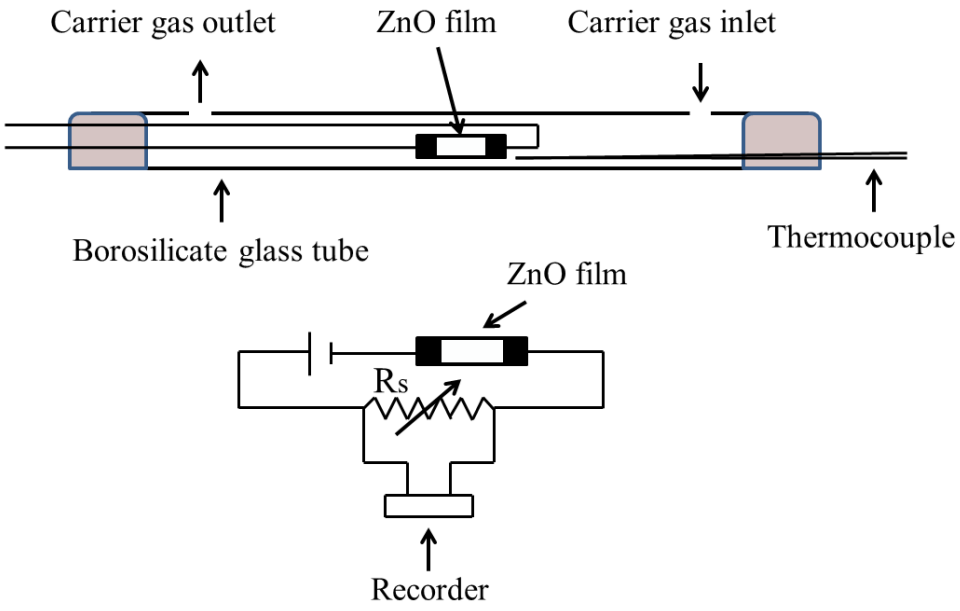

Figure 1: Experimental arrangement of a gas sensor set up (Seiyama *et al.*, 1962)

1.2 Background

The evolution of metal oxide semiconductors (MOS) has resulted in drastic improvements in science & technology. Metal oxide semiconductors such as Zinc Oxide (ZnO), Copper Oxide (CuO), Iron Oxide (Fe_2O_3), Titanium Oxide (TiO_2), Tin Oxide (SnO_2), Tungsten oxide (WO_3) Indium Oxide (In_2O_3) Cerium Oxide (Ce_2O_3), etc are very potential materials for the fabrications of future devices such as gas sensors, bio-sensor devices (Ansari *et al.*, 2008), water purification, photocatalysis, field emission (FE) devices (Lee *et al.*, 2002), transducers, piezoelectric sensors (Arnold *et al.*, 2003) and resonators (Klingshirn, 2007), transparent electrodes (Wahyuono *et al.*, 2016), optoelectronic devices, dye-sensitized solar cells (Qiang *et al.*, 2016; Roopa Kishore *et al.,* 2021; Kashyout *et al.*, 2010; Qi *et al.,* 2008; Chen *et al.,* 2017; Zhu *et al.,* 2017; Comini *et al.,* 2000). The MOS nanomaterials are very interesting due to their various features such as easy fabrication, low cost, good thermal and chemical stability, high photostability, etc. Their physical and chemical characteristics are strongly affected by parameters: size and shape (Wang *et al.,* 2008).

Typically, ZnO is an n-type metal oxide semiconductor. It has a band gap of 3.37 eV. It possesses a large exciton binding energy of about 60 meV at ambient temperature (Wahyuono *et al.,* 2016). ZnO has been regarded as the potential material for resistive-type gas sensors. The gas sensing efficiency of ZnO can be changed by metal doping into it, fictionalizations by other noble metal particles, compositing with other metal oxides, and UV activations (Zhu & Zeng, 2017). Furthermore, the potential of a metal oxide semiconductor for gas sensing action depends on the interaction of analyte gas molecules and oxygen species that has been adsorbed on the surface of sensing materials, which, then depends on the surface morphology of the sensing materials. It is also influenced by external factors including operating temperature, kind of exposed gas, and sensor geometry (Ansari *et al.,* 2008; Arnold *et al.,* 2003; Lee *et al.,* 2002).

There are several chemicals as well as physical routes to deposit ZnO films such as spin coating, spray pyrolysis, physical vapour deposition, chemical vapour deposition, dip coating, sol-gel, laser ablation, sputtering, etc. (Hasnidawani *et al.,* 2016; Shrestha *et al.,* 2010; Mani & Rayappan, 2013; Marouf *et al.,* 2016; Mostafa & Mwafy, 2020; Shinde *et al.,* 2005; Sun *et al.,* 2019; Saravanavel *et al.,* 2021). With the development of various synthesis techniques, ZnO nanostructures can be easily grown on glass, quartz, and flexible polymer substrates in different morphologies: nanowires, nanorods, nanofibers, nanoflakes, etc (Blachowicz & Ehrmann, 2020; Kaneti *et al.,* 2013; Mitra *et al.,* 1998; Wang, 2009; Yi *et al.,* 2005). The ZnO films prepared on the glass substrate in different morphologies are depicted in Figure 2. The effectiveness of ZnO for gas sensing is highly influenced by the presence of oxygen vacancies in its nanostructure, which can

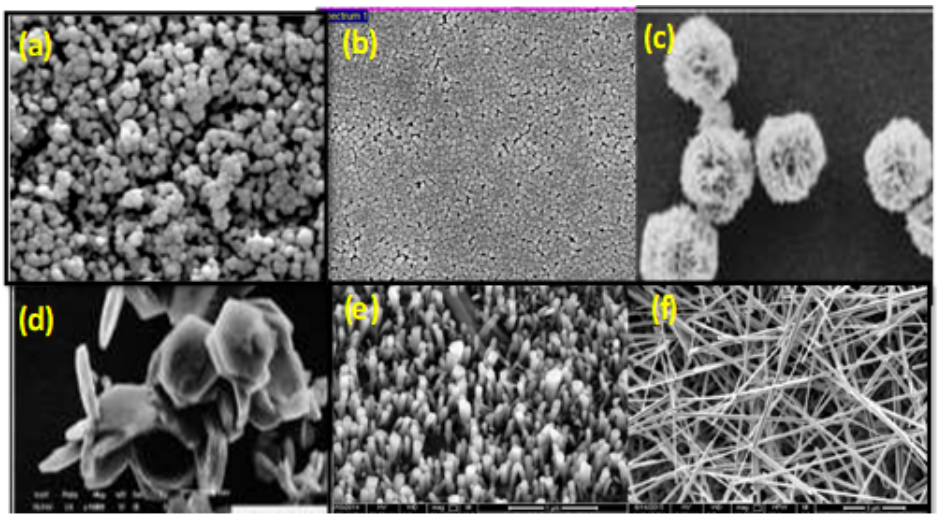

Figure 2: SEM micrographs of ZnO nanostructures (a) nanoparticles, (b)Nanostructured film (c) nanoflowers (d) nanoflakes (e) nanorods and (f) nanofibers (Hasnidawani *et al.*, 2016; Shrestha *et al.*, 2010; Marouf *et al.*, 2016; Mostafa & Mwafy, 2020; Shinde *et al.*, 2005; Sun *et al.*, 2019; Saravanavel *et al.*, 2021)

be enhanced by modifying the surface morphology (Zhu & Zeng, 2017). However, ZnO has some drawbacks due to the abundance of grain boundaries (GBs) and inherent point defect states. Figure 3 shows the defect states along with the ionization energies within the band gap of ZnO. Here, i = interstitial, O = oxygen, Zn = Zinc, V = vacancy and x = zero or neutral charge. The terms in subscript denote the atomic sites and those in superscript denote the charges. The neutral and charged Zn interstitials are Zn_i^x, Zn_i^+, and Zn_i^{++}. The neutral and charged zinc vacancies are V_{Zn}^x, V_{Zn}^-, V_{Zn}^{--}. Similarly, the neutral and charged oxygen vacancies are V_o^x, V_o^+, V_o^{++} (Kaur et al., 2015; Schmidt-Mende & MacManus-Driscoll, 2007). Zn_i^x, Zn_i^+, Zn_i^{++}, V_o^x, V_o^+, V_o^{++} are donor defects and V_{zn}^x, V_{zn}^-, V_{zn}^{--} are acceptor defects. The defects ionization energy has values ranging from 0.05 to 2.8 eV. The oxygen vacancies and Zn interstitial defects are the most common ionic defects. As both defects can donate two electrons, one cannot say which defects dominate in native undoped ZnO by the electrical measurement. The concentration of the various defects depends on the temperature. It is due to the different ionization energies of different defects. The partial pressures of oxygen and zinc are also important factors. At high temperatures, the oxygen vacancies predominate depending upon the ratio of the partial pressure of oxygen to that of zinc. Under the situation with a high concentration of zinc vapour, Zn interstitials predominate as defects (Schmidt-Mende & MacManus-Driscoll, 2007). By increasing the oxygen vacancies, the concentration of oxygen molecules to be adsorbed can be increased to maintain the charge neutrality and hence the gas sensing efficiency of ZnO can be increased. The grain boundary (GB) regions in ZnO nanostructure contains numerous defects which create the potential barriers (or depletion layers) at the interfaces of grains (Gupta & Carlson, 1985). The depletion layers developed at the grain boundary strongly prevent the drift of majority

charge carriers.

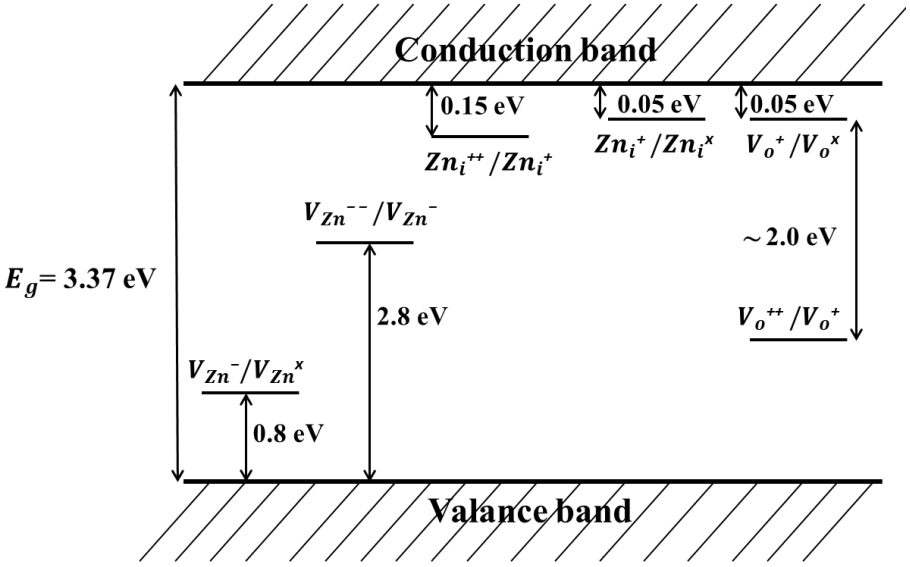

Figure 3: Energy states of native point defect states in band gap region of ZnO (Schmidt-Mende & MacManus-Driscoll, 2007)

The widening of the depletion layer at the grain boundary of ZnO by extracting the electrons from the conduction band with the adsorption of oxygen molecules is shown in Figure 4. It reduces the conductivity of ZnO which greatly helps to monitor the gas-sensing performance of ZnO. Based on these characteristics, numerous reports on ZnO-based gas sensors have been published. Most of the papers have reported operating

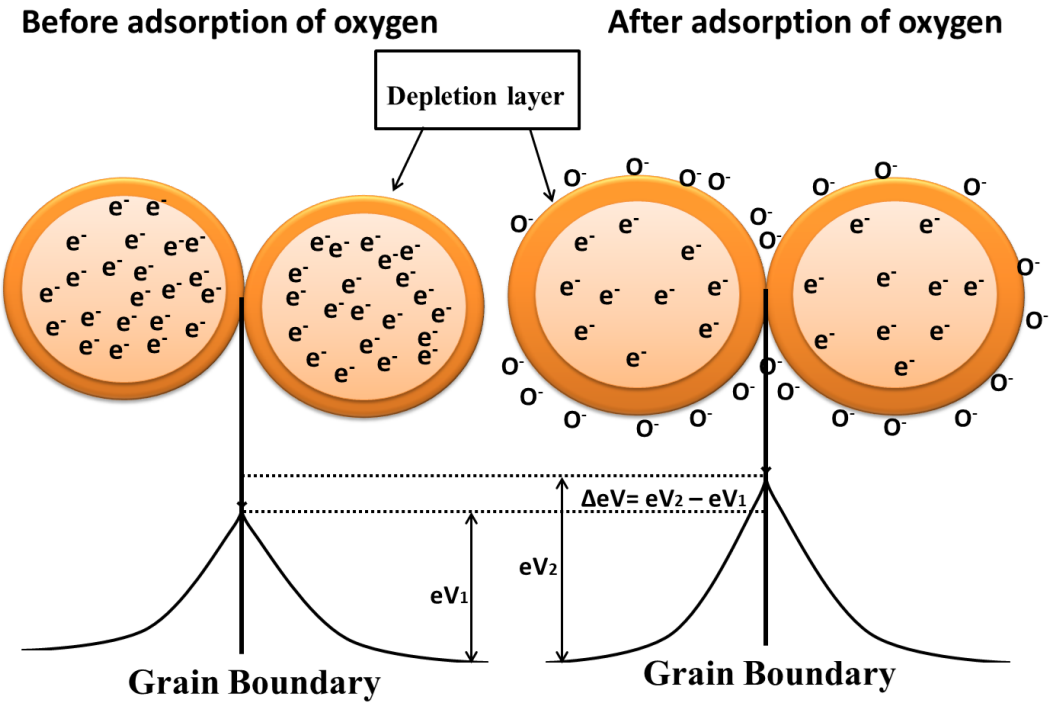

Figure 4: Schematic of widening of the depletion layer at the grain boundary of ZnO due to the adsorption of oxygen (Dey, 2018)

temperatures greater than 300 °C with low sensitivity or response. So, the problem of reducing the working or operating temperature of ZnO gas sensors with significant gas response or sensitivity still exists.

In this thesis work, the electrical, optical, structural, and gas sensing properties of the undoped, metal-doped, and metal-metal-doped ZnO films grown on the glass substrates are discussed. The films were grown using suitable methods such as spin coating, spray pyrolysis, co-precipitation, etc.

1.3 Properties of ZnO

1.3.1 Crystal Structure

ZnO crystallizes in three different forms of crystal lattices; wurtzite, zinc blende and rock salt. Among these three crystal lattices, the wurtzite structure is thermodynamically stable at ambient condition (Rai *et al.,* 2022). This structure is mostly used as a transparent conducting oxide (TCO) in the field of thin film technology. Figure 5(a) depicts the schematic of the wurtzite structure with hexagonal symmetry (Özgür *et al.,* 2005). In the hexagonal structure a = b ≠ c, where the lattice parameter a is called the basal lattice parameter and c is called the axial lattice parameter. The values of a and c are 3.2498 Å, and 5.20660 Å, with c/a ratio of 1.60 (Zhang *et al.,* 2012). The lattice parameters can

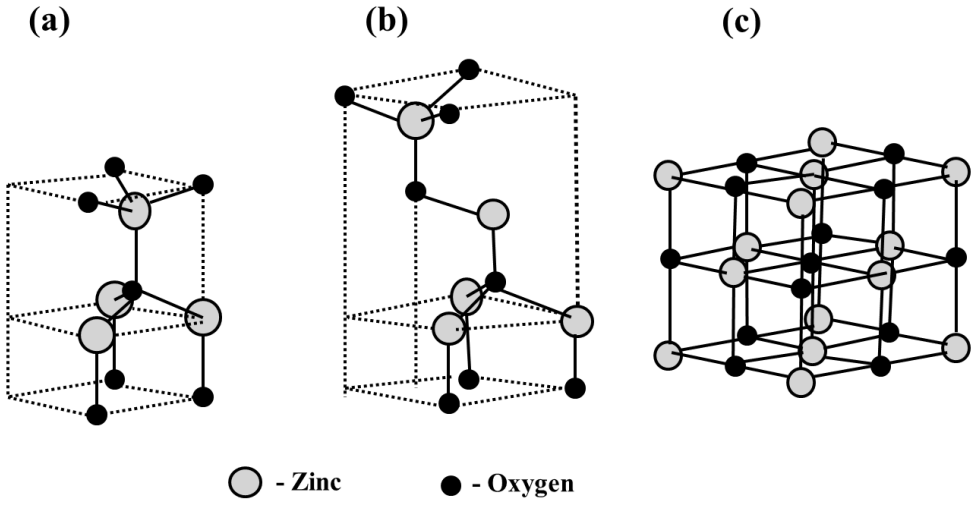

Figure 5: (a) Hexagonal wurtzite, (b) zinc blend and (c) rock salt structure of ZnO (Rai *et al.,* 2022)

be varied by lattice strain in ZnO (Hsu *et al.*, 2014). Wurtzite structure consists of alternate hexagonally close-packed (HCP) sub-lattices, with one kind of atom replaced by another along the c-axis. Ions Zn^{2+} and O^{2-} are alternately piled along the c-axis. The top and bottom surfaces are terminated into Zn^{2+} and O^{2-} ions of basal planes as illustrated in Figure 5(a). The basal planes are perpendicular to the c-axis and have different surface energies, which makes them favorable to crystal development. The polar

surface of ZnO molecules favors adhering to the incoming precursor molecules. The Zn^{2+} terminated surface becomes an O^{2-} terminated surface, or vice versa, after the deposition of the layer. This process is repeated and promotes growth along the c-axis (Chevtchenko *et al.,* 2006; Xu & Wang, 2011). The surface morphology of ZnO varies with the preparation methods due to the difference in growth rate and the systems' free energy (Eftekhari *et al.,* 2006). The zinc blend structure of ZnO is shown in Figure 5(b). Unlike the wurtzite structure, the zinc blende structure has cubic symmetry and is metastably derived from the mineral compound ZnS (Rai *et al.,* 2022). The symmetry is made up of two face-centered cubic sublattices that are shifted across the body diagonally by 1/4 of the length of the body. Each unit cell has 8 atoms: 4 of them are of one kind such as group II and another 4 atoms are of another kind such as group VI. Each atom of one kind is tetrahedrally structured with the four atoms of another kind. Due to tetrahedral coordination in zinc blend, the 12 next closest neighbors and the 4 closest neighbors have a comparable bond distance as in the wurtzite structure. The zinc blend structure differs from the wurtzite structure only in the bond angle of the second-closest neighbor atom and in the stacking pattern of densely packed diatomic planes (Rai *et al.,* 2022).

The rock salt structure is another possible structure of ZnO which is shown in Figure 5(c). It is obtained by applying high pressure to the wurtzite structure. The rock salt structure is six-fold coordinated and belongs to the Fm3m group. ZnO has a hexagonal wurtzite structure at a temperature and pressure of T = 298.15 K and p = 100 kPa, respectively (Rai *et al.*, 2022). Increasing the pressure of about 9 GPa, ZnO changes into rock salt polymorph (de Brito Farias & Watanabe, 2012)

1.3.2 Optical Properties

ZnO has gained interest due to its wide band gap and high room temperature exciton binding energy. It is highly transparent in the visible spectrum and a strong UV emitter as well as absorber (Cui *et al.*, 2016; Lany & Zunger, 2005; Zhang *et al.,* 2012). The optical characteristics of ZnO are influenced by its intrinsic and extrinsic defects. Light interacts with ZnO through a variety of physical processes, including optical absorption, transmission, reflection, photoluminescence, and cathodoluminescence. The various factors: surface roughness, scattering at the grain boundary, band gap, and oxygen defects influence the optical transmissions of ZnO. For example, the transmittance of undoped and 3-9% Fe-ZnO dramatically reduced in the near UV region due to the absorption (Figure 6). For all samples, the absorption edge emerges at about 360 nm. The absorption edge is shifted towards a shorter wavelength on increasing the Fe content. The transmittance is decreased on increasing the Fe content. The oxygen deficiencies are associated with decreased optical transmittance (Wisz *et al.,* 2017).

The light absorption causes the transition of electrons from the valance band to the

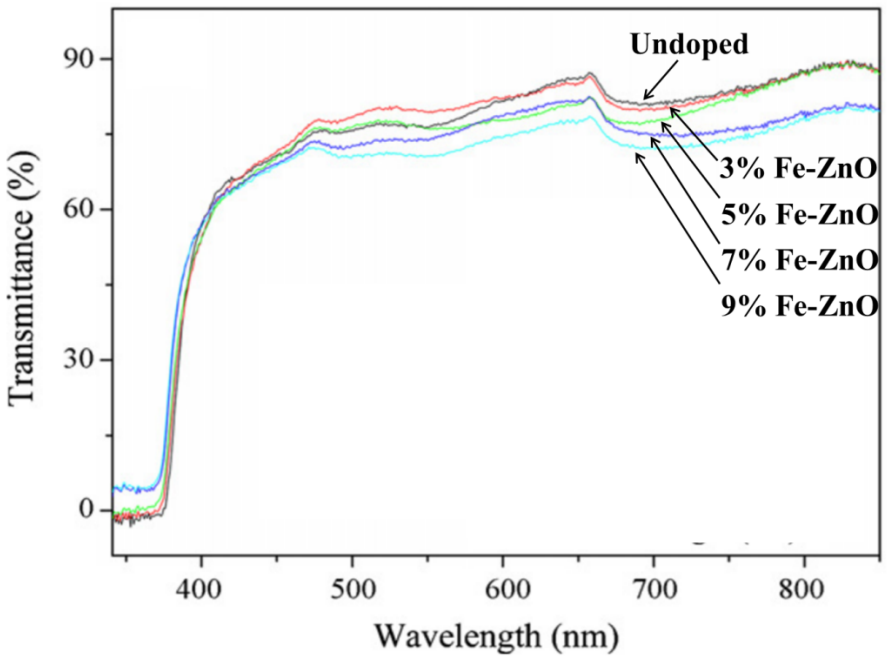

Figure 6: Optical transmission spectra of ZnO and 3-9% Fe-ZnO films (Zhang *et al.*, 2009)

conduction band, producing holes in the valence band and electrons in the conduction band. These electron-hole pairs are bounded by coulomb interaction and are located at the same spatial point. Such electron–hole pairs are called excitons. Excitons serve as energy carriers similar to photons. The excitons are formed only when the electron and hole have the same group velocity (Ferblantier *et al.*, 2005; Vasudevan *et al.*, 2022). The transition of electrons between various bands is shown in Figure 7. The electron transition from the valence band (VB) to the conduction band (CB), from defect level(DL)

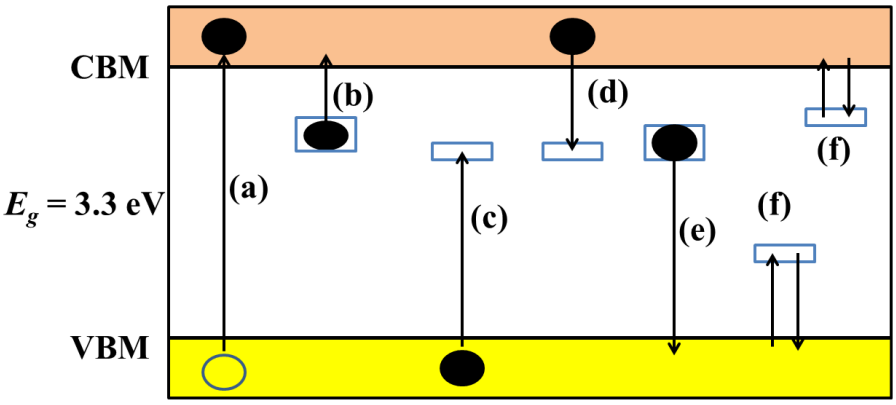

Figure 7: Light interaction on ZnO (a) band to band transition, (b-c) intrinsic defect transition, (d) capture, (e) recombination, (f) trapping and de-trapping (Özgür *et al.*, 2005)

to the CB, and from the VB to DL due to the optical absorption are depicted in Figure 7(a-c). Similarly, the electron transition from the conduction band to the defect state and from the defect state to the valance band is shown in Figure 7(d-e), which corresponds to the optical emission in the materials. The trapping and de-trapping of charge carriers from

the conduction band and valance band by defect centers during the absorption process are represented in Figure 7(f). Available defect states present in the band gap region are responsible for the optical absorption and emission in the materials (Özgür *et al.,* 2005). It is also affected by its surface morphology. Figure 8 depicts the absorbance spectra of ZnO films of different surface morphologies such as nanoplates, nanoflowers, and nanofibers. The ZnO film exhibits a significant absorption around 380 nm . The absorption edge corresponding to ZnO nanofibers is slightly moved towards the long wavelength regions in comparison to that corresponding to ZnO nanoflowers and nanoplates (Cui *et al.,* 2016). The distribution of defects in ZnO affects the frequencies of emission spectra.

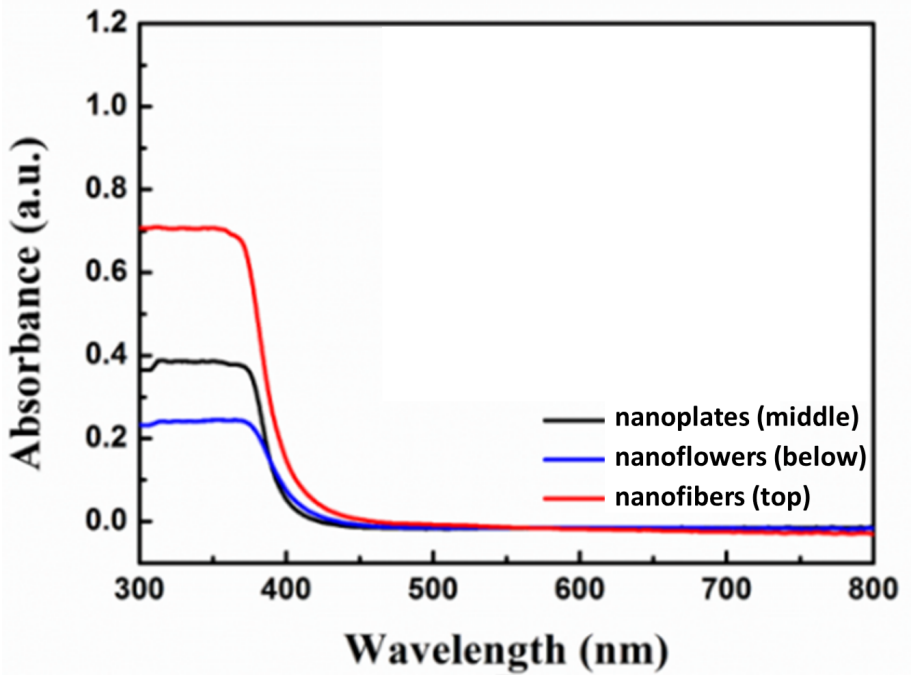

Figure 8: Absorbance spectra of ZnO films of different surface morphologies (Cui *et al.,* 2016)

Shallow-level and deep-level defects in ZnO are the causes of defect emissions in the visible range. Figure 9 shows the band diagram of deep-level emission of ZnO. The three basic visible emissions are blue-green, yellow, and orange-red emissions (Djurišić *et al.,* 2007; Lany & Zunger, 2005). These emissions depend on the types of defects formed and are independent of the surface morphology. The defect states in ZnO are formed during the growth phase and are controlled by factors such as the deposition temperature, oxygen pressure, and annealing temperatures. Neutral oxygen vacancies (V_o), charged oxygen vacancies (V_o^-, V_o^{--}), oxygen interstitial (O_i), zinc vacancies (V_{Zn}), zinc interstitial (Zn_i), oxygen anti-site (O_{Zn}) and zinc anti-site (Zn_o) are the familiar intrinsic defects in ZnO. The visible emission in the wavelength range of 425 nm to 700 nm is caused by these defects. Green emissions are thought to originate from oxygen vacancies (Bube, 1992).). The two intrinsic defects that occur most frequently in ZnO are oxygen vacancy and zinc vacancy. These defects are introduced when the host atom, say zinc or oxygen,

is missing in the usual crystal structure. By adjusting the kind and number of defect states, the electrical, optical, and gas-sensing properties of ZnO can be manipulated.

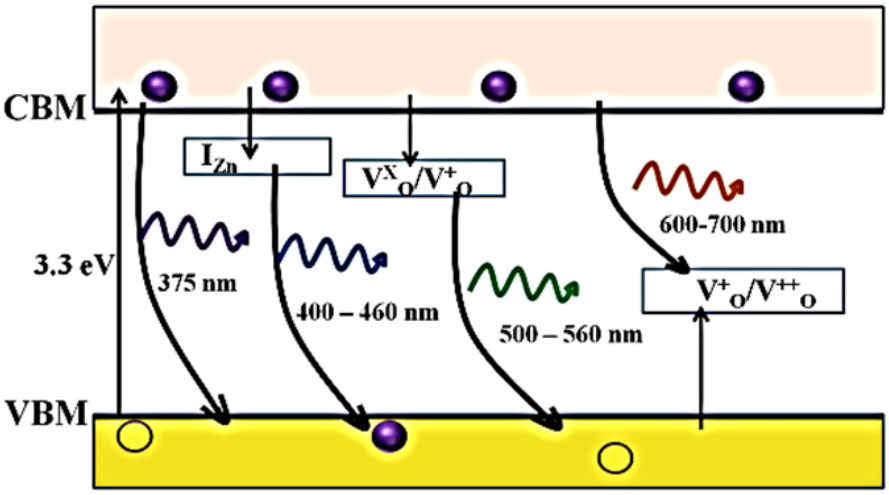

Figure 9: Band diagram of deep level emission of ZnO nanostructure (Bube, 1992)

1.3.3 Electrical Properties

In-depth understanding of the electrical properties of MOS is required for gas sensing. ZnO has the carrier concentrations between 10^{16} and 10^{19} cm^{-3} (Li *et al.*, 2003; Tampo *et al.,* 2004). At room temperature, the electron mobility ranges from 0.1 $cm^2V^{-1}s^{-1}$ to 100 $cm^2V^{-1}s^{-1}$ (Baik & Lee, 2005; Nakahara *et al.,* 2001; Lau & Fonash, 1987; Mridha & Basak, 2007). The electrical properties of ZnO can be altered by metal doping and the value of resistivity depends on the types of metal doped into it (Shrestha *et al.,* 2010; Mridha & Basak, 2007; Xu *et al.,* 2004). Figure 10(a)-(b) shows the

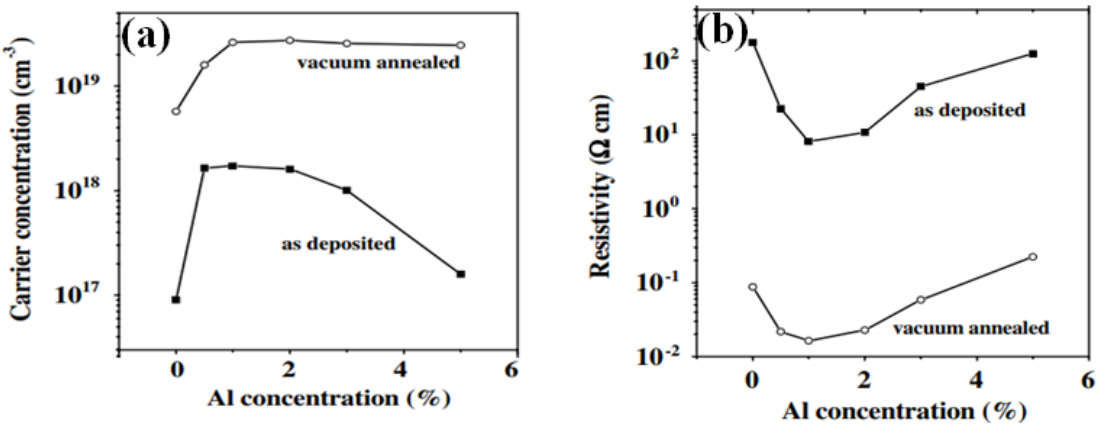

Figure 10: Variation of carrier concentrations and resistivity of as-deposited and vacuum annealed Al-ZnO films with different Al concentration (Mridha & Basak, 2007)

results of the measurement of carrier concentration and resistivity of as-deposited and vacuum-annealed Al-ZnO films. The carrier concentration of vacuum-annealed films

is more than that of the as-prepared film due to the reduction of the thickness of the film (Mridha & Basak, 2007; Liu *et al.,* 2014). The electrical property of ZnO is also temperature dependent. Figure 11 shows the variation of resistance of post-heated and preheated Al-ZnO films with t emperature. Firstly, the resistance of ZnO decreases on heating, acquires a minimum value at a particular temperature, then increases on further heating, and then acquires a stable saturation value. The curve is divided into three parts: region I, region II, and region III. The reduction of resistance, in region I, is due to the thermal activation of electrons into the conduction band. The increase of

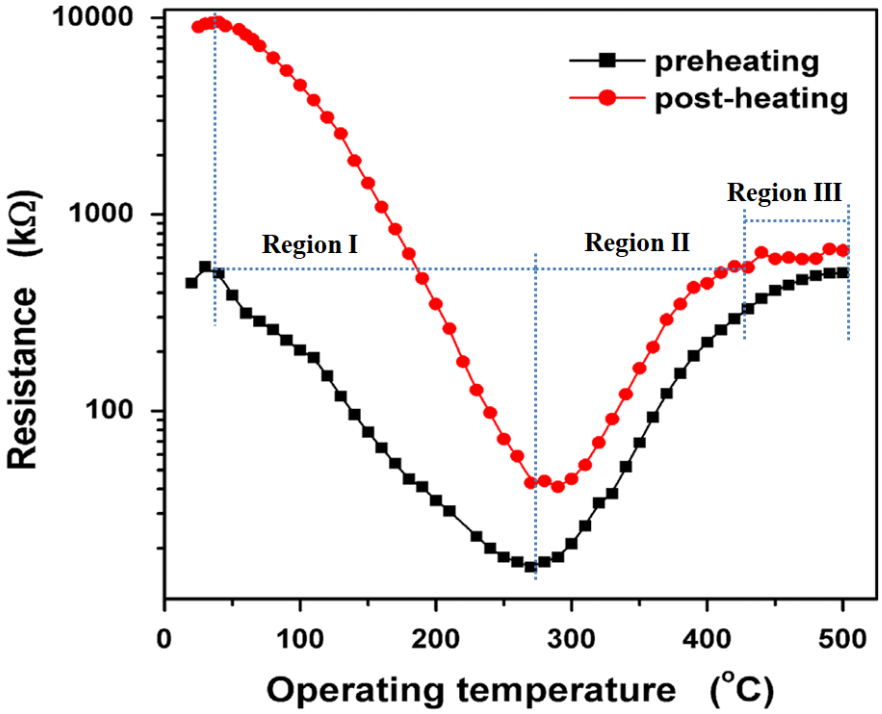

Figure 11: Variation of resistance with a temperature of Al-ZnO films prepared under different heat-treating processes (Liu *et al.,* 2014)

resistance, in region II, is due to oxygen adsorption on the ZnO surface. The adsorbed oxygen captures electrons from the conduction band of ZnO due to which the electron concentration decreases and resistance increases. The stable value, in region III, is due to the equilibrium between the thermal excitation of electrons and oxygen adsorption (Liu *et al.,* 2014).

1.3.4 ZnO as a Gas Sensor

The phenomenon of oxygen adsorption and desorption on the ZnO surface is responsible to change its conductivity. In the ambient atmosphere, the oxygen molecules present in the surrounding atmosphere are adsorbed on the ZnO surface, which extracts the electrons from the conduction band to produce negatively charged oxygen species (O^-, O^{2-}, and O_2^-). As a result, the resistance of the ZnO surface increases. On the exposure

of analyte gases (reducing gases), the molecules of the gas interact with the oxygen species adsorbed on the surface of ZnO and release the electron back to the conduction band. Hence, the resistance decreases. The gas-sensing characteristics of ZnO with exposure to various toxic and non-toxic gases were studied by a number of researchers. The gas sensing performance of the ZnO depends on (a) the number of adsorbed oxygen species (Zhu & Zeng, 2017), (b) surface morphology (Kaneti *et al.,* 2013), and (c) the operating temperature (Joshi *et al.,* 2021). The gas response can be increased by increasing the oxygen vacancies or the specific surface area (Zhu & Zeng, 2017). The specific surface area depends on the nature of the surface i .e. surface m orphology. The ZnO nanostructure having a large surface area exhibited a higher gas response to the analyte gas (Hosseini *et al.,* 2015).

The ZnO sensor exhibits good response to the gases at particular higher operating temperatures (Kaneti *et al.,* 2013; Radhakrishnan *et al.,* 2021; Seiyama *et al.,* 1962). The operating temperature depends on the activation energy. Activation energy is the least energy needed to excite atoms or molecules to a state in which they undergo a chemical reaction. (Hongsith *et al.,* 2010; Khayatian *et al.,* 2014). The operating temperature can be reduced by decreasing the activation energy. The activation energy of the reaction and surface morphology can be changed by metal doping and metal-metal doping into ZnO (Acharya *et al.,* 2012; Bougrine *et al.,* 2003; Lokesh *et al.,* 2016; Santhaveesuk *et al.,* 2010). Thus, metal doping and co-doping into ZnO could be a possible way of improving the sensitivity or gas response even at the lower operating temperature of ZnO sensors.

1.4 Motivation

Due to increasing industrialization, the production of toxic vapour: ammonia, acetaldehyde, formaldehyde, methane, ethanol, and acetone is increasing worldwide. Exposure to these toxic vapour has an adverse effect on living beings. E xposure to even low concentrations of acetone can seriously harm human vital organs like the liver, lungs, kidney, and central nervous system (Liu *et al.,* 2014). Occupational Safety and Health Administration (OSHA) regulation states that exposure of NH_3 with a lower limit of 35 ppm for 8 h and an upper limit of 50 ppm for 5 min poses serious health risks. This threshold limit has a direct impact on one's well-being (Mani & Rayappan, 2013). Ethanol intake in excess has harmful effects on living creatures (Yang *et al.,* 2009). Hence, the proper monitoring of these chemicals is necessary to develop a clean and healthy society. The nanostructured semiconductor-based devices help to control the existing demand. Many researchers are concentrating on the creation of low-cost and environmentally friendly gas sensing devices using nanomaterial of metal oxide semiconductors because of their tunable electrical and optical properties with respect to requirements. In recent times, MOS-based gas sensors having a high operating temperatures greater than 300

°C and low responses are highly reported. To the best of my knowledge, the reports on low-temperature MOS-based gas sensors with high response are limited which motivated us to work in this field. X-ray diffraction (XRD), Scanning Electron Microscope (SEM), Energy Dispersive X-ray (EDX), and Fourier Transform Infra-Red (FTIR) Spectroscopy is the major effective tools used for the characterization of the ZnO films. A series of meticulous experiments have been done for the confirmation of quality material deposition. The reported results obtained here have shown significantly the development of the experimental works on nanomaterial at our university.

1.5 Rationale of Study

With the evolution of metal oxide semiconductors, large improvements have been made in gas detection technology. On the other hand, the MOS gas sensors continue to have some drawbacks such as low gas response or sensitivity and high operating temperatures. The principle of the MOS gas sensor is based on the phenomena of adsorption and desorption of the oxygen molecules of the ZnO surface, which are largely determined by its surface structure. Hence, an in-depth understanding of surface morphology is crucial for MOS gas sensor fabrication (Wei *et al.*, 2011). The ZnO nanostructures with a variety of morphologies, including nanorods, nanofibers, nanoflakes, nanosheets, nanoparticles, etc. have been extensively studied to explore the factors affecting the performance of ZnO-based gas sensors. The ZnO having a large specific area adsorbs the more oxygen molecules and results in higher gas response or sensitivity. The specific surface area also depends on the thickness of the film. Hence, the role of optimization of film thickness is also an important task in thin film-based gas sensors. Operating temperature is another vital sensing parameter in ZnO-based sensors. The gas response of MOS based sensor inherently depends on the operating or working temperature. The working temperature is correlated with the activation energy (Khayatian *et al.,* 2014; Zhu & Zeng, 2017). The reaction rate coefficient of the molecules of exposed gas with the adsorbed oxygen species is higher at higher operating temperatures. So, on increasing temperature, the value of gas response increases and becomes maximum at a fixed temperature at which the thermal energy is equal to the activation energy of the reaction. On further increasing the temperature, the oxygen molecules desorb from the surface of the ZnO, which reduces gas response (Hongsith *et al.,* 2010; Khayatian *et al.,* 2014). The electrical, optical, structural, and surface properties along with the activation energy of the ZnO can be tailored by various strategies like doping metal into the ZnO, functionalization by noble metal particles on the ZnO surface; fabricating nanocomposites of the ZnO with other metal oxides, etc. These methods are helpful in enhancing gas sensing performance. In these prospects, researchers are affording to enhance the sensing performance at lower operating temperatures. With these motivations, this research work on the study

of the ZnO nanostructure for sensing various toxic gases has been carried out. In this investigation, it was expected that the gas response can be increased or the operating temperature of ZnO-based gas sensors can be reduced by metal doping and co-doping into the ZnO which will be helpful to monitor the traces of toxic gases in the environment and will play an important role in the development of clean and healthy society.

1.6 Objectives

Based on the background of the study, there is still a problem to get a gas sensor working at lower operating temperatures with an increased gas response. Metal doping and metal-metal co-doping into ZnO could be one of the possible ways of enhancing the gas response and lowering the operating temperature of the ZnO-based gas sensor. Keeping this in mind, the following objectives were set in this study.

General Objectives:

To study the structural, electrical and optical properties of the undoped, metal-doped and co-doped ZnO films for gas sensing applications

Specific Objectives:

(i) To prepare undoped, metal (Fe & Sn) doped and metal co-doped (Fe-Al) Zinc Oxide (ZnO) films by employing spin coating, spray pyrolysis and doctor blade methods.

(ii) To study the structural, electrical, and optical properties of the prepared samples.

(iii) To study the sensing characteristics of ZnO-based gas sensors towards various toxic gases such as ethanol, acetone, and ammonia.

1.7 Organization of the Thesis

The structure of the thesis is organized as follows:

(i) In Chapter 1, a brief history of gas detection, improvement in the gas detection technology using nanostructured zinc oxide (ZnO), properties of ZnO, motivation, and objective of the work are discussed. This chapter is named “Introduction”.

(ii) In Chapter 2, the available related literature about this work is discussed and the chapter is termed as “Literature Review”. This chapter aims to prepare the required background and justify the objectives of our work.

(iii) The experimental method, theoretical background, necessary formulas, and algorithm used during the entire work are presented in Chapter 3. This chapter is

named "Materials and Methods". The ZnO film deposition, its characterizations, and gas sensing measurements techniques are explored in this chapter.

(iv) The results of this work are presented and discussed in chapter 4 and this chapter is named “Results and Discussion”. This chapter is divided into 6 sections say 4.1, 4.2, 4.3, 4.4, 4.5, and 4.6. In section 4.1, the results and discussion of characterizations and ammonia vapour sensing properties of ZnO film are included. In section 4.2, the acetone sensing performance of ZnONPs films at various temperatures is discussed. In section 4.3, the result of ethanol sensing performance of undoped and Fe-ZnO films is presented and discussed. Similarly, the results of ethanol sensing performance of undoped and Sn-ZnO films prepared by spray pyrolysis technique are discussed in section 4.4. Likewise, the gas sensing properties of Fe-Al-ZnO films prepared by the spin coating technique are discussed in section 4.5. The effect of applied potential on the gate electrode in the gas sensing performance of ZnO is discussed in section 4.6.

(v) The conclusions and possible extensions of the current work in the future are presented in Chapter 5. The chapter is named “Conclusion and Recommendation”.

(vi) Finally, the summary is presented in chapter 6.

CHAPTER 2

2. LITERATURE REVIEW

Literature on the ZnO film preparation and characterization for gas sensing applications are reviewed systematically. Some of them are discussed here.

2.1 Gas sensing characteristics of MOS sensors

Metal oxide semiconductors (MOS) have caught the interest of researchers for gas detection due to their features such as portability, affordability, and high response. Among various MOS, ZnO is nontoxic, inexpensive, and the most attractive potential material for the detection of harmful gases (Eftekhari *et al*., 2006; Kaneti *et al*., 2013; Tampo *et al.,* 2004). Many efforts have been done to detect toxic gases using ZnO since 1962 (Seiyama *et al.,* 1962). The change in the electrical conductivity of metal oxide semiconductors with the exposure of gas was first noted in the 1950s by Carl Wagner (Wagner, 1950). T. Seiyama fabricated ZnO based gas sensor in 1962 to detect several gases such as toluene, benzene, ethyl ether, ethyl alcohol, propane, and carbon dioxide at an operating temperature higher than 400 °C. In 1966, T. Seiyama and S. Kawaga succeeded to detect ethanol vapour and CO_2 using ZnO film. They concluded that the gas sensing characteristics of the ZnO film are temperature dependent (Seiyama & Kagawa, 1966). In the presence of gas, the conductivity of ZnO changed only at a temperature greater than 200 °C. The change was fast at higher temperatures (>203 °C), which was due to the increment in the rate of adsorption and desorption of the oxygen species. The value of the response was higher at the higher temperature of 500 °C.

The ability of ZnO to detect gases is based on the phenomenon of oxygen molecule adsorption and desorption on its surface. In the air atmosphere, oxygen molecules are adsorbed on the surface of zinc oxide which takes the electrons from the conduction band and becomes oxygen ions. Hence, ZnO exhibits more resistance. At the exposure of analyte gas (reductive gas), the molecules of gas interact with the adsorbed oxygen ions, which makes the electron release again back to the ZnO. Hence, the resistance of ZnO decreases (Hassan *et al.,* 2014). This change of resistance determines the sensing ability of the ZnO sensor. In 2013, Kanetti and the group studied the gas sensing capability of ZnO synthesized in the form of nanoplates and nanorods, prepared by the solvothermal method. They reported that the sensitivity of the nanoplate-based sensor was 2 times greater than that of nanorod-based sensors. It was due to the higher specific surface area of the nanoplates (Kaneti *et al.,* 2013). Further, Cui and group, in 2016, prepared the ZnO with different morphologies: nanoflowers, nanorods, and nanofibers. Their results showed good gas response for ZnO nanofibers than other studied morphologies for the

formaldehyde detection at room temperature (Cui *et al.,* 2016).

The gas sensing capacity of ZnO is highly temperature dependent. The sensitivity of the ZnO sensor increases for increasing the temperature (Seiyama & Kagawa, 1966). It reaches the maximum value at a particular temperature and declines on further increasing the temperature (Khayatian *et al.,* 2014).). In 2010, Hongsith and the group introduced an explanation for the temperature-dependent gas-sensing characteristics of ZnO. The gas response depends on the reaction rate coefficient of the gas molecules exposed to the surface of ZnO and oxygen ions adsorbed to the ZnO surface, which further depends on the temperature of the ZnO surface. On increasing the temperature, the reaction rate increases and becomes maximum at a particular temperature when the thermal energy overcomes the limit of activation energy of the reaction and the high response results at that particular temperature. Above this particular temperature, desorption of oxygen occurs and response decreases (Hongsith *et al.,* 2010; Khayatian *et al.,* 2014). The operating temperature of the ZnO also depends on the activation energy. The activation energy of the ZnO can be adjusted by metal doping into it (Acharya *et al.,* 2012; Khalid *et al.,* 2019).

2.2 Undoped, metal-doped, and co-doped ZnO Gas Sensor

The investigation on the gas detection by ZnO has been accelerated after the reports published by Seiyama in 1962 (Seiyama *et al.,* 1962). A number of researchers synthesized the undoped and metal-doped ZnO films of different morphologies utilizing different techniques, to study its gas sensing task. The literature, related to this work, is studied systematically. Some of them are discussed below.

Bott, in 1984, investigated the sensing capabilities of crystalline ZnO film towards CO, H_2, CH_4, and water vapour in the temperature ranging from 300 to 500 °C. They reported that ZnO was more sensitive to CO and H_2 but insensitive to CH_4 and water vapour. Additionally, it showed good stability and a response time of ∼2 min (Bott *et al.,* 1984). Likewise, Saito and group also investigated the sensing capability of porous ZnO and Pt/ZnO ceramics towards CO and C_3H_8 at the high temperatures of 300 and 400 °C. Their results showed that ZnO exhibited the highest response of 18.4 for 4000 ppm of C_3H_8 and 6 for 4000 ppm of CO at a temperature of 400 °C respectively. On the other hand, the highest response of Pt/ZnO for the exposure of the same concentration of C_3H_8 and CO at the same temperatures were only 4.8 and 1.2 respectively (Saito *et al.,* 1985). Nanto H. and his research group prepared the pristine and metal (Al, Ga, In) doped ZnO films by sputtering technique and investigated their sensing performance with the exposure of 200 ppm of various gases; ammonia, hydrogen, butane, methane, ethyl alcohol, and acetone at the temperature of 350 °C. They reported the highest response

of 89 for 200 ppm of acetone when measured by undoped ZnO. Whereas the metal (Al, Ga, and In) doped ZnO showed the highest response (−94, −88, and −82) for the same concentrations of ammonia (Nanto *et al.,* 1986). After a few years in 1989, Lampe, U. & Muller, J. studied ZnO film for oxygen s ensing. They found that the resistance was increased first on increasing the pressure of oxygen and then acquired the saturation value. The resistance was decreased by decreasing the oxygen pressure (Lampe & Müller, 1989). Sberveglieri, G., and group also investigated the oxygen sensing task of pure ZnO and Li-ZnO films. These films were deposited on the glass substrates adopting RF sputtering technique. The results showed that the Li-ZnO was more sensitive than the undoped ZnO. It was due to the formation of a deeper donor level with respect to undoped film (Sberveglieri *et al.,* 1990). Mitra, P., and the group reported that the palladium-sensitized ZnO film shows maximum sensitivity of 99.9% with the exposure of 1 vol.% H_2 at the optimized temperature of 250 °C. (Mitra *et al.,* 1998).

Miki-Yoshida and coworkers in 2000, prepared metal (Al, In, Cu, Fe, and Sn) doped ZnO films by the spray pyrolysis m ethod. They studied the ethanol sensing capabilities of these films at temperatures ranging from 435–675K. According to their findings the 0.4 at. % Sn-doped ZnO and 1.8 at% Al-doped ZnO, showed a gas response of 190 and 160 respectively at the temperature of 675 K (Miki-Yoshida *et al.,* 2000). Wan and their group fabricated the ZnO nanowires with microelectromechanical system (MEMS) technology and studied their sensing characteristics towards ethanol at temperatures of 200, 250, and 300 °C. The result revealed the maximum response of 47 at 300 °C towards the exposure of 200 ppm of ethanol (Wan *et al.,* 2004).

In 2006, Chou and his coworkers prepared Al-ZnO films using RF sputtering techniques for ethanol sensing. These films were then characterized by using XRD and SEM for their structural and morphological study. They found a sensitivity of 20% at an exposure of 400 ppm of ethanol at 250 °C. The resistance was decreased upon introducing ethanol vapor into the chamber, and it was again increased when the gas was turned off (Chou *et al.,* 2006).

Choopun and group, in 2007, prepared ZnO nanobelt film u sing a n R F sputtering technique. The as-prepared film was used to detect the ethanol of different concentrations (50 - 2000 ppm) at different operating temperatures (200 - 290 °C). The sample showed the maximum response at 220 °C at an exposure of all ethanol concentrations. They expressed the sensitivity (S) empirically as $S = 1 + mC^n$, where C represents the gas concentration and m and n are constants. The value of m varies with the nature of the sensor material, the kind of analyte gas, and the operating temperature. The value of n depends on the kind of adsorbed oxygen species onto the sensor surface. It is 0.5 for O^{2-} and 1 for O^{-}. The value of n was reported to be 0.5, indicating that the adsorbed oxygen species was O^{2-} at 220 °C (Choopun *et al.,* 2007).

Liewhiran, & Phanichphant, in 2007, studied the effects of a thickness (5, 10 & 15 μm) and cracks on the ZnO nanoparticles film prepared by the doctor-blade method for ethanol sensing. Their result demonstrated that the sensor properties were found to be influenced by the film thickness. The thinner film exhibited a higher and faster response. It was because of the presence of more cracks with increasing crack width in the thick films which reduced the specific surface area. It also reduced the connectivity of films and degraded the characteristics of electronic materials. (Liewhiran & Phanichphant, 2007).

A study using ZnO thin film as a methane sensor was completed by Mitra and Mukhopadhyay, in 2007. They fabricated a ZnO semiconducting layer with palladium (Pd) as a catalyst. The catalyst was created using palladium chloride ($PdCl_2$) solution by adopting a wet chemical process. They studied the fundamental features of a sensing element, including sensitivity, response time, and recovery process. They also investigated the variation of sensitivity with temperature and found the maximum value of sensitivity of about 86% at 200 °C for 1 vol. % methane (Mitra & Mukhopadhyay, 2007).

Zhang and group studied the acetone sensing characteristics of ZnO micro bullets, ZnO–Fe_2O_3–$ZnFe_2O_4$ composites prepared by the solvothermal process. They reported that ZnO–Fe_2O_3–$ZnFe_2O_4$ composite sensor showed a very good and quick response and recovery towards acetone. It also showed good selectivity for acetone at a lower working temperature of 190 °C. ZnO–Fe_2O_3–$ZnFe_2O_4$ composite sensor was able to detect acetone in the range of 1-1000 ppm (Zhang *et al.,* 2010).

In 2011, Wei and their group reported on the development of a ZnO nanostructure-based sensor. ZnO nanostructures have versatile properties such as large surface area, nontoxicity; biocompatibility, excellent conductivity, and high chemical, and thermal stability. They pointed out some crucial problems like low selectivity, reproducibility, and stability for ZnO-based gas sensors (Wei *et al.,* 2011). Ang Wei and group investigated the ammonia sensing properties of ZnO nanorods at room temperature and at 150 °C. ZnO nanorods were grown by employing a hydrothermal route. Their results showed the measured sensitivities were about 8% and 60% for the exposure of ammonia (500 ppm) at room temperature and 150 °C, respectively (Wei *et al.,* 2011).

Yu, and group, in 2011, prepared micro-lotus nanosheets of undoped and Fe-doped ZnO films by a hydrothermal route. In this experiment, the 1% Fe-ZnO sample showed good sensing performance towards acetone and ethanol at 400 °C, which is due to the sample's higher porosity (Yu *et al.,* 2011). In 2013, Mun and colleagues investigated the porous ZnO nanosheet stability to detect NO_2 gas. They used the heat evaporation method to create porous ZnO nanosheets. The morphology, crystal structure, and sensing capabilities of the sample were investigated at room temperature. They reported that the responses of the many networked ZnO nanosheet gas sensors were enhanced by 1.8 to 3.3

fold at an exposure of 1- 5 ppm of NO_2 (Mun *et al.,* 2013). Mahajan, in 2013, investigated the photo-sensing and gas-sensing characteristics of Mn-ZnO thin film prepared using successive ionic layer adsorption and reaction (SILAR) technique. They reported that the gas-sensing characteristics of the thin film can be enhanced by Mn doping into the ZnO lattice. The maximum sensitivity towards 200 ppm of LPG was obtained at 200 °C. The main features of the research work were fast response and recovery times (8 and 10 sec). The gas response was increased with gas concentration (Mahajan *et al.,* 2013).

In 2013, Santhaveesuk & Choopun created Sn-ZnO tetrapods employing a simple thermal oxidation reaction process. They investigated the ethanol sensing capabilities of the as-prepared sample. The sample showed the highest response of 21 at 340 °C towards 200 ppm of ethanol (Santhaveesuk & Choopun, 2013).

Zhao, in 2013, synthesized pristine and Al-ZnO nanofibers using the electrospinning technique for ethanol detection at temperatures between 150 and 350 °C with a 50 °C interval. They claimed that the Al-ZnO nanofibers-based sensor exhibited better gas-sensing performance than the pristine one. The ZnO nanofibers-based sensor displayed the highest response of 3.5 at 300 °C for 500 ppm of ethanol, whereas the Al- ZnO nanofibers displayed the highest response of 14 at 250 °C (Zhao *et al.,* 2013).

Saydi and his group prepared ZnO and 1 wt% Mn-ZnO nanoparticles using the reverse micelle method and characterized it for their structural and optical investigation using XRD and UV-Vis spectrophotometer respectively. Their report showed that the nanoparticles ranged in size from 18 to 21 nm. These films were then used to detect gasoline and ethanol vapors at different t emperatures. They reported that the optimum operating temperatures of the ZnO and Mn-ZnO sensors were 360 and 350 °C for ethanol and 290 and 335 °C for gasoline, respectively. This clearly showed that the Mn impurities reduced the sensing capability of the ZnO sensor (Saydi *et al.,* 2014). X. Liu, in 2014, prepared 0.55 M of 1.5% film on a quartz substrate by the sol-gel route to study ethanol sensing. They found that the sample exhibited the highest response of 37 at a temperature of 500 °C (Liu *et al.,* 2014).

Hijri and group, in 2014, used a modified s ol-gel t echnique t o s ynthesize Al-ZnO nanoparticles which were annealed at 400 °C. They studied morphology and structural characteristics using TEM and XRD. The mean crystallite size was found to be approximately 60–70 nm. They investigated the electrical and sensing characteristics of the prepared samples for carbon monoxide. The remarkable reduction in the resistance of the Al-ZnO sensor was noticed after exposing carbon monoxide to the temperature ranging from 250-300 °C. The gas sensor fabricated using Al-ZnO showed a better response than the undoped ZnO sensor and hence they concluded that their materials could be utilized to detect the sub-ppm concentration of CO in air (Hjiri *et al.,* 2014).

Hosseini, in 2015, synthesized ZnO nanorods on quartz substrate by vapour phase transport (VPT) technique. The ZnO nanorods were vertically aligned with flower-like structures. Prepared ZnO structure was utilized for the detection of hydrogen sulfide (H_2S) at ambient temperature as well as at 250 °C. The result revealed a response of 296 at an exposure of 1 ppm H_2S at ambient temperature and 2.4 at 250 °C. The response was decreased with increasing relative humidity and the sample had good stability (Hosseini *et al.,* 2015).

Mani and group, in 2016, reported on the preparation of ZnO, Co-ZnO, Ni-ZnO, and Cu-ZnO nanostructured films by spray pyrolysis method for gas s ensors. They reported that the gas responses of ZnO, Co-ZnO, Ni-ZnO, and Cu-ZnO films as 2.85, 800, 2.59, and 21.36 respectively towards 10 ppm acetaldehyde at ambient temperature. They reported that the Co-ZnO sensor has the selectivity towards acetaldehyde at ambient temperature (Mani & Rayappan, 2016). In 2016, the research group of K. K. Lokesh synthesized the nanofibers of n-ZnO/p-NiO using an electro-spinning method and tested the sensing capability towards ammonia (NH_3) at room temperature. At room temperature, n-ZnO/p-NiO showed a high response of 67 at an exposure of 250 ppm of NH_3 and showed the highly selective nature to NH_3 (Lokesh *et al.,* 2016).

In 2017, Bhatia and co-workers published a report on the preparation of ZnO nanoparticles utilizing two different r outes: a simple heat treatment and thermal evaporation routes, using 0.17 M of zinc acetate dehydrate, $Zn(CH_3COO)_2 : H_2O$ as the primary precursor solution. The result of XRD analysis revealed a hexagonal wurtzite structure with a preferred orientation along the (101). From FE-SEM, they measured the grain size and found 50 ± 5 nm. They observed the peaks between 400 and 500 cm^{-1} for ZnO stretching modes in the FTIR spectra. The band gap was in the range of 3.32 to 3.36 eV. The film was deposited on the glass substrate and then utilized as a gas sensor. Gas sensing results showed that the thermally evaporated sample exhibited a higher response of 14.4 at an exposure of 50 ppm of ethanol at 250 °C. This value of response was nearly three times greater than that of the simply heat-treated sample (Bhatia *et al.,* 2017).

In 2017, Zhu and Zeng presented strategies for creating a room temperature gas sensor utilizing ZnO. According to them, the operating temperature can be reduced by modifying the surface morphology of ZnO, metallic doping into ZnO, and light activation. The gas response can be increased by reducing grain size and increasing specific area, defect density, and porosity. The operating temperature can only be somewhat decreased by modifying the surface. Metal doping, conducting polymer doping, and inorganic doping into ZnO are effective ways of realizing room-temperature ZnO gas sensors. Size distributions, the nature of metal dopants, and their concentration will influence the gas-sensing capabilities of ZnO at room temperature. They also reported that the bimetallic doping on the ZnO nanostructure will be more effective than the monometallic

doping to enhance the sensing ability and decrease the operating or working temperature. Conducting polymer doping on ZnO nanostructures could also be used to improve sensing properties at lower operating temperatures (Zhu & Zeng, 2017). In such a context, they prepared the chromium-doped ZnO (Cr-ZnO) nanorods prepared by the hydrothermal route and found them to be effective to improve the ethanol sensing ability of ZnO. They also investigated the gas-sensing mechanism using first-principles c alculations upon surface adsorption models. They found that the Cr-ZnO surface is enabled to transfer a large number of electrons and adsorb more oxygen molecules than pristine ZnO, which is crucial for the improvement in the ethanol gas response (Zhu *et al.,* 2017).

Poloju and group used co-precipitation followed by the sol-gel route to prepare ZnO nanoparticles, ZnO/CuO & Al-ZnO/CuO nanocomposites. They characterized the materials and then investigated the ammonia sensing performance of prepared samples at room temperature. They found that the Al-ZnO/CuO-based sensor showed a response of 3010.71, excellent stability, and quick response (response time of 14 sec) and recovery (recovery time of 9 sec) towards 500 ppm of NH_3 gas at room temperature than the ZnO and ZnO/CuO based sensors (Poloju *et al.,* 2018).

In 2018, Goudarzi and Khojier prepared the undoped and Mg-ZnO films using spray pyrolysis technique. They used these samples to monitor NH_3 at ambient temperature. They reported that the Mg-doped ZnO (Mg-ZnO)exhibited the best response of about 800 at 100 ppm of ammonia (Goudarzi & Khojier, 2018).

Vijayakumar and group, in 2020, prepared the undoped, Fe, Al and Fe-Al doped ZnO films by spray pyrolysis technique for investigating the gas sensing capabilities s towards the ammonia, acetone, xylene, and ethanol at ambient temperature in 60 % humidity. All the samples exhibited a high response to ammonia. Fe-Al-ZnO film showed the highest response of 20 to 10 ppm of NH_3. The response and recovery times were 26 sec and 12 sec respectively. This high value of response for the NH_3 was due to the smaller kinetic diameter and lower ionization energy, which allows its molecules to diffuse through the sensor surface of the film (Vijayakumar *et al.*, 2 020). Sahoo, in 2020, prepared the pristine, Fe-doped, In-doped, and Fe-In-doped ZnO films using the spray pyrolysis route. They studied the surface structure-dependent LPG gas sensing properties of prepared samples. Here, they reported that the grain size of ZnO decreased after 3 at.% In doping from 99 nm to 79 nm. The surface morphology was changed from a spherical granular shape to a nanoflake after co-doping Fe and In into ZnO. They found that the 3% In-ZnO sample responded better than the other samples, which was due to the smaller spherical grain size and compact morphology (Sahoo *et al.,* 2020).

Jaballah and peers studied the gas sensing efficacies of undoped ZnO, 1% Mg-ZnO, 5% Al-ZnO, and 5% Al-1% Mg-ZnONPs films made using the modified sol-gel method.

They reported that the 5% Al-1% Mg co-doped ZnONPs film-based sensor had a higher response of 70 for 2000 ppm of H_2 and 2 for 20 ppm of CO at 250 °C and were able to detect less than 2 ppm of H_2 and 1 ppm of CO (Jaballah *et al.,* 2021).

From the above discussion, we came to understand that, the ZnO-based sensors generally work well at the operating temperature greater than 300 °C towards ethanol and acetones. To the best of my knowledge, only limited reports on MOS gas sensing at ambient temperature have been published to date. The researchers are trying to enhance the gas sensing capability at low temperatures using different strategies such as surface modifications and metal doping into ZnO. Metal doping is one of the good ways to enhance the sensing ability of ZnO. Only a few reports are available on gas sensing using metal-metal doping. Therefore, we focused our attention to study the structural, electrical, and optical properties of undoped, metal-doped, and metal-metal co-doped ZnO in the detection of various commonly available toxic gases.

2.3 Research gap

The gas sensing properties of the ZnO depends on the concentration of adsorbed oxygen ions, surface morphology, temperature, humidity, etc (Hosseini *et al.,* 2015). The concentrations of adsorbed oxygen ions depend on the oxygen vacancies (defects) in ZnO (Cui *et al.,* 2016; Zhu & Zeng, 2017). Generally, higher operating temperatures of ZnO-based gas sensors have been reported up to date. The high operating temperature reduces the stability and consumes more power. Hence, a number of investigators are working tirelessly to increase the sensitivity or gas response at lower operating temperatures using different strategies such as metal doping and surface modifications. There are some advancements reported for room temperature operation of ZnO gas sensors (Wei *et al.,* 2011; Mani & Rayappan, 2014). The metal doping and co-doping into ZnO are reported to be one of the excellent ways of enhancing the sensitivity of ZnO sensor (Santhaveesuk & Choopun, 2013; Zhu *et al.,* 2017; Sahoo *et al.,* 2020). Based on the published reports, the majority of previous research concentrated on single-metal doping. There are only a few reports available on metal co-doping which would significantly enhance the ZnO sensor performance. As the doping changes the surface morphologies and the activation energy of ZnO (Sahoo *et al.,* 2020), the gas sensing performance is assumed to be enhanced even at lower operating temperatures. Therefore, in the present work, the study on the effect of Fe, Sn, and Fe-Al co-doping in the structural, electrical, and optical properties of ZnO to increase its gas sensing performance towards ammonia, acetone, and ethanol is set to explore.

CHAPTER 3

3. MATERIALS AND METHODS

In this chapter, the ZnO film preparation using available methods, its characterization, and gas sensing measurements are described.

3.1 ZnO Film Preparation Techniques

There are several techniques that can be employed to prepare thin films of undoped and metal-doped metal oxide semiconductors. Some of them are vacuum evaporation, chemical bath deposition, dip coating, thermal evaporation, physical vapour deposition, electrochemical deposition, spray pyrolysis, spin coating, doctor blade etc. In this study, the ZnO films were prepared by using spin coating, spray pyrolysis, and doctor blade methods. All the samples were deposited on the ultrasonically cleaned glass substrates.

3.1.1 Substrate Cleaning

The glass substrates were first thoroughly cleaned with lanoline detergent, distilled water, and acetone in an ultrasonic bath. They were then dried for 30 minutes in a hot air oven at 50°C to remove all the unwanted dust (Koirala & Joshi, 2017).

3.1.2 Preparation of Undoped, Fe-ZnO and Fe-Al-ZnO Films

Figure 12 depicts the flow chart followed to prepare ZnO films using the spin coating method. At first, 0.35 M precursor solution was prepared by dissolving zinc acetate dehydrate (ZnAc) into the ethanol at (70 ± 5) °C. The molar ratio of DEA to ZnAc was maintained 1:1 (Shrestha *et al.*, 2010; Shakti & Gupta, 2010). The fluctuation in the set temperature was taken as an error in it. A magnetic stirrer was used to mix the solution for 1 hr to get a homogeneous solution. The same molar of Fe and Al dopant solutions were prepared by dissolving ferric nitrate tetrahydrate and aluminum chloride in ethanol in two different beakers. All these solutions were then filtered with WHATMAN filter paper. Prior to depositing Fe-ZnO films, the required amount of ferric chloride solution was mixed with the zinc acetate precursor solution. The as-prepared solution was then mixed with the zinc acetate precursor solution to prepare 1, 2 3, and 4 at.% Fe-ZnO solutions. Similarly, Fe and Al dopant solutions and zinc acetate precursor solutions were then mixed to prepare 1%Fe-1%Al, and 3%Fe-1%Al-ZnO solutions.

All these solutions were stirred using a magnetic stirrer for 1 hr to get homogeneous solutions and then aged for 24 hr. As-prepared precursor solutions were utilized to deposit the films on glass substrates by a spin coating method using a spin coater (VTC-50A)

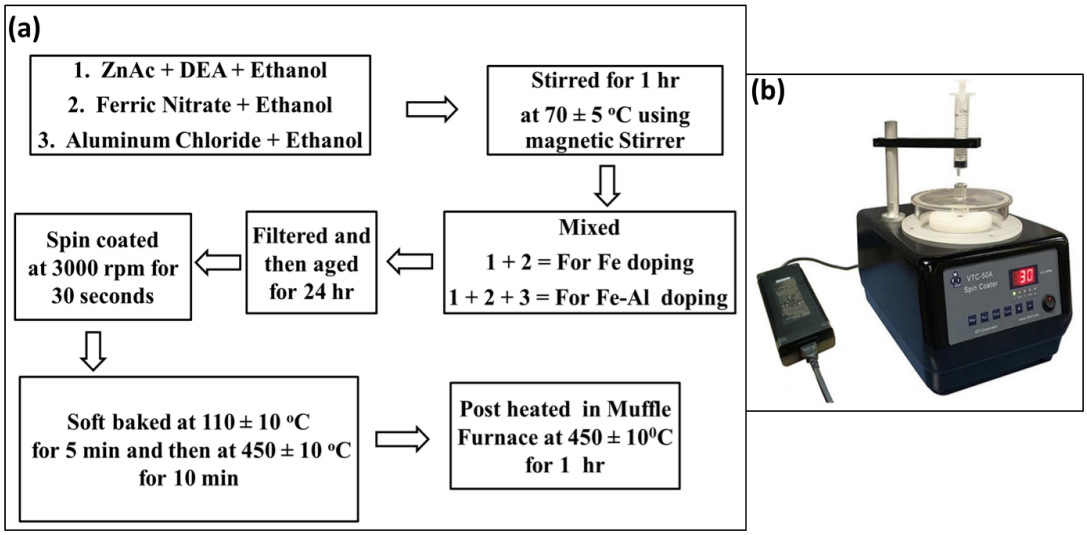

Figure 12: (a)Preparation of ZnO, Fe-ZnO and Fe-Al-ZnO films, and (b) Spin coater

available at the physics laboratory of Amrit campus, Tribhuvan University. In the coating process, a few drops of the prepared solution were put on the center of the glass substrate which was positioned in the middle of the spin coater. The glass substrate is then rotated at a speed of 3000 rpm for 30 sec in order to disseminate the coating material by centrifugal force. The deposited film was soft-baked for 5 minutes at (110 ± 10) °C and then for 10 minutes at (450 ± 10) °C. During post-heating, the deposited film is first converted into brown color then into rainbow color. These steps were repeated to deposit more coats as second, third, fourth, and fifth coats, and so on until we get the appropriate thickness of the film. Finally, the film was heated at (450 ± 10) °C for 1 hr (Shrestha *et al.,* 2010).

3.1.3 Preparation of Undoped and Sn-ZnO Films

Figure 13 depicts the block diagram of the preparation method of the ZnO and Sn-doped ZnO (Sn-ZnO) films by spray pyrolysis technique. At first, zinc acetate dehydrate was dissolved in distilled water to create the 0.35 M ZnO precursor solution. The solution was shaken for about one hr at (60 ± 10) °C using a magnetic stirrer to produce a clear, homogeneous solution. The same molar Sn dopant solution was made by dissolving stannous chloride in distilled water in a separate beaker. The solution was stirred for 1 hr at (60 ± 10) °C with the help of a magnetic stirrer to obtain a clear and homogeneous solution. The stannous chloride solution and the zinc acetate solution are mixed in the volume ratios of 1:99, 2:98, and 3:97 to get the solutions of 1, 2 and 3 at. % Sn-ZnO solution. Afterward, the solutions were aged for 24 h at ambient temperature after being filtered with WHATMAN filter paper.

Using homemade spray pyrolysis apparatus, different sets of undoped and Sn-ZnO films were prepared on the glass substrates. A nebulizer [Model No: CN-01W] was used to spray the solution over the glass substrates heated at 380 ± 10 °C. The main deposition

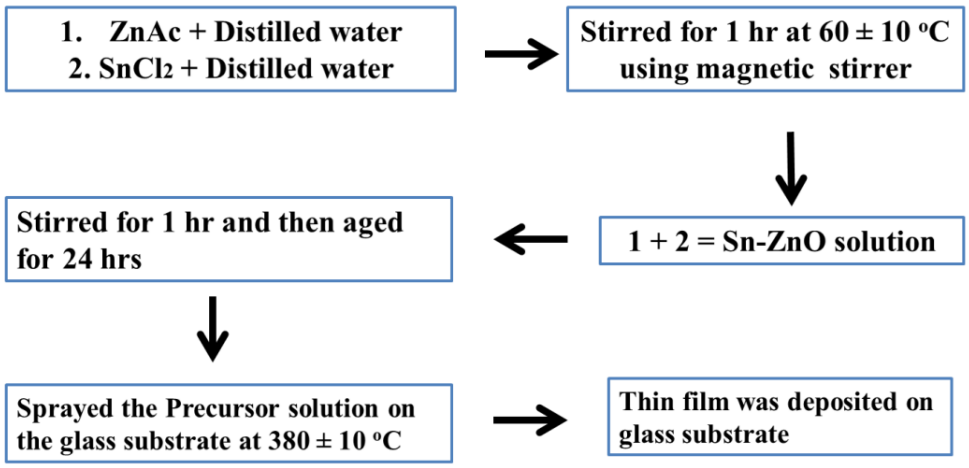

Figure 13: Block-diagram for preparation of ZnO and Sn-ZnO films

Table 1: Deposition parameters set to deposit ZnO films using spray pyrolysis

Parameter	Scale
Spray nozzle diameter	0.5 mm
Flow rate	0.33 ml/min
Substrate temperature	380 ± 10 °C
Carrier gas pressure	2.5 bar
Nozzle to substrate distance	2 cm
Number of layers deposited	5

parameters are the flow rate, carrier gas pressure, the substrate to nozzle distance, nozzle diameter, number of layers, and substrate temperature (Mani & Rayappan, 2015). The parameters set for film deposition are presented in Table 1. Finally, the films were annealed at 500 ± 10 °C in the programmable muffle furnace (Nabertherm GmbH, LT 3/11/B4 10 Serial No. 36140, Germany) for 1 hr available at the physics research laboratory of Amrit Campus.

3.1.4 Preparation of ZnO Film by Doctor Blade Method

Firstly, the glass substrates were coated with fluorine-doped tin oxide (FTO) layers employing the spray pyrolysis technique. For this, 21.051 gm of $SnCl_2 : 2H_2O$ was dissolved in 10 ml conc. HCl by stirring using a magnetic stirrer at (90 ± 10) °C in a beaker. Then, the distilled water (40 ml) was added and shaken for 15 min at temperature (60 ± 10) °C. The ammonium fluoride (NH_4F) solution was prepared by dissolving it in 50 ml of distilled water in another beaker. Afterward, these two solutions were mixed and shaken for 1 hr with the help of a magnetic stirrer. The final solution was aged for 24 hrs (Koirala & Joshi, 2017).

Figure 14 shows the flow chart used to prepare ZnO film on FTO glass substrate using doctor blade method. Prior to this deposition, ZnO nanoparticles were prepared. To prepare the ZnO nanoparticles, 0.5 M Zinc acetate dehydrates was dissolved into ethanol

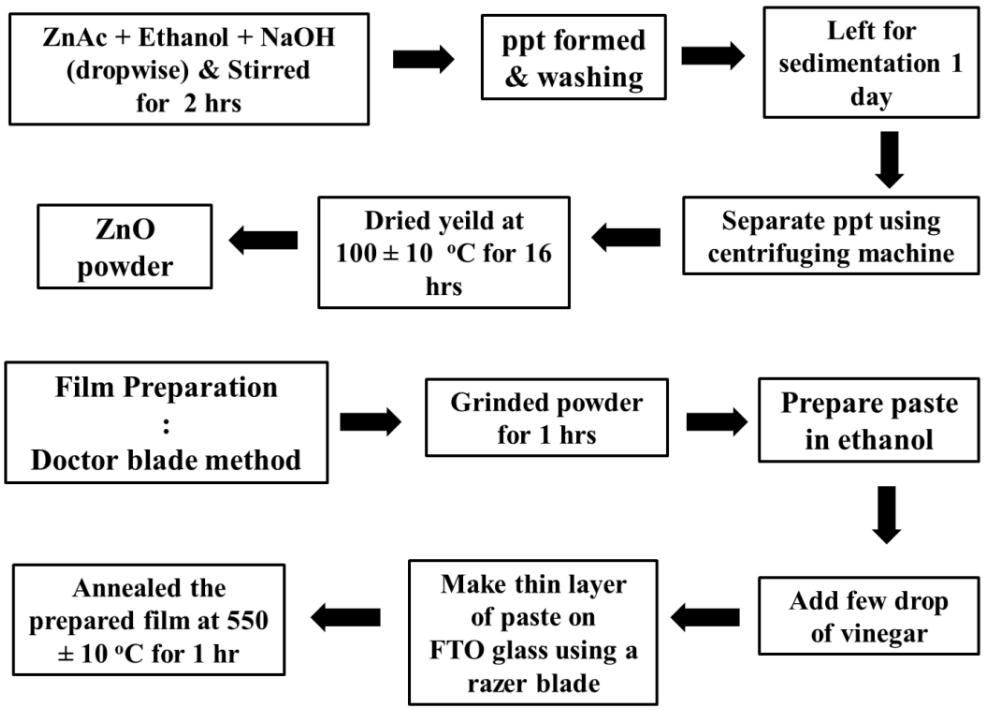

Figure 14: Block-diagram of preparation of ZnO nanoparticles film

and stirred for 2 hr at 60 ± 10 °C. The 2.0 M NaOH was put into this mixture dropwise at fixed stirring conditions to p recipitate. The solution's pH was held constant at 1 2. To remove organic contaminants, the residue was centrifuged at 2500 rpm, filtered extremely carefully, and washed with distilled water multiple times. The residue was then dried for 16 hrs in a programmable muffle furnace at 100 ± 10 °C. The paste of ZnONPs was prepared using ethanol and 3-5 drops of vinegar. The vinegar acts as a binding agent. The ZnO films were deposited over FTO coated glass substrate using a doctor blade method. In this method, the film was made by spreading the above-prepared ZnO paste with the help of a Razor blade. The deposited layers were heated at 550 ± 10 °C for 1 hr. Before testing, the as-prepared film was aged for an additional 7 days in an ambient atmosphere to increase stability (Zhang *et al.,* 2018). Ultimately, as-prepared ZnONPs are characterized using FTIR and XRD.

3.2 Characterization Technique

3.2.1 Optical Characterization: UV-Visible Spectroscopy

Optical characteristics of as-prepared samples were investigated by Ocean Optics spectrophotometer (Model: HR4000CG-UV-NIR, Singapore). Figure 15 shows the schematic

diagram of the transmittance measurement of the ZnO prepared. In the wavelength range of 360–1000 nm, the transmitted light from the sample is allowed to pass through the optical fiber to the UV-Vis spectrophotometer. The spectrometer is interfaced with a PC

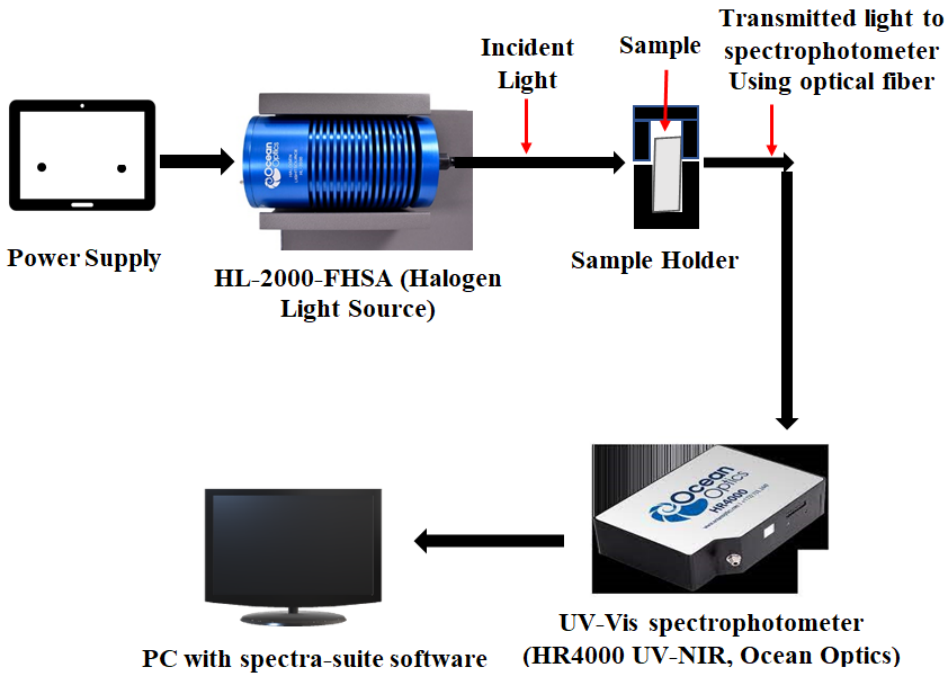

Figure 15: Schematic diagram of transmittance measurement of the sample using UV-Vis spectrophotometer

for scanning and accumulating the data. The accumulated data is then analyzed to get the result of the experiment. The necessary theory for this is described below.

If the light of intensity I_0 is incident on the film of thickness t, then the transmitted light intensity I is given by

$$I = I_0 e^{-\alpha t} \tag{3.1}$$

where α is called the absorption coefficient, and αt is called optical density.
From equation (3.1), the value of α is determined by

$$\alpha = \frac{\ln(\frac{100}{T})}{t} \tag{3.2}$$

Here, T is the transmittance that can be recorded by a UV-Visible spectrophotometer.

The energy difference between the conduction band edge and the top of the valance band edge determines a semiconductor band gap. The conductivity of the semiconductor is zero at a temperature of 0 K because every state in the valance band is completely filled and every state in the conduction band is vacant. As the temperature (T) increases, the thermal

excitation of electrons causes them to move from the valance band to the conduction band and holes are formed in the valance band. Both the electrons and the holes contribute to the electrical conductivity of semiconductors. Thus, intrinsic conductivity is a function of temperature. Under the intrinsic condition, the hole concentrations and electron concentrations are equal. The intrinsic conductivity and intrinsic carrier concentrations are controlled by E_g/k_BT, here E_g is the band gap, k_B is the Boltzmann constant, and T is the temperature in kelvin. For large E_g/T, the concentration of intrinsic carriers and the conductivity will be low.

In this work, the optical band gap was obtained by the optical absorption process. The presence of bound electrons and ions causes the absorption of UV and IR regions of the spectrum, which is described by the electronic band theory and the theory of inter-band excitation. There are two types of optical absorption.

a. Direct optical absorption
b. Indirect optical absorption

In the direct absorption process, photons are absorbed by the material, resulting in the creation of electrons and holes. It occurs when the bottom of the conduction band edge and the top of the valance band edge have the same wave vector. The absorption starts at the frequency ν of light for which $E_g = h\nu$. Here, h is Planck's constant. In this process, the electron is transferred vertically between the two bands without a change in momentum (Kittel, 1996).

In the indirect absorption process, both photons and phonons are absorbed. It occurs when the bottom of the conduction band edge and the top of the valance band edge are separated in k-space. In the indirect transition at low temperatures, the threshold energy is higher than the true band gap. The threshold energy for the indirect absorption between the band edges is $h\nu = E_g + h\nu_p$. Here ν_p is the frequency of the released phonon having wave vector k. At high temperatures, the phonons are already thermally activated in the crystal. If a photon is absorbed along with a phonon, the threshold energy is $h\nu = E_g - h\nu_p$. In the process, the wave vector is always conserved. In general, the transition occurs between all points of the two bands, for which both wave vectors and energy are conserved (Kittel, 1996). The relation of optical absorption coefficient (α) with hν is given by empirical formula:

$$(\alpha h\nu)^n = A\left(h\nu - E_g\right) \tag{3.3}$$

where n = 2, and 1/2 for allowed direct and indirect transition, respectively. Here, A is an energy constant, and ν is the frequency. The plot of $(\alpha h\nu)^2$ or $(\alpha h\nu)^{1/2}$ vs. hν yields a portion of a straight line. The intercept of the straight line on the hν-axis gives the value of the direct or indirect optical band gap value of the material.

3.2.2 Surface Morphology and Elemental Composition

The surface morphology of the sample was investigated by scanning electron microscopy ((Model: JEOL, JSM-7001F, Japan). An electron beam is used in an electron microscope to magnify the image of the sample. According to de-Broglie, material particles in motion can behave as wave. The wavelength of the electron moving with velocity v and accelerated by potential V is given by

$$\lambda = \frac{h}{mv} = \frac{h}{\sqrt{2meV}} = \frac{1.22}{\sqrt{V}} \text{ nm} \tag{3.4}$$

For V = 10000 Volts, λ = 0.012 nm. This wavelength is considerably shorter than the wavelength of visible light (400 to 700 nm). Thus, an SEM has far better resolution than an optical microscope. In the SEM, the SEM image is created by scanning the material with a focused beam of electrons and collecting the secondary or back-scattered electrons.

Figure 16 depicts a schematic illustration of an SEM (Young & Kalin, 1986). It is made up of an electron gun, a lens setup, scanning coils, a collector, and a cathode ray tube (CRT). The main component of an electron gun is a tungsten "hairpin" filament. The electron gun emits electrons using thermionic emission with a 2 eV energy spread. These electrons are focused and scanned across the sample after passing through a number of lenses. The secondary electrons come out of the sample due to striking the incident electron beam. Some incident electrons are backscattered, and some are absorbed. The absorbed electron is measured as electron-beam-induced current. X-rays are also emitted in this process. These secondary electrons are accelerated by applying a potential difference of 10–12 kV and detected with an Evehart-Thornly (ET) detector. Scintillation material is the basic component of the detector. The scintillator emits light when these accelerated electrons hit the detector. This light is permitted to incident on a photocathode after passing through a photomultiplier in a light pipe, which produces electrons. These electrons are amplified to produce extremely high gains, and it must run at high potentials between 10 and 12 kV. The brightness of a CRT can be controlled by detecting and amplifying each of these signals. Thus, each point on the display and each point on the sample are established to have a one-to-one correlation. Following the mapping procedure, the magnification M is calculated as:

$$M = \frac{Length\ of\ CRT\ display}{Length\ of\ sample\ scan} \tag{3.5}$$

Lanthanum hexaboride (LaB_6) sources with greater brightness and a 0.2 – 0.3 eV reduced energy spread have mostly replaced tungsten sources. Compared to LaB_6, field-emission guns are around 100 times brighter and 1000 times brighter than tungsten sources with longer lifetimes.

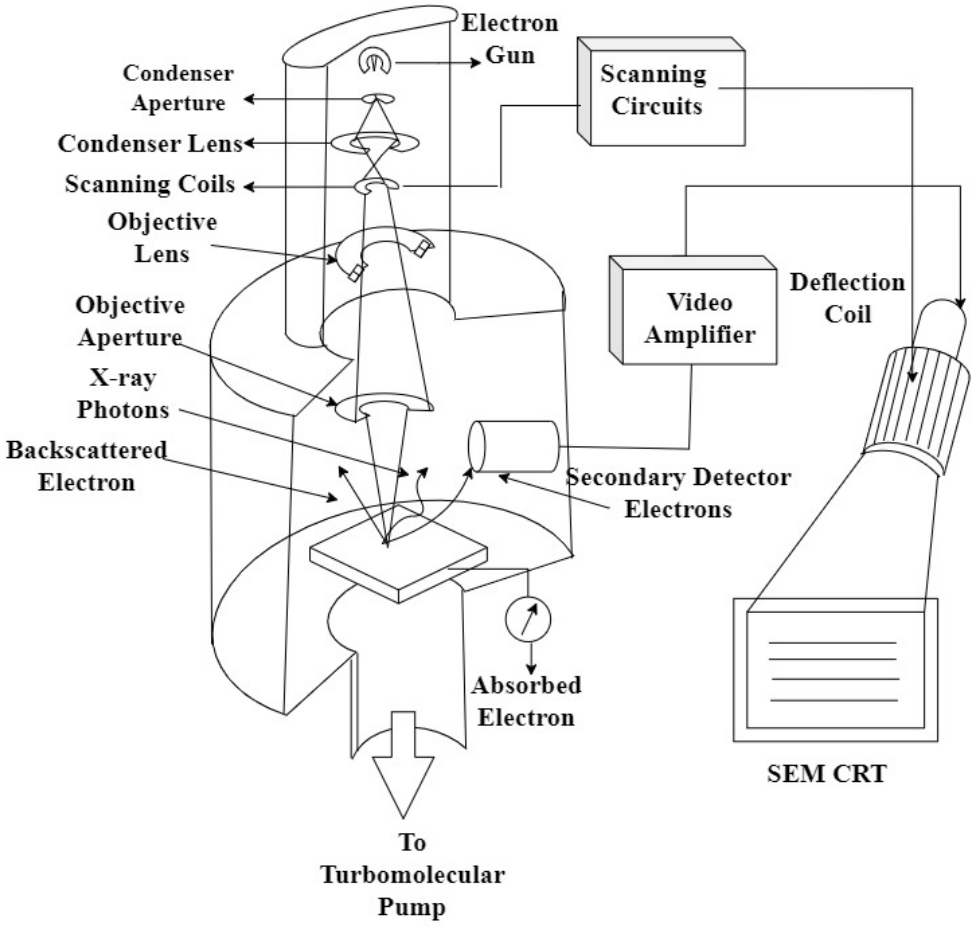

Figure 16: Schematic diagram of scanning electron microscope (Young & Kalin, 1986)

The elemental compositions were studied by energy dispersive X-ray (EDX) analysis. It is an analytical technique. The fundamental idea is that each element has a distinct atomic structure, which leads to a distinct collection of peaks on the electromagnetic emission spectrum. The material to be tested is exposed to an intense electron beam. The inner and outer shell electrons of the material's atoms interact with these incident electrons elastically. Due to this interaction, the electrons in the outermost shells release soft X-rays, whereas the electrons in the innermost shells emit characteristic X-rays that depend on the energies of these shells and are characteristics of the atoms generating them. Therefore, information regarding the types of atoms present in the film and their concentration can be obtained by evaluating the energy of these characteristics X-rays (Hamuyuni *et al.,* 2016). In addition, Auger electrons are also produced to detect elements with an atomic number less than 11. An energetic electron is bombarded at the target to produce the vacancy in the inner shell, which leads to the emission of an energetic electron, called an Auger electron. The energy of the Auger electron is then used to determine which element emitted it. The spectrum was then produced by the analysis of the energy of Auger electrons with the relative abundance of the electrons. The peak in the spectrum identifies the element present in the samples (Hamuyuni *et al.,* 2016).

3.2.3 Structural Characterization

The structural investigation of the sample was carried out using X-ray diffraction (Model: Bruker AXS, D2PHASER A26-X1-A2BOB2A-, Serial No: 207047). It has been utilized to determine the overall structure of bulk solids, such as lattice constants, crystal orientation, strain, etc. The schematic diagram of X-ray diffraction by a crystal is depicted in Figure 17. This technique is based on the idea that the wave will exhibit the phenomenon of diffraction when it interacts with the atomic planes in a crystal. In this technique, the X-ray beam is incident on a sample at a certain angle called the glancing angle, and the X-rays scattered by neighboring planes are analyzed. At particular angles of incidence, X- rays scattered by neighboring parallel atomic planes will interfere destructively or constructively. The constructive interference gives a large output signal at those particular angles. Constructive interference occurs only when the path difference of the interfering waves is an integer multiple of the wavelength of the X-ray. For constructive interference:

$$2d \sin\theta = n\lambda \tag{3.6}$$

where λ is the X-ray wavelength, and d is the separation between two neighboring planes, i.e., lattice spacing. n is the order of diffraction. θ is the glancing angle. This is Bragg's law. Factor d is related to the (hkl) indices of the planes and the dimensions of the unit cell. One of the limitations of the X-ray diffraction technique is that it provides bulk information. The thickness cannot be measured for the thin film with roughness over 50 nm, XRD works only when there is a difference in electron density between the layer of sample and substrate.

The crystallite size is determined by Debye Scherer's formula:

$$D = \frac{K\lambda}{\beta cos\theta} \tag{3.7}$$

where, K - shape factor, λ - wavelength, β - full width at half maxima and θ-Bragg's angle (Bhatia *et al.,* 2017).

The lattice strain (ε) of sample is determined as:

$$\varepsilon = \frac{\beta}{4\tan\theta} \tag{3.8}$$

The lattice parameters a and c are evaluated using formula for hexagonal crystal structure (Pramod & Pandey, 2014; Srinivasulu *et al.,* 2017):

$$\mathrm{a} = \frac{\lambda}{\sqrt{3}\sin\theta} \tag{3.9}$$

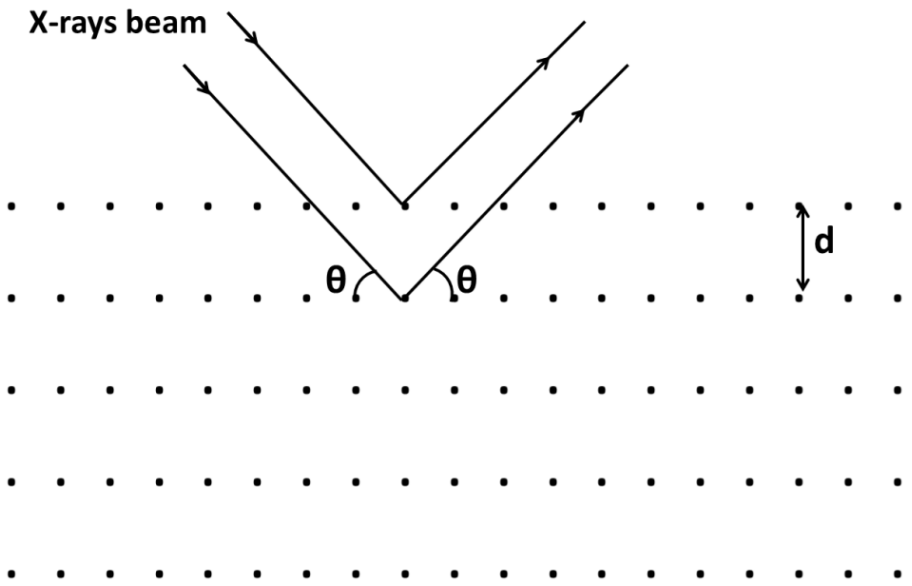

Figure 17: Schematic diagram of X-ray diffraction (Kittel, 1996)

$$c = \frac{\lambda}{\sin\theta} \tag{3.10}$$

3.2.4 Fourier Transform Infrared (FTIR) Spectroscopy

The various characteristic functional group of the samples were investigated using FTIR spectroscopy (Model: Perkin Elmer -16.10.2) In the latter half of the 19^{th} century, Michelson and Lord Rayleigh established the basis for Fourier Transform Infrared (FTIR) Spectroscopy. By applying a Fourier transformation, Rayleigh was able to relate an interferogram with their spectra.

Figure 18 depicts the block diagram of the FT-IR spectrometer. (Michelson, 1891; Rayleigh, 1892). The fundamental component of FTIR is Michelson interferometer. The interferometer is coupled to the three optical inputs: a He-Ne laser, white light, and a spectral signal. The mirrors and beam splitter for all three optical signals are the same (Koenig, 1981). The computer controls optical components, gathers and saves data, performs calculations, and generates spectra. As the computer and spectrometer are directly connected, it is possible to edit the spectra in an innovative way to remove interfering absorbance by subtracting the interfering component-related absorption bands from composite spectra (Ferraro & Basile, 2012).

The FTIR spectrometer works on the following principles: The interferometer first generates a signal or intensity *I(x)*) known as an interferogram. The interferogram is

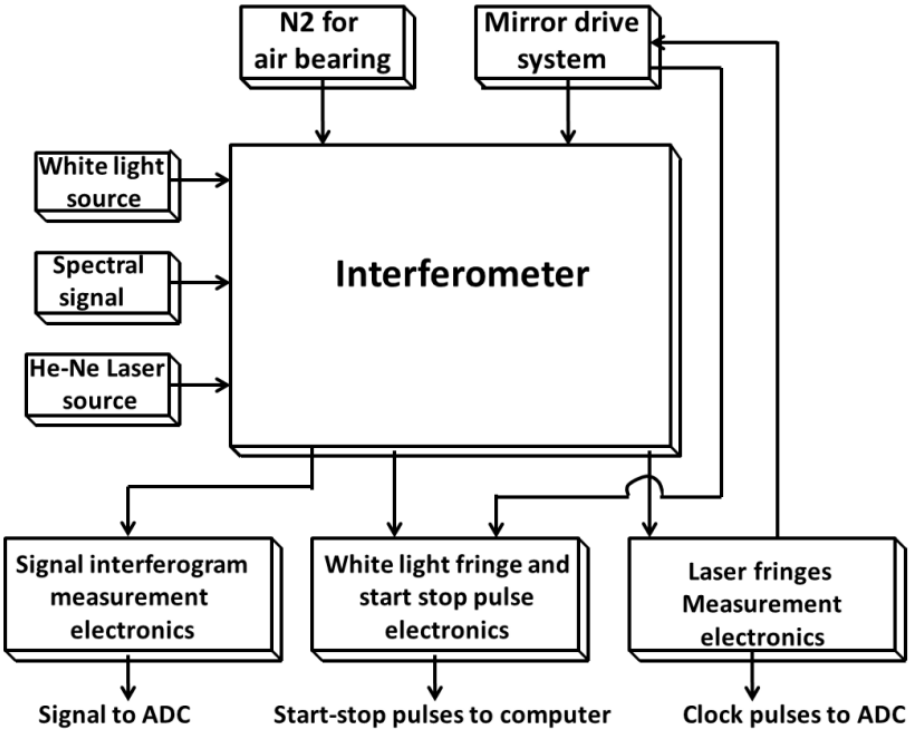

Figure 18: Block diagram of FTIR spectrometer (Horlick & Yuen, 1978)

produced by the infrared detectors. The intensity *I(x)* is then converted into the spectrum *S(f)* by using the Fourier Transform. Here, x is the path difference between the interfering beams, and f is the frequency of the spectrum. Thus,

$$S(f) = \int_{-\infty}^{\infty} I(x)\ e^{i2\pi fx}\, dx = F^{-1}[I(x)] \tag{3.11}$$

and

$$I(x) = \int_{-\infty}^{\infty} S(f)\ e^{-i2\pi fx}\, df = F[S(f)] \tag{3.12}$$

In this case, the first and second integrals are the inverse Fourier transform and the Fourier transform respectively. A dedicated computer is used to perform this calculation (Hoffmann & Knözinger, 1987). Michelson Interferometer a fundamental part of FTIR is shown in Figure 19. The collimated infrared light beam from the infrared source is incident into a beam splitter, where it is separated into two independent optical paths by 50% reflection and 50% transmission. A fixed mirror M_2 reflects the beam back to the beam splitter. The splitter partly reflects the beam to the detector and partly transmits to the source. Mirror M_1 is placed in another leg of the interferometer. It can be moved back and forth parallel to itself. For smooth movement and good stability, it is supported by the bearing. The mirror M_1 known as a movable mirror also reflects the light back to the splitter. The splitter reflects the beam coming from mirror M_1 partly to the source

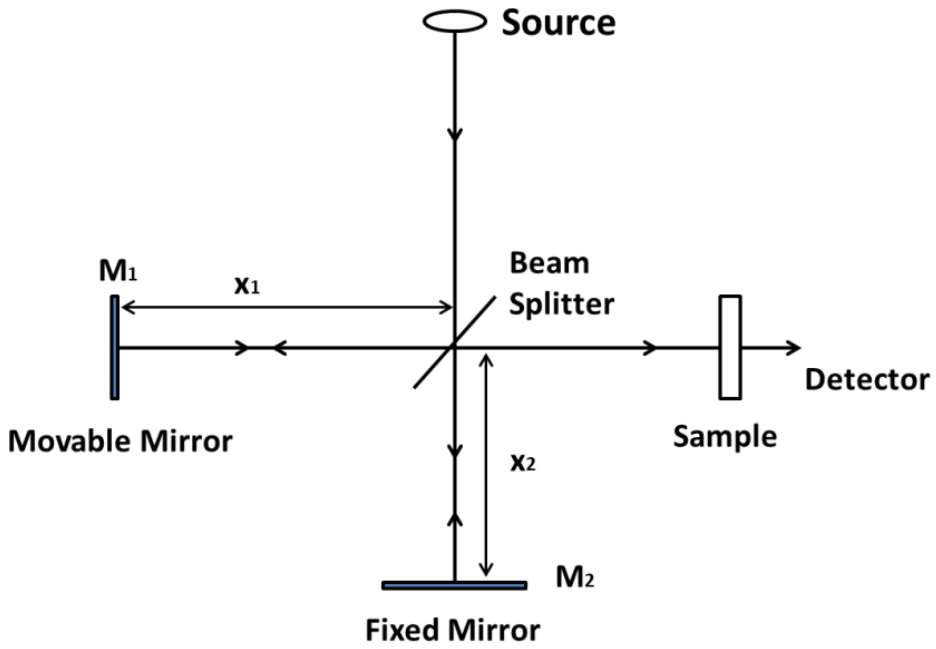

Figure 19: Schematic diagram of Michelson Interferometer (Michelson, 1891)

and transmits partly to the detector. These two beams then superimpose or interfere and produce interference maxima and minima. The light entering to the detector is the combination of these two beams.

When $x_1 = x_2$ the path differences of the interfering beams are the same or two beams meet in phase. If M_1 is displaced by a distance of y, the optical path difference and hence the phase difference (δ) is introduced. The retardation is 2y. This is due to the fact that the light travels a further distance y to reach the mirror and the same distance y to reach the beam splitter.

Now, think about the detector's output signal for a monochromatic source of light. When $x_1 = x_2$, the two beams reinforce each other and the detector output is maximum. If M_1 is displaced by $\lambda/4$ then the retardation is $\lambda/2$ and two wavefronts arrive at the detector out of phase, and the destructive interference occurs with zero output. When M_1 is displaced by an additional $\lambda/4$, the retardation is λ and constructive interference resumes. Thus, the interferogram or detector output is composed of a sequence of maxima and minima, which is represented by the equation:

$$I(x) = S(f)\,[1 + \cos(2\pi x f)] \tag{3.13}$$

Here, *S(f)* is the source intensity modified by the sample.
When the source emits more than one frequency then

$$I(x) = \int_0^f S(f)\,[1 + \cos(2\pi x f)]\;df \tag{3.14}$$

For an instant, suppose the source spectral distribution, $S(f) = A$ for $0 \leq f \leq f_1$. The interferogram can be obtained by removing the unmodulated term from equation (3.14) as:

$$I(x) = \int_0^{f_1} A\cos(2\pi x f)\, df \tag{3.15}$$

The interferogram narrows as f_1 increases and becomes maximum at $x = 0$ where $x_1 = x_2$, because of constructive interference. The robust maximum at $x = 0$ is called a center burst. The interferogram wings contain the high-resolution spectral information corresponding to the maximum distance that the M_1 can travel L. The interferogram contains both spectral information of the source and the transmittance of the characteristics of the sample, which is the spectral response and is determined by using the Fourier transform as:

$$S(f) = \int_0^{\infty} I(x)\cos(2\pi x f)\, dx \tag{3.16}$$

Here, *S(f)* gives the required spectrum as it contains the spectral content of the source, sample, and ambient path of the instrument. The derivation of these basic integral equations is described below.

Assuming a wave is incident on a beam splitter whose amplitude is:

$$E(x, f)\, df = E_o(f)\; e^{i(\omega t - 2\pi f x)} df \tag{3.17}$$

where $E_o(f)$ - Maximum amplitude of the beam at $x = 0$.

The beam splitter divides the beam's amplitude into two beams. Let the distance traveled by these two beams be x_1 and x_2 before superimposing. Each beam suffers one transmission through the beam splitter and one reflection from the beam splitter. Assume r and t are the reflectance and transmittance respectively, and then the amplitude of the recombined wave E is given as:

$$E(x_1, x_2, f)\, df = rt\, E_o(f)\; [e^{i(\omega t - 2\pi f x_1)} + e^{i(\omega t - 2\pi f x_2)}] df \tag{3.18}$$

The intensity in the fixed spectral range df is given as:

$$I(x_1, x_2, f)\, df = E(x_1, x_2, f)\; E^*(x_1, x_2, f)\, df \tag{3.19}$$

$$I(x_1, x_2, f)\, df = 2\, E_0^2\, |rt|^2 [1 + \cos 2\pi (x_1 - x_2) f] df$$

$$I\,(x_1, x_2, f)\,df = 2\,E_0^2\,|rt|^2[1 + \cos 2\pi x f]df \tag{3.20}$$

where $x = x_1 - x_2$.

Integrating equation (3.20), the total intensity throughout the whole spectral range is: obtained, which is

$$I_r\,(x)\,df = 2\,|rt|^2 \int_0^\infty E_0^2\,[1 + \cos 2\pi f(x_1 - x_2)]df \tag{3.21}$$

The intensity can be converted into a spectrum by Fourier cosine transform of equation (3.21) as:

$$E_0{}^2(f) = \frac{1}{\pi}\,|rt|^2 \int_0^\infty [Ir(x) - \frac{1}{2}I_r(0)]cos2\pi fx]df \tag{3.22}$$

Here, $I_r(0)$ and $I_r(x)$ are the fluxes associated for path differences of $x = 0$, and $x = x_1 - x_2$ respetively. $\left[I_r\,(x) - \frac{1}{2}I_r\,(0)\right] = I(x)$ is the interferogram. The spectrum *S(f)* is given from equation (3.22) as:

$$S\,(f) \propto\ E_0{}^2(f) =\ A \int_0^\infty I\,(x)\cos\,(2\pi f x)dx \tag{3.23}$$

Here, A is a constant. With the use of a computer, the interferogram is Fourier transformed to change the space domain into the wavenumber domain (Hoffmann & Knözinger, 1987).

The experimental procedure for computing a spectrum in an interferometer is described as follows. In order to obtain the spectrum, firstly $I_r(x)$ is measured by capturing with respect to the arm displacement. $I_r(0)$ is also determined experimentally and $I(x)$ is calculated. By substituting the value of $I(x)$ in equation (3.23), the value of the integral is calculated in the computer for each selected value of frequency f. Finally, $S(f)$ is computed for each value of f which gives the required spectrum.

Figure 20 shows an example of FTIR spectra of ZnONPs which was used to study the various characteristic functional groups present in it. The major bands are plainly visible at 400 cm^{-1}, 574 cm^{-1}, 880 cm^{-1}, 1,407 cm^{-1}, 1,628 cm^{-1} and 3,420 cm^{-1}. The creation of ZnONPs was confirmed by the sharp infrared (IR) band, which spans from 400 to 650 cm^{-1} and corresponds to metal oxide vibration. The alkane sp^2 hybridized = C – H bond and the alkane sp^3 hybridized C – H bond bending, respectively, were revealed by the peak at 880 cm^{-1}. The peaks in the regions 1407 cm^{-1} and 1628 cm^{-1} were appeared due to the vibrating, stretching, and bending modes of the water molecules in the prepared sample. The appearance of an enormous depression peak in the region of 3,420 cm^{-1}

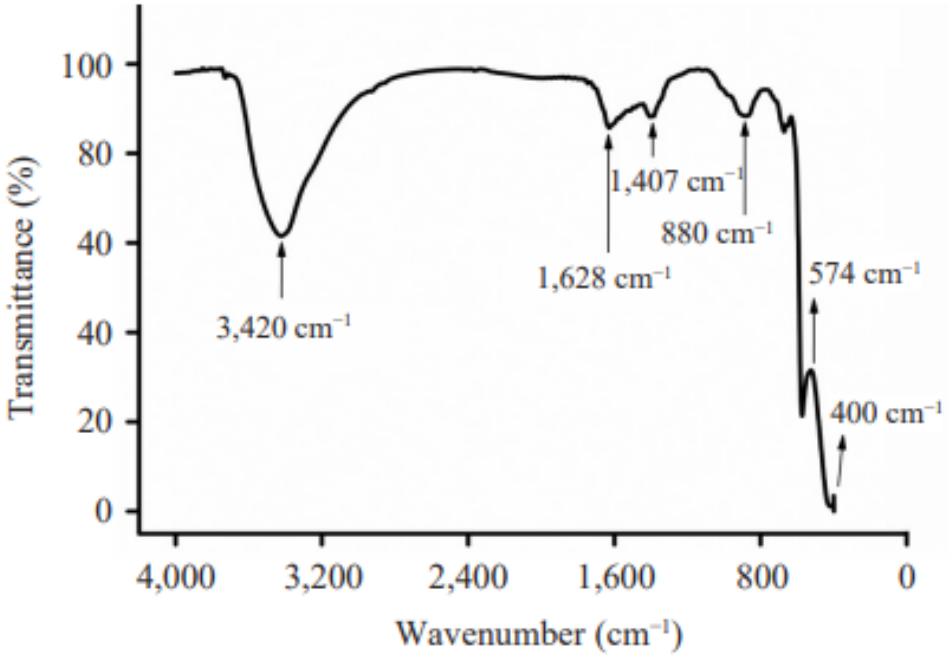

Figure 20: FTIR spectra of ZnO nanoparticles (Joshi *et al.*, 2021)

revealed the existence of hydroxyl group (Joshi *et al.,* 2021).

3.3 Sensing Mechanism

3.3.1 Sensing Mechanism: Classical Model

The sensing mechanism of MOS material is based on changes in its conductivity in different environments. The resistance of the MOS sensor changes significantly when it is exposed to gas. In air environment, the oxygen molecules are adsorbed on the MOS surface, which extracts the electrons from the conduction band to produce negatively charged oxygen species (O^-, O^{2-}, and O_2^-), and leads to the formation of a depletion layer. As a result, the MOS acquires stable resistance in the air. Figures 21 and 22 demonstrate a change in the depletion layer when ZnO is exposed to reductive gases and oxidative gases respectively. The resistance of the ZnO increases or decreases depending upon the nature of the analyte gases. On the exposure of reducing gases, the molecules of the gas interact with the adsorbed oxygen species and return the electron back to the conduction band. As a result, the depletion layer becomes thinner and the resistance decreases. This sudden decrease in resistance or increase in current is measured by electrical instruments as the sensor's signal. This is repressed in equation (3.24) as:

$$R' + O^- \rightarrow R'O + e^- \tag{3.24}$$

where R' stand for the molecule of reductive gas and O for the molecule of adsorbed oxygen species. The reverse phenomenon occurs on exposure to oxidative gases. The

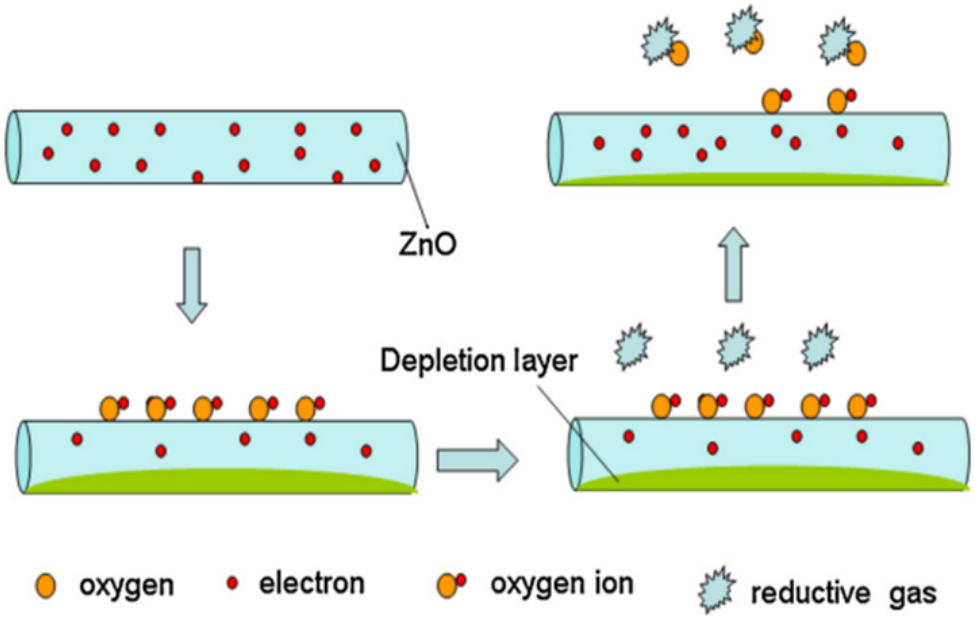

Figure 21: Sensing mechanism of ZnO for reductive gas (Wei *et al.,* 2011)

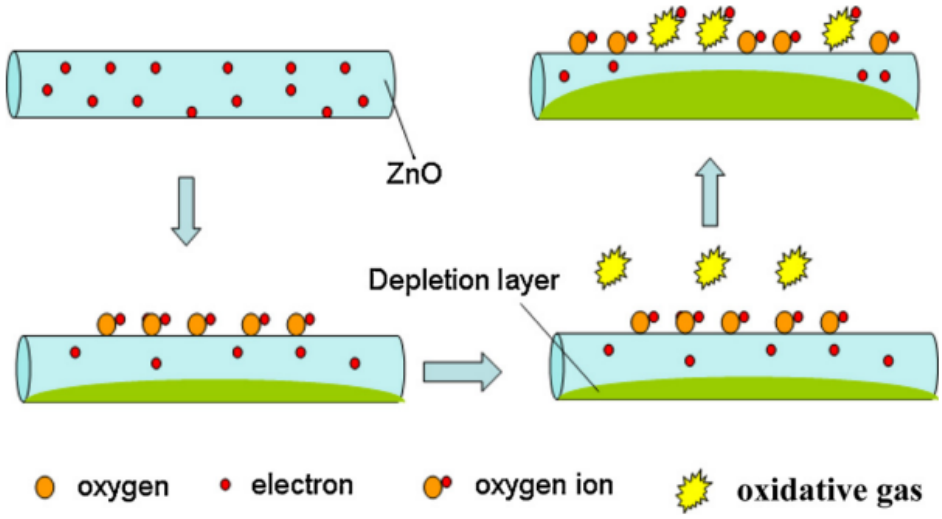

Figure 22: Sensing mechanism of ZnO for oxidative gas (Wei *et al.,* 2011)

oxidative gas molecules extract the electrons from the conduction band, which widens the depletion layer more. As a result, the surface resistance increases further (Wei *et al.,* 2011).

ZnO sensors generally work well at temperatures greater than 100 °C for the sensing ethanol and acetone (Hsu *et al.,* 2014; Khayatian *et al.*, 2014; Prajapati & Sahay, 2013; Qi *et al.,* 2008; Santhaveesuk *et al.,* 2010). At temperatures between 100 and 200 °C, oxygen molecules are adsorbed and converted into O_2^- ions by taking electrons from the

conduction band of ZnO. The adsorption process is represented in the equation (3.25):

$$O_2\,(gas) + e^- = O_2^-\,(adsorb)\,,\ (\text{ low temperature }) \tag{3.25}$$

At temperatures higher than 200 °C oxygen ion molecules dissociate into atoms with a single or double electric charge by taking electrons from the conduction band of ZnO. This is represented in equations (3.26) and (3.27):

$$\frac{1}{2}O_2\,(gas) + e^- = O^-(adsorb) \tag{3.26}$$

Or

$$\frac{1}{2}O_2\,(gas) + 2e^- = O^{--}(adsorb) \tag{3.27}$$

After the interaction with the molecules of the reductive type of analyte gas, oxygen ions return the electron back to the conduction band of ZnO. For example, the interaction of oxygen ion with the ethanol molecule is shown in equations (3.28) and (3.29) below.

$$CH_3CH_2OH\ (adsorb) + O^-\,(adsorb) \rightarrow C_2H_4O + H_2O + 1e^- \tag{3.28}$$

Or

$$CH_3CH_2OH\ (adsorb) + O^{2-}\,(adsorb) \rightarrow C_2H_4O + H_2O + 2e^- \tag{3.29}$$

Because of this, the resistance of ZnO decreases, and conductivity increases.
In the consequence of the equations (3.28) and (3.29), the rate of change of electron density can be written as:

$$\frac{dn}{dt} = K_{th}\,(T)\,[O^{2-}(adsorb)]^1[CH_3CH_2OH(adsorb)]^1 \tag{3.30}$$

Or,

$$\frac{dn}{dt} = K_{th}\,(T)\,[O^{2-}(adsorb)]^{1/2}[CH_3CH_2OH(adsorb)]^{1/2} \tag{3.31}$$

Equations (3.30) and (3.31), collectively, can be written as:

$$\frac{dn}{dt} = K_{th}(T)[O^{2-}(adsorb)]^b[CH_3CH_2OH(adsorb)]^b \tag{3.32}$$

Here, n is the electron density in a gaseous environment. The value of b depends on the kind of oxygen species adsorbed on the ZnO surface. Hence, it is called a charge parameter. Its value is 1 for O^- and 1/2 for O^{2-}. $K_{th}(T)$ is the reaction rate coefficient

and is defined as,

$$K_{th}(T) = A \exp(-\frac{E_a}{k_B T}) \tag{3.33}$$

Here, E_a and k_B are the activation energy of the reaction and the Boltzmann constant respectively. T is the temperature in kelvin.
Integrating equation (3.32), one get

$$n = K_{th}(T)[O^{2-}(adsorb)]^b[CH_3CH_2OH(adsorb)]^b t + n_0 \tag{3.34}$$

Here, the quantities n and n_0 are the electron density of the sensor at their operating temperature in gas and air. At the equilibrium, in gaseous and air atmospheres, these quantities remain constant with time. Thus, equation (3.34) can be written as:

$$n = \Gamma_t K_{th}(T)[O^{2-}(\text{ adsorb })]^b[CH_3CH_2OH(\text{ adsorb })]^b + n_0 \tag{3.35}$$

Here, Γ_t is a time constant. In terms of resistances R, the electron density is defined by $n = \frac{\alpha}{R}$, where α is proportionality constant. So, equation (3.35) can be written as:

$$\frac{1}{R_g} = (\Gamma_t K_{th}(T)[O^{2-}(\text{ adsorb })]^b[CH_3CH_2OH(\text{ adsorb })]^b)/\alpha + 1/R_a \tag{3.36}$$

Here, R_a and R_g are the sensor's resistance in air and gas respectively. The gas response (S or R) is defined as R_a/R_g . Hence, the response formula can be written as:

$$S \; or \; R = \frac{R_a}{R_g} = \frac{(\Gamma_t K_{th}(T)[O^{2-}(\text{ absorb })]^b[CH_3CH_2OH(\text{ adsorb })]^b}{n_0} + 1 \tag{3.37}$$

According to this equation, the gas response varies with the reaction rate coefficient and electron density. Both parameters increase exponentially with temperature. These factors compete with each other and give maximum response only at specific temperatures (Hongsith *et al.,* 2010).

3.3.2 Gas Sensing Parameters

The following parameters are typically used to describe the capability of a sensor to detect gases: sensitivity or response (R), operating temperature, response time, recovery time, detection limit, selectivity, stability, and repeatability. The sensitivity (S) or gas response (R) is calculated by measuring the sensor signal before and after exposing the gas. The sensor signals may be resistance, conductance, capacitance, current, voltage, etc. The sensitivity or gas response is defined as the ratio of the change in amplitude of the sensor

signal after exposure to gas to the amplitude of the initial signal before exposing the gas.

$$S \; or \; R = (\Delta R/R) \times 100\% \tag{3.38}$$

If the sensor signal is resistance, then the above equation takes the form:

$$S = [(R_a - R_g)/R_a] \times 100\% \quad \text{for reducing gas} \tag{3.39}$$

$$S = [(R_g - R_a)/R_a] \times 100\% \quad \text{for oxidative gas} \tag{3.40}$$

where R_a and R_g represent the resistance of the sensor in air and gaseous environment, respectively (Wei *et al.,* 2011).

The gas response or sensitivity may be measured in terms of the ratio of the amplitudes of the sensor signal in air and gaseous environment (Mani & Rayappan, 2013).

$$S \; or \; R = R_a/R_g, \quad \text{for reducing gas} \tag{3.41}$$

$$S \; or \; R = R_g/R_a, \quad \text{for oxidative gas} \tag{3.42}$$

The gas response or sensitivity of the MOS gas sensor is a temperature-dependent quantity. The temperature at which the MOS gas sensor shows the maximum value of gas response or sensitivity is considered as the working or operating temperature (Wei *et al.*, 2011). After exposing the gas, the sensor signal changes and acquires the saturation value after some time. The time taken to change the sensor signal by 90% of the saturation value after exposure of the gas to the sensing element is considered as the response time. After acquiring the saturation value of the sensor signal the gas is ejected. The sensor signal then starts changing and tends to acquire the original value. The time taken to change the sensor signal by 90% to achieve the original signal state after ejection of the gas is considered the recovery time. The MOS gas sensor's sensitivity or gas response also varies with the amount of gas exposed to it. Generally, the value of sensitivity or gas response is higher for a higher amount of the exposed gas. The lowest concentration of exposed gas at which the sensor may respond is supposed to be the detection limit. A gas sensor does not show the same value of sensitivity or gas response upon exposure to the same amount of various gases separately. It shows the large value of sensitivity or gas response for the particular gas. It means it responds very well to that particular gas in comparison to other gases and is said to be selective for that gas. Thus, the selectivity of a sensor means how effectively it responds to one gas in comparison to other gases. The stability and repeatability of a sensor are evaluated by measuring the sensor signal number of times between 'ON' and 'OFF' states. If the results are the same for each measurement in a similar condition, then the stability and repeatability of the device are

considered good.

3.4 Sensor Set up

3.4.1 Gas Sensing at Room Temperature

Figure 23 depicts a schematic diagram of the sensor setup that was used to measure the sensing capabilities of ZnO films to detect ammonia at room temperature. It consists of two chambers: the left one is placed on the hot plate to heat liquid ammonia over its boiling point and is connected to the right test chamber through a glass tube. A digital temperature controller (TALBOYS 7X7 CER HP 230 V ADV, Henry Troemner, LLC,

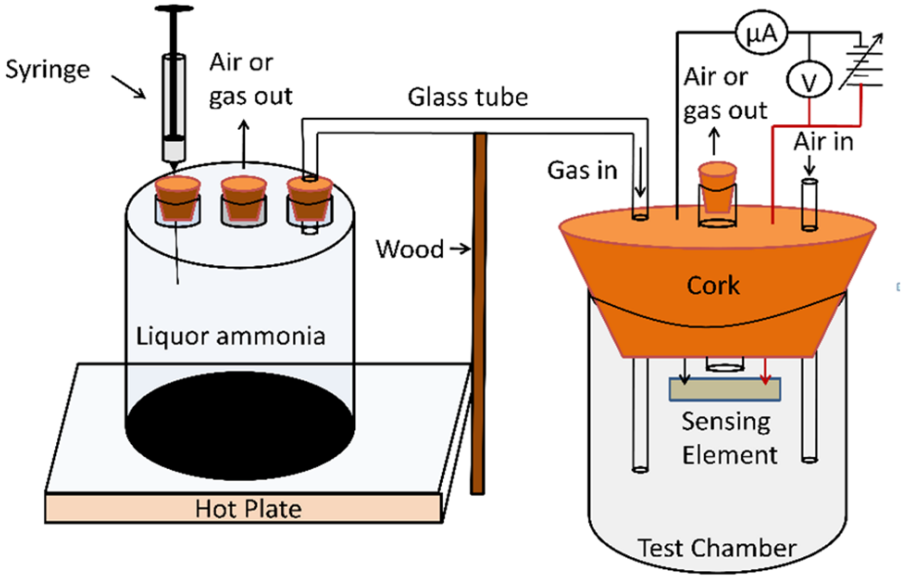

Figure 23: Schematic diagram of a sensor setup for gas sensing at room temperature

USA) is used to control the temperature of the hot plate. There are three apertures for the inlet of gas, the inlet of air, and the outflow in the test chamber. The ZnO film is implanted within the test chamber to measure its gas-sensing capabilities when exposed to different concentrations of gas.

3.4.2 Gas Sensing Above Room Temperature

The gas sensing capability or performance of ZnO films at higher temperatures (100 – 350 °C) is also measured by measuring the film resistance before and after exposing the analyte gas. For this purpose, a gas-detecting device made of an airtight glass chamber with two apertures - an inlet and an outlet, was utilized. Figure 24 shows the schematic diagram of the sensor setup. The glass chamber is placed on the hot plate. The temperature of the hot plate is controlled by a digital temperature controller (TALBOYS 7X7 CER HP 230 V ADV, manufactured by Henry Troemner, LLC, USA). The film is retrofitted inside the chamber. A Ni-Cr micro-heater is used to heat up the sample up to 350 °C. Using a

variable voltage regulator, the current flowing through the heating coil can be adjusted to control the working temperature of the heater. In order to stop the formation of liquid of analyte gas, the chamber's initial temperature was kept above the boiling point of the liquid form of analyte gas. The temperature fluctuation was noted to be ± 7 °C during the experiment.

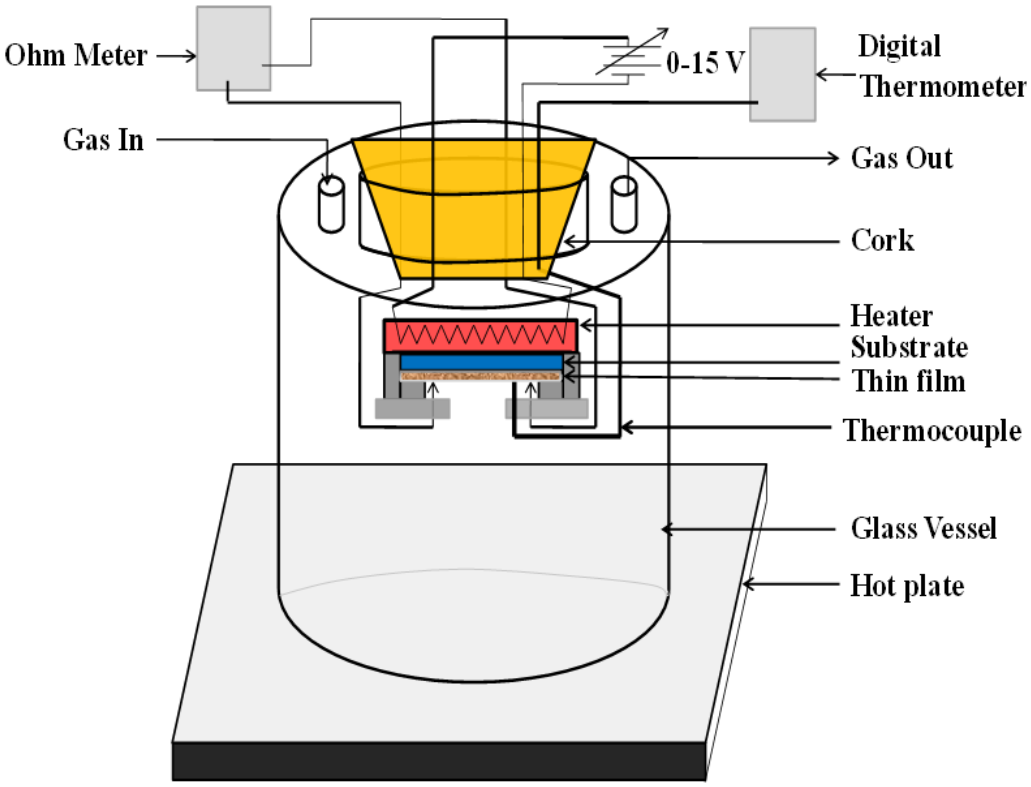

Figure 24: Sensor setup for gas sensing at higher temperature

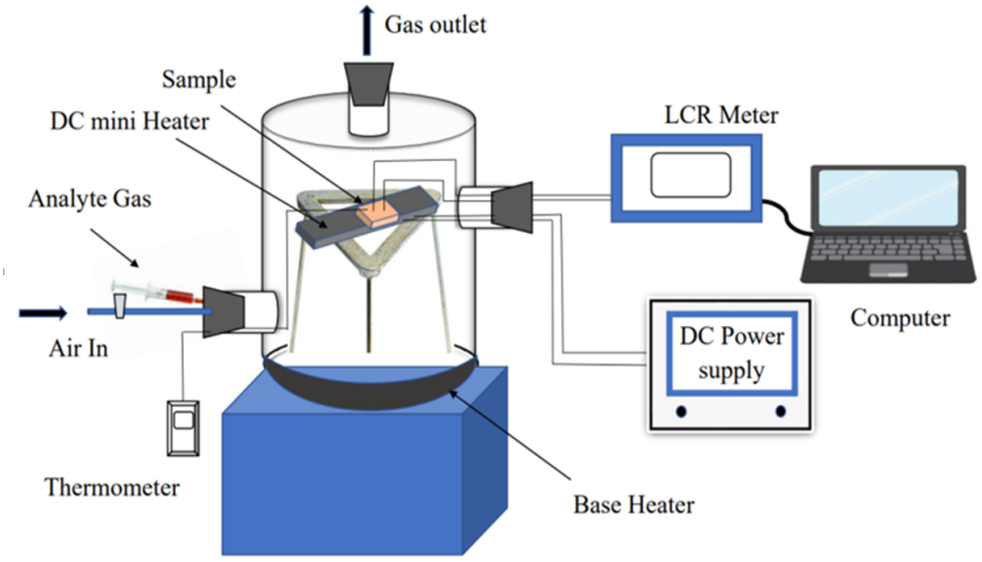

Figure 25: Alternative Gas sensor setup for gas sensing at higher temperature

Figure 25 shows another sensor setup used to measure the gas response. It consists of an airtight steel cylinder with two holes, one for gas input and one for gas outflow. At its base, the chamber has an electrical heater controlled by a variable voltage regulator. The starting temperature within the chamber was fixed at 120 ± 10 °C, which is higher than the boiling point of liquid ethanol, to prevent condensation. The sample inside the chamber was heated using a Ni-Cr microheater. The temperature of the microheater was changed using a variable voltage regulator. The sample temperature was controlled by changing the current flowing through the coil of the microheater. Two electrodes were made on the sample using copper wire and silver paste. The reading of the resistance of the sample before and after exposure to gas was recorded by an LCR meter (Hioki, 3536) which was interfaced with the computer.

Figure 26 (a) depicts the schematic diagram of the gas sensor setup to investigate the impact of applied gate electrode potential on the gas-detecting capabilities of ZnO films at ambient temperature. It consists of a steel chamber with three openings; (a) for gas inlet and driving air, (b) for wires and thermocouples, and (c) for gas outlets. Gas leakage was prevented using cork and O-ring. Figure 26(b) shows the zoom-in of the sensing device placed in the steel chamber. The sensing device consisted of ZnO film. The FTO glass plate was fixed just above parallel to it at a distance of 1.00 ± 0.07 mm with the

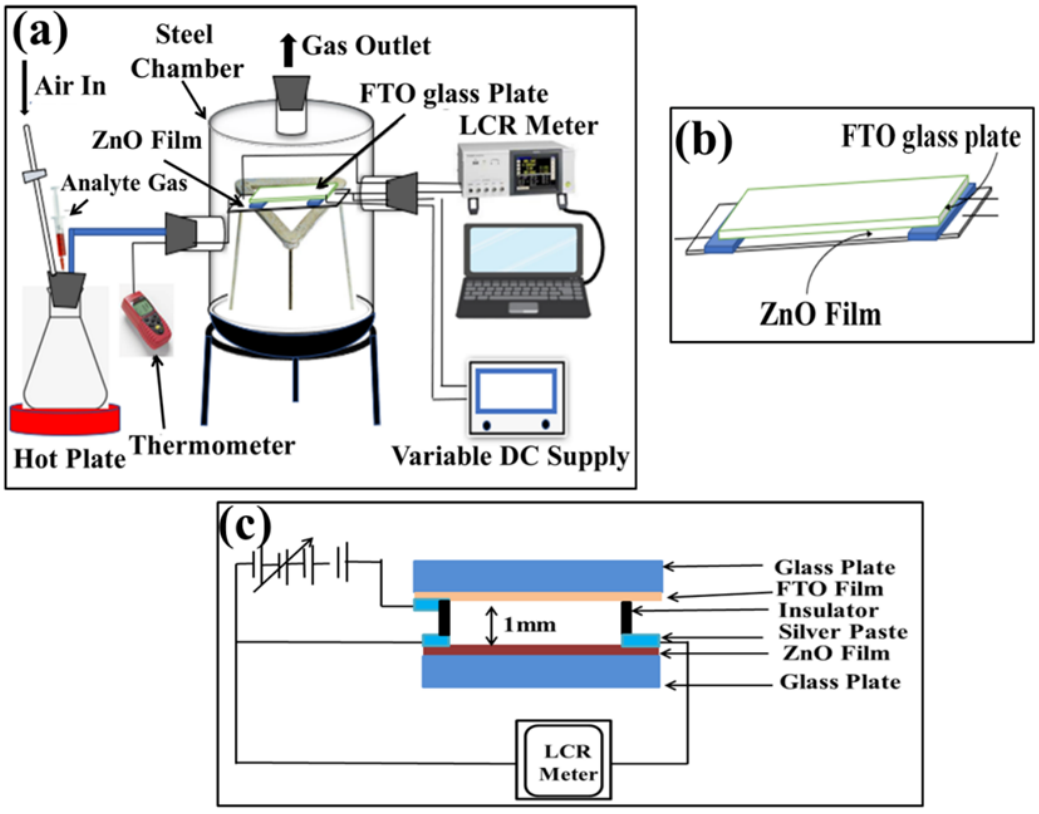

Figure 26: (a) Schematic diagram of a gas sensor set up, (b) Zoom in of a sensing device, and (c) circuit diagram to measure the sensitivity at different applied potentials

help of insulating support. Two electrodes were made at two ends of the ZnO film and one in the FTO film using a silver paste to establish good contact of the electrode with the film. Figure 26(c) shows the circuit diagram used to measure the gas response of the device. The ZnO film is connected to an LCR meter to measure its electrical resistance in the presence of air and gas respectively. To apply the positive gate potential on the FTO glass plate, the positive terminal of the variable DC power supply (0 – 25V) was connected to the FTO glass plate (say gate) and the negative terminal to the ZnO film. For the room temperature ammonia sensing, ammonia vapour was fed into the sensor setup using another external conical flask placed over a hot plate maintained at 120 ± 10 °C. A syringe was used to put liquid ammonia in the conical flask. Air was supplied using a nebulizer for the ejection of the analyte gas from the chamber. The nebulizer is not shown in the figure.

CHAPTER 4

4. RESULTS AND DISCUSSION

In this chapter, the optical & structural properties, surface morphology, elemental composition, and gas sensing performance of the prepared undoped, metal-doped, and metal-metal-doped ZnO films are discussed. The samples were prepared using different methods such as spin coating, spray pyrolysis, and doctor blade method. The various vapours (ethanol, acetone, ammonia, methanol, and isopropanol) detection capacities of as-prepared films were studied at room temperature as well as higher temperatures and reported along with the underlying mechanism.

4.1 Characterization of Spin-Coated ZnO Film

The optical & structural properties, surface morphology, elemental composition, and gas sensing capabilities of spin-coated ZnO film for ethanol, methanol, isopropanol, acetone, and ammonia at ambient temperature, are described in this section. The method of preparation of spin coating was described in section 3.1.2 of chapter 3.

4.1.1 Structural Analysis

The X-ray diffraction (Cu-Kα radiation of wavelength 1.54056 Å with a Bruker AXS, D2 PHASER A26-X1-A2BOB2A-, Serial No. 207047 diffractometers) was utilized to investigate the structural characteristics of ZnO film. Figure 27 depicts the XRD pattern of the ZnO film prepared by spin coating. The XRD pattern showed the polycrystalline nature with the presence of several distinct peaks. The sharp diffraction peaks were detected at 2θ = 31.8627 ± 0.0053, 34.5092 ± 0.0039, 36.3202 ± 0.0040, 47.5594 ± 0.0020, 56.3553 ± 0.0046, 62.7900 ± 0.0161, 67.8320 ± 0.0053, and 68.9580 ± 0.0111°, respectively. These peaks were found to be consistent with the values on JCPDS card no., 36-1451. The absence of impurity peaks confirms the formation of pure ZnO. The

Table 2: (hkl), 2θ, FWHM, d-spacing, crystallite size (D) and strain (ε) of spin-coated ZnO film on glass substrate

(hkl)	**2θ (°)**	**FWHM (°)**	***d*-spacing (Å)**	***d*-spacing (Å) (JCPDS)**	***D* (nm)**	**Strain (ε) 10^{-3}**
(100)	31.8627 ± 0.0053	0.2804 ± 0.0139	2.8150	2.8143	29.4733 ± 1.4576	4.29 ± 0.21
(002)	34.5092 ± 0.0039	0.2701 ± 0.0095	2.6043	2.6033	30.1947 ± 1.0407	3.87 ± 0.13
(101)	36.3202 ± 0.0040	0.3071 ± 0.00955	2.4781	2.4759	27.2350 ± 0.8468	4.09 ± 0.13
(102)	47.5594 ± 0.0020	0.3493 ± 0.0053	1.9141	1.9111	28.9097 ± 0.5085	2.97 ± 0.05
(110)	56.5553 ± 0.0046	0.2990 ± 0.0146	1.6286	1.6247	30.1545 ± 1.4763	2.43 ± 0.12
(103)	62.7900 ± 0.0161	0.3764 ± 0.05658	1.4808	1.4771	25.9832 ± 4.1061	2.56 ± 0.40
(112)	67.8320 ± 0.0053	0.4119 ± 0.0161	1.3823	1.3781	24.7766 ± 1.0329	2.51 ± 0.10
(201)	68.9580 ± 0.0111	0.4706 ± 0.0687	1.3625	1.3582	24.1183 ± 4.1495	2.54 ± 0.44

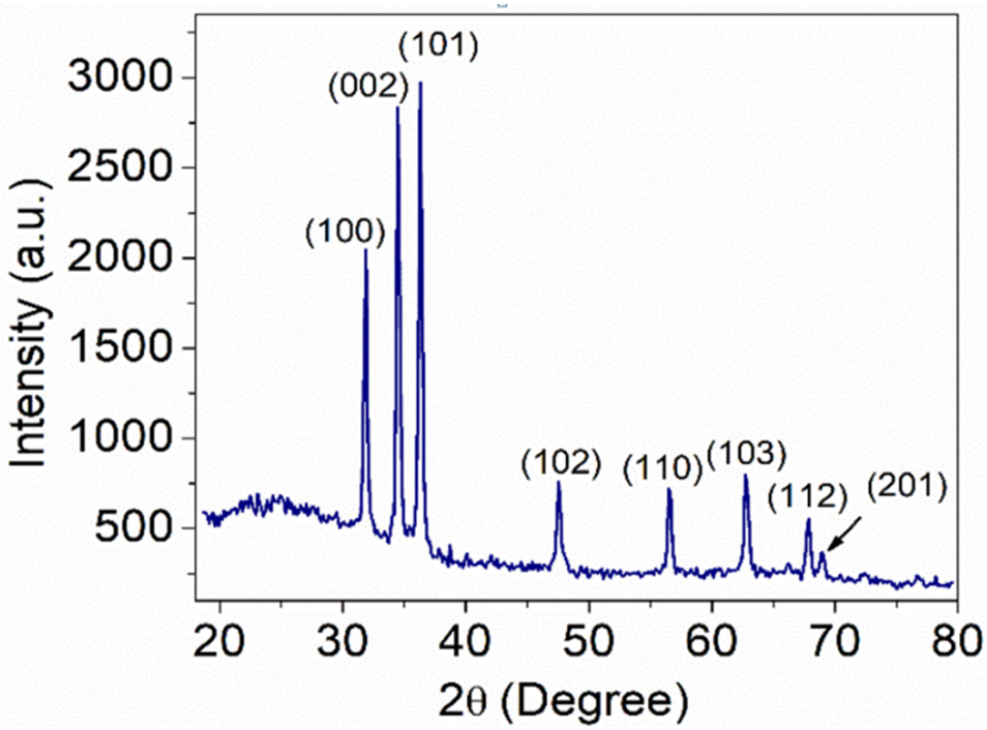

Figure 27: XRD pattern of spin-coated ZnO film on glass substrate

d-spacing was calculated using Braggs law: $2d \sin\theta = n\lambda$. The crystallite size (D) was calculated employing Debye Scherer's formula: $D = \frac{0.9\lambda}{\beta \cos\theta}$. The lattice strain ($\varepsilon$) was determined using the formula: $\varepsilon = \frac{\beta}{4 \tan\theta}$ (Pramod & Pandey, 2014; Srinivasulu *et al.*, 2017). The detailed calculation of 2θ, d-spacing, D, and ε are illustrated in Table 2. The calculated value of d-spacing was found to be slightly different (<0.32%) from the JCPDS value, indicating the deposition of quality of the film on the glass substrate. The mean values of the crystallite size and the strain with respect to prominent peaks corresponding to planes (100), (002), and (101) are 28.9677 nm, and 4.08×10^{-3}, respectively. The FWHM was found by fitting the peaks. The errors in D, and ϵ were calculated using errors found in 2θ, and FWHM during fitting the peaks.

4.1.2 Optical Analysis

Figure 28(a) depicts the optical transmittance spectrum of ZnO film. The transmittance was observed to be higher than 80% in the visible region. As is typical for ZnO, a dramatic drop in transmittance at shorter wavelengths close to the UV region was observed (Goh et al., 2014). From transmittance data, the optical band gap was computed using a Tauc plot: $(\alpha h\nu)^2 = A\left(h\nu - E_g\right)$ where α, A, $h\nu$, and E_g are the absorption coefficient, energy constant, photon energy, and optical band gap, respectively. Figure 28(b) shows the Tauc plot corresponding to the transmittance spectrum. The optical band gap (E_g) was determined by extrapolating the linear part of the plot into the $h\nu$-axis, which showed a value of 3.202 ± 0.023 eV. This value agrees with the value reported in the published

literature(Mani & Rayappan, 2013). The error in the optical band gap was determined by using the standard errors found in the slope and the intercept of the linear fit in the linear portion of the graph.

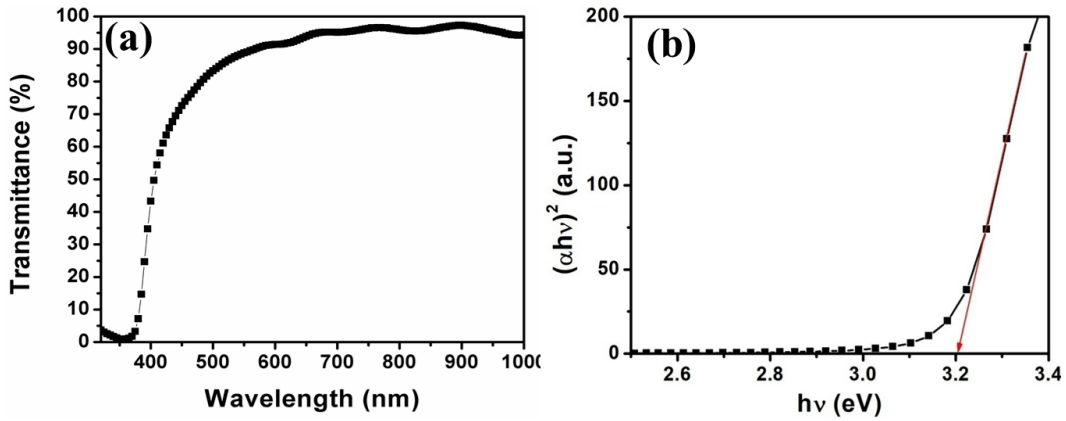

Figure 28: (a) Transmission spectrum and (b) Tauc plot of spin-coated ZnO film on glass substrate

4.1.3 Surface Morphology

The morphology of the sensor surface plays a critical role in the gas sensing task (Shao *et al.,* 2016; Yu *et al.,* 2011). Figure 29(a) depicts the SEM image of ZnO film deposited on a glass substrate by the spin coating method. It clearly shows the surface consisting of spherical grains. Energy dispersive X-ray (EDX) analysis was carried out to study its elemental compositions. Figure 29(b) depicts the EDX spectrum of as-prepared

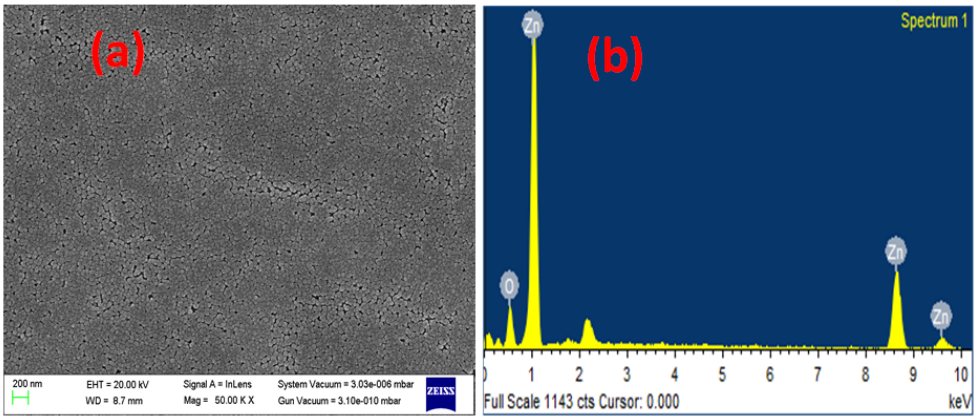

Figure 29: (a) SEM micrograph and (b) EDX spectrum with Zn and O content in ZnO film

Table 3: Elements present in spin-coated ZnO film

Element	Atomic %
O	47.67
Zn	52.33
Total	100

ZnO film. The spectra clearly showed the peaks associated with the elements zinc (Zn) and oxygen (O). The contents of zinc and oxygen present in ZnO, in terms of atomic percentages, are depicted in Table 3. The atomic percentage of Zinc and oxygen are 52.33 and 47.67% respectively.

4.1.4 Sensor Performance Towards Ammonia

The gas sensing efficacy of ZnO film was examined by recording the currents flowing through the ZnO film in the air (I_a)) and in the analyte gas (I_g) by applying a constant potential difference (p.d.) of 10 V across ZnO film (Jha *et al.,* 2018), which was taken as a baseline. The gas response (R) is given by $\frac{I_g}{I_a}$. Figure 30 depicts the response characteristics of the ZnO sensor at the exposure of 400 ppm of ammonia vapor against the sensing time. In figure, I and E represent the injection and ejection of gas. It shows that the response increased quickly after injecting the ammonia vapor and attained the constant maximum value of ~38.5 after the time of about 39 sec. The vapor was then ejected. The response was then decreased and attained an original minimum value of ~1

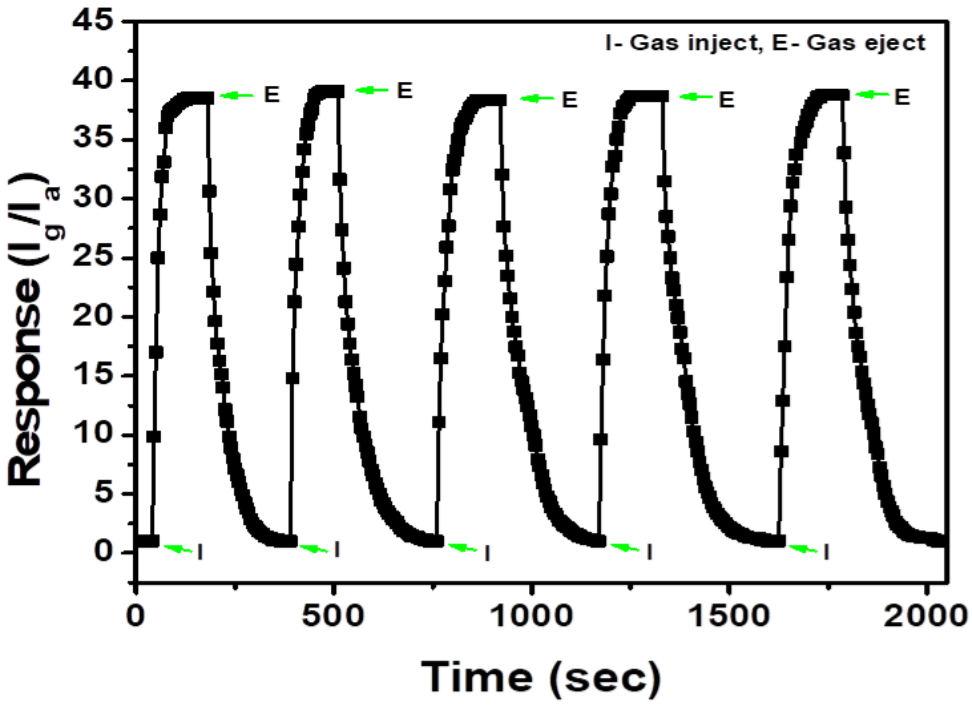

Figure 30: Response of ZnO film with 400 ppm of NH_3

after the time of 95 sec. The process of injection and ejection of gas was repeated for up to 5 cycles. Nearly the same value of the response was found in each cycle, indicating the good reproducibility of the device. The sensor's efficacy in sensing various amounts of ammonia vapour was also studied by following the injecting and ejecting of the various amount of it ranging from 400 – 20 ppm.

The variation of gas response with time with the exposure of various concentrations

of NH_3 is shown in Figure 31(a). As ammonia concentrations dropped, a decline in gas response was observed. The two important parameters: response time and recovery time were also measured. Figure 31(b) illustrates the measurement of the ZnO sensor's response and recovery times following exposure to ammonia vapor at a 400 ppm concentration. The rate at which exposed gas interacts with adsorbed oxygen ions on the surface of ZnO determines the response time, whereas the rate of adsorption of oxygen molecules on the surface of ZnO following the ejection of vapor determines the recovery time (Hongsith *et al.,* 2010). The sensor geometry affects the values of these two

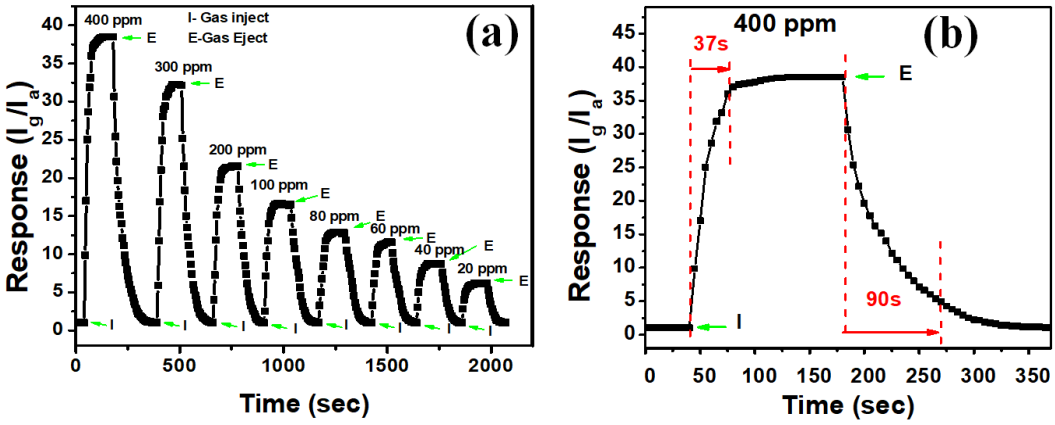

Figure 31: (a) Response at different concentrations of ammonia and (b) Calculation of response time and recovery time with 400 ppm of NH_3

parameters as well. The calculation of response time and recovery time with the exposure of 400 ppm of ammonia is depicted in Figure 31(b). Table 4 shows the calculated values of response and recovery times. The response and recovery times were observed to be

Table 4: Gas response, response time and recovery time of ZnO sensor on exposure of various concentrations of NH_3 vapour

Ammonia Concentration (ppm)	**Response** (I_g/I_a)	**Response time (sec)**	**Recovery time (sec)**
20	6.1 ± 0.8	24	43
40	8.7 ± 0.4	26	51
60	10.1 ± 0.4	28	62
80	12.9 ± 0.6	29	64
100	16.5 ± 0.6	30	66
200	21.5 ± 0.4	33	69
300	32.2 ± 0.6	35	75
400	38.5 ± 0.6	37	90

37 and 90 sec respectively with the exposure of 400 ppm of ammonia vapour. These values were 24 and 43 sec for 20 ppm of ammonia vapour. With the exposure of low ppm of ammonia vapour, less number of ammonia molecules are available to interact with adsorbed oxygen molecules and hence had acquired the saturation value of response

quickly which results low response and short response time. The oxygen molecules are adsorbed after the ejection of ammonia vapor which results the fast recovery for low concentrations of ammonia. The same experiment was performed with the same conditions for 8 days to determine the repeatability (reproducibility) and stability of the sensing device. The experiment was repeated 8 times each day by exposing 400 ppm of ammonia vapour and the standard error was calculated. Figure 32 shows the results of the experiment. The response was found to be slightly decreasing from 38.5 ± 0.6 to 35.7 ± 0.6, demonstrating the device's consistency over the course of each measurement. This experiment was repeated under the same condition by exposing 400 ppm of various vapours of ethanol, methanol, acetone, isopropanol, etc. The corresponding values of gas response were calculated. The measured gas response for various vapors is shown in Figure 33. This is the average value of the response with the standard error of the experiment repeated 8 times at ambient temperature. Among the studied varieties, the ZnO sensor exhibits pronounced selectivity for ammonia vapour.

In the ambient atmosphere, the oxygen molecules are ionosorbed on the surface of ZnO. The ionosorbed oxygen molecules extract the electrons from the conduction band of ZnO. Due to this the width of the space charge (depletion) region and the height of the potential barriers increase (Yu *et al.*, 2011). Figure 34(a) shows schematically

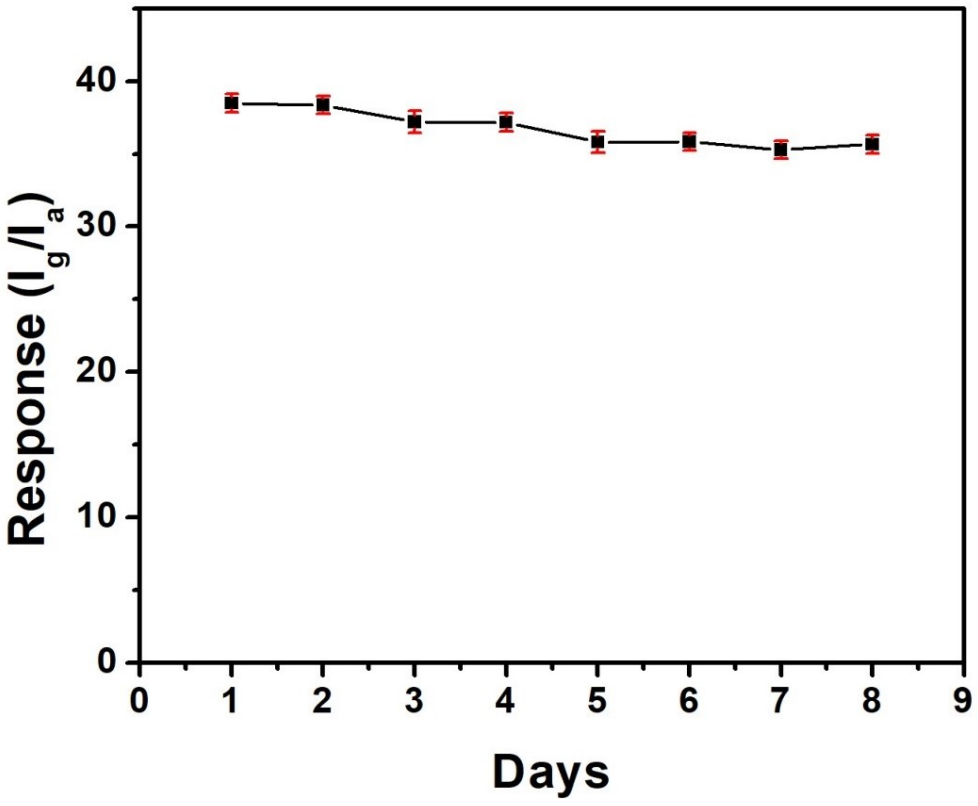

Figure 32: Repeatability and stability of ZnO sensor at 400 ppm of NH_3 at room temperature

growth of the depletion layer and the barrier height. This current was denoted by I_a. On the exposure of reducing gas, say ammonia, the molecules of reducing gas

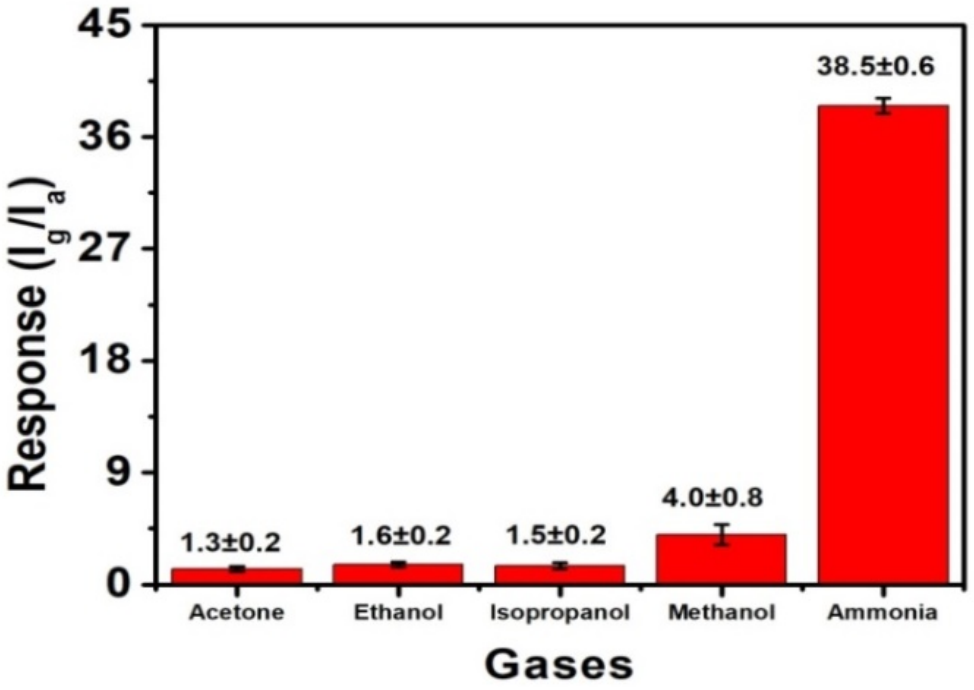

Figure 33: Selectivity of ZnO sensor measured at 400 ppm of various gases at room temperature

react with the ionosorbed oxygen ions and releases the electrons back to the surface of ZnO. As a result, the potential barriers decline, thus decreasing the resistance of ZnO. Figure 34(b) depicts the phenomenon of the decrease of the depletion layer. The release of electrons due to the interaction between ammonia and O_2^- is represented as: $4NH_3 + 3O^-_{2(ads)} = 2N_2 + 6H_2O + 6e^-$ (Dey, 2018). The results of the measurement of

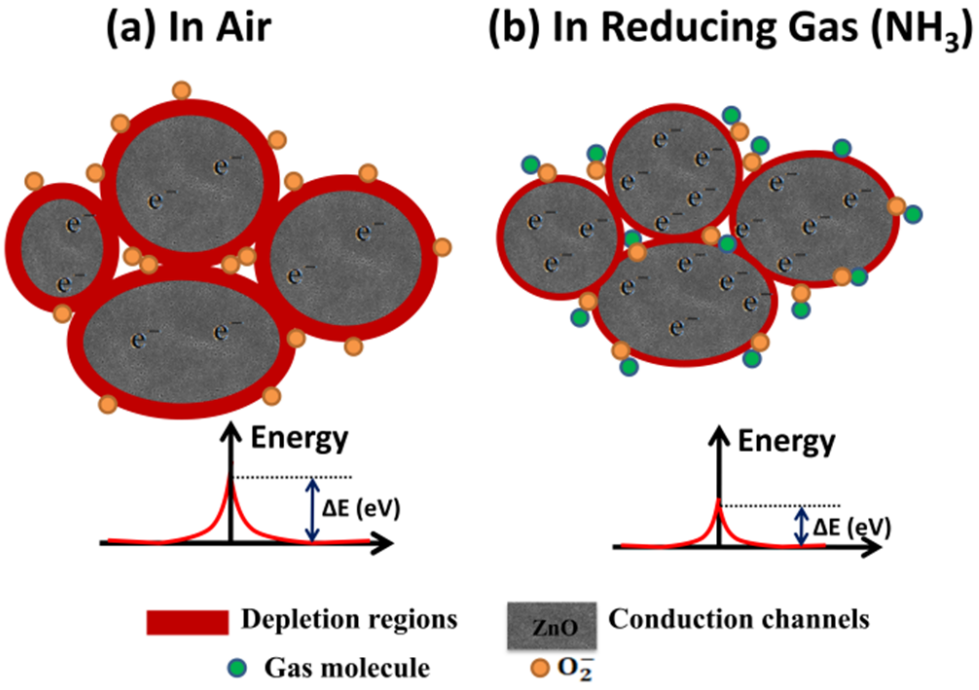

Figure 34: Illustration of the working mechanism of ZnO sensor (a) in the air (b) in reducing gas

response on the exposure of 400 ppm of various gases showed a high response value for the ammonia vapour. Ammonia's smaller kinetic diameter and low ionization energy are responsible for showing the high response (Anasthasiya *et al.*, 2018). Small-diameter ammonia vapour diffuses readily inaccessible ZnO pores and can interact with more ionosorbed oxygen ions in the pores than the other gases. It results in a higher response for the ammonia than the other gases. For the sake of clarity, the molecular weight, kinetic diameter, and ionization energy of several gas molecules are listed in Table 5 (Goel *et al.,* 2012; Zhu *et al.,* 2008).

Table 5: Molecular weight, Kinetic diameter, and ionization energy of various molecules (Goel *et al.,* 2012; Zhu *et al.,* 2008)

Vapour	**Ammonia**	**Methanol**	**Ethanol**	**Acetone**	**Isopropanol**
Molecular weight	17	32	46	58.05	60.1
Kinetic diameter (nm)	0.26	0.37	0.45	0.46	0.46
Ionization energy (eV)	10.18	10.5	10.47	9.69	10.12

The results of this study were compared to the reported sensitivities of ZnO-based sensors made using various techniques. This comparison is presented in Table 6. The comparison demonstrates that the sensitivity herein is found to be about ~38 which is better than metal (Co, Ni) doped-ZnO prepared by spray pyrolysis technique. We, therefore, draw the conclusion that the spin-coated ZnO film used in this study may be one of the good sensors for detecting low quantities of ammonia vapour at ambient temperature.

Table 6: Comparison of sensing capability of ZnO based ammonia sensor of this works with published works

Materials/method	**Operating Temperature (ºC)**	**Concentration (ppm)**	**Response** $(R_a/R_g or I_g/I_a)$	**Reference**
In_2O_3 – MgO Pd loaded with TiO_2	~530	300	~25	(Takao *et al.,* 1994)
Spray deposited Co doped ZnO	RT	100	3.48	(Mani & Rayappan, 2015)
Spray deposited Ni doped ZnO	RT	100	2.52	(Mani & Rayappan, 2014)
Hydrothermally grown ZnO nanowires	350	200 10	4.2 1.5	(Shao *et al.,* 2016)
ZnO nanowires by SILAR	RT	50	80.2	(Anasthasiya *et al.,* 2018)
Spin coated ZnO grain	RT	400 60 20	38.5 ± 0.6 11.2 ± 0.4 6.1 ± 0.8	This work

4.2 Characterization of ZnO Film Prepared by Doctor Blade Method

In this section, structural and optical properties of ZnO nanoparticles prepared by the co-precipitation method are investigated for acetone sensing. The sample preparation

method is described in section 3.1.4 of chapter 3. The results of the investigation on acetone sensing using ZnONPs films prepared by the doctor blade method are discussed.

4.2.1 Structural Analysis

At first, as-prepared ZnO nanoparticles were examined using XRD. The captured XRD pattern is shown in Figure 35(a). It was collected in the 20°-85° angular range, employing CuK_{α} radiation with a wavelength of 1.54056 Å. The intense peaks were obtained at 2θ = 31.0618 ±, 33.7285 ± 0.0064, 35.5518 ± 0.0074, 46.8524 ± 0.0093, 55.9166 ± 0.0058, 62.1954 ± 0.0497, 65.7034 ± 0.0100, 67.2904 ±, 68.4153 ±, 71.8966 ± 0.0386, 76.3435 ± 0.0282 and 80.6931 ± 0.0396° and were labeled with reference to JCPDS d-spacing values of card no. 36-1451 as (100), (002), (101), (102), (110), (103), (200), (112), (201), (004), (202), and (104) planes (Al-Hardan *et al.*, 2013; Prajapati & Sahay, 2013). The numerous distinct peaks demonstrated that ZnO is polycrystalline. The d-spacing was calculated using Braggs law: $2d \sin\theta = n\lambda$. The Two lattice parameters, a and c, were determined using formulas: $a = \frac{\lambda}{\sqrt{3}\ sin\theta}$ and $c = \frac{\lambda}{sin\theta}$ (Pramod & Pandey, 2014; Srinivasulu *et al.*, 2017). The crystallite size (D) was calculated utilizing the Debye-Scherrer formula: $D = \frac{0.9\lambda}{\beta \cos\theta}$ (Bhatia *et al.*, 2017). The inset of Figure 35(a) depicts the calculation method of full width at half maxima (β). The mean crystallite size of ZnO was estimated by taking into account the entire peaks, and this value was 21.8253 nm. The values of observed 2θ, FWHM, d-spacing, and crystallite size (D)

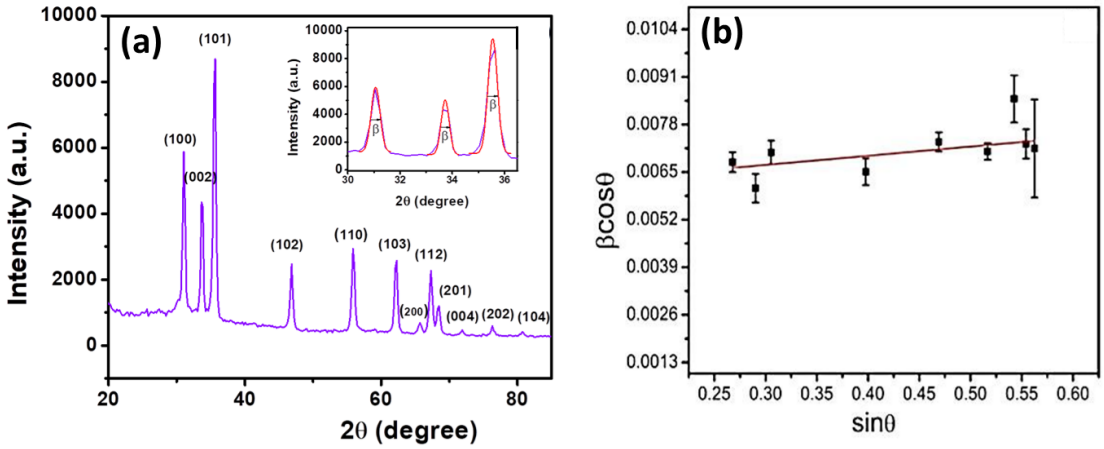

Figure 35: (a) XRD pattern (Inset: Determination of β) and (b) W-H plot of as-prepared ZnONPs with standard errors in the values of $\beta \cos\theta$

are presented in Table 7. The values of a and c were found to be (3.3205 ± 0.0027) Å & (5.3082 ± 0.0051) Å. The value of c/a ratio was 1.5986 ± 0.0002, confirming the formation of the wurtzite hexagonal phase of ZnO (Srinivasulu *et al.*, 2017). The errors in D, a, and c were calculated using the standard error found in 2θ, and FWHM during the fitting of the individual peaks. The average microstrain (4ε) as well as crystallite size

(D) was also computed utilizing Williamson-Hall (W-H) plot: $\beta\cos\theta = \frac{0.94\lambda}{D} + 4\varepsilon\sin\theta$ (Hassan *et al.*, 2014). Figure 35(b) shows the W-H plot which is a plot of $\beta\cos\theta$ versus $\sin\theta$ including standard errors along the $\beta\cos\theta$-axis. The microstrain and crystallite size were evaluated from the slope and intercept of the linear fit of the W-H p lot. The average microstrain and crystallite size were found to be 0.0025 ± 0.0012 and 24.3799 ± 2.1753 nm respectively. No impurity peaks observed in the XRD pattern indicated the good purity of the product material.

Table 7: Observed 2θ, FWHM, d-spacings and crystallite size (D) of ZnO

Plane (hkl)	**2θ (degree)**	**FWHM (degree)**	***d*-spacing (Å)**	***d*-spacing (Å) JCPDS**	***D* (nm)**	**Average D (nm)**
(100)	31.0618 ± 0.0064	0.4027 ± 0.0154	2.8756	2.8143	21.3784 ± 0.8176	21.8253
(002)	33.7285 ± 0.0074	0.3627 ± 0.0154	2.6541	2.6033	23.8975 ± 1.0148	
(101)	35.5518 ± 0.0075	0.4232 ± 0.0184	2.5221	2.4759	20.5788 ± 0.8966	
(102)	46.8524 ± 0.0093	0.4062 ± 0.0209	1.9367	1.9111	22.2517 ± 1.1448	
(110)	55.9166 ± 0.0058	0.4748 ± 0.0149	1.6424	1.6247	19.7768 ± 0.6206	
(103)	62.1954 ± 0.0497	0.4726 ± 0.0129	1.4908	1.4771	20.4976 ± 0.5622	
(200)	65.7034 ± 0.0100	0.5796 ± 0.0369	1.4194	1.4071	17.0354 ± 1.0848	
(112)	67.2904 ± 0.0087	0.5002 ± 0.0230	1.3898	1.3781	19.9191 ± 0.9154	
(201)	68.4153 ± 0.0206	0.4949 ± 0.0766	1.3696	1.3582	20.2662 ± 2.3180	
(004)	71.8966 ± 0.0177	0.4096 ± 0.0386	1.3116	1.3017	25.0192 ± 2.3568	
(202)	76.3143 ± 0.0282	0.4277 ± 0.0663	1.2463	1.2380	24.6682 ± 2.6718	

4.2.2 Fourier Transform Infrared Analysis

Fourier transform infrared (FTIR) spectroscopy is a useful method to produce an infrared spectrum of absorption or emission of material (solid or liquid or gas). High-resolution spectral data are concurrently gathered over a broad spectral range by an FTIR spectrometer. The obtained spectrum was analyzed to study the various characteristic bonds and functional groups present in the materials. The FTIR spectrum of the so-prepared ZnONPs was collected in the range of 400 – 4000 cm^{-1}, using a Perkin Elmer -16.10.2 FTIR spectrophotometer in attenuated total reflectance (ATR) mode. Figure 36

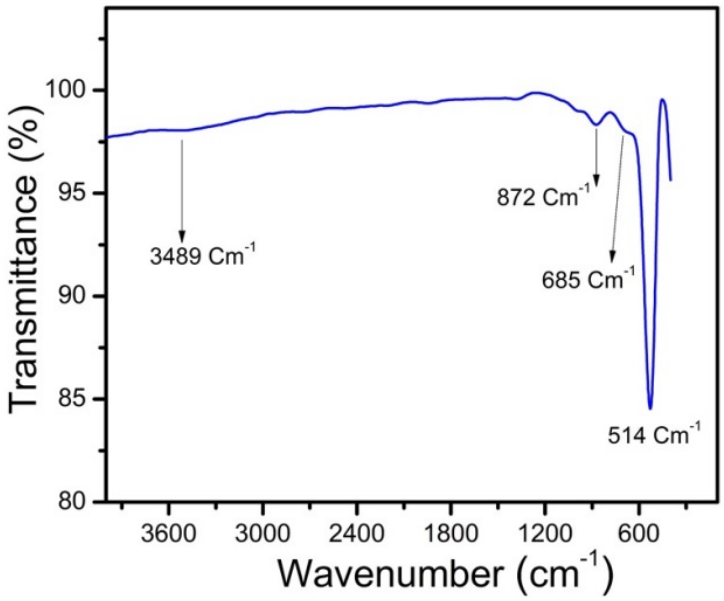

Figure 36: FTIR spectrum of as-prepared ZnONPs

shows the obtained spectra. It clearly displays a strong, well-defined characteristic peak at 514 cm^{-1}, and low peaks present at 685 and 872 cm^{-1} due to Zn-O stretching (Joshi *et al.*, 2021). A strong peak at 514 cm^{-1} indicates the Zn-O stretching vibration which confirms the formation of the ZnO. Weak peak present at 3489 $c\,m^{-1}$ indicates the OH stretching mode of surface hydroxyl groups.

4.2.3 Sensing Performance Towards Acetone

Here, the description of the sensing measurement at various temperatures toward acetone vapour is discussed. The sensor performance was evaluated using formula: Gas Response (R) = $\frac{R_a}{R_g}$. Here R_a and R_g are resistances of ZnO film in air and in a gaseous environment. The reaction rate of test gas with the adsorbed oxygen species varies with the temperature (Xu *et al.*, 2015). Hence, in order to determine the operating temperature, the sensing capability in terms of gas response was measured in the temperature ranging from 100 to 310 °C at the exposure of 800 ppm of acetone. The responses that were measured at various temperatures were displayed in Figure 37(a-b). The highest value of gas response was recorded to be 25.697 ± 0.012 at 285 ± 7 °C. Figure 37(b) depicts the plot of response with temperature. The response increased with temperature. The response was poor at low temperatures.

The two important sensing parameters, response time and recovery time, are graphically calculated. Geometrical calculations of response time and recovery time were shown in Figure 38. The calculated values of response and recovery time were observed as 39 and 79 sec, respectively when 800 ppm of acetone was exposed to the sensing element at 285 ± 7 °C. In this experiment, the gas response along with the response time and recovery

time were also studied with exposure to different amounts of acetone ranging from 40 to 800 ppm. Figure 39(a) depicts the response curves with exposure to different acetone concentrations. The computed values of gas response, response time, and recovery

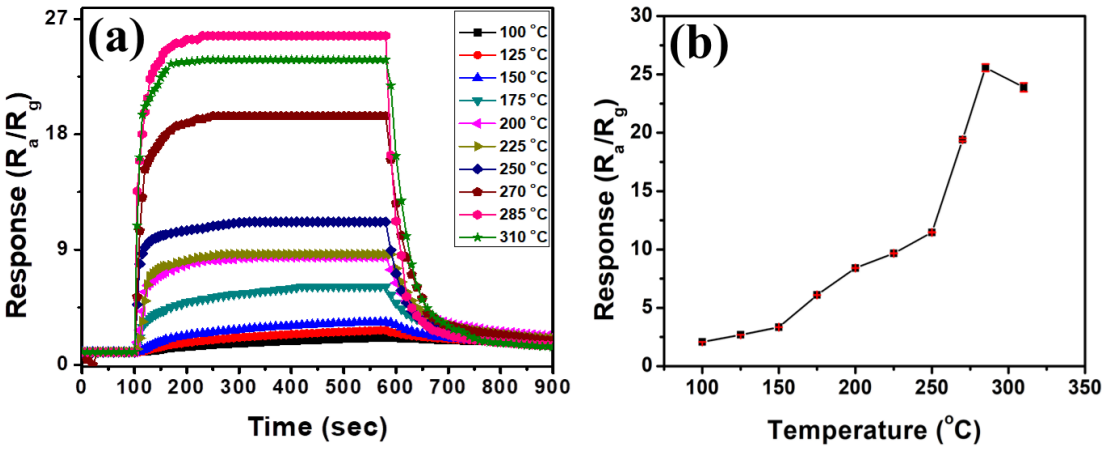

Figure 37: (a) Response vs time at different temperatures (b) variation of response with the temperature of ZnONPs film prepared by doctor blade method

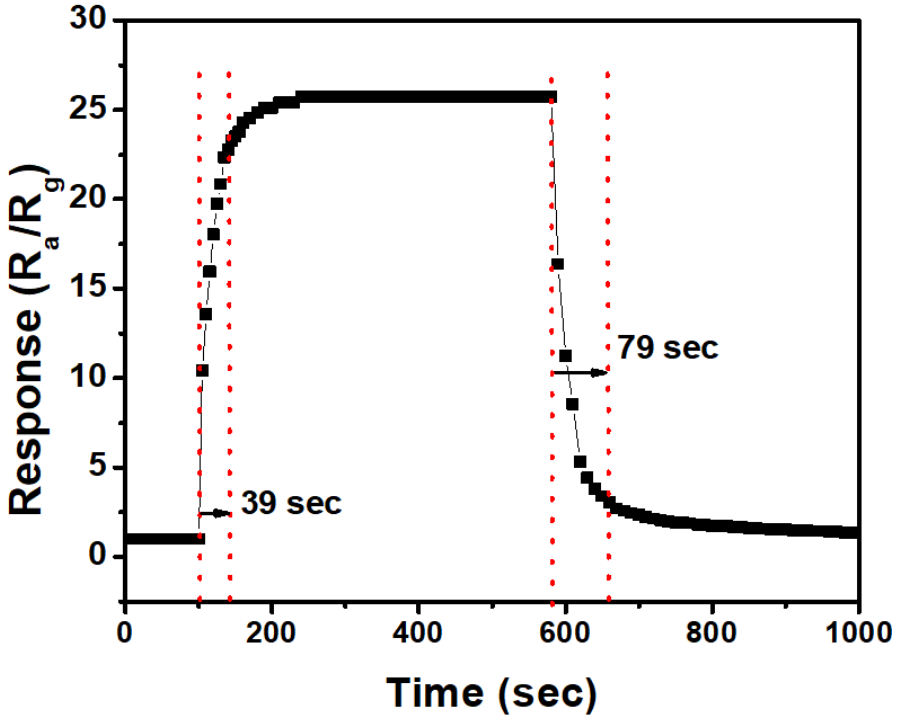

Figure 38: Geometrical calculation of response and recovery times of ZnONPs film with an exposure of 800 ppm of acetone at 285 ± 7 °C

time at 285 ± 7 °C with varying acetone concentrations ranging from 40 to 800 ppm are presented in Table 8. The response value was found to be higher with exposure to higher concentrations of acetone. The linear rise of gas response with concentrations was found [Inset of this Figure 39(a)]. The gas response was measured at an exposure of

800 ppm of acetone at 285 ± 7 °C for three cycles depicted in figure 39(b). At each cycle, the maximum values of the response were found nearly the same. This result, evidently, showed good stability. The results obtained herein were compared with the available

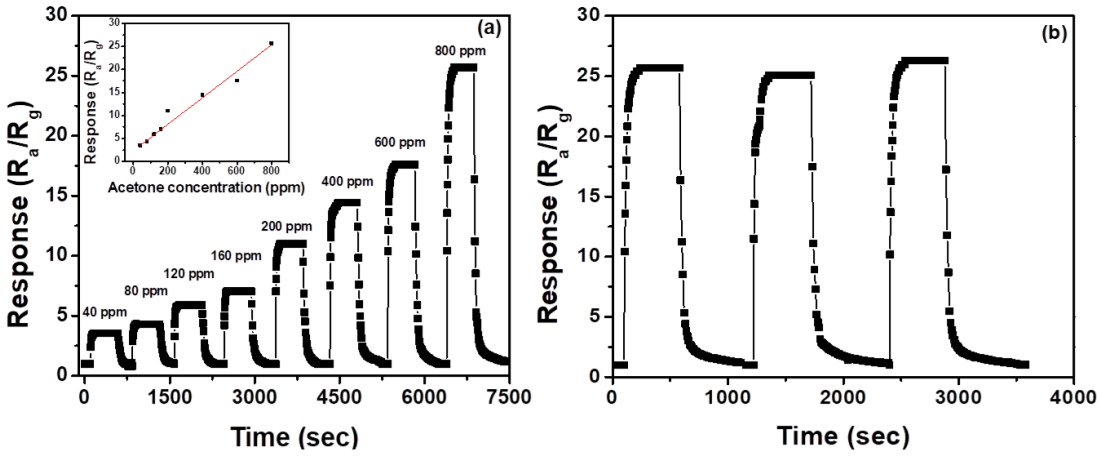

Figure 39: : (a) Response curves at various concentrations of acetone [inset: variation of response with acetone concentration] (b) stability curves for 800 ppm acetone

Table 8: Response, response time and recovery time at different concentrations of acetone at 285 ± 7 °C

Concentration (ppm)	**Response** (R_a/R_g)	**Response time (sec)**	**Recovery time (sec)**
40	3.500 ± 0.002	21	91
80	4.299 ± 0.002	23	101
120	5.899 ± 0.003	21	99
160	7.052 ± 0.003	22	100
200	11.009 ± 0.006	26	95
400	14.430 ± 0.007	28	97
600	17.562 ± 0.008	31	88
800	25.697 ± 0.012	39	79

published values for analogous systems but prepared using different techniques such as thermal oxidation, hydrothermal, spray pyrolysis, electrospinning and spray pyrolysis, RF co-sputtering, co-precipitation, etc. which are presented in table 9. The working temperature was observed to be marginally lower than the values published temperature for a similar type of sensor prepared by alternative methods.

Table 9: Comparison of operating temperature, response, response time, and recovery times with reported works

Materials	Operating Temp. (°C)	Conc. (ppm)	Response (R_a/R_g)	Res/Rec time (sec)	Reference
ZnO nanosheets by Solvothermal	420	500	70	NR	(Xiao *et al.,* 2012)
La-doped ZnO by Solvothermal	385 425	1000	1800 1826	16/3	(Chu *et al.,* 2012)
Hydrothermally grown Ag doped ZnO neddle	370	200	30.233	10/21	(Al-Hadeethi *et al.,* 2017)
Pt-ZnO by Thermal Oxidation	400	400	188	NR	(Wongrat *et al.,* 2017)
Pd-ZnONPS by Chemical Solution	340	100	76	8/10	(Zhang *et al.,* 2018)
RF Sputtered Cr doped ZnO	400	500	90	210/70	(Al-Hardan *et al.,* 2013)
La doped ZnO by Electro-spinning	340	200	68	2/23	(Xu *et al.,* 2015)
ZnONPS by Precipitation	285	800 40	25.697 ± 0.012 3.500 ± 0.002	39/79 21/91	This work

The gas sensing characteristics can be explained using the model in Figure 34 in section 4.1.4. On the exposure of acetone vapour onto the ZnO surface, the acetone molecules interact with the ionosorbed oxygen ions and release the electrons back to the ZnO surface which reduces the potential barrier height [Figure 34 (b)] and increases the conductivity of materials. The release of electrons due to the interaction of acetone molecule with oxygen ions adsorbed onto ZnO surface is represented as: $CH_3COCH_{3(ads)} + 8O^-_{(ads)} = 3CO_2 + 3H_2O + 8e^-$. By measuring the resistances of the ZnO in air and in gas, the gas response of ZnO can be evaluated (Chu *et al.,* 2012). In Figure 37, the poor response was observed at lower temperatures with the exposure of 800 ppm of acetone. It is due to the presence of fewer molecules of acetone which results the lower reaction rate of the molecules of acetone vapour with the oxygen ions adsorbed on the ZnO surface and the high activation energy of the ZnO. The gas response (R) is related to the reaction rate coefficient $K_{Eth}(T)$ of the molecules of analyte gas and adsorbed oxygen ions on the ZnO surface as $R = \frac{R_a}{R_g} = \frac{\Gamma_t K_{Eth}(T)[O^{2-}(adsorb)]^b[CH_3COCH_3adsorb]^b}{n_0} + 1$. Here, Γ_t is the time constant, and b is a charge parameter. The value of b is 1 and 0.5 for O^- and O^{2-} respectively. $O^{2-}(adsorb)$ is the concentration of adsorbed oxygen on the sensor surface, $CH_3COCH_3\ (adsorb)$ is the concentration of acetone vapour and n_o is free electrons concentration at operating temperature in the air environment. The reaction rate coefficient (K_{Eth}) of the test gas with the oxygen ions is related to the absolute temperature (T) and the activation energy (E_a) of the reaction as $K_{Eth}\ (T) = Aexp\left(-\frac{E_a}{k_BT}\right)$, where k_B is Boltzmann constant (Hongsith *et al.*, 2010). With the increase in temperature, the charge carriers rise. When the thermal energy approaches to break the limit of activation energy barriers of the reaction, the charge concentrations rise significantly

which results high response at that optimal temperature. The desorption of oxygen occurred from the ZnO surface above the optimum temperature, which resulted in the reduction of gas response at higher temperature (Khayatian *et al.,* 2014). In Figure 39(a), the high value of gas response for exposure to higher concentrations was observed which was due to an increase in the covering of acetone molecules on the film which accelerated the pace of interaction of molecules of acetone with the adsorbed oxygen ions. As a result, a large number of electrons were released to the conduction band of ZnO which changed the resistance of ZnO in large magnitude and resulted in the high response.

4.3 Characterization of Spin Coated Undoped and Fe-ZnO Films

The structural & optical properties, surface morphology, elemental analysis, and gas sensing capability, in terms of electrical resistance, of ZnO and Fe-ZnO films prepared by spin coating, are described in this section. The film preparation method is described in section 3.1.2 of chapter 3. The results of the investigation on ethanol sensing using these films at various temperatures are extensively discussed.

4.3.1 Structural Analysis

The structural characteristics of ZnO and Fe-ZnO films were examined using the X-ray diffraction technique. Figure 40 displays the X-ray diffraction patterns of undoped and $1-4\%$ Fe-ZnO films. Diffraction peaks were found to be oriented along (100), (002),

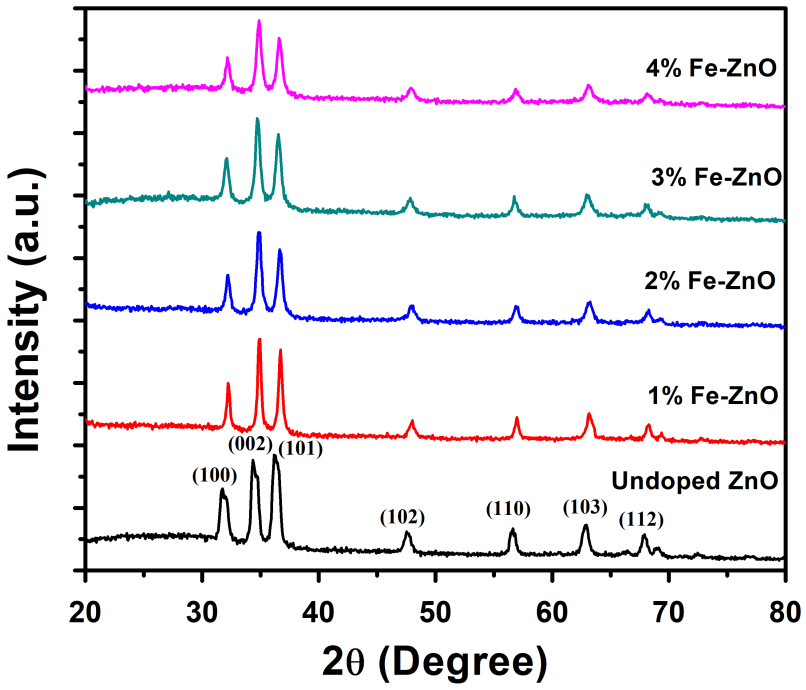

Figure 40: XRD pattern of ZnO and Fe-ZnO films deposited on glass substrates by spin coating

(101), (102), (110), (103), and (104) planes. These peaks were found to be consistent with the values of JCPDS card number 36 − 1451. The presence of multiple peaks in the captured XRD indicates the polycrystalline nature of ZnO films. No impurity peaks are observed in the pattern. Identical XRD patterns were observed for 1 − 4% Fe-ZnO, with the major peaks orientated along (100), (002), and (101) but minor peaks shift towards a greater angle that shows a decrease in d-spacing for Fe doping. This could be as a result of the smaller ionic radius Fe^{3+} (0.68 Å) replacing Zn^{2+} ions (0.74 Å)(Xu & Li, 2010). All patterns showed high intense diffraction peaks corresponding to preferential c-axis orientation (002) for all Fe-ZnO films. As in the previous section, *d*-spacing and crystallite size (D) were calculated using Braggs law: $2d \sin\theta = n\lambda$ and Debye Scherrer's formula: $D = \frac{0.9\lambda}{\beta \cos\theta}$. The calculated values of d-spacing and mean crystallite size (D) corresponding to the prominent peaks (100), (002), and (101) of ZnO and 1 − 4% Fe-ZnO films are displayed in Table 1 0. The mean crystallite sizes of ZnO and 1% Fe-ZnO were observed to be about 23 nm. The value of D decreased steadily with increasing Fe concentrations, from 23.1622 nm for 1% Fe-ZnO to 16.4475 nm for 4% Fe-ZnO film. The decrease in D after doping was due to the replacement of Zn^{2+} ions (ionic radii, 0.74 Å) by the Fe^{3+} ions (ionic radii, 0.68 Å) at their lattice sites which leads the change in surface morphology of the Fe-ZnO films. The error in D was determined using the standard errors found in 2θ and full width at half maxima (β) of the individual peaks during fitting.

Table 10: 2θ, (hkl), d-spacing and crystallite size of spin-coated ZnO Films

Sample	Plane (hkl)	2θ (Degree)	d (Å)	d (Å) JCPDS	D (nm)	Mean D (nm)
ZnO	(100)	31.7541 ± 0.0106	2.8156	2.8143	23.6500 ± 0.8039	23.2707
	(002)	34.4202 ± 0.0112	2.6034	2.6033	25.0522 ± 1.2477	
	(101)	36.2394 ± 0.0081	2.4732	2.4759	21.1100 ± 0.6949	
1%Fe-ZnO	(100)	32.2501 ± 0.0049	2.7735	2.8143	25.2925 ± 0.0049	23.1622
	(002)	34.9135 ± 0.0028	2.5677	2.6033	23.4078 ± 0.4258	
	(101)	36.7189 ± 0.0039	2.4456	2.4759	20.7861 ± 0.4910	
2% Fe-ZnO	(100)	32.2106 ± 0.0063	2.7717	2.8143	21.0226 ± 1.0452	18.8451
	(002)	34.8792 ± 0.0044	2.5659	2.6033	18.6060 ± 0.4973	
	(101)	36.6756 ± 0.0044	2.4444	2.4759	16.9065 ± 0.4448	
3% Fe-ZnO	(100)	32.1838 ± 0.0047	2.7791	2.8143	18.4740 ± 0.8592	17.2754
	(002)	34.8766 ± 0.0040	2.5704	2.6033	17.3526 ± 0.4329	
	(101)	36.6371 ± 0.0035	2.4508	2.4759	15.9998 ± 0.4712	
4% Fe-ZnO	(100)	32.0905 ± 0.0084	2.7869	2.8143	17.1118 ± 0.9679	16.4475
	(002)	34.7727 ± 0.0084	2.5779	2.6033	17.5211 ± 0.9679	
	(101)	36.5402 ± 0.0305	2.4571	2.4759	14.7097 ± 0.3345	

4.3.2 Optical Analysis

The optical transmission spectra of ZnO and Fe-ZnO films were captured within the wavelength ranging from 360 nm to 1100 nm. Figure 41(a) depicts the transmittance spectra of the ZnO and Fe-ZnO films. All the films have transmittance values of more than 80%, indicating that films are highly transparent. This figure also showed a substantial decline in transmittance at short wavelengths close to the ultraviolet range, but high in the visible range for Fe-ZnO films. The optical band gap was calculated using Tauc plot (Rambu *et al.*, 2013) and is depicted in figure 41(b). The calculated values of optical band gap for undoped ZnO, 1%, 2%, 3%, and 4% Fe-ZnO were 3.208 ± 0.023, 3.221 ± 0.019, 3.224 ± 0.011, 3.235 ± 0.021, and 3.247 ± 0.022 eV respectively which was

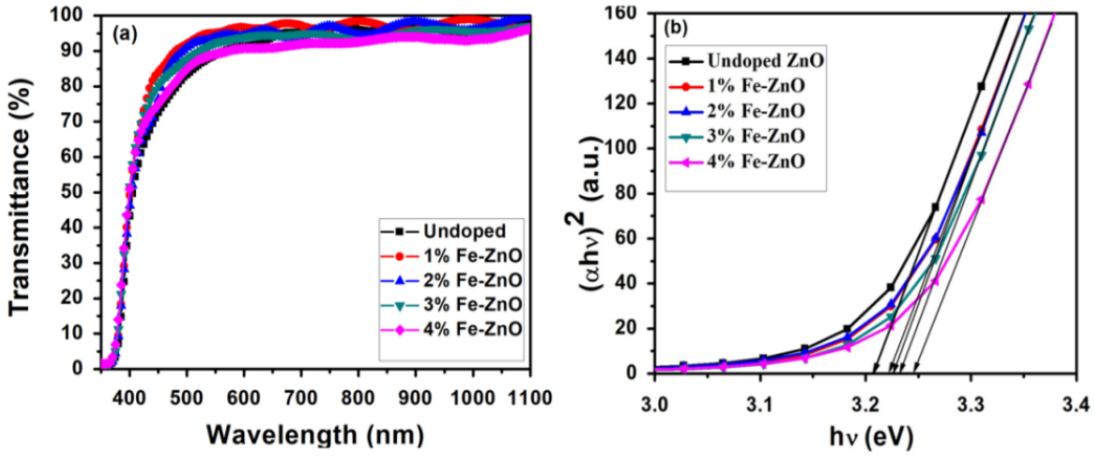

Figure 41: (a) Transmittance and (b) optical band gap of spin-coated undoped and 1 – 4% Fe-ZnO films on glass substrates

increased after Fe doping into ZnO. This increase in the optical band gap in Fe-ZnO was observed to be compatible with findings on related systems due to a reduction in the grain size of the film (Liu *et al.*, 2014). When Zn^{2+} ions are replaced by Fe^{3+} ions at their lattice positions, more free charge carriers are added which causes shifting the Fermi level into the conduction band and widens the band gap. The error in the optical band gap was determined by using the standard errors found in the slope and the intercept of the linear fit in the linear portion of the curve.

4.3.3 Surface Morphology

The surface morphology of prepared films was examined using scanning electron microscopy (SEM). The SEM micrographs of ZnO and 1-4% Fe-ZnO films are depicted in Figure 42(a) through (e), respectively. SEM images were captured at the laboratory of Indian Institute of Technology (IIT), Roorkee, India, using Zeiss Scanning electron microscope. Images clearly show the surface consisting of spherical grains. The surface morphology of Fe-ZnO changed by increasing the Fe doping concentration. The grain size decreased after doping Fe. A reduction in the grain size was observed in the 2% Fe-ZnO film in comparison to that of undoped ZnO and 1% Fe-ZnO films which led to the increase in the specific area. An increase in a specific area due to a reduction in the grain size facilitates the adsorption of a large number of oxygen molecules. It leads to enhancement in the gas sensing properties (Hosseini *et al.*, 2015). The elemental composition of as-prepared films was studied using EDX at the laboratory of Indian Institute of Technology (IIT), Roorkee, India. The EDX spectra of the ZnO and Fe-ZnO films are displayed in Figure 43. The existence of zinc, oxygen, and iron can be seen in the EDX patterns. It validates the purity of the films and the incorporation of Fe-ions into the ZnO structure. The elements present in the prepared samples are presented in terms of atomic percentage in the inset of Figure 43.

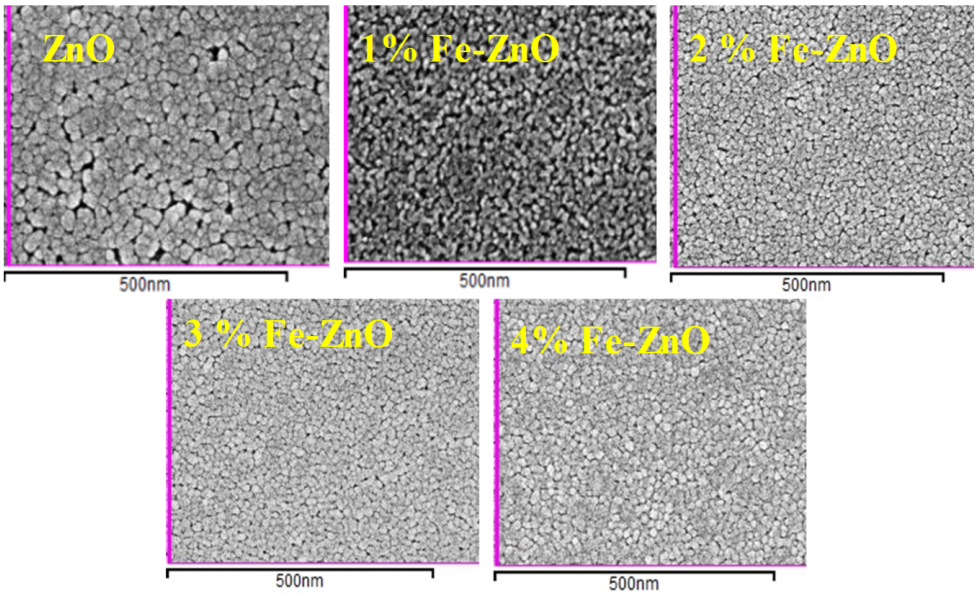

Figure 42: SEM micrographs of spin-coated undoped and Fe-ZnO films

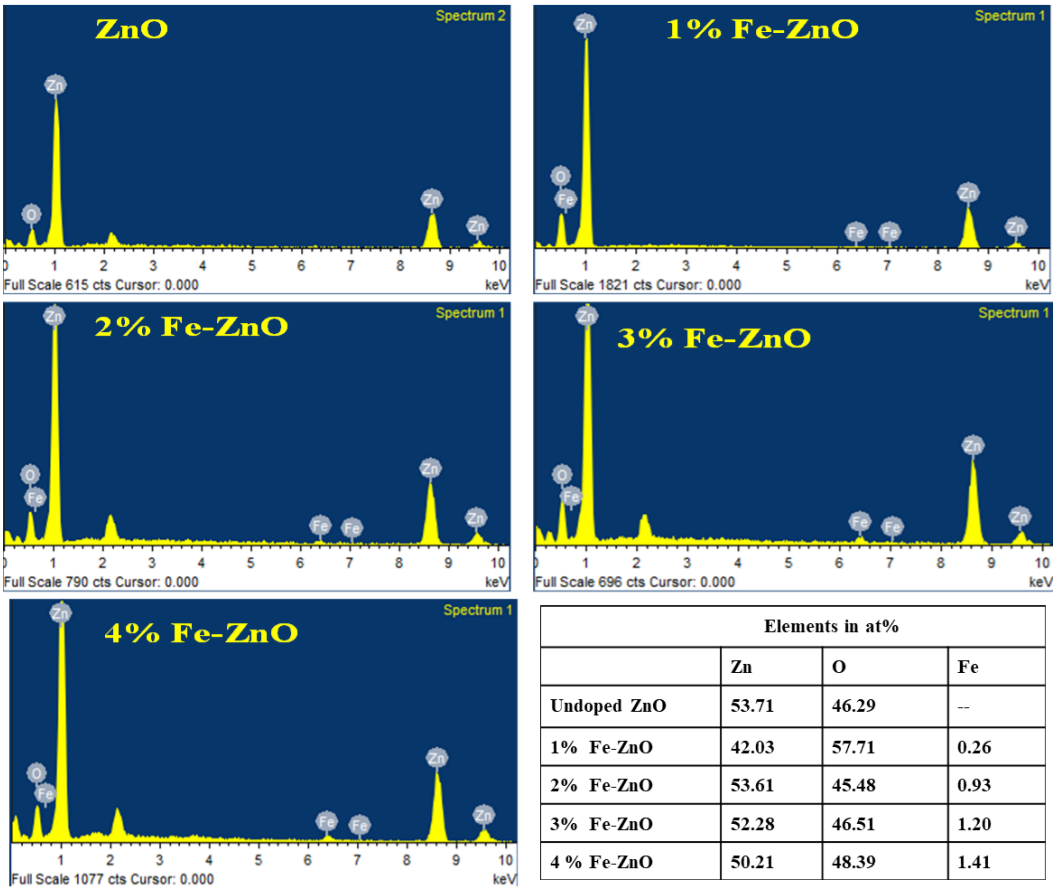

Elements in at%			
	Zn	O	Fe
Undoped ZnO	53.71	46.29	--
1% Fe-ZnO	42.03	57.71	0.26
2% Fe-ZnO	53.61	45.48	0.93
3% Fe-ZnO	52.28	46.51	1.20
4 % Fe-ZnO	50.21	48.39	1.41

Figure 43: EDX spectra and elemental composition of ZnO and Fe-ZnO films

4.3.4 Sensing Performance Towards Ethanol

The gas response of the ZnO gas sensor depends on the rate of interaction between the molecules of exposed gas and the adsorbed oxygen ions on the ZnO surface which

is temperature dependent. Hence, to study the sensing behavior of the sample, the temperature should be optimized at first (Hongsith *et al.*, 2010; Khayatian *et al.*, 2014; Sawalha *et al.*, 2009). To find the working temperature, the resistances R_a and R_g of ZnO film were measured separately in air and in the presence of vapour of ethanol at temperatures ranging from 100 °C to 300 °C in the interval of 20 °C. The gas response (R) was calculated using the formula $R = \frac{R_a}{R_g}$, (Lui *et al.*, 2014). The plot of the gas response at various temperatures at an exposure of 400 ppm of the ethanol vapor is depicted in Figure 44. The gas response increased with temperature until it reached the maximum value at a particular temperature called working or operating temperature and then it declined. The working temperature for the ZnO and 1 - 4% Fe-ZnO was observed to be 260 ± 7, 240 ± 5, 260 ± 7, 240 ± 5, and 240 ± 5 °C respectively. Here,

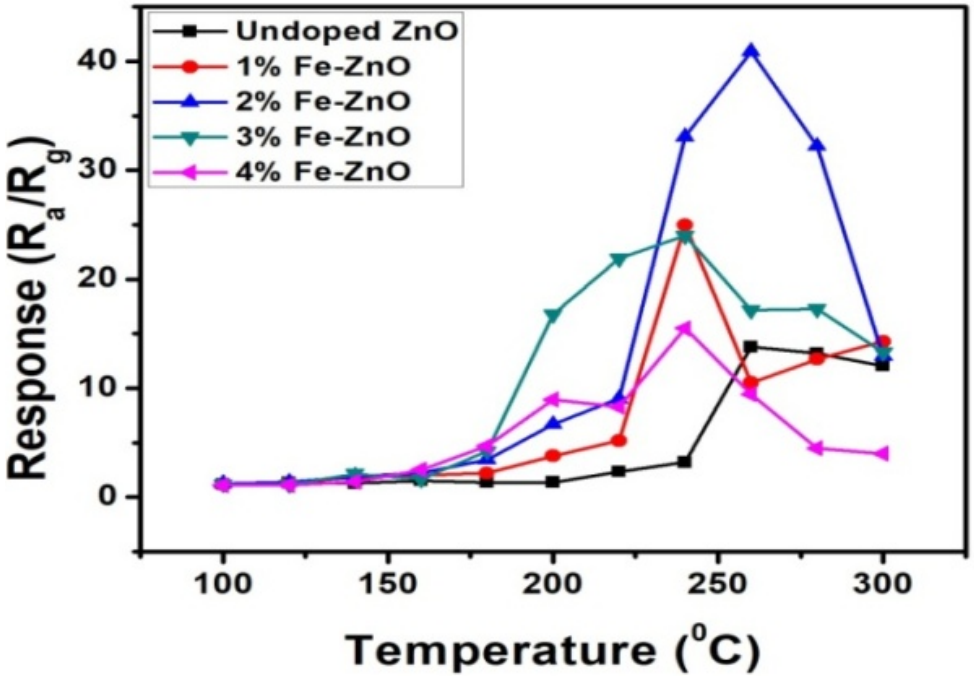

Figure 44: Response of ZnO and 1-4% Fe-ZnO films versus temperature

the error in the temperature is calculated by measuring temperature fluctuation at set temperatures. In this work, the ethanol sensing performances of the ZnO sensors were also studied with the exposure of various ethanol concentrations ranging from 40-400 ppm at their operating temperatures. Figure 45(a) illustrates the gas response of ZnO and 1-4% Fe-ZnO at their operating temperatures at an exposure of different amounts of ethanol vapour ranging from 40 to 400 ppm. The results revealed that the response increased as the ethanol content increased. The maximum response was found to be 40.91 ± 0.23 for 2% Fe-ZnO at 260 ± 7 °C. Here, the errors in the response are standard errors. The error in the response was introduced due to the fluctuation of temperature as well as the precision of the resistance measuring device. This error was minimized by taking a large number of data to calculate the response. The two important parameters:

response time and recovery times were also measured. Figure 45(b) illustrates the graph of the response of ZnO and 2% Fe-ZnO along with computed values for response and recovery times. Table 11 shows the results of gas response, response, and recovery times

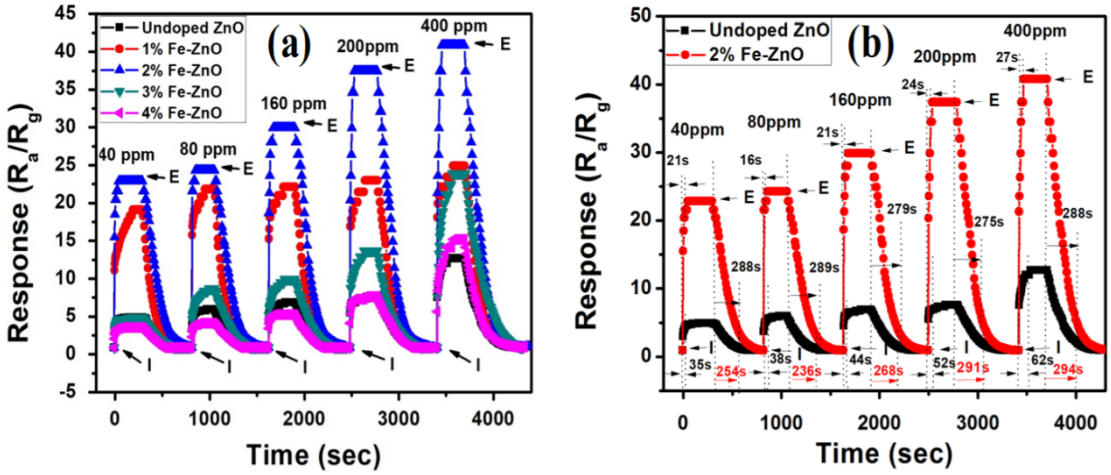

Figure 45: (a) Response of ZnO and 1-4% Fe-ZnO at its operating temperatures at different concentrations of ethanol (b) Zoom in response values of ZnO and 2% Fe-ZnO along with values of response and recovery times

of ZnO and 2% Fe-ZnO samples. It was clearly observed that the ZnO and 2% Fe-ZnO shows a higher response at exposure to a higher concentration of ethanol vapour. The response and recovery times were found higher for the higher concentration of ethanol. The 2% Fe-ZnO showed the highest and quick response than undoped ZnO. The response of 2%Fe-ZnO was observed to be 22.94 ± 0.09 with response time and recovery time of 21 and 288 sec at 40 ppm of ethanol. Similarly, its response at 400 ppm of ethanol was observed to be 40.91 ± 0.23 with response and recovery times of 27 and 288 sec respectively. The result of this study was compared with the published reports. The results of the available reports and the present study are depicted in table 12. In this work, the spin-coated 2% Fe-ZnO films exhibited a response of 40.91 ± 0.23 at 400 ppm and 22.94 ± 0.09 at 40 ppm of ethanol at a working temperature of 260 ± 7 °C. This result was found to be better than the published reports (Ge *et al.,* 2007; Hassan *et al.,* 2014; Hsu *et al.,* 2014; Khayatian *et al.,* 2014).

Table 11: Gas response, response time and recovery time of ZnO and 2% Fe-ZnO at different ppm of ethanol

Ethanol Concentration (ppm)	Undoped ZnO			2% Fe-ZnO		
	Gas Response (R_a/R_g)	Response time (sec)	Recovery time (sec)	Gas Response (R_a/R_g)	Response time (sec)	Recovery time (sec)
40	5.00 ± 0.01	35	254	22.94 ± 0.09	21	288
80	5.99 ± 0.02	38	236	24.37 ± 0.11	16	289
160	6.98 ± 0.04	44	268	30.00 ± 0.14	21	279
200	7.67 ± 0.03	52	291	37.50 ± 0.20	24	275
400	12.78 ± 0.03	62	294	40.91 ± 0.23	27	288

Table 12: Comparison of gas sensing results of ZnO-based ethanol sensor in this work with published reports

Sample/method	Working Temperature °C	Ethanol concentration (ppm)	Response (R_a/R_g)	Reference
Sn doped ZnO Prepared by thermal oxidation	340	1000	30.4	(Santhaveesuk *et al.,* 2010)
Hydrothermally grown Fe doped ZnO	400	500	55	(Yu *et al.,* 2011)
Microwave-assisted hydrothermally grown ZnO	350	500	250	(Hamedani *et al.,* 2011)
Microwave-assisted hydrothermally grown CuO	210	1000	9.8	(Yang *et al.,* 2011)
Al doped ZnO by Sol-gel process	500	2000	92	(Liu *et al.,* 2014)
Hot wire assisted Ti-doped ZnO	250	500	2.76	(Hsu *et al.,* 2014)
RF sputtered Fe doped ZnO	300	300	2.91	(Hassan *et al.,* 2014)
Hydrothermally grown Fe doped ZnO	250	500	19	(Khayatian *et al.,* 2016)
Thermally evaporated ZnO	300	300	2.91	(Bhatia *et al.,* 2017)
Spin coated Fe-ZnO	260	400 40	40.91 ± 0.23 22.94 ± 0.09	This work

The gas sensing characteristics can be explained using a model in Figure 34 in section 4.1.4. When ethanol vapor is exposed to the ZnO film, the adsorbed oxygen interacts with ethanol molecules, releasing electrons back into the ZnO film. This process reduces the height of the potential barrier and increases the material conductivity. The release of electrons during the interaction of ethanol molecules with oxygen ions is presented as:$CH_3CH_2OH + 6O^-_{(ads)} = 2CO_2 + H_2O + 6e^-$ (Hongsith *et al.*, 2010). The gas response of ZnO can be evaluated by measuring the resistances of the ZnO in air and in gas. From the above figure (Figure 44), with the rise of the temperature, the response was increased. With the increase in temperature, thermal energy rises. When it gets closer to the threshold for breaking through the activation energy barrier of reaction, the charge

concentrations rise rapidly and give a high response. Above this threshold temperature, desorption of oxygen molecules takes place from the ZnO surface, thereby reducing the response of the gas sensor (Dey, 2018; Khayatian *et al.,* 2014).

In this experiment, the 2% Fe-ZnO exhibited a better response than other samples. The response value for 2% Fe-ZnO for 400 ppm ethanol vapour was 40.91 ± 0.23, which was almost three times greater than that of undoped ZnO. This improvement in the gas response of Fe-ZnO samples was due to the higher specific surface area as well as the charge carrier concentrations. In Fe-ZnO, the grains are smaller than that in ZnO, which increased the specific surface area of Fe-ZnO samples [Figure 4 2]. As a result, the concentrations of adsorbed oxygen molecules increased on the surface of Fe-ZnO than that of undoped ZnO. Thus, more molecules of ethanol vapour interacted with the adsorbed oxygen molecules which, in turn, released more electrons to the ZnO surface and improved the gas response. The response is also enhanced by an increase in carrier concentration on Fe doping. When Zn^{2+} ions are replaced with Fe ions (Fe^{3+}), it surpluses the charge carriers in the conduction band. This helps to adsorb the additional number of oxygen molecules on the ZnO surface to maintain charge neutrality and speed up the reaction paces between the molecules of the exposed gas and adsorbed oxygen ions. More active adsorption centers are available only for the appropriate percentage of dopant. Therefore, 2%Fe-ZnO showed a higher response than others. However, in excessive Fe doping, such as 3% and 4% Fe-ZnO, there may be more scattering atoms on the ZnO surface (Ge *et al.,* 2007) which reduces oxygen-capturing sites and slows down surface reactions (Zhang *et al.,* 2010), which further reduces the response.

4.4 Characterization of Undoped and Sn-ZnO Films Prepared by Spray Pyrolysis

In this section, the structural & optical properties, surface morphology, elemental composition, and the ethanol vapour sensing performance of ZnO and Sn-ZnO films prepared by spray pyrolysis method is described. The film preparation method is described in section 3.1.3 of chapter 3. The results of sensing measurement at different temperatures towards ethanol are also discussed.

4.4.1 Structural Analysis

The structural characteristics of as-synthesized undoped ZnO and Sn-doped ZnO (Sn-ZnO) films were examined employing the X-ray diffraction te chnique. Figure 46 depicts the XRD pattern with several peaks corresponding to planes oriented along (100), (002), (101), (102), (110), (103), and (112) in the pure ZnO. The observed peaks were found to be consistent with the values of JCPDS card number 36 – 1451. The peaks corresponding to planes (100), (110), and (112) orientation disappeared in the Sn-ZnO films. It is because; Sn doping led the crystallinity to degenerate (Tsay *et al.,* 2008). The intense

peaks corresponding to the (002) plane were observed in Sn-ZnO, which indicates the c-axis orientation of Sn-ZnO films. This result is similar to the earlier published reports (Ajili *et al.,* 2013; Caglar *et al.,* 2009; Yung *et al.,* 2009; Miki-Yoshida *et al.,* 2000). The determined values of 2θ, d-spacing, the crystallite size (D), and lattice strain (ε) corresponding to intense peaks are presented in Table 13. The calculated value of d-spacing was found to be close to the standard JCPDS value. The crystallite size corresponding to the intense peaks was found to be decreased from 34.6912 ± 1.0582 nm for undoped to 25.9281 ± 1.3388 nm for 2% Sn-ZnO. The D value slightly increased for 3% Sn-ZnO but was smaller than the undoped case. This decrease in D is because of the replacement of Zn^{2+} (ionic radius, 0.74 Å) by Sn^{4+} (ionic radius, 0.69 Å) after doping Sn into ZnO. The slight increase in D for 3% Sn-ZnO may be attributed to the substitution of Sn^{2+} ion (ionic radius, 1.12 Å) along with Sn^{4+} whose ionic radii is greater than that of Zn^{2+} and Sn^{4+} ions (Zhang *et al.,* 2019; Chahmat *et al.,* 2014). The value of lattice strain (ε) was high for Sn-ZnO indicating a bigger lattice misfit. It implies that Sn doping arises the lattice defects and the charge imbalance surrounding the dopants (Srinivasulu *et al.,* 2017). The error in D and ϵ were calculated using standard errors found in 2θ and FWHM of the peaks during fitting.

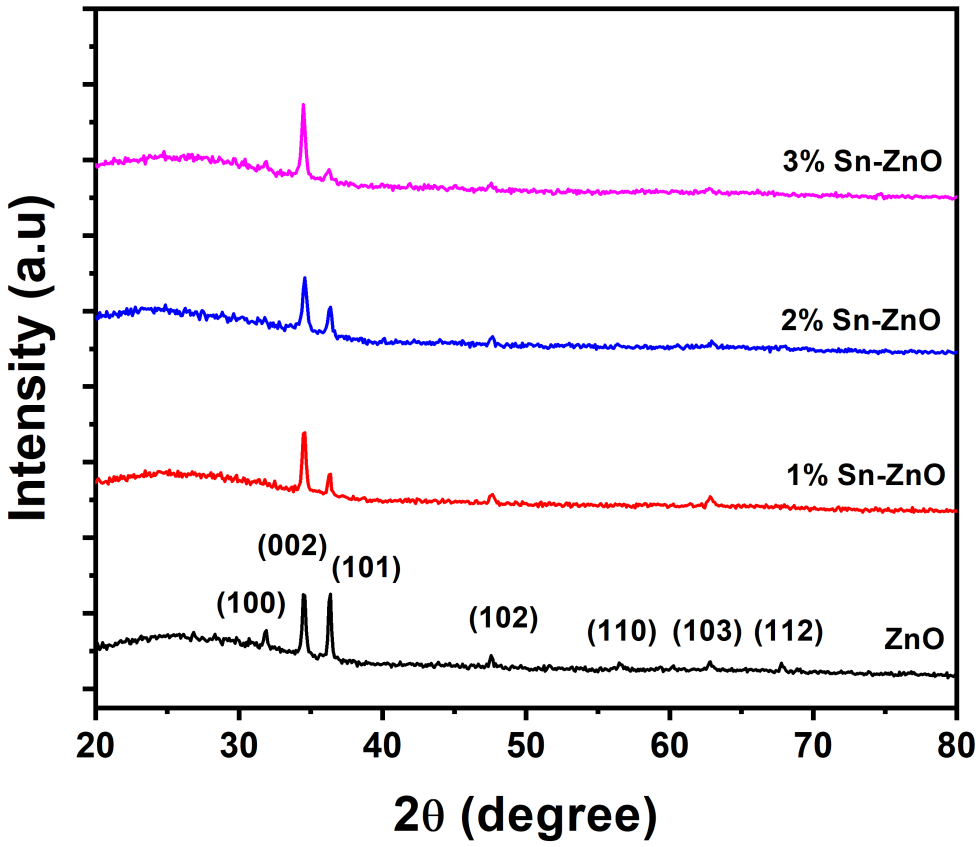

Figure 46: XRD of ZnO and Sn-ZnO films prepared by spray pyrolysis

Table 13: (hkl), 2θ, d-spacing, crystallite size (D) and lattice strain (ε) of ZnO and Sn-ZnO films deposited on glass substrate by spray pyrolysis

Sample	**Plane (hkl)**	**2θ (degree)**	**FWHM (degree)**	***d*-spacing (Å)**	***d*-spacing (JCPDS)**	**(D) nm**	**Strain (ε) ($\times 10^{-3}$)**
ZnO	(002)	34.5270 ± 0.030	0.2397 ± 0.0075	2.5946	2.6043	34.6912 ± 0.0582	3.43 ± 0.11
1% Sn-ZnO	(002)	34.5296 ± 0.0024	0.2726 ± 0.0058	2.5944	2.6043	30.5049 ± 0.6468	3.830 ± 0.08
2% Sn-ZnO	(002)	34.5741 ± 0.0065	0.3208 ± 0.0165	2.5912	2.6043	25.9281 ± 1.3385	4.500 ± 0.23
3% Sn-ZnO	(002)	34.4858 ± 0.0054	0.2748 ± 0.0129	2.5976	2.6043	30.2521 ± 1.4198	3.870 ± 0.18

4.4.2 Optical Analysis

The transmission spectra of ZnO and Sn-ZnO films were captured between 360 and 1000 nm wavelength. Figure 47(a) shows the observed transmission spectra. The undoped ZnO film was highly transparent having a transmittance of greater than 80% in the UV-visible region. The transmittance was decreased for Sn-ZnO films. Figure 47(a) showed a decrease in transmittance at short wavelengths close to the ultraviolet region and improvement in the visible region for all films. The low optical transmittance for Sn-ZnO films may be caused by a rise in photon scattering by crystal defects and photon absorption by free charge carriers (Bougrine *et al.,* 2003). The absorption edge was found to be red-shifted after Sn doping. The optical band gap (E_g) of ZnO films was computed using the Tauc plot, which is depicted in figure 47(b). The computed values of E_g are presented in Table 14. The E_g was reduced from 3.275 ± 0.038 eV for the undoped ZnO to 2.412 ± 0.027 eV for the 3% Sn-ZnO following the reported trends (Acharya *et al.,* 2012; Xiong *et al.,* 2011; Yung *et al.,* 2009). The error in the optical band gap was determined by using the standard errors that appeared in the slope and intercept of the linear fit in the linear portion of the curve. The splitting of the conduction band causes the E_g value to drop after doping Sn. The bottom conduction band of Sn-ZnO is made up of Sn-5p and Zn-4s states close to the Fermi level, whereas the top conduction band is made up of Sn-5s and Zn-4p states in the Sn-ZnO sample. Likewise, the top and bottom valance bands are made up of O-s and Zn-3d. In doping Sn into ZnO, Sn^{4+} replaces the Zn^{2+} from their lattice site and 4 electrons of Sn in place of 2 electrons of Zn are available in the ZnO matrix. All four valance electrons of Sn take part in chemical bonding with the ZnO matrix's atom. Also, Sn serves as the doubly ionized donor. Sn^{2+} creates the deep states in the conduction band. It has the electronic structure of $5s^2$. The chemical bond is formed by only 5p electrons. The 5s electrons form the deep donor states. The stability of 5s in the conduction band is related to the distortion in the geometry of Sn. This distortion leads to the mixing of 5s and 5p states creating the hybrid states or shallow donor and broadening the energy levels with the

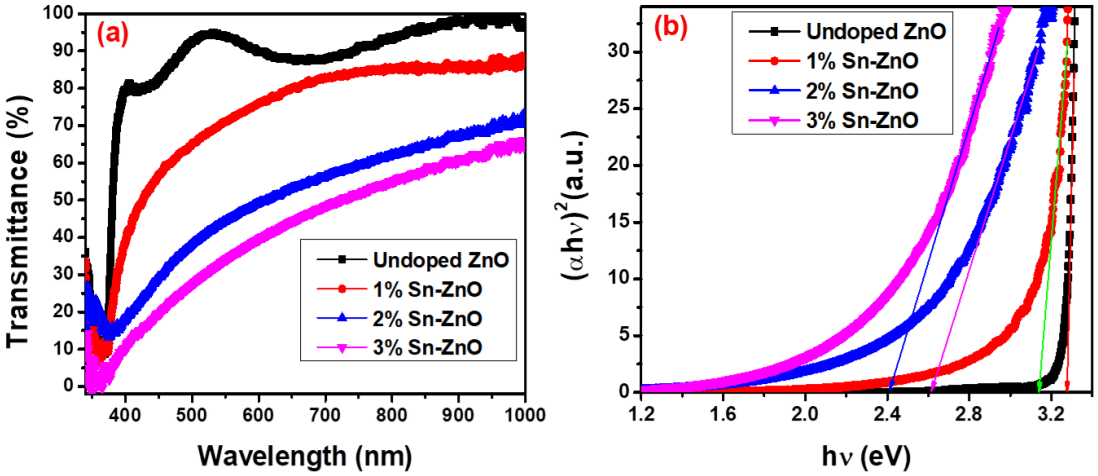

Figure 47: (a). Transmittance spectra and (b) Tauc plots of ZnO and Sn-doped ZnO films deposited on glass substrates by spray pyrolysis

formation of impurity-induced bands that combines with conduction band minimum (CBM). As a result, the conduction band minimum shifts below the Fermi level, and the band degeneracy occurs in Sn-ZnO (Acharya *et al.,* 2012; Xiong *et al.,* 2011). The position of the Sn-s state affects the conduction b and. The Sn-s states move to the lower energy for the higher doping concentration of Sn into ZnO and promote the narrowing of the optical band gap (Bougrine *et al.,* 2003).

Table 14: Transmittance and optical band gap of ZnO and Sn-ZnO films deposited on glass substrates by spray pyrolysis

Sample	Transmittance (%)	Optical Band Gap (eV)
ZnO	85.48 ± 0.365	3.275 ± 0.002
1% Sn-ZnO	77.128 ± 0.235	3.138 ± 0.002
2% Sn-ZnO	53.500 ± 0.284	2.614 ± 0.002
3% Sn-ZnO	45.351 ± 0.309	2.412 ± 0.002

4.4.3 Surface Morphology

Surface quality of sensor affects its sensing performance (Shao *et al.,* 2016; Wei *et al.,* 2011). The surface morphology and elemental composition were studied by capturing SEM images and EDX spectra using a field-emission scanning electron microscope (JEOL, JSM-7001F, Japan) in our collaborator's laboratory (Department of Electrical and Biological Physics, Kwangwoon University, Seoul 01897, Korea). Figure 48(a-d) depicts the SEM micrographs of ZnO, and 1-3% Sn-ZnO films deposited on a glass substrate using the spray pyrolysis technique. The grainy structures were observed from the SEM images. The average sizes of grains were found to increase in the Sn-doped films with higher concentrations of Sn. Figure 49(a-b) depicts the EDX spectra of ZnO and 1 – 3% Sn-ZnO films. The spectra clearly showed peaks for the elements zinc (Zn),

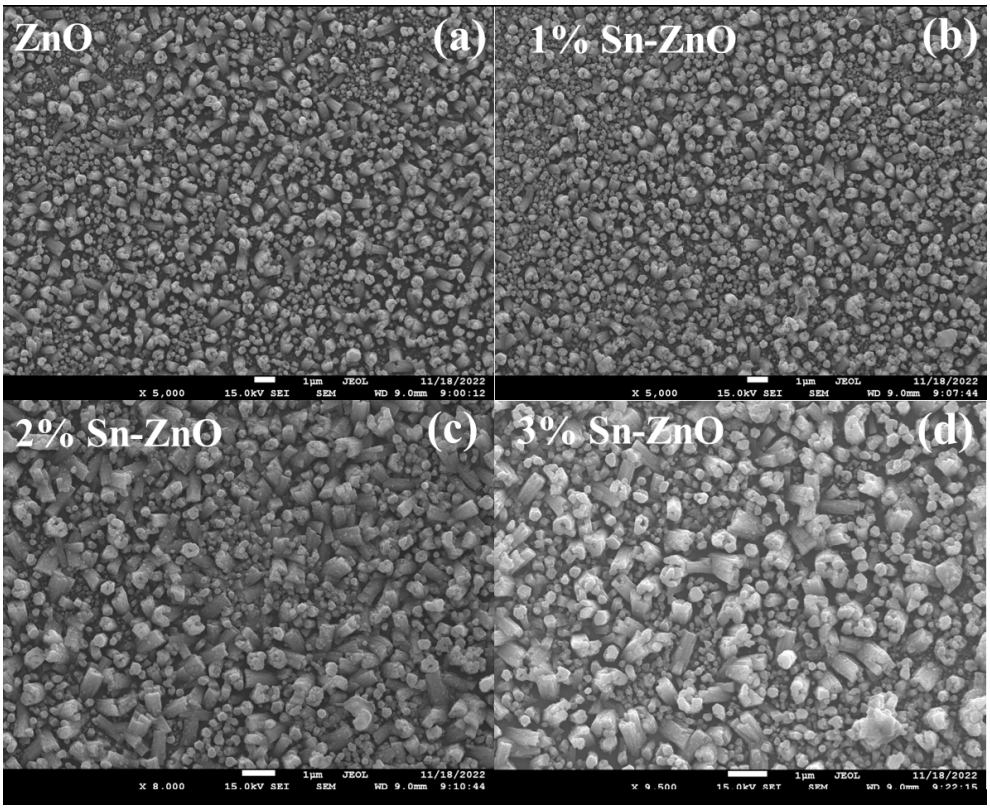

Figure 48: FE-SEM images of (a) ZnO, (b) 1% Sn-ZnO, (c) 2% Sn-ZnO and (d) 3% Sn-ZnO films prepared by spray pyrolysis

oxygen (O), and tin (Sn) were clearly seen in the spectra. The contents of zinc, oxygen, and tin in terms of atomic percentage are depicted in Table 15. The atomic percentage of zinc, oxygen, and tin is 50.00, 50.00 & 0.00; 48.34, 48.34, & 3.32; 45.67, 45.67, & 8.66 and 42.31, 42.31 & 15.38, in ZnO, 1% Sn-ZnO, 2% Sn-ZnO, and 3% Sn-ZnO films respectively. While performing the EDX experiment, a carbon tape was used to hold the sample, and conducting electrode was used to collect the backscattered electrons from the sample. As a result, the several peaks corresponding to the several elements such as C, Si, etc along with the peaks corresponding to Zn, O, and Sn were observed in the EDX spectra. In order to normalize, the experiment was done excluding other elements except Zn and O in ZnO films and Zn, O, and Sn in Sn-ZnO films. Therefore, in normalized conditions, the atomic percentage of Sn in Sn-ZnO films was found to be greater than the targeted percentage.

Table 15: Content of element present in ZnO and Sn-ZnO films prepared by spray pyrolysis

Element	**Atomic % of elements in samples**			
	ZnO	**1% Sn-ZnO**	**2% Sn-ZnO**	**3% Sn-ZnO**
Zn	50.00	48.34	45.67	42.31
O	50.00	48.34	45.67	42.31
Sn	-	3.32	8.66	15.38
Total	100.00	100.00	100.00	100.00

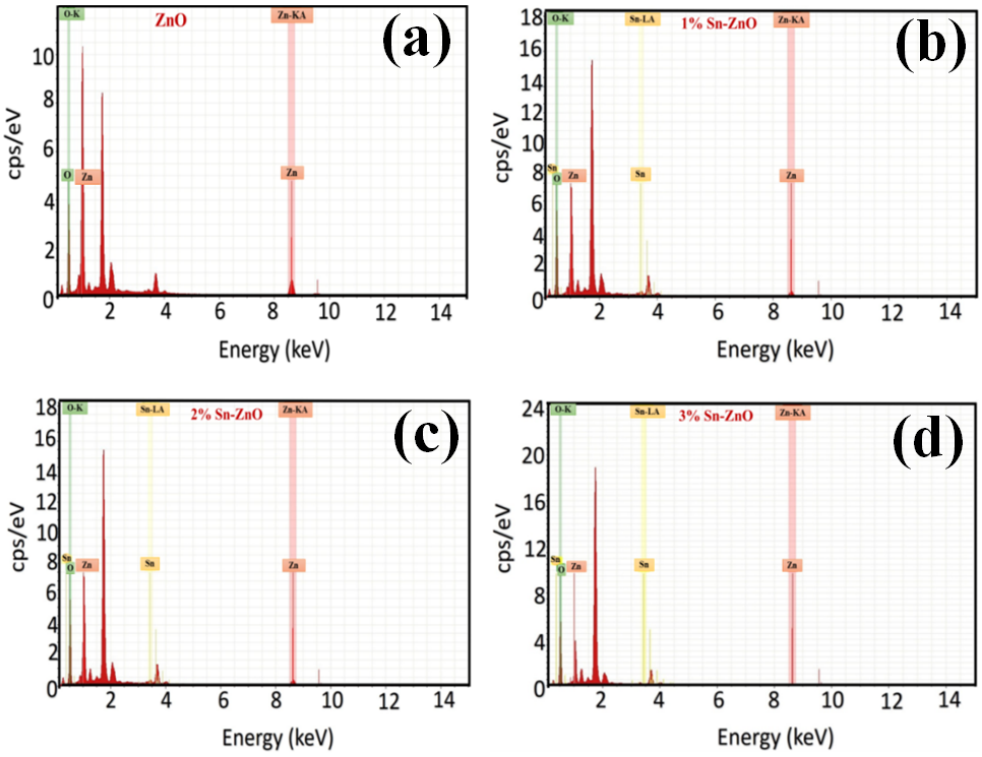

Figure 49: EDX spectra of (a) ZnO, (b) 1% Sn-ZnO, (c) 2% Sn-ZnO and (d) 3% Sn-ZnO films prepared by spray pyrolysis

4.4.4 Sensing Performance Towards Ethanol

Prior to measuring the gas sensing task of the sensor, its working temperature is optimized. Figure 50 depicts the variation of gas response of as-prepared ZnO & Sn-ZnO films with temperature in the range of 80 – 330 °C at the exposure of 400 ppm of ethanol vapour. The response first increased with the temperature reaching its optimum value and then declined with the further rise of the temperature. Undoped ZnO showed the highest response of 110.718 ± 0.076 at 290 ± 7 °C. Likewise, 1, 2, and 3% Sn-ZnO showed the highest response of 40.654 ± 0.015, 17.659 ± 0.011, and 8.339 ± 0.004 at 260, 220, and 240 °C respectively. These results are presented in Table 16. The operating or working temperatures for undoped and 1 – 3% Sn-ZnO films were found to be 290 ± 7, 260 ± 6, 220 ± 5, and 240 ± 5 °C, respectively. The errors in the response are standard errors. The errors in the temperature are the maximum fluctuations in the set temperature during the experiment.

The operating temperature was decreased for Sn-ZnO. Further, the gas sensing performances of all the films were thoroughly examined at their operating temperature by exposing the different amounts of ethanol vapours. Figures 51(a) and 51(b) illustrate the transient resistance response i.e. the variation of resistance with time for undoped ZnO when injecting and ejecting different concentrations 1 – 60 ppm and 80 – 400 ppm of ethanol vapour at the operating temperature of 290 ± 7 °C. Figure 51(c) is the zoom in of

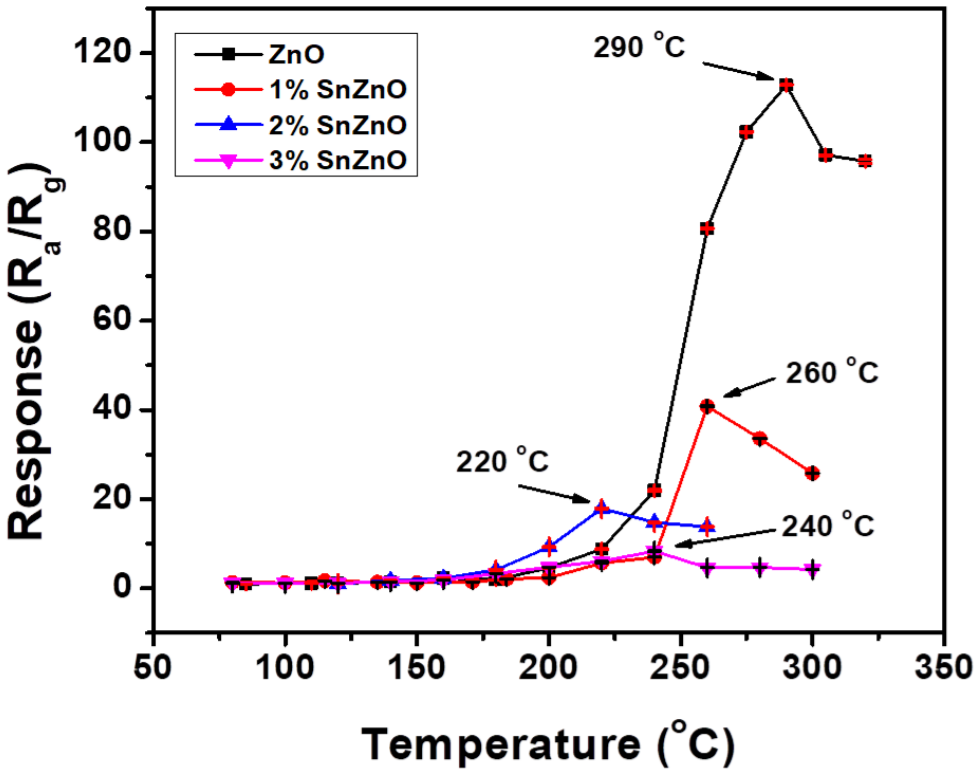

Figure 50: Gas response of ZnO and Sn-ZnO films as the function of temperature, at the exposure of 400 ppm ethanol vapour

Table 16: Operating temperature and maximum response of ZnO and 1-3% Sn-ZnO at 400 ppm of ethanol

Sample	Undoped ZnO	1% Sn-ZnO	2% Sn-ZnO	3% Sn-ZnO
Maximum Response	110.718 ± 0.076	40.654 ± 0.015	17.659 ± 0.011	8.339 ± 0.004
Operating Temperature (°C)	290 ± 7	260 ± 6	220 ± 5	240 ± 5

the transient resistance response at an exposure of 1 ppm of ethanol to show the error bars clearly. The error bars are indicated in red colour. Figures 51(d) is the zoom-in of the lower portion of the transient resistance response at an exposure of 300 and 400 ppm of ethanol respectively. The resistances of ZnO films were measured using an LCR meter (Hioki IM3536). Here error in the resistance is the basic accuracy (BA), which was calculated using the equation: $BA = \pm[X + Y|\frac{10 \times observed\ Resistance}{Range} - 1|]\%$, for 1 kΩ range or higher, and $BA = \pm[X + Y|\frac{Range}{10 \times observed\ Resistance} - 1|]\%$, for 100 Ω range or lower. Here, X and Y are the coefficients. The values of X vary from 0.1 to 1 and that of Y varies from 0.01 to 1, depending upon the range of measurement of resistance. The values of X and Y for different ranges of resistance if listed in Table 17. Similarly,

Table 17: Values of X and Y at different ranges of resistance measurement in LCR meter

Range	100 MΩ	10 MΩ	1 MΩ	100 kΩ	1 kΩ	100 Ω	10 Ω	1 Ω	100 mΩ
X	1	0.5	0.2	0.1	0.1	0.1	0.2	0.3	1
Y	1	0.3	0.1	0.01	0.01	0.02	0.15	0.3	1

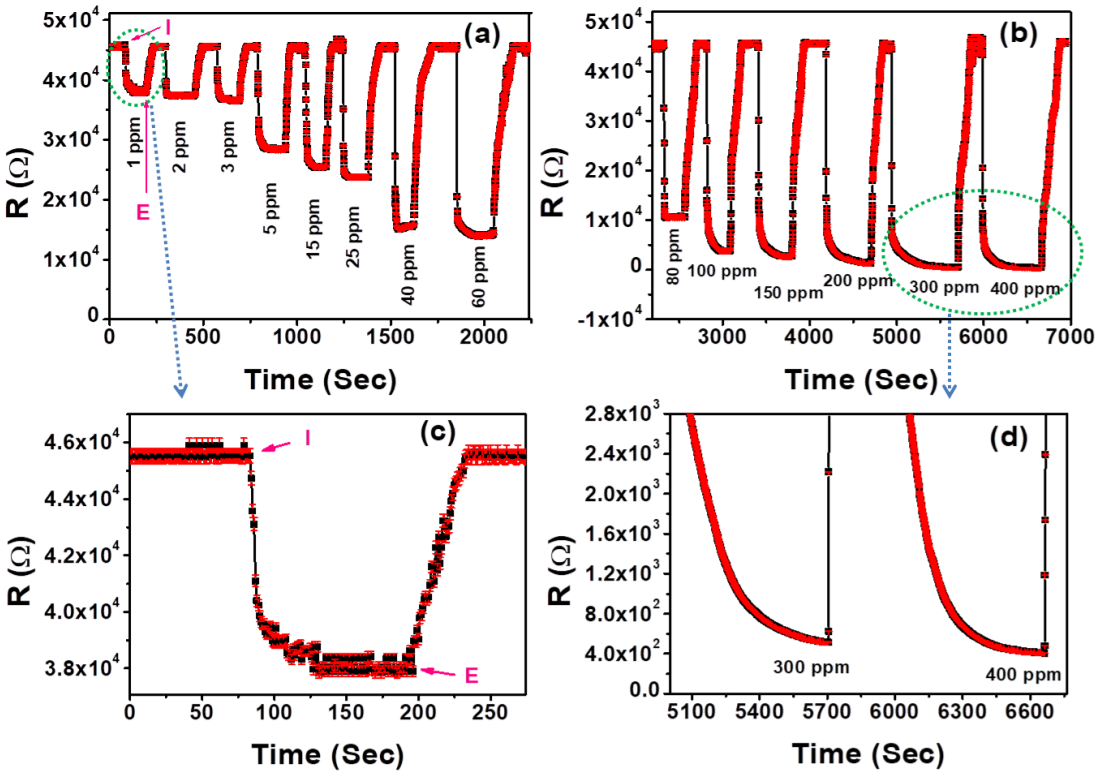

Figure 51: Transient resistance responses of undoped ZnO films for the concentrations from (a) 1 to 60 ppm, (b) 80 to 400 ppm, and (c-d) zoom in of the response for 1, 300 & 400 ppm at their optimized operating temperature 290 °C

Figures 52(a) and 52(b) illustrate the transient resistance responses of 1% Sn-ZnO for injecting and ejecting the different concentrations 1 – 60 ppm and 80 – 400 ppm of ethanol vapour, at the optimized working temperature of 260 ± 6 °C. Figure 52(c) is the zoom in of the transient resistance response of 1 ppm of ethanol to show the error bars labeled in red colour. Figure 52(d) is a zoom-in of the lower portion of the transient resistance response at the exposure of 300 and 400 ppm of ethanol. It clearly shows the resistance was decreased to 2817.450 ± 3.329 and 2461.031 ± 2.821 Ω at the exposure of 300 and 400 ppm of ethanol respectively. Figures 53(a) and (b) illustrate the transient resistance responses of 2% Sn-ZnO for injecting and ejecting the different concentrations 0.5 – 40 ppm and 60 – 400 ppm of ethanol vapour, at the optimized working temperature of 220 ± 5 °C. The error bars are presented in red marks. Figure 53(c) is a zoom-in of the transient resistance response at an exposure of 0.5 ppm of ethanol to show the error bars clearly. The error bars are labeled in red colour. Figure 53(d) is the zoom-in of the lower part of the transient resistance response at the exposure of 300 and 400 ppm of ethanol. It clearly illustrates the resistance was decreased to 12123.3 ± 25.60841 and 12142.300 ± 25.672 Ω at an exposure of 300 and 400 ppm of ethanol respectively which was nearly the same.

Figure 54(a) illustrates the transient resistance responses of 3% Sn- ZnO for injecting and ejecting the different concentrations 5 – 400 ppm of ethanol vapour at the optimized

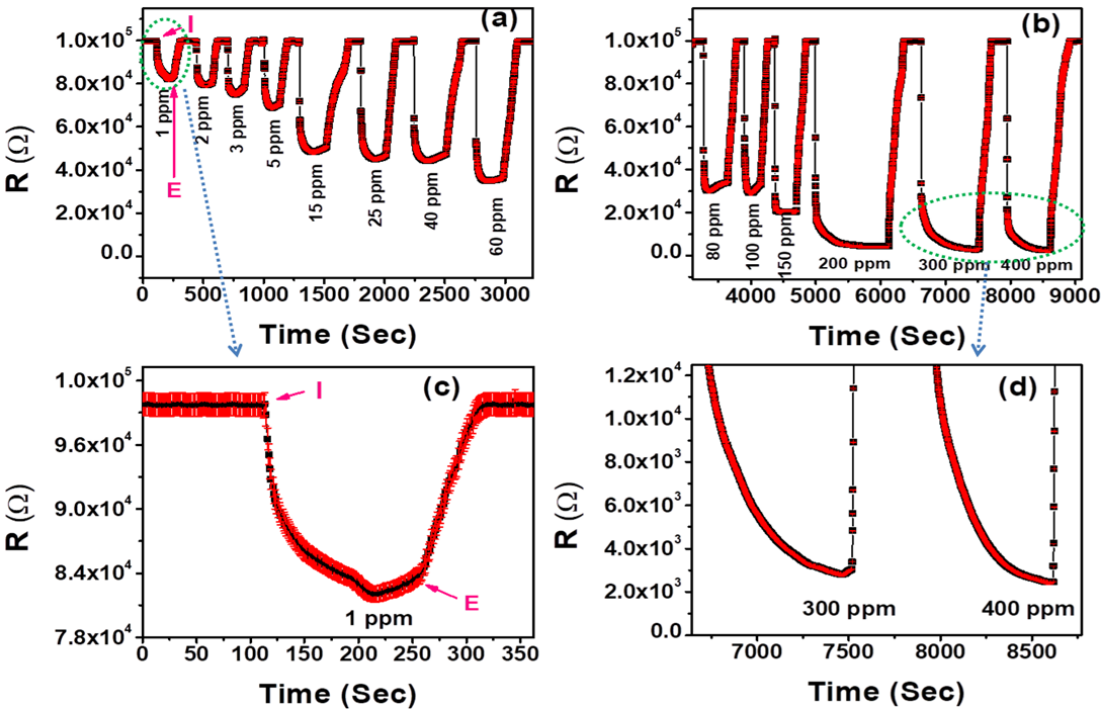

Figure 52: Transient resistance responses of 1% Sn-ZnO film for the concentrations from (a) 1 to 60 ppm, (b) 80 to 400 ppm and (c-d) zoom in of the response for 1, 300 & 400 ppm at their optimized operating temperature 260 °C

working temperature of 240 ± 5 °C. The Zoom-in of the transient resistance response at the exposure of 5 ppm of ethanol to show the error bar is depicted in Figure 54(b). The resistance of the films was deceased quickly in all cases after being exposed to ethanol. The value of change in resistance was large for the exposure to higher concentrations of ethanol. The value of change of resistance was increased continuously on exposure to higher concentrations of ethanol vapour for undoped ZnO. But, for the 2, and 3% Sn-ZnO, the saturation values of change of resistance were obtained with the exposure of 300 ppm onwards. The gas responses of ZnO and Sn-ZnO thin films to ethanol vapour at different concentrations ranging from 0.5 to 400 ppm ethanol are depicted in Figure 55. The value of response for undoped ZnO was increased significantly when exposed to higher concentrations of ethanol. But, for the 2, and 3 % Sn-ZnO, the saturation values of response were obtained with the exposure of 300 ppm onwards. It is clearly demonstrated in the inset of Figure 55. The calculated values of response along with the standard errors with the exposure of various concentrations of ethanol are presented in Table 18. Undoped ZnO film exhibited the highest response of 110.718 ± 0.076 at a working temperature of 290 °C towards 400 ppm of ethanol. In this experiment, the undoped, 1%, 2%, and 3% Sn doped ZnO samples could detect lower concentrations up to 1, 1, 0.5, and 5 ppm of ethanol with values of the response of 1.197 ± 0.001, 1.212 ± 0.001, 2.216 ± 0.012 and 1.169 ± 0.001 respectively. The gas response of 2% Sn-ZnO was good enough which confirms that it is useful for the detection of lower concentrations.

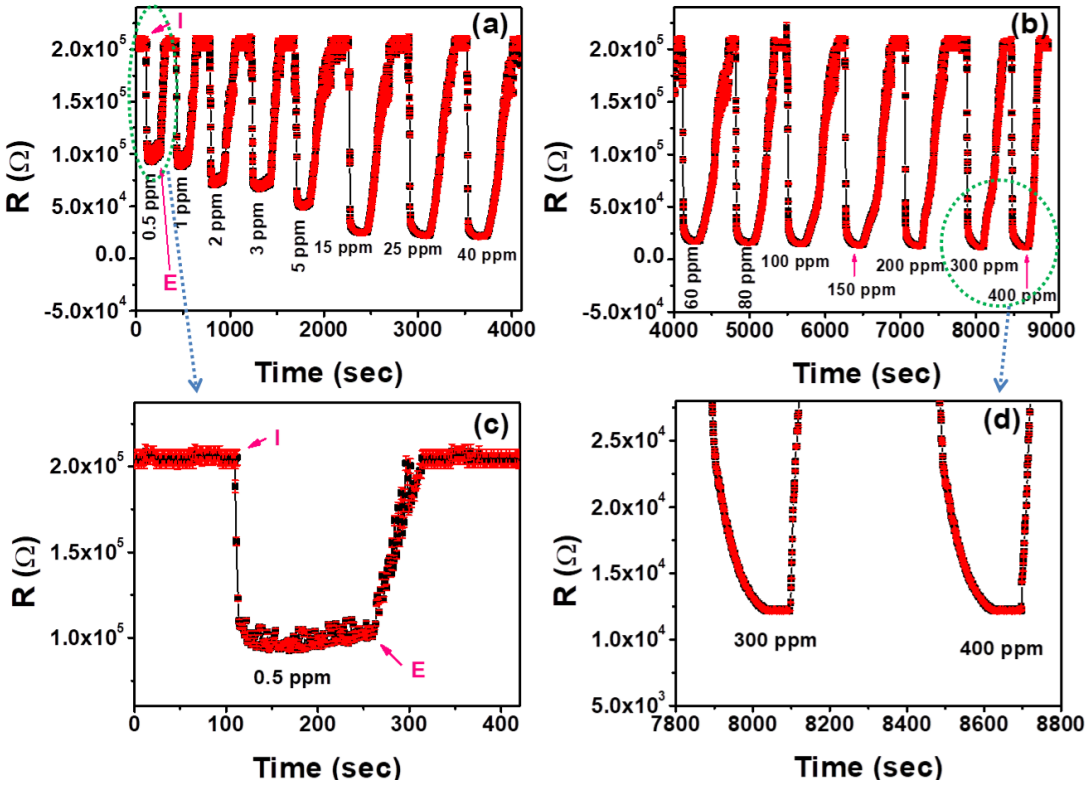

Figure 53: Transient resistance responses of 2% Sn-ZnO films from (a) 0.5 to 40 ppm, (b) 60 to 400 ppm, and (c-d) zoom in of the response for 0.5, 300 & 400 ppm at optimized operating temperature 220 °C

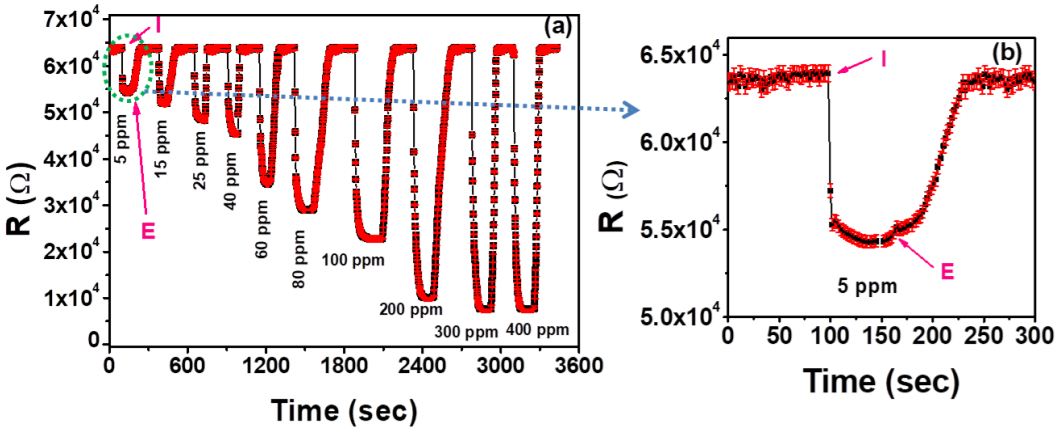

Figure 54: Transient resistance response of 3% Sn-ZnO films for the concentrations (a) 5-400 ppm and (b) zoom in of the response for 0.5 ppm at optimized operating temperature 240 °C

The sensing capability of the undoped ZnO film was also studied at the temperature 220 ± 5 °C and the result was compared with that of 2% Sn-ZnO film at the same temperature. Figure 56(a) and (b) shows the results of measurement transient resistance responses of the undoped and 2% Sn-ZnO film towards 400 ppm of ethanol vapour at 220 ± 5 °C. The results show the good repeatability of the proposed films with the response of 8.778 ± 0.005 for ZnO and 17.989 ± 0.011 for 2% Sn doped ZnO samples respectively. The 2% Sn-ZnO showed a higher value of gas response compared to undoped ZnO at this temperature.

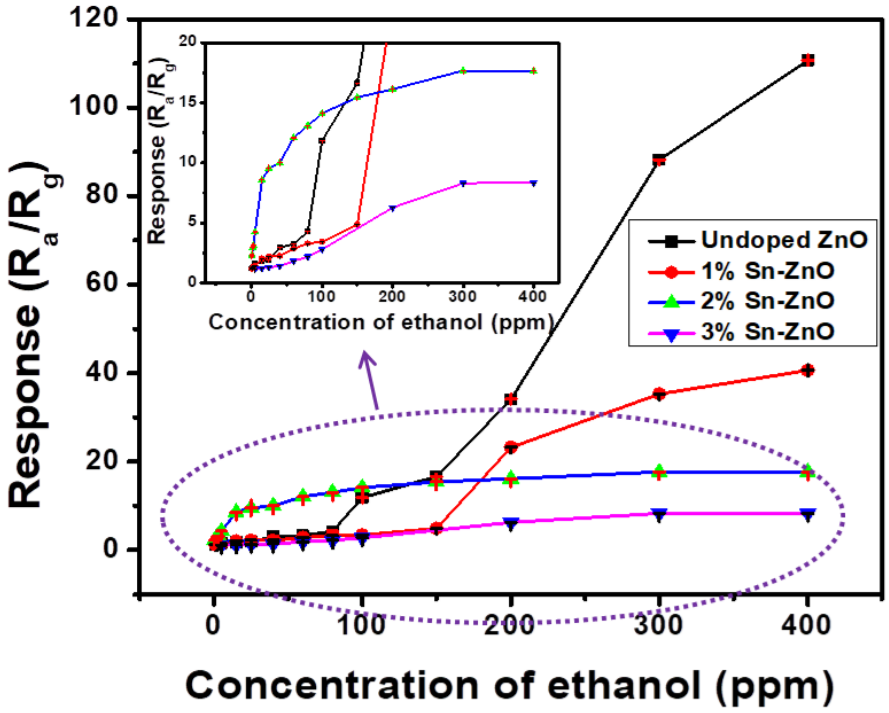

Figure 55: Gas response with exposure of different ppm of ethanol at their respective optimized operating temperatures

Table 18: Responses of ZnO and 1 – 3% Sn-ZnO films at various concentrations of ethanol

Concentration of Ethanol (ppm)	Response (R_a/R_g)			
	ZnO	1% Sn-ZnO	2% Sn-ZnO	3% Sn-ZnO
0.5	–	–	2.216 ± 0.012	–
1	1.197 ± 0.001	1.212 ± 0.001	2.332 ± 0.012	–
3	1.246 ± 0.001	1.325 ± 0.001	3.118 ± 0.014	–
5	1.600 ± 0.001	1.444 ± 0.001	4.258 ± 0.012	1.169 ± 0.001
15	1.786 ± 0.001	2.039 ± 0.002	8.588 ± 0.012	1.225 ± 0.001
40	2.959 ± 0.004	2.246 ± 0.001	10.022 ± 0.012	1.402 ± 0.001
60	3.250 ± 0.002	2.837 ± 0.001	12.101 ± 0.011	1.824 ± 0.003
80	4.293 ± 0.003	3.305 ± 0.001	13.089 ± 0.009	2.186 ± 0.002
100	11.846 ± 0.003	3.421 ± 0.001	14.129 ± 0.013	2.795 ± 0.001
200	34.119 ± 0.059	23.253 ± 0.001	16.135 ± 0.011	6.278 ± 0.008
300	88.163 ± 0.043	35.266 ± 0.021	17.669 ± 0.011	8.319 ± 0.006
400	110.718 ± 0.076	40.654 ± 0.015	17.659 ± 0.011	8.339 ± 0.004

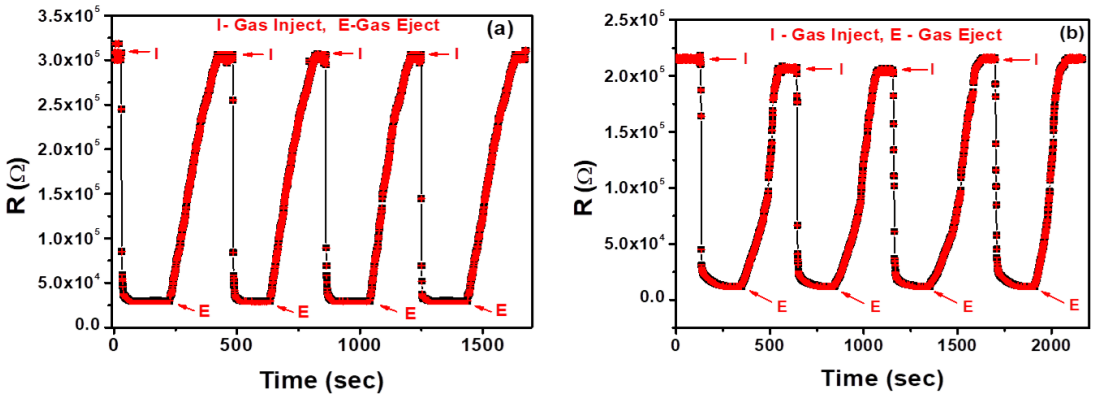

Figure 56: Cyclic resistance responses of (a) ZnO and (b) 2% Sn-ZnO films at 220 °C to towards 400 ppm of ethanol vapor

The response and recovery times of ZnO, 1, 2, and 3% Sn-ZnO at the exposure to 400 ppm of ethanol vapour at their working temperature were also measured. Figure 57(a) through (d) illustrates the geometrical calculations of response and recovery times of MOS sensors with respect to their definitions. For ZnO, 1, 2, and 3% Sn-ZnO films, the response times are determined to be 22, 30, 15, and 24 sec respectively. The 2% Sn-ZnO showed a quick response than others. Similarly, the recovery times were found to be 188, 228, 119, and 36 sec for ZnO, 1, 2, and 3% Sn-ZnO films accordingly. The quick recovery was found in the ZnO doped with higher concentrations of Sn.

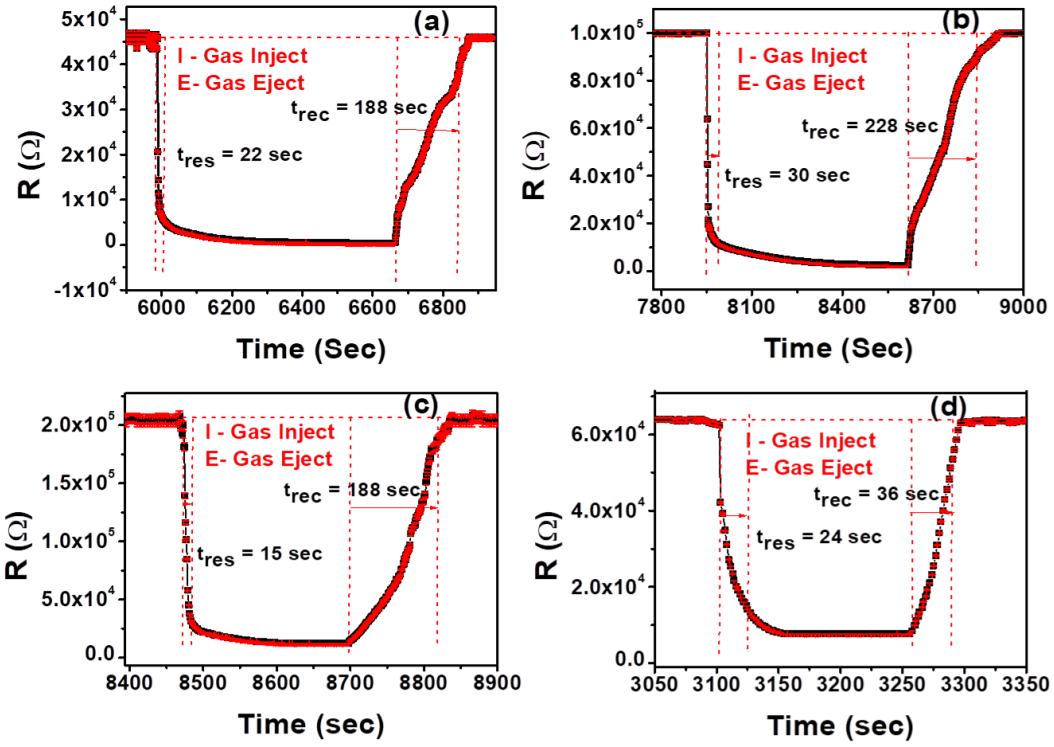

Figure 57: Response time and recovery time of (a) ZnO, (b) 1% Sn-ZnO, (c) 2% Sn-ZnO, and (d) 3% Sn-ZnO films for 400 ppm of ethanol vapor at their operating temperature

The present result of sensing of 2% Sn-ZnO was compared with the published reports of the various metal-doped ZnO films. It is presented in Table 19. The working temperature was seen to be considerably lower than the values published for a comparable system prepared using alternative techniques. The 2%Sn-ZnO film could detect as low as 0.5 ppm of ethanol vapour at the lower operating or working temperature of 220 ± 5 °C. The result obtained in this work was found to be good in comparison to the published reports.

Table 19: Comparison of performance of ZnO-based ethanol sensor in this work with reported work

Materials	Method	Operating Temperature (°C)	Ethanol (ppm)	Response (R_a/R_g)	Reference
Ti-ZnO	Furnace system with Ti hotwire assistance	500	1000	3.89	(Hsu *et al.,* 2014)
Sn-ZnO	Thermal oxidation reaction	340	1000	30.4	(Santhaveesuk & Choopun, 2013)
Cu-ZnO	Spray Pyrolysis	400	80	30	(Miki-Yoshida *et al.,* 2000)
Fe-ZnO	RF magnetron sputtering	300	300	2.91	(Hassan *et al.,* 2014)
Fe-ZnO	Hydrothermal/ dip coating	250	500	19	(Khayatian *et al.,* 2016)
Sn-ZnO	Spray pyrolysis	220	400 0.5	17.659 ± 0.011 2.216 ± 0.012	This work

In this case, the gas sensing mechanism is similar to as explained in the previous section 4.3.4. In Figure 50, the gas response was increased with temperature, attains maximum value at a particular temperature, and then decreased with increasing the temperature. The variation of gas response with the temperature is due to the fact that the gas response varies with the reaction rate (K_{Eth}) coefficient of the test gas with the oxygen species adsorbed on the ZnO surface. The reaction rate coefficient varies with the absolute temperature (T) and the activation energy (E_a) as $K_{Eth}(T) = A \exp\left(-\frac{E_a}{k_B T}\right)$, where k_B is Boltzmann constant (Santhaveesuk & Choopun, 2013; Hongsith *et al.*, 2010). With the rise in temperature, the thermal energy rises. When it gets closer to the limit of the activation energy barrier of the reaction, the charge concentrations rise dramatically, and more oxygen is adsorbed, which gives a high response. Beyond this temperature, oxygen species desorbed from the ZnO surface and lower the response (Khayatian *et al.,* 2016). The decrease in the activation energy of ZnO after Sn doping is responsible for the decrease in the optimal operating or working temperature from 290 ± 7 °C to 220 ± 5 °C for the Sn-ZnO films (Bougrine *et al.,* 2003). From the observation of SEM images in Figure 48, it was clearly seen that the average size of grains was increased in the Sn-ZnO samples in comparison to that of undoped ZnO, which decreased the specific surface area of Sn-ZnO. Therefore, the gas response was decreased for Sn-ZnO films. In Figure 55, the saturation values of response were obtained for 2 and 3% Sn-ZnO with the exposure of 300 ppm onwards. It is attributed to the smaller number of adsorbed oxygen ions on the surface of Sn-ZnO films.

The measurements of response time and recovery time are shown in Figure 56. It revealed a faster response and recovery with a response time of 15 sec and recovery time of 119 sec for 2% Sn-ZnO than that of undoped ZnO at an exposure of 400 ppm of ethanol vapour. Such speedy response and recovery nature were due to the increased reaction rate of ethanol vapour molecules with the adsorbed oxygen ions in the surface of 2%

Sn-ZnO. In Figure 57, 2% Sn-ZnO showed a response higher than that of undoped ZnO at 220 ± 5 °C. It may be due to the lowering of the activation energy after Sn doping into ZnO (Acharya *et al.,* 2012). The charge concentration increased significantly at this temperature in 2% Sn-ZnO but not for undoped ZnO. So, more oxygen species were adsorbed in 2%Sn-ZnO than that in undoped ZnO at 220°C.

4.5 Characterization Spin Coated ZnO and Fe-Al-ZnO Films

Only a few reports are available for metal-metal co-doped ZnO-based sensors to date. In this respect, we prepared the Fe-Al co-doped ZnO films by a spin coating method and studied the structural & optical properties, surface morphology, and elemental composition for ethanol sensing. The sample preparation method is described in section 3.1.2 of chapter 3. The results of gas sensing measurements are discussed in this section.

4.5.1 Structural Analysis

The structural investigation of as-prepared undoped and Fe-Al co-doped ZnO films was done using X-ray diffraction (XRD). Figure 58 depicts the XRD pattern of as-prepared ZnO films. The XRD pattern revealed that all samples were polycrystalline, with diffraction peaks aligned along (100), (002), (101), (102), (110), (103), and (112). The peaks closely matched the standard values of JCPDS card number 36 – 1451. All the samples showed three distinct diffraction peaks with high intensity. The most preferential

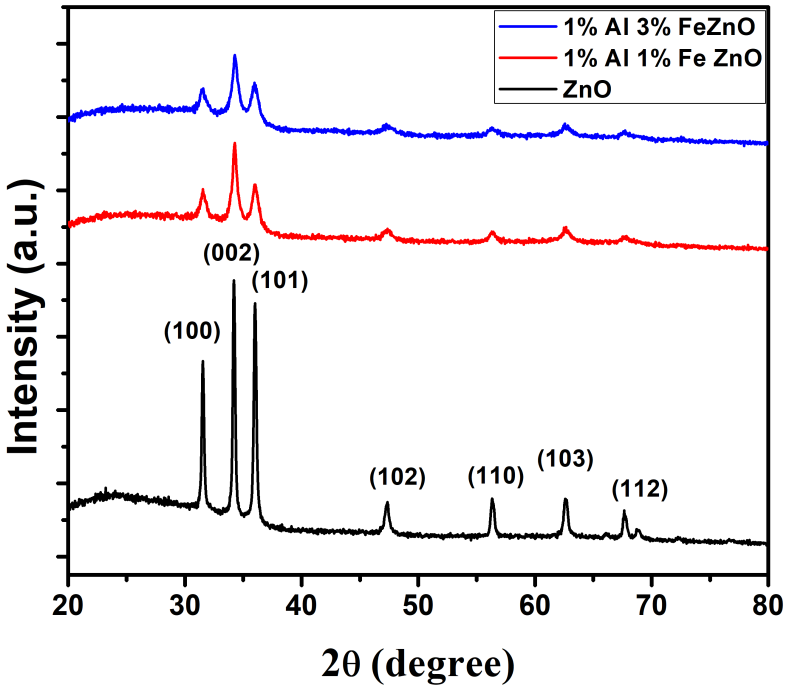

Figure 58: XRD patterns of spin-coated ZnO and Fe-Al-ZnO films

orientation was found to be along (002). A slight shift in the peak positions toward larger angles was found in Fe-Al-ZnO films, which corresponds to a slight decrease in the d-spacing. This shift in the d-spacing might be the result of the substitution of Fe^{3+} (ionic radius, 0.68 Å) or Fe^{2+} (ionic radius, 0.78 Å) and Al^{3+} (ionic radius, 0.53 Å) ions for Zn^{2+} ions (ionic radius, 0.74 Å). The relative intensities of the diffraction peaks were reduced in the case of Fe-Al-ZnO, indicating a decrease in the crystallinity. This is due to strain and lattice disorder brought on by the substitution of Fe and Al ions for Zn ions. The d-spacing and crystallite size (D) were calculated using Braggs law: $2d\ sin\theta = n\lambda$, and Debye Scherrer's formula: $D = \frac{0.9\lambda}{\beta cos\theta}$ with respect to three high intense peaks of undoped and Fe-Al-ZnO films (Hassan *et al.,* 2014).The lattice strain (ε) was calculated using the formula: $\varepsilon = \frac{\beta}{4tan\theta}$ (Pramod & Pandey, 2014; Srinivasulu *et al*., 2017). The (hkl), 2θ and calculated values of d-spacing, D and ε are presented in the Table 20. The

Table 20: (hkl), 2θ, FWHM, d-spacing and crystallite sizes of spin-coated ZnO and Fe-Al-ZnO films

Sample	**(hkl)**	**2θ (degree)**	**FWHM (degree)**	***d*-spacing (Å)**	***d*-spacing (JCPDS)**	**Crystallite size, (D) nm**	**Strain (ε) ($\times 10^{-3}$)**
ZnO	(100)	31.5412 ± 0.0016	0.2260 ± 0.00361	2.8330	2.8143	36.5081 ± 0.5829	3.49 ± 0.25
	(002)	34.1997 ± 0.0013	0.2266 ± 0.0031	2.6186	2.6033	36.6574 ± 0.4950	3.21 ± 0.18
	(101)	36.0154 ± 0.0016	0.2566 ± 0.0037	2.4907	2.4759	32.5316 ± 0.4728	3.45 ± 0.21
1%Fe-1%Al-ZnO	(100)	31.5639 ± 0.0070	0.5534 ± 0.0228	2.8310	2.8143	14.9097 ± 0.61337	8.54 ± 1.69
	(002)	34.2649 ± 0.0043	0.4389 ± 0.0103	2.6138	2.6033	18.9299 ± 0.4443	6.21 ± 0.55
	(101)	36.0103 ± 0.0063	0.5898 ± 0.0211	2.4910	2.4759	14.1581 ± 0.4056	7.92 ± 1.28
3%Fe-1%Al-ZnO	(100)	31.5357 ± 0.0104	0.5914 ± 0.0299	2.8335	2.8143	13.9512 ± 0.7059	9.14 ± 2.56
	(002)	34.3008 ± 0.0041	0.4926 ± 0.0097	2.6112	2.6033	16.8684 ± 0.3337	6.97 ± 0.39
	(101)	35.9677 ± 0.0064	0.5137 ± 0.0279	2.4939	2.4759	16.2529 ± 0.8832	6.90 ± 2.95

mean D was found to be significantly decreased from 35.2324 nm for undoped to 15.6908 nm for 3%Fe-1%Al-ZnO. The mean values of the strain (ε) was increased from 3.38×10^{-3} for undoped ZnO to 7.67×10^{-3} for 3%Fe-1%Al-ZnO. This significant decrease in D is due to substitution of Zn^{2+} ions (ionic radius, 0.74 Å) by Fe^{2+} ions (ionic radius 0.78 Å), Fe^{3+} ions (0.68 Å) and Al^{3+} ions (0.53 Å). The increase in ε may be caused by stress brought on by the disparity in the ionic radii of the dopant and Zn (Srinivasulu *et al.,* 2017). Here, the errors in D and ε were calculated using the standard errors in 2θ and FWHM of the individual peaks during fitting.

4.5.2 Optical Analysis

The transmission spectra of ZnO and Fe-Al-ZnO films were captured within the wavelength range of 360-1000 nm at ambient conditions. Figure 59(a) displays the plot of captured transmittance of as-prepared ZnO and Fe-Al-ZnO films. The mean transmittance of the undoped and Fe-Al ZnO films was found to be above 85% and a substantial decline at the short wavelengths close to the ultraviolet range. The optical band gap (E_g) of ZnO films was evaluated from the Tauc plot (Rambu *et al.,* 2013) depicted in Figure 59(b). The calculated values of optical band gaps were 3.270 ± 0.025 eV for undoped ZnO, 3.243 ± 0.075 eV for 1%Fe-1%Al-ZnO and 3.221 ± 0.059 eV for 3%Fe-1%Al-ZnO. The error in the optical band gap was determined by using the standard error in the slope and intercept of the linear fit in the linear portion of the g r aph. It clearly revealed a significant decrease in optical band gap energy. The drop in E_g was found to be consistent with reports on comparable systems (Goktas *et al.,* 2018; Khalid *et al.,* 2019). There are two reasons for decreasing the optical band gap. First, Al doping introduces defects/impurities states and produces the new shallow donor states due to the hybridization of the Al dopant and ZnO matrix, and hence the optical band gap decreases. Second, the optical band gap was decreased due to the "s-d" and "p-d" exchange interaction between localized "d " electrons in Fe in the ZnO matrix and the band electrons of ZnO which modifies the Fermi energy state by raising the top edge of the valance band and lowering the bottom edge of the conduction band. (Goktas *et al.,* 2018).

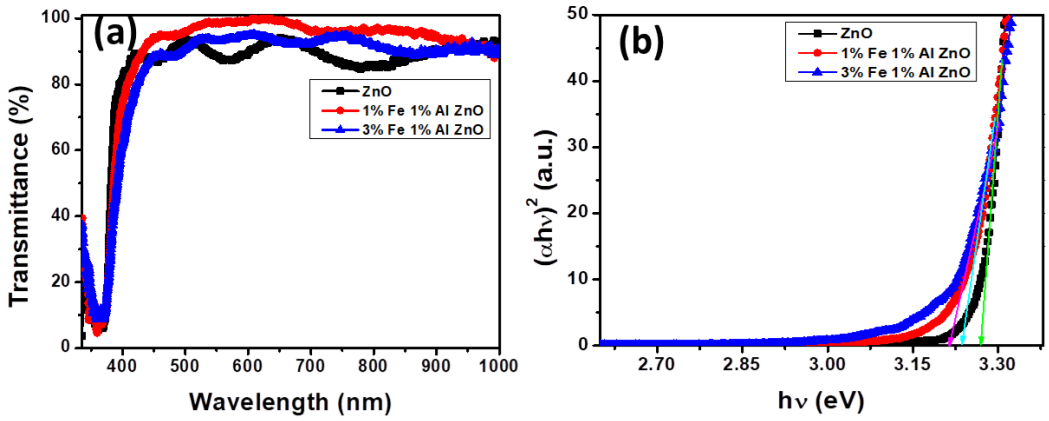

Figure 59: (a) Transmittance and (b) Tauc plots of spin-coated ZnO and Fe-Al-ZnO films

4.5.3 Surface Morphology

The sensing capability of ZnO films also depends on the surface morphology (Zhu & Zeng, 2017). Figures 60(a) through (c) show the SEM images of as-prepared undoped, 1%Fe-1%Al and 3%Fe-1%Al-ZnO films. Figure 60(a) clearly shows the grainy surface for the undoped. A reduction in the grain size was observed in the Fe-Al ZnO film in comparison to that of undoped ZnO film which led to an increase in the specific surface

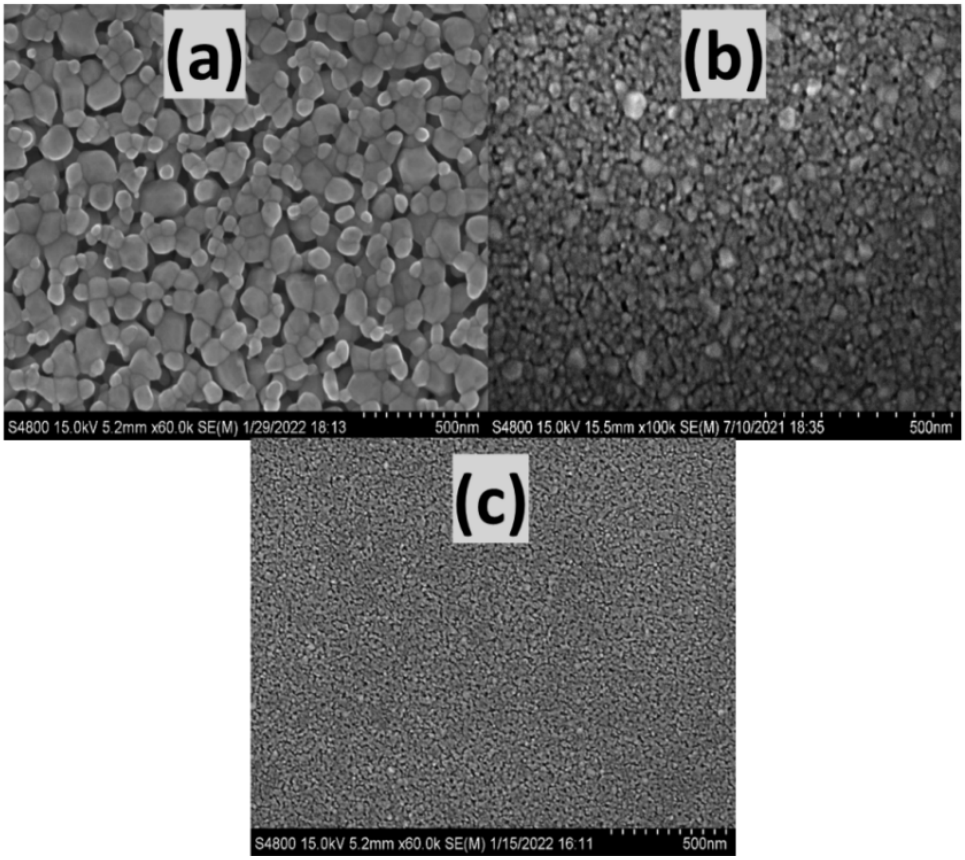

Figure 60: SEM images of spin-coated (a) ZnO, (b) 1%Fe-1% Al-ZnO and (c) 3%Fe-1% Al-ZnO films

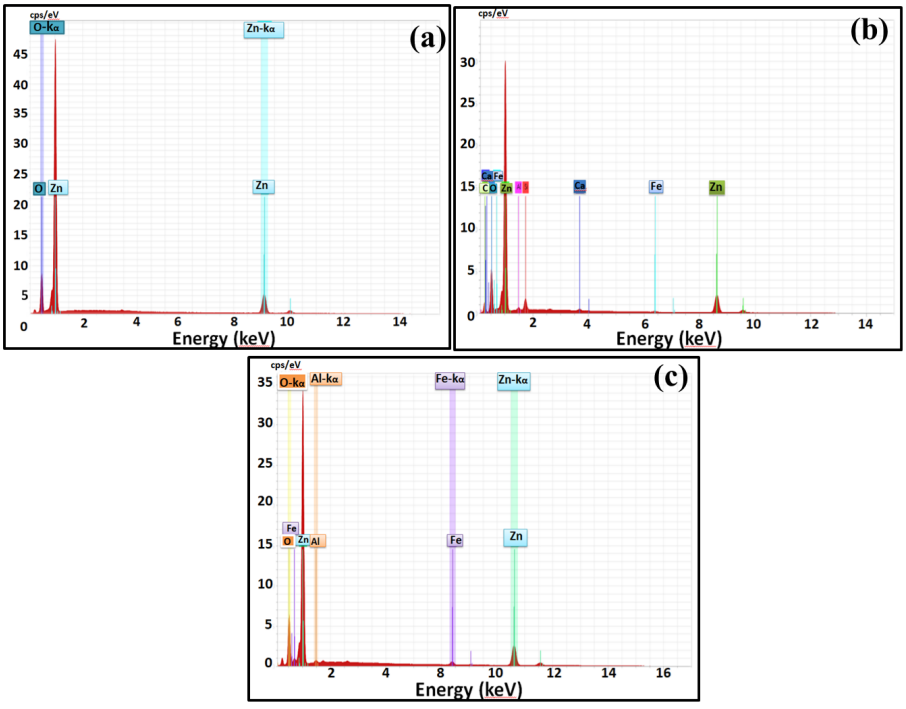

Figure 61: EDX spectra of spin-coated (a) ZnO (b) 1%Fe-1%Al-ZnO and 3%Fe-1%Al-ZnO films

area. This reduction in the grain size in Fe-Al-ZnO isdue to the substitution of Fe^{3+} (ionic radius, 0.68 Å) or Fe^{2+} (ionic radius of 0.78 Å) and Al^{3+} ions (ionic radius 0.53

Table 21: Elemental composition of spin-coated ZnO, and Fe-Al-ZnO films

Sample	Elements present (at.%)						
	Zn	**O**	**Fe**	**Al**	**Si**	**C**	**Ca**
ZnO	44.97	37.63	-	-	-	17.40	-
1%Fe1%Al-ZnO	32.79	33.60	0.66	1.24	4.20	26.81	0.71
3%Fe 1% Al-ZnO	29.94	31.00	1.67	1.20	-	-	-

Å) in the lattice sites of Zn^{2+} ions (ionic radius of 0.74 Å). The elemental composition of as-prepared films was studied by analyzing the EDX spectra. Figure 61(a) through (c) displays the EDX spectra of prepared undoped, 1%Fe-1%Al-ZnO and 3%Fe-1%Al-ZnO films. The concentrations of elements, zinc (Zn), oxygen (O), aluminum (Al), and iron (Fe) were investigated by analyzing the spectra. These spectra showed well incorporation of Al and Fe in Fe-Al-ZnO. The elements present in as prepared films are depicted in Table 21. The result shows that the atomic percentages of zinc and oxygen are 44.97 and 37.63% respectively in ZnO. The concentration of zinc and oxygen decreased on Fe-Al-ZnO. The iron and aluminum contents can be clearly seen as 0.66% & 1.24% in 1%Fe-1%Al-ZnO and 1.67% & 1.20% in 3%Fe-1%Al-ZnO films. Silicon (Si) and Calcium (Ca) peaks were also observed in EDX spectra of 1%Fe-1%Al-ZnO film in Figure 61(b) which might have come from the substrate.

4.5.4 Sensing Performance Towards Ethanol

As in the previous case, the sensing capability of ZnO films was studied by evaluating the gas response using the formula: response, $(R) = \frac{R_a}{R_g}$, where R_a and R_g are the resistances of the ZnO film in the air environment and the analyte gas environment, respectively (Bhatia *et al.,* 2017). Firstly, the response of the samples was measured at a different temperature ranging from 80 – 350 °C with an exposure of 400 ppm of ethanol vapour. Figure 62 shows the variation of response with temperature. Undoped, 1%Fe-1% Al, and 3%Fe-1%Al-ZnO films showed the maximum responses of 62.345 ± 0.037, 152.304 ± 0.003 and 93.225 ± 0.027 at the temperatures of 260 ± 6, 290 ± 7, and 300 ± 7 °C, respectively, which are called the optimized operating temperatures of undoped, 1% Fe-1%Al, and 3% Fe-1%Al-ZnO films. Here, the errors in the response are the standard errors. The fluctuation in the set temperature during the experiment was taken as the error in the temperature.

Figure 63(a) – (c) shows the transient resistance response of the ZnO and Fe-Al-ZnO films when exposed to ethanol vapour in a range of concentrations (1 – 400 ppm) at their respective operating temperatures. Figure 63(a) shows that the resistances of undoped ZnO decreased from 440577.861 ± 209.231 Ω (in air) to 290513.322 ± 88.792 Ω (in ethanol) for an exposure of 1 ppm of ethanol vapour. Similarly, Figure 63(b) shows the resistance of 1%Fe-1% Al-ZnO deceased from 39848.141 ± 8.792 Ω to 24516.901 ±

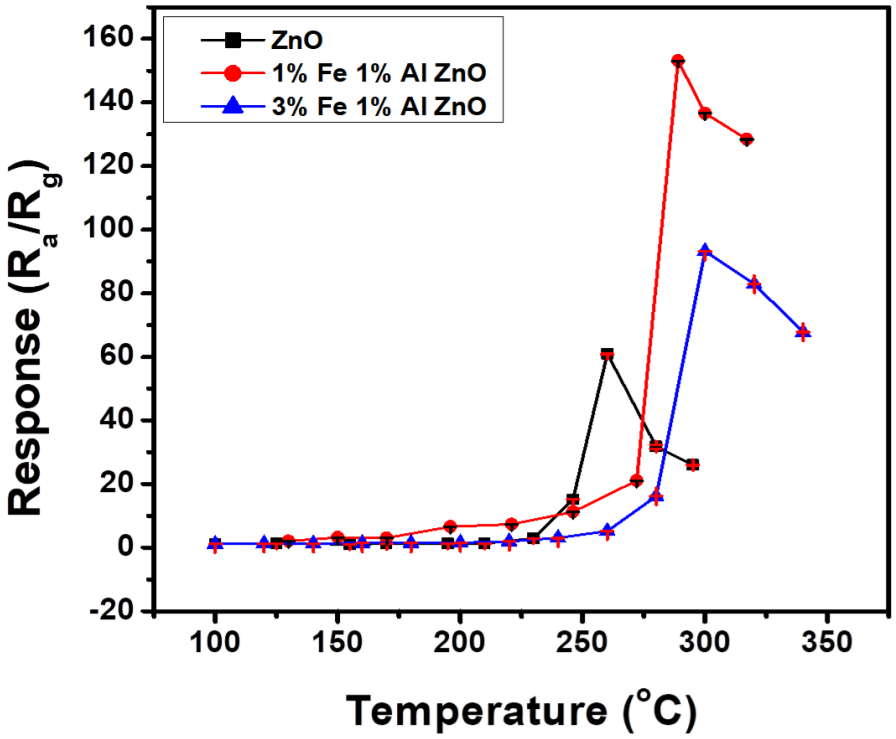

Figure 62: Temperature dependent response of ZnO, 1%Fe-1%Al-ZnO and 3%Fe-1%Al-ZnO films prepared by spin coating technique at the exposure of 400 ppm of ethanol

8.953 Ω for the same ppm exposure. Whereas 3%Fe-1%Al-ZnO films showed a change in resistance only for exposure of 2 ppm ethanol and above. Similarly, the resistance changes from 403614.856 ± 75.534 Ω to 6405.761 ± 3.877 Ω for undoped ZnO, from 36778.968 ± 29.673 Ω to 241.312 ± 0.044 Ω for 1%Fe-1%Al-ZnO and from 97721.625 ± 126.421 Ω to 1065.153 ± 0.241 Ω for 3%Fe-1%Al-ZnO respectively for the exposure of 400 ppm. The basic accuracy in the measurement of the resistance was taken as the error in the resistance. Figure 63(d) shows the variation of responses of undoped, 1%Fe-1%Al-ZnO, and 3%Fe-1%Al-ZnO film at an exposure of various concentrations of ethanol. The calculated values of responses at different concentrations of ethanol are presented in Table 22. The response was increased with exposure to higher concentrations of ethanol in all samples. Fe-Al-ZnO showed an improved gas response. The 1%Fe-1%Al-ZnO film showed the higher response of 152.304 ± 0.003 at 290 ± 7°C at the exposure of 400 ppm ethanol which is ~2.5 times greater than that for undoped ZnO. It could detect as low as 1 ppm of ethanol with a response value of 1.628 ± 0.002.

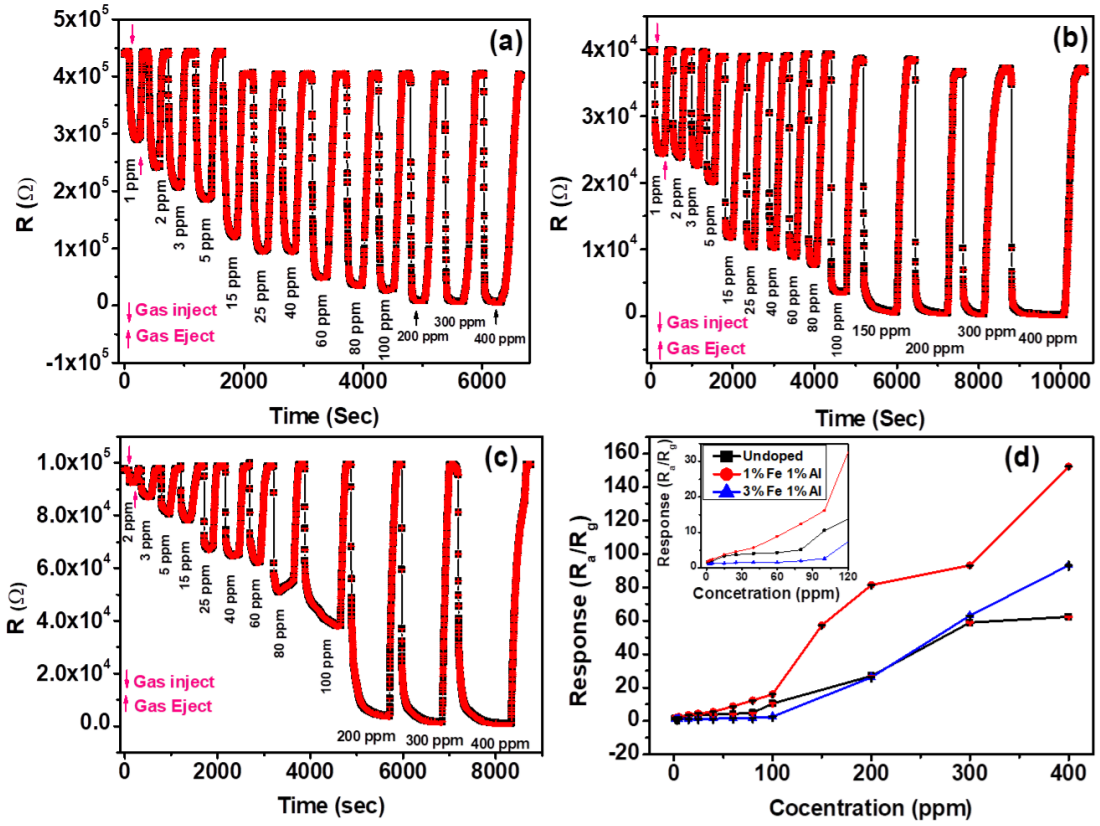

Figure 63: Transient resistance responses of (a) ZnO (b) 1%Fe-1%Al-ZnO (c) 3%Fe-1%Al-ZnO films and (d) response of undoped ZnO, 1%Fe-1% Al-ZnO and 3%Fe-1%Al-ZnO films on the exposure of 1-400 ppm of ethanol at their optimized operating temperatures

Table 22: Response of ZnO, 1%Fe-1%Al-ZnO and 3%Fe-1%Al-ZnO at various concentrations of ethanol

Concentration (ppm)	Response (R_a/R_g)		
	Undoped ZnO	1%Fe-1%Al-ZnO	3%Fe-1%Al-ZnO
1	1.515 ± 0.001	1.628 ± 0.002	-
2	1.671 ± 0.002	1.817 ± 0.002	1.049 ± 0.001
3	1.775 ± 0.002	2.117 ± 0.001	1.113 ± 0.002
5	1.955 ± 0.001	2.361 ± 0.001	1.231 ± 0.001
15	3.270 ± 0.002	3.650 ± 0.001	1.268 ± 0.001
25	3.732 ± 0.002	4.610 ± 0.002	1.472 ± 0.001
40	3.976 ± 0.002	5.644 ± 0.003	1.533 ± 0.001
60	4.315 ± 0 .003	8.843 ± 0.010	1.595 ± 0.002
80	5.031 ± 0.005	12.369 ± 0.001	1.944 ± 0.013
100	10.531 ± 0.015	16.141 ± 0.002	2.604 ± 0.012
200	26.980 ± 0.006	81.454 ± 0.008	26.233 ± 0.024
300	59.023 ± 0.014	93.147 ± 0.008	63.087 ± 0.029
400	62.345 ± 0.037	152.304 ± 0.003	93.225 ± 0.027

Figure 64(a) through (c) displays the transient resistance plots for all the samples at their optimized working temperature from which corresponding response time and recovery times were determined. The resistance was decreased after being exposed to ethanol

vapour and eventually reached saturation. Table 23 displays the measured values of response, response time, and recovery time of undoped and Fe-Al-ZnO towards exposure to 400 ppm of ethanol. The undoped ZnO film demonstrated a quicker response than the Fe-Al-ZnO film with a response time of 14 sec for 400 ppm of ethanol vapor. The 1%Fe-1%Al-ZnO film showed the highest response than others. Hence, this was found to be the most suitable for ethanol sensing.

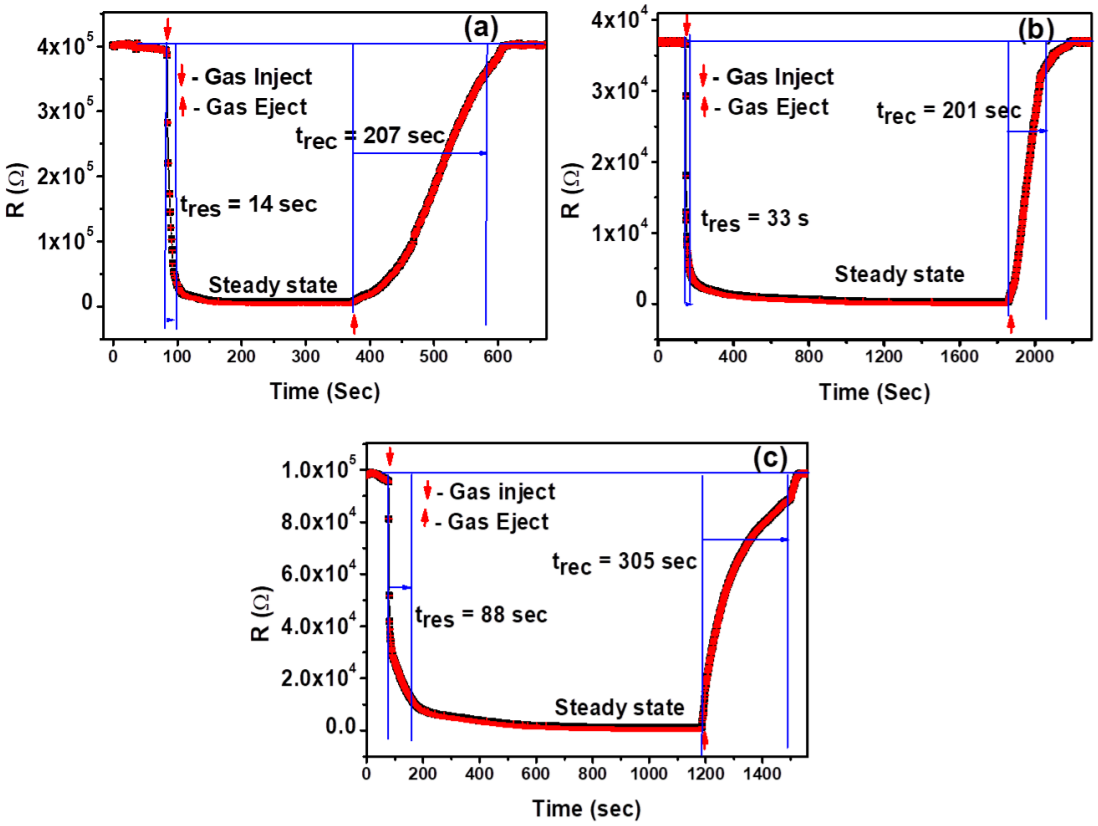

Figure 64: Response time and recovery time of (a) ZnO, (b) 1% Fe-1% Al-ZnO and (c) 3% Fe 1%-Al-ZnO films

Table 23: Gas response, response time and recovery time of ZnO and Fe-Al-ZnO films for 400 ppm of ethanol

Sample	Response	Response time (sec)	Recovery Time (sec)
ZnO	62.345 ± 0.037	14	207
1%Fe 1% Al-ZnO	152.304 ± 0.003	33	201
3% Fe 1% Al-ZnO	93.225 ± 0.027	88	307

In this case, the ethanol sensing mechanism is the same as explained in section 4.3.4. Figure 62 shows the variation of response with temperature. The 1%Fe 1%Al and 3% Fe 1% Al-ZnO showed the response of 152.304 ± 0.003 and 93.225 ± 0.027 at the higher operating temperature of 290 ± 7, and 300 ± 7 °C with an exposure of 400 ppm of ethanol. But the undoped ZnO showed the lower value of the response, 62.345 ± 0.037 at the working temperature of 260 ± 6 °C with the exposure of the same concentrations

of ethanol vapour. The increase in the operating or working temperature in Fe-Al-ZnO may be due to an increase in activation energy after Fe and Al doping (Khayatian *et al.,* 2016). The gas response varies with the reaction rate coefficient (K_{Eth}), which depends on the activation energy (E_a) as well as the temperature of the sensing element described by $K_{Eth}(T) = A \exp\left(-\frac{E_a}{k_B T}\right)$, where k_B is Boltzmann constant (Hongsith *et al.*, 2010). The thermal energy of activation of charge carriers in ZnO increases with temperature. At a particular temperature, when the thermal energy is enough to break the barriers of the activation energy of the reaction, the charge concentrations increased drastically and give a high response at the particular temperature. The activation energy term is divided into two parts: (a) contribution from thermal activation of charge carriers into the conduction band and (b) contribution from the energy needed to create the defect which is directly related to the change in charge carriers concentrations in the conduction band. Suitable donor doping can create electronic defects which raise the impact of oxygen partial pressure on the conductivity. Along with oxygen, a small amount of reducing gas such as carbon monoxide is also present in gases which changes the conductivity (Kwon *et al.,* 1995).

There are two reasons for the enhancement of the response of Fe-Al-ZnO. (i) The Fe-Al doping into ZnO improved the specific surface a rea. The grain size was significantly decreased in Fe-Al-ZnO. Due to this the specific surface area of the Fe-Al-ZnO increased, which increased the oxygen adsorption and reaction sites in Fe-Al-ZnO (Sahoo *et al.,* 2020). (ii) Fe and Al co-doping into ZnO had a synergistic effect. W hen Al^{3+} and Fe^{3+} replaced the Zn^{2+}, the additional free charges were available in the host ZnO and the additional oxygen ions would be attracted to Al^{3+} and Fe^{3+} ions to preserve charge neutrality, and more oxygen molecules were adsorbed into the ZnO surface (Walker *et al.,* 2019) and gave the high response. The response of 1%Fe-1%Al-ZnO is greater than that of undoped and 3%Fe-1%Al-ZnO which may be due to the more active adsorption sites available only for the appropriate percentage of dopant. However, for excessive Fe concentrations in 3%Fe-1%Al-ZnO, the scattering atom may present on the surface of ZnO that decreased the oxygen adsorption sites and reaction rates. Hence, the gas response decreased (Ge *et al.,* 2007; Yu *et al.,* 2011; Zhang *et al.,* 2010).

4.6 Effect of Gate Electrode Potential on the Sensing Characteristics of ZnO Film Prepared by Spray Pyrolysis

The structural & optical properties, surface morphology, and gas sensing capability of undoped ZnO film prepared by spray pyrolysis method are described in this section. The ZnO film preparation method is described in section 3.1.3 of chapter 3 in detail. The gas sensing properties were studied by and without applying the potential at the gate electrode. The results of ammonia vapour detection at room temperature are discussed

below.

4.6.1 Structural Analysis

The X-ray diffraction (XRD) was employed to examine the structural characteristics of ZnO thin films. Figure 65 depicts the XRD pattern of a ZnO film deposited on a glass substrate by the spray pyrolysis method. A sharp diffraction peak at 2θ = 34.4218 ± 0.0024° was observed corresponding to (002) plane along with a less intense peak at 2θ = 36.2715 ± 0.0296° corresponding to the plane (101), indicating the preferential orientation along (002) plane. It was observed to be in close agreement with the values of JCPDS card number 36-1451. It confirmed the formation of ZnO. Here, the error in the 2θ reading is the standard error found while fitting the peak.

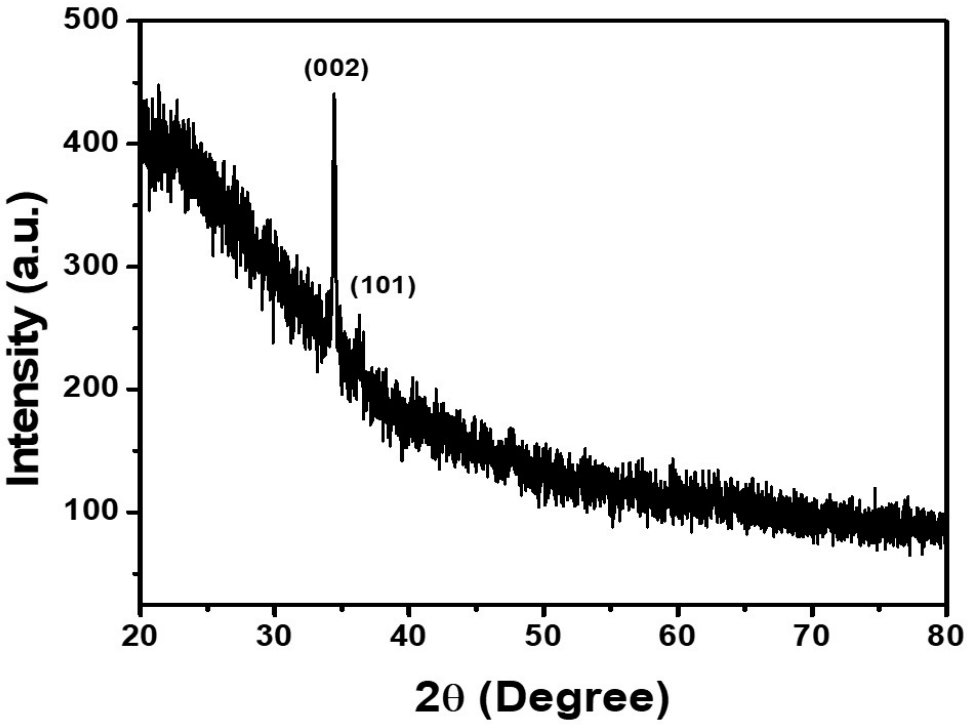

Figure 65: X-ray diffraction pattern of ZnO film on glass substrate prepared by spray pyrolysis

The d-spacing was calculated using Braggs law: $2d\ sin\theta = n\lambda$. The crystallite size of ZnO was determined using Debye Scherer's formula: $D = \frac{0.9\lambda}{\beta \cos\theta}$. The lattice strain ($\varepsilon$) was determined using the formula: $\varepsilon = \frac{\beta}{4tan\theta}$ (Pramod & Pandey, 2014; Srinivasulu *et al.*, 2017). The detail calculation of 2θ, d-spacing, D and ε are illustrated in Table 24. The calculated value of d-spacing was found to be slightly different from the JCPDS value, indicating the deposition of quality of the film on the glass substrate. The values for D and ε corresponding to (002) plane were noticed to be 37.9671 ± 1.3716 nm and (3.08 ± 0.11)×10^{-3}, respectively. The errors in D and ϵ were calculated using standard errors found in 2θ and FWHM of the individual peaks during fitting.

Table 24: (hkl), 2θ, FWHM, d-spacing, crystallite size (D) and strain (ε) of ZnO film

(hkl)	**2θ (°)**	**FWHM(°)**	***d*-spacing (Å)**	***d*-spacing (Å) (JCPDS)**	**(D) nm**	**Strain (ε) ($\times 10^{-3}$)**
(002)	34.4218 ± 0.0028	0.2189 ± 0.0079	2.6023	2.6033	37.9671 ± 1.3716	3.08 ± 0.11
(101)	36.2715 ± 0.0296	0.6123 ± 0.0095	2.4737	2.4759	13.6487 ± 0.2111	8.16 ± 0.13

4.6.2 Optical Analysis

The transmission spectra of the ZnO sample within the wavelength ranging from 360 nm to 900 nm at ambient temperature as measured by HR 4000 ocean optics spectrophotometer is depicted in Figure 66(a). In the visible spectrum, the average optical transmittance of ZnO film exceeded 8 2%. At shorter wavelengths, close to the UV range, a dramatic decline in transmittance was observed, which is due to the abundant absorption of light. The optical band gap was calculated using a Tauc plot, (Rambu *et al.,* 2013). The optical band gap of 3.297 ± 0.113 eV is obtained by extrapolating the linear part of the curve into the $h\nu$-axis. It was consistent with the value in the published literature (Mani & Rayappan, 2015). The error in the optical band gap was determined by using the standard errors found in the slope and the intercept of the linear fit in the linear portion of the graph.

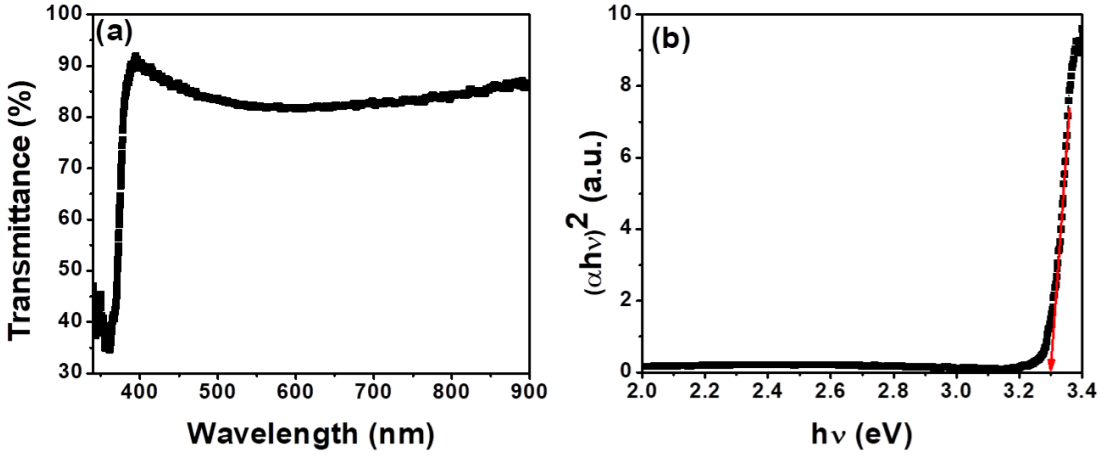

Figure 66: (a) Transmittance spectra and (b) Tauc plot of ZnO prepared by spray pyrolysis

4.6.3 Surface Morphology

The morphology of the sensor surface plays a critical role in determining the gas response in gas sensing task (Shao *et al.,* 2016;Yang *et al.,* 2011). Figure 67 depicts the SEM micrograph of ZnO film prepared by the spray pyrolysis m ethod. It clearly shows the surface consisting of nearly spherical shaped grains. Energy dispersive X-ray (EDX) was employed to study the elemental analysis of the prepared film.

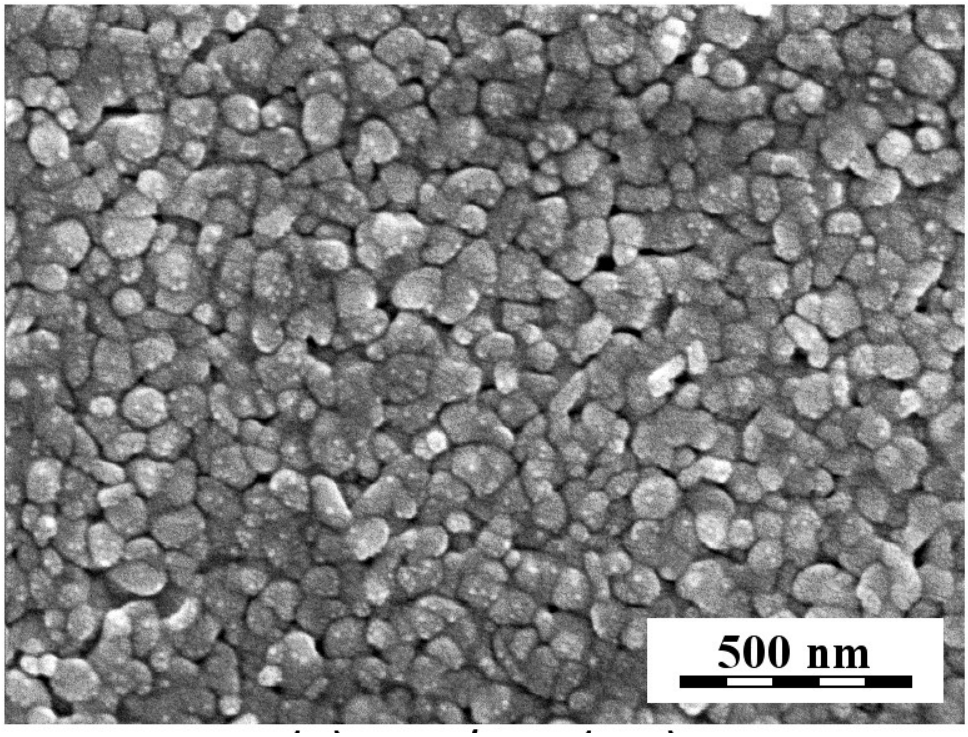

Figure 67: SEM image of ZnO film prepared by spray pyrolysis

4.6.4 Sensing Performance Towards Ammonia

The gas sensing capability of the ZnO film was investigated by measuring the resistances of ZnO film in air and in 400 ppm of ammonia vapour at different gate electrode potentials using a special detector as shown in Figure 26. Figures 68(a) and 68 (b – e) show the transient resistance response of ZnO in the absence and presence of the applied gate electrode potentials. The resistance was decreased after the injection of ammonia vapour and then acquired the saturation values in the absence and presence of applied gate electrode potential. After the ejection of ammonia vapour, the resistance again increased and acquired the original value. The resistance was decreased by a large value in the presence of the applied field than that in the absence of the field. The gas response (R) was calculated using the formula: $R = \frac{R_a}{R_g}$, where R_a and R_g are the resistances of the ZnO in the air and in the gas respectively. The stable values of resistances of ZnO in air and ammonia vapour and the corresponding values of responses at different applied potentials are depicted in Table 25. The stable values of the resistance were changed from (1014.11 ± 1.567) x 10^5 to (3342.611 ± 3.708) x10^3 Ω, (1256.511 ± 2.859) x 10^5 to (3462.071 ± 1.383) x 10^3 Ω, (1290.091 ± 2.486) x 10^5 to (3286.512± 3.699) x 10^3 Ω, (1391.372 ± 1.661) x 10^5 to (3291.921 ± 3.353) 10^3 Ω, and (1829.392 ± 2.093) x 10^5 to (3288.932 ± 1.992) x 10^3 Ω at the applied gate electrode potential of 0, 6, 12, 18 and 24 V respectively. The basic accuracy or measurement accuracy is taken as the error in the resistance. Figure 68(f) depicts the variation of gas response at different applied gate

electrode potentials. The ZnO showed a high gas response at the higher gate electrode potential. The measured values of gas response were found to be 30.292 ± 0.042, 36.324 ± 0.022, 38.893 ± 0.082, 42.662 ± 0.071 and 54.581 ± 0.062 at gate electrode potentials of 0, 6, 12, 18, and 24 V respectively. Here, the standard errors are calculated in response to each case. The gas response was found to increase from 30.292 ± 0.042 at the gate electrode potential of 0 V to 54.581 ± 0.062 at the gate electrode potential of 24 V. This shows that the application of potential at the gate electrode enhanced the performance ZnO sensor towards detecting the ammonia vapour.

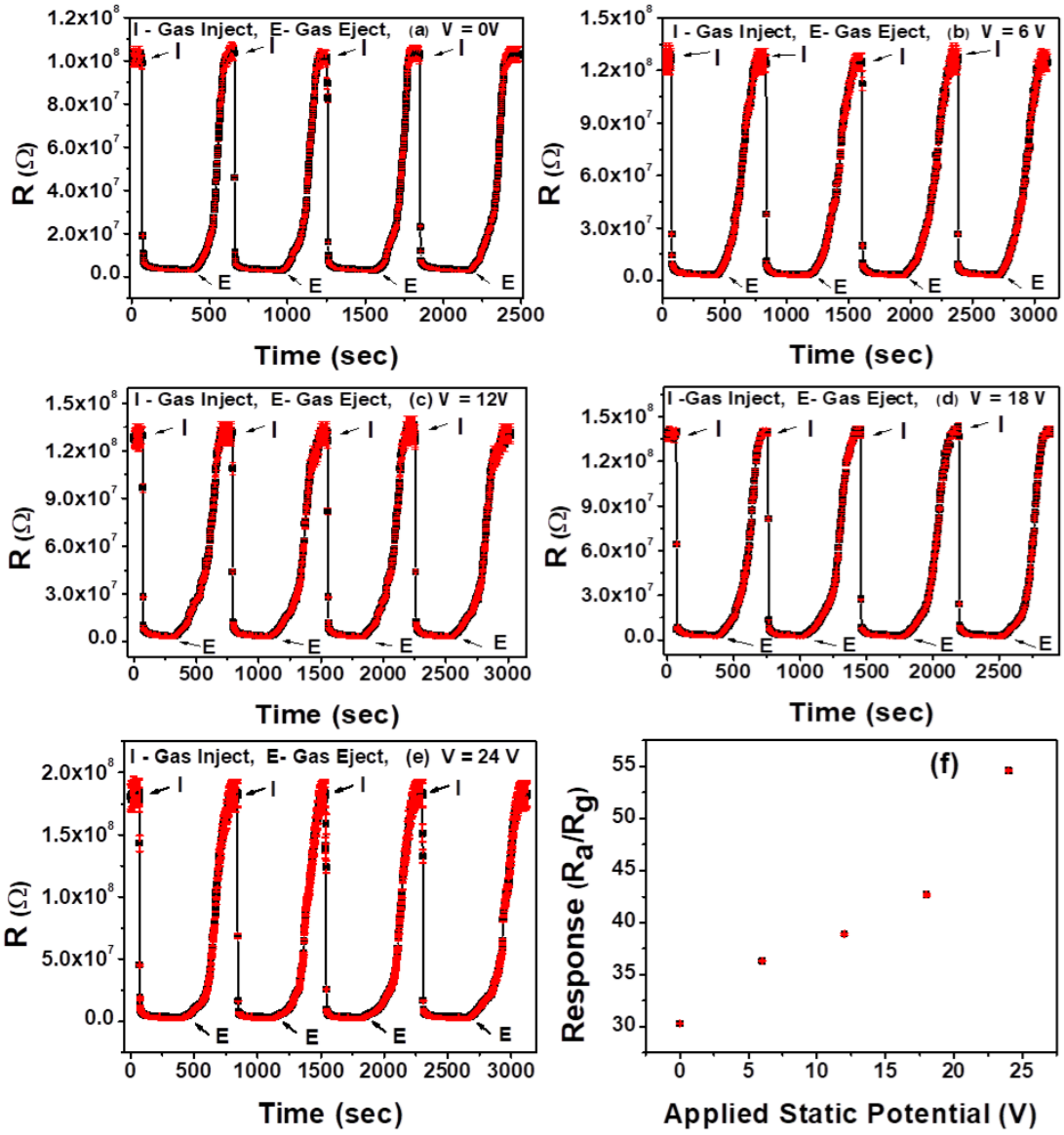

Figure 68: Variation of resistance of ZnO film with time with the exposure of 400 ppm of ammonia for 4 cycles at (a) 0 V, (b) 6 V, (c) 12 V, (d) 18 V, (e) 24 V, and (f) response at applied static potentials of 0-24 V

Table 25: Resistances and response at different applied potential

Applied Potential (V)	Resistance ((Ω)		Response (R_a/R_g)
	In air (R_a) $\times 10^5$	In gas (R_g) $\times 10^3$	
0	1014.111 ± 1.567	3342.611 ± 3.708	30.292 ± 0.042
6	1256.511 ± 2.859	3462.071 ± 1.383	36.324 ± 0.022
12	1290.091 ± 2.486	3286.512 ± 3.699	38.893 ± 0.082
18	1391.372 ± 1.661	3291.921 ± 3.353	42.662 ± 0.071
24	1829.392 ± 2.093	3288.932 ± 1.992	54.581 ± 0.062

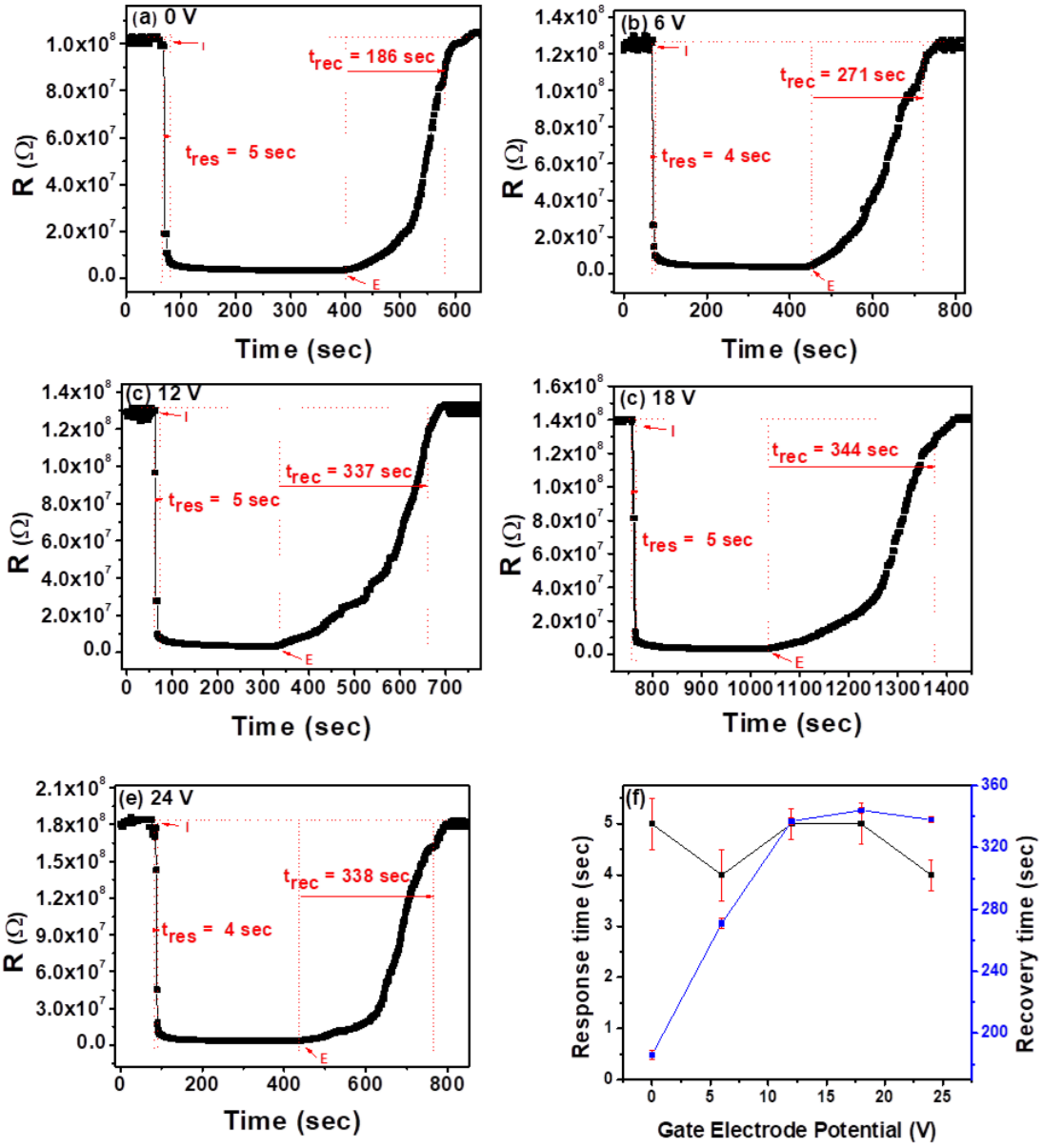

Figure 69: Response and recovery times at applied static potential of (a) 0 V (b) 6 V (c) 12 V (d) 18 V, (e) 24 V, and (f) response and recovery time of ZnO at different applied gate potentials

Figure 69(a) through (e) shows the measurement of the response and recovery times at different gate electrode potentials. It is the graph between variations of the resistance

of ZnO film with time after injection and ejection of the ammonia vapour. The sample showed a quick response with a response time of about 4 – 5 sec at all applied static field but, a slow recovery with recovery times of 186, 271, 337, 344, and 338 sec at applied gate potential of 0, 6, 12, 18, and 24 V respectively. Figure 69(f) shows the variation of response time and recovery time at all applied potentials. The response time was found to be almost the same, 4 – 5 sec at all applied potentials. But, the recovery time was increased first from 186 sec at the potential of 0 V to 338 sec at the applied potential of 12 V and remained nearly constant at higher gate electrode potential.

In Figure 68(a) to (e), a quick reduction in the resistance was observed with the exposure of 400 ppm of ammonia vapour. It can be explained using the model shown in Figure 70. Figure 70(a) shows that the oxygen molecules are adsorbed onto the ZnO surface in the air, which takes the electrons from the conduction band of ZnO, and oxygen ions O_2^- are formed. It causes the depletion region to increase which, in turn, increases the resistance of ZnO and acquires the stable value of resistance. The resistance measured at this state is termed as R_a and this resistance is taken as the base resistance under the study. When the positive potential is applied to the gate electrode, the electrons in the ZnO surface were attracted by the positively charged FTO surface just above the film. It helps to adsorb extra oxygen molecules onto the ZnO surface. These oxygen molecules draw extra electrons from the ZnO surface which widens the depletion layers more and increases the base resistance. This is illustrated in Figure 70(b). In Figure 70(c), at the exposure of NH_3 vapour onto the ZnO surface, the molecules of ammonia react with O_2^-

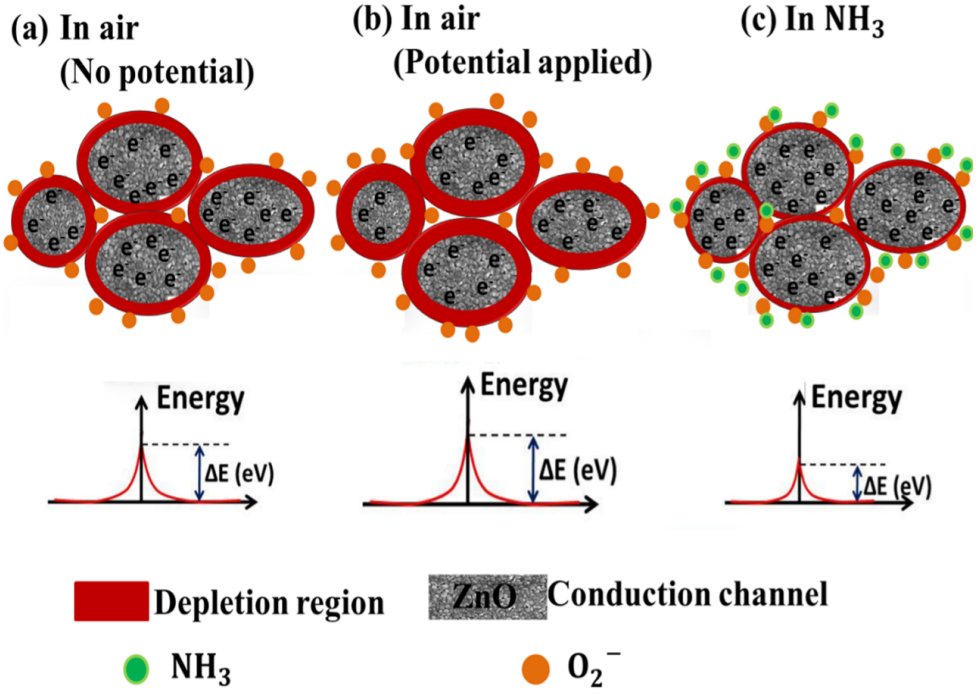

Figure 70: (a) Sensing mechanism of ZnO sensor in the air (a) with zero gate electrode potential, (b) with applied gate potential and (c) in NH_3 vapour

ions and liberate the electron back to the ZnO surface. The depletion layer and hence the resistance then decreases and acquires a lower stable value of resistance. The resistance measured at this stage was taken as R_g.

In figure 68(f), the response increased on increasing the applied gate electrode potential. It is due to the fact that after applying the positive potential to the gate electrode, the base resistances (R_a) of ZnO increased by adsorbing the extra oxygen molecules. When the ammonia vapour was exposed to the ZnO surface, more ammonia molecules interacted with more oxygen ions than that in the absence of the field and an additional number of electrons was released which lowers the resistance (R_g) up to the lower value. The difference in the value resistances of ZnO in air and in ammonia is large when gate electrode potential was applied than that when there was no gate electrode potential.

The reaction rate of exposed gas molecules with the adsorbed oxygen determines the response time. The higher the reaction rate, the faster the release of electrons by adsorbed O_2^- molecule and the smaller the response time. In figure 69(f), the response times were found to be nearly the same at all values of the applied electric field. It is because of the same reaction rate of the exposed ammonia molecules with the oxygen molecules adsorbed in the ZnO surface. But, the recovery time was increased first up to the value of 337 sec in increasing the applied gate electrode potential up to 12 V and then acquiring the saturation value. It is due to the fact that recovery time depends on the number of adsorbed oxygen molecules onto ZnO. As the gate potential increased, more electrons accumulated at the ZnO surface and more O_2^- molecules adsorbed. So, the recovery time is large at higher applied gate potentials. The saturation value of recovery time at the gate potential higher than 12 V may be due to the same rate of adsorption of oxygen onto the ZnO surface after the ejection of ammonia vapour.

CHAPTER 5

5. CONCLUSION AND RECOMMENDATIONS

5.1 Conclusion

In this work, at first, the undoped, metal (Fe and Sn) doped and metal-metal (Fe – Al) co-doped ZnO films were prepared by spin coating technique, spray pyrolysis technique and doctor blade methods. As prepared films were then characterized using ocean optics UV-NIR spectrophotometer, and X-ray diffraction (XRD) to study their optical and structural properties respectively. Their surface morphology and elemental composition were investigated via SEM and EDX spectrum respectively. The presence of functional groups in the compound was investigated by FTIR spectroscopy. Sensing characteristics of the above prepared ZnO films were measured towards detecting traces of toxic gases ammonia, ethanol, and acetone.

Spin-coated ZnO film was characterized and used to detect vapours of ammonia, acetone, ethanol, isopropanol, and methanol at room temperature. XRD analysis results showed its polycrystalline nature. The optical band gap was 3.202 ± 0.023 eV. EDX results confirmed the purity of the sample. SEM image revealed the grainy structure of ZnO film. The gas sensing measurement showed the highest response towards ammonia among the tested vapours. The values of gas response towards 400 and 20 ppm of ammonia were found to be 38.5 ± 0.6 and 6.1 ± 0.8 respectively. The corresponding response and recovery times were found to be 37 and 90 sec at 400 ppm of ammonia. Hence, the spin-coated ZnO film could be useful to construct a low-cost stable ammonia sensor that can detect efficiently the low concentrations of 20 ppm of ammonia vapour.

Similarly, in another set, ZnONPs film prepared by the doctor blade method was used to monitor the acetone. XRD analysis revealed its polycrystalline nature. The characteristic bands were confirmed by the FTIR spectrum. The gas sensing performance was measured in the temperature range from 100 to 300°C with the exposure of 800 ppm of acetone. The results showed the highest response of 25.697 ± 0.012 at a working temperature of 285 ± 7 °C. The corresponding response and recovery times were 39 and 79 sec respectively. This operating temperature was lower than the published values that were prepared by different methods. The results of sensing measurement with the exposure of various concentrations of acetone, 40 – 800 ppm, revealed the increasing response with increasing concentrations. The lowest and highest values of response were 3.500 ± 0.002 for 40 ppm and 25.697 ± 0.012 for 800 ppm of acetone.

Likewise, in the third set of experiments, Fe-ZnO and Fe-Al-ZnO prepared by spin coating and Sn-ZnO films by prepared by spray pyrolysis were used to monitor different

concentrations of ethanol. The XRD analysis of these films revealed the polycrystalline nature with decreasing crystallite size for increasing the doping concentrations. In Fe-ZnO films, the optical measurement show that the optical band gap increased for increasing Fe concentrations. SEM image clearly showed the grainy structure of ZnO film with decreasing grain sizes as the doping concentrations of Fe increased. EDX spectra confirmed the presence of elements zinc (Zn) and oxygen (O) only in the ZnO film and the presence of iron (Fe), zinc (Zn), and oxygen (O) only in the Fe-ZnO films. 2% Fe-ZnO film exhibited the highest and lowest response of 40.91 ± 0.23 and 22.94 ± 0.09 with an exposure of 400 and 40 ppm of ethanol respectively, at working temperature 260 ± 7 °C. The response and recovery times were 27 sec and 288 sec for 400 ppm of ethanol respectively. The optical analysis of $1-3$% Sn-ZnO films showed a decreased optical band gap for increasing Sn content. Captured SEM image clearly showed the grainy structures with increasing grain sizes on increasing Sn content. The EDX spectra illustrated the purity of ZnO layers. The gas sensing results showed a gas response of 17.659 ± 0.011 at 400 ppm exposure of ethanol for 2% Sn-ZnO film at an operating temperature of 220 ± 5 °C. This operating temperature was found to be a lower temperature than the reported value for similar sensors.

Additionally, Fe-Al-ZnO films were used to detect ethanol vapour of different concentrations. The optical measurement showed a decreased optical band gap value for Fe-Al-ZnO. SEM micro-graphs clearly illustrated the fine grains of ZnO. The sizes of these grains decreased after co-doping of $Fe-Al$ into ZnO. The gas sensing result showed that the Fe-Al doping improves the gas response of ZnO. 1%Fe 1%Al-ZnO showed the highest value of the response 152.304 ± 0.003 at 290 ± 7 °C for 400 ppm of ethanol which was nearly 2.5 times that of undoped ZnO. The results of gas sensing measurement towards ethanol showed that 1% Fe 1% Al-ZnO could detect 1 ppm of ethanol at 290 °C with the value of response of 1.626 ± 0.004.

The effect of gate electrode potential on the gas sensing properties of ZnO film prepared by spray pyrolysis technique was also investigated at room temperature for exposure of 400 ppm of ammonia vapours. Prior to this, prepared ZnO film was characterized using XRD and SEM. The XRD showed the preferential orientations along the (002) plane. The SEM image showed the nearly spherical grains. The gas sensing measurement revealed the enhancement in the gas response at the higher gate electrode potential. The value of response increased from 30.292 ± 0.042 to 54.581 ± 0.062 when the applied gate electrode potential increased from 0 to 24V. The result will be useful to construct a highly efficient room temperature gas sensor.

5.2 Recommendations

The selectivity of the MOS-based gas sensor is one of the great problems in the field of gas sensing technology which can be improved by adding the impurities like single or multiple metals, conducting polymers, etc. to the MOS nanostructures. Moreover, LPG is a highly inflammable gas used in domestic work. The leakages of this gas may cause abrupt accidents in the houses. Based on the reports available, the sensing performance of the MOS sensor towards LPG is low even at the high temperature (> 300 °C). The room temperature sensing performance of MOS-based sensors towards the LPG is rarely reported. Therefore, it will be a useful topic for researchers working in this field. Despite this, the following works can be suggested to be done in the future.

- To use different additives like one or two metals, conducting polymers, and nanocomposites to MOS-based sensor for increasing the sensitivity towards the targeted gas.
- To examine the selectivity of the prepared MOS sensor towards the mostly used toxic gases like ethanol, acetone, formaldehyde, acetaldehyde, isopropanol, CO, etc., at room temperature.
- To detect lower concentrations (below 0.5 ppm i.e. in the ppb level) of the toxic gases.

CHAPTER 6

6. SUMMARY

6.1 Summary

In this thesis work, the undoped, metal (Fe & Sn) and metal-metal (Fe – Al) co-doped ZnO films were prepared using effective and economic metal oxide semiconducting deposition methods such as spin coating, spray pyrolysis and doctor blade. These samples were optically and structurally characterized by UV-Vis spectrophotometer and X-ray diffraction analysis respectively. The surface morphology and elemental composition of these samples were investigated by SEM and EDX. The FTIR spectrum was utilized to study the presence of functional groups of ZnONPs. The sensing performance of these samples was studied towards widely used most common toxic vapours of ammonia, ethanol and acetone at various temperatures.

At first, ZnO film prepared by spin coating technique was used to monitor toxic vapours such as ammonia, ethanol, acetone, methane, and isopropanol at ambient temperature. The band gap of 3.202 ± 0.023 eV was determined from the Tauc plot. XRD and SEM analysis confirmed the polycrystalline nature and grainy surface of ZnO respectively. The gas sensing results show the selectivity of ZnO film towards ammonia vapour at room temperature. The result showed a low response <5 at the exposure of 400 ppm of ethanol, acetone, isopropanol, and methanol, but a high response of 38.5 ± 0.6 at the exposure of the same amount of ammonia. The sample showed good stability with the sensing capability better than those of the other similar works reported previously. The result of this work will be useful to develop a low-cost, effective MOS gas sensor for detecting low concentrations (20 ppm) of ammonia at room temperature.

The investigation on the acetone sensing capabilities of ZnONPs film produced by the doctor blade method showed a maximum response of 25.697 ± 0.012 at a working temperature of 285 ± 7 °C at an exposure of 800 ppm of acetone. This operating temperature was lower than that of a comparable system that was prepared using a different method. The response and recovery time were found to be 39 and 79 sec, respectively.

The investigation on the ethanol vapour sensing performance of ZnO and 1 – 4% Fe-ZnO films prepared by spin coating technique revealed the enhancement in response after Fe doping into ZnO. It was due to the surface modification after Fe doping. The result illustrated that Fe doping decreased the grain size and increased the specific surface area. And hence, Fe-ZnO films showed a high response. The 2% Fe-ZnO film showed a good response of 40.91 ± 0.23 with the exposure of 400 ppm of ethanol vapour at 260 ± 7

°C. 2% Fe doped ZnO can be utilized to detect below 40 ppm of ethanol vapours with a response value of 22.94 ± 0.09 which was better than the available published reports of a similar system but prepared by different methods.

The investigation on the ethanol detection capability of ZnO and Sn-doped ZnO films prepared by spray pyrolysis technique revealed decreased response after Sn doping into ZnO. 2% Sn-ZnO sample showed the highest response of 17.659 ± 0.011 at the lower operating temperature of 220 ± 5 °C and a wide range of detection of ethanol vapour at that temperature. It could measure as low as 0.5 ppm of ethanol vapour which was better than the available previous reports. It also showed a quick response time of 15 sec and a recovery time of 119 sec respectively.

The study on the ethanol sensing capability of Fe-Al-ZnO film prepared by spin coating technique showed a large enhancement in the gas response compared to undoped film. It is due to the surface modification after Fe and Al co-doping. The grain size became significantly smaller which increased the specific surface area after Fe-Al co-doping into ZnO. 1%Fe- 1% Al-ZnO showed the highest gas response of 152.304 ± 0.003 at a working temperature of 290 ± 7 °C at the exposure of 400 ppm of ethanol. The response time and recovery time were 33 and 201 sec respectively. The assembled sensor in this experiment was able to detect very low, 1 ppm ethanol with a response value of 1.626 ± 0.004.

Ultimately, the ammonia sensing measurement of the ZnO film prepared by the spray pyrolysis method showed the enhancement in the gas response when the positive potential was applied to the gate electrode in the study performed with ZnO film as a FET structure. Therefore, we conclude that a ZnO-based FET structure would be one of the useful techniques to fabricate the room temperature gas sensor with a large value of the response.

Among ZnO, Fe-ZnO, Sn-ZnO and Fe-Al-ZnO samples, Fe-Al-ZnO exhibited a better response for 400 ppm of ethanol vapour than others. It is because of a synergy effect of Fe and Al doping into ZnO which modifies the crystalline nature and then helps adsorb the additional oxygen ions and results in a high response.

REFERENCES

Acharya, A., Moghe, S., Panda, R., Shrivastava, S., Gangrade, M., Shripathi, T., ... Ganesan, V. (2012). Growth and characterization of nano-structured Sn doped ZnO. *Journal of molecular structure*, ***1022***, 8–15.

Ajili, M., Castagné, M., & Turki, N. K. (2013). Study on the doping effect of Sn-doped ZnO thin films. *Superlattices and Microstructures*, ***53***, 213–222.

Al-Hadeethi, Y., Umar, A., Ibrahim, A. A., Al-Heniti, S. H., Kumar, R., Baskoutas, S., & Raffah, B. M. (2017). Synthesis, characterization and acetone gas sensing applications of Ag-doped ZnO nanoneedles. *Ceramics International*, ***43***(9), 6765–6770.

Al-Hardan, N., Abdullah, M., & Aziz, A. A. (2013). Performance of Cr-doped ZnO for acetone sensing. *Applied surface science*, ***270***, 480–485.

Amoore, J. E., Johnston, J. W., & Rubin, M. (1964). The stereochemical theory of odor. *Scientific American*, ***210***(2), 42–49.

Anasthasiya, A. N. A., Ramya, S., Balamurugan, D., Rai, P., & Jeyaprakash, B. (2018). Adsorption property of volatile molecules on ZnO nanowires: computational and experimental approach. *Bulletin of Materials Science*, ***41***, 1–7.

Ansari, A. A., Kaushik, A., Solanki, P., & Malhotra, B. (2008). Sol–gel derived nanoporous cerium oxide film for application to cholesterol biosensor. *Electrochemistry Communications*, ***10***(9), 1246–1249.

Arnold, M. S., Avouris, P., Pan, Z. W., & Wang, Z. L. (2003). Field-effect transistors based on single semiconducting oxide nanobelts. *The Journal of Physical Chemistry B*, ***107***(3), 659–663.

Baik, J. M., & Lee, J.-L. (2005). Fabrication of vertically well-aligned (Zn, Mn) O nanorods with room temperature ferromagnetism. *Advanced Materials*, ***17***(22), 2745–2748.

Bartle, K. D., & Myers, P. (2002). History of gas chromatography. *TrAC Trends in Analytical Chemistry*, ***21***(9-10), 547–557.

Bhatia, S., Verma, N., & Bedi, R. (2017). Ethanol gas sensor based upon zno nanoparticles prepared by different techniques. *Results in physics*, ***7***, 801–806.

Blachowicz, T., & Ehrmann, A. (2020). Recent developments in electrospun ZnO nanofibers: A short review. *Journal of Engineered Fibers and Fabrics*, ***15***, 1558925019899682.

Bott, B., Jones, T., & Mann, B. (1984). The detection and measurement of CO using ZnO single crystals. *Sensors and Actuators*, ***5***(1), 65–73.

Bougrine, A., El Hichou, A., Addou, M., Ebothé, J., Kachouane, A., & Troyon, M. (2003). Structural, optical and cathodoluminescence characteristics of undoped and tin-doped ZnO thin films prepared by spray pyrolysis. *Materials Chemistry and Physics*, ***80***(2), 438–445.

Bube, R. H. (1992). *Photoelectronic properties of semiconductors*. Cambridge University Press.

Caglar, Y., Aksoy, S., Ilican, S., & Caglar, M. (2009). Crystalline structure and morphological properties of undoped and Sn doped ZnO thin films. *Superlattices and microstructures*, ***46***(3), 469–475.

Chahmat, N., Souier, T., Mokri, A., Bououdina, M., Aida, M., & Ghers, M. (2014). Structure, microstructure and optical properties of Sn-doped ZnO thin films. *Journal of alloys and compounds*, ***593***, 148–153.

Chen, N., Li, Y., Deng, D., Liu, X., Xing, X., Xiao, X., & Wang, Y. (2017). Acetone sensing performances based on nanoporous TiO_2 synthesized by a facile hydrothermal method. *Sensors and Actuators B: Chemical*, ***238***, 491–500.

Chevtchenko, S., Moore, J., Özgür, Ü., Gu, X., Baski, A., Morkoç, H., . . . Nause, J. (2006). Comparative study of the (0001) and (000 1^{-}) surfaces of ZnO. *Applied physics letters*, ***89***(18), 182111.

Choopun, S., Hongsith, N., Mangkorntong, P., & Mangkorntong, N. (2007). Zinc oxide nanobelts by RF sputtering for ethanol sensor. *Physica E: Low-dimensional Systems and Nanostructures*, ***39***(1), 53–56.

Chou, S. M., Teoh, L. G., Lai, W. H., Su, Y. H., & Hon, M. H. (2006). ZnO: Al thin film gas sensor for detection of ethanol vapor. *Sensors*, ***6***(10), 1420–1427.

Chu, X., Zhu, X., Dong, Y., Ge, X., Zhang, S., & Sun, W. (2012). Acetone sensors based on La^{3+} doped ZnO nano-rods prepared by solvothermal method. *Journal of Materials Science & Technology*, ***28***(3), 200–204.

Comini, E., Cristalli, A., Faglia, G., & Sberveglieri, G. (2000). Light enhanced gas sensing properties of indium oxide and tin dioxide sensors. *Sensors and Actuators B: Chemical*, ***65***(1-3), 260–263.

Cui, J., Shi, L., Xie, T., Wang, D., & Lin, Y. (2016). UV-light illumination room temperature HCHO gas-sensing mechanism of ZnO with different nanostructures. *Sensors and Actuators B: Chemical*, ***227***, 220–226.

de Brito Farias, T. M., & Watanabe, S. (2012). A comparative study of the thermoluminescence properties of several varieties of Brazilian natural quartz. *Journal of Luminescence*, ***132***(10), 2684–2692.

Dey, A. (2018). Semiconductor metal oxide gas sensors: A review. *Materials science and Engineering: B*, ***229***, 206–217.

Djurišić, A., Leung, Y., Tam, K., Hsu, Y., Ding, L., Ge, W., . . . others (2007). Defect emissions in ZnO nanostructures. *Nanotechnology*, ***18***(9), 095702.

Eftekhari, A., Molaei, F., & Arami, H. (2006). Flower-like bundles of ZnO nanosheets as an intermediate between hollow nanosphere and nanoparticles. *Materials Science and Engineering: A*, ***437***(2), 446–450.

Ferblantier, G., Mailly, F., Al Asmar, R., Foucaran, A., & Pascal-Delannoy, F. (2005). Deposition of zinc oxide thin films for application in bulk acoustic wave resonator. *Sensors and Actuators A: Physical*, ***122***(2), 184–188.

Ferraro, J. R., & Basile, L. J. (2012). *Fourier transform infrared spectra: applications to chemical systems*. Academic press.

Ge, C., Xie, C., & Cai, S. (2007). Preparation and gas-sensing properties of Ce-doped ZnO thin-film sensors by dip-coating. *Materials Science and Engineering: B*, ***137***(1-3), 53–58.

Goel, S., Wu, Z., Zones, S. I., & Iglesia, E. (2012). Synthesis and catalytic properties of metal clusters encapsulated within small-pore (SOD, GIS, ANA) zeolites. *Journal of the American Chemical Society*, ***134***(42), 17688–17695.

Goh, E., Xu, X., & McCormick, P. (2014). Effect of particle size on the UV absorbance of zinc oxide nanoparticles. *Scripta Materialia*, ***78***, 49–52.

Goktas, A., Aslan, F., Yeşilata, B., & Boz, İ. (2018). Physical properties of solution processable n-type Fe and Al co-doped ZnO nanostructured thin films: role of Al doping levels and annealing. *Materials Science in Semiconductor Processing*, ***75***, 221–233.

Goudarzi, S., & Khojier, K. (2018). On the dependence of structural and ammonia gas sensing properties of ZnO thin films on Mg doping. In *AIP Conference Proceedings* (Vol. **1920**, p. 020049).

Gupta, T. K., & Carlson, W. G. (1985). A grain-boundary defect model for instability/stability of a ZnO varistor. *Journal of materials science*, ***20***, 3487–3500.

Hamedani, N. F., Mahjoub, A. R., Khodadadi, A. A., & Mortazavi, Y. (2011). Microwave assisted fast synthesis of various ZnO morphologies for selective detection of CO, CH_4 and ethanol. *Sensors and Actuators B: Chemical*, ***156***(2), 737–742.

Hamuyuni, J., Daramola, M. O., & Oluwasina, O. O. (2016). Energy-Dispersive X-Ray Spectroscopy: Theory and Application in Engineering and Science. *Encyclopedia of Physical Organic Chemistry*, 1–23.

Hasnidawani, J., Azlina, H., Norita, H., Bonnia, N., Ratim, S., & Ali, E. (2016). Synthesis of ZnO nanostructures using sol-gel method. *Procedia Chemistry*, ***19***, 211–216.

Hassan, M. M., Khan, W., Naqvi, A., Mishra, P., & Islam, S. (2014). Fe dopants enhancing ethanol sensitivity of ZnO thin film deposited by RF magnetron sputtering. *Journal of Materials Science*, ***49***, 6248–6256.

Hjiri, M., El Mir, L., Leonardi, S., Pistone, A., Mavilia, L., & Neri, G. (2014). Al-doped ZnO for highly sensitive CO gas sensors. *Sensors and Actuators B: Chemical*, ***196***, 413–420.

Hoffmann, P., & Knözinger, E. (1987). Dynamic range problems in Fourier transform IR and far-IR spectroscopy. *Applied spectroscopy*, ***41***(8), 1303–1306.

Hongsith, N., Wongrat, E., Kerdcharoen, T., & Choopun, S. (2010). Sensor response formula for sensor based on ZnO nanostructures. *Sensors and Actuators B: Chemical*, ***144***(1), 67–72.

Horlick, G., & Yuen, W. (1978). A Modular Michelson Interferometer for Fourier Transform Spectrochemical Measurements from the Mid-infrared to the Ultraviolet. *Applied Spectroscopy*, ***32***(1), 38–46.

Hosseini, Z., Mortezaali, A., et al. (2015). Room temperature H_2S gas sensor based on rather aligned ZnO nanorods with flower-like structures. *Sensors and Actuators B: Chemical*, ***207***, 865–871.

Hsu, C.-L., Gao, Y.-D., Chen, Y.-S., & Hsueh, T.-J. (2014). Vertical Ti doped ZnO nanorods based on ethanol gas sensor prepared on glass by furnace system with hotwire assistance. *Sensors and Actuators B: Chemical*, ***192***, 550–557.

Jaballah, S., Alaskar, Y., AlShunaifi, I., Ghiloufi, I., Neri, G., Bouzidi, C., . . . El Mir, L. (2021). Effect of Al and Mg doping on reducing gases detection of ZnO nanoparticles. *Chemosensors*, ***9***(11), 300.

Jha, R. K., Wan, M., Jacob, C., & Guha, P. K. (2018). Enhanced gas sensing properties of liquid-processed semiconducting tungsten chalcogenide (WX i, x= O and S) based hybrid nanomaterials. *IEEE Sensors Journal*, ***18***(9), 3494–3501.

Joshi, L. P., Khatri, B. V., Gyawali, S., Gajurel, S., & Chaudhary, D. K. (2021). Green Synthesis of Zinc Oxide Nanoparticles Using Ixora Coccinea Leaf Extract for Ethanol Vapour Sensing. *Journal of Physical Science*, ***32***(2), 15–26.

Kaneti, Y. V., Yue, J., Jiang, X., & Yu, A. (2013). Controllable synthesis of ZnO nanoflakes with exposed (1010) for enhanced gas sensing performance. *The Journal of Physical Chemistry C*, ***117***(25), 13153–13162.

Kashyout, A., Soliman, H., Hassan, H. S., & Abousehly, A. (2010). Fabrication of ZnO and ZnO: Sb nanoparticles for gas sensor applications. *Journal of Nanomaterials*, ***2010***, 1–8.

Kaur, G., Mitra, A., & Yadav, K. (2015). Pulsed laser deposited Al-doped ZnO thin films for optical applications. *Progress in Natural Science: Materials International*, ***25***(1), 12–21.

Khalid, N., Hammad, A., Tahir, M., Rafique, M., Iqbal, T., Nabi, G., & Hussain, M. (2019). Enhanced photocatalytic activity of Al and Fe co-doped ZnO nanorods for methylene blue degradation. *Ceramics International*, ***45***(17), 21430–21435.

Khayatian, A., Kashi, M. A., Azimirad, R., & Safa, S. (2014). Enhanced gas-sensing properties of ZnO nanorods encapsulated in an Fe-doped ZnO shell. *Journal of Physics D: Applied Physics*, ***47***(7), 075003.

Khayatian, A., Safa, S., Azimirad, R., Kashi, M. A., & Akhtarianfar, S. (2016). The effect of fe-dopant concentration on ethanol gas sensing properties of fe doped ZnO/ZnO shell/core nanorods. *Physica E: Low-dimensional Systems and Nanostructures*, ***84***, 71–78.

Kittel, C. (1996). Introduction to solid state physics.(7^{th} edn), john willey and sons inc. *New York*, 308.

Klingshirn, C. (2007). ZnO: material, physics and applications. *ChemPhysChem*, ***8***(6), 782–803.

Koenig, J. L. (1981). Fourier transform infrared spectroscopy of chemical systems. *Accounts of Chemical Research*, ***14***(6), 171–178.

Koirala, M. P., & Joshi, L. P. (2017). Structural and optical properties of fluorine doped tin oxide thin film deposited by home built spray pyrolysis unit. *Himalayan Physics*, ***6***, 58–60.

Kwon, C. H., Hong, H.-K., Yun, D. H., Lee, K., Kim, S.-T., Roh, Y.-H., & Lee, B.-H. (1995). Thick-film zinc-oxide gas sensor for the control of lean air-to-fuel ratio in domestic combustion systems. *Sensors and Actuators B: Chemical*, ***25***(1-3), 610–613.

Lampe, U., & Müller, J. (1989). Thin-film oxygen sensors made of reactively sputtered ZnO. *Sensors and Actuators*, ***18***(3-4), 269–284.

Lany, S., & Zunger, A. (2005). Anion vacancies as a source of persistent photoconductivity in II-VI and chalcopyrite semiconductors. *Physical Review B*, ***72***(3), 035215.

Lau, W., & Fonash, S. (1987). Highly transparent and conducting zinc oxide films deposited by activated reactive evaporation. *Journal of electronic materials*, ***16***, 141–149.

Lee, C., Lee, T., Lyu, S., Zhang, Y., Ruh, H., & Lee, H. (2002). Field emission from well-aligned zinc oxide nanowires grown at low temperature. *Applied Physics Letters*, ***81***(19), 3648–3650.

Li, X., Yan, Y., Gessert, T., Perkins, C., Young, D., DeHart, C., . . . Coutts, T. (2003). Chemical vapor deposition-formed p-type ZnO thin films. *Journal of Vacuum Science & Technology A: Vacuum, Surfaces, and Films*, ***21***(4), 1342–1346.

Liewhiran, C., & Phanichphant, S. (2007). Influence of thickness on ethanol sensing characteristics of doctor-bladed thick film from flame-made ZnO nanoparticles. *Sensors*, ***7***(2), 185–201.

Liu, X., Pan, K., Li, W., Hu, D., Liu, S., & Wang, Y. (2014). Optical and gas sensing properties of Al-doped ZnO transparent conducting films prepared by sol–gel method under different heat treatments. *Ceramics International*, ***40***(7), 9931–9939.

Lokesh, K., Kavitha, G., Manikandan, E., Mani, G. K., Kaviyarasu, K., Rayappan, J. B. B., . . . Maaza, M. (2016). Effective ammonia detection using n-ZnO/p-NiO heterostructured nanofibers. *IEEE Sensors Journal*, ***16***(8), 2477–2483.

Lovelock, J. E. (1958). A sensitive detector for gas chromatography. *Journal of Chromatography A*, ***1***, 35–46.

Mahajan, S. V., Upadhye, D. S., Shaikh, S. U., Birajadar, R. B., Siddiqui, F. Y., Ghule, A. V., & Sharma, R. (2013). Mn doped nanostucture ZnO thin film for photo sensor and gas sensor application. In *AIP Conference Proceedings* (Vol. **1512**, pp. 652–653).

Mani, G. K., & Rayappan, J. B. B. (2013). A highly selective room temperature ammonia sensor using spray deposited zinc oxide thin film. *Sensors and actuators B: Chemical*, ***183***, 459–466.

Mani, G. K., & Rayappan, J. B. B. (2014). Selective detection of ammonia using spray pyrolysis deposited pure and nickel doped ZnO thin films. *Applied surface science*, ***311***, 405–412.

Mani, G. K., & Rayappan, J. B. B. (2015). A highly selective and wide range ammonia sensor—Nanostructured ZnO: Co thin film. *Materials Science and Engineering: B*, ***191***, 41–50.

Mani, G. K., & Rayappan, J. B. B. (2016). ZnO nanoarchitectures: Ultrahigh sensitive room temperature acetaldehyde sensor. *Sensors and Actuators B: Chemical*, ***223***, 343–351.

Marouf, S., Beniaiche, A., Guessas, H., & Azizi, A. (2016). Morphological, structural and optical properties of ZnO thin films deposited by dip coating method. *Materials Research*, ***20***, 88–95.

Michelson, A. A. (1891). Visibility of Interference-Fringes in the Focus of a Telescope. *Publications of the Astronomical Society of the Pacific*, ***3***(16), 217–220.

Miki-Yoshida, M., Morales, J., Solis, J., et al. (2000). Influence of Al, In, Cu, Fe and Sn dopants on the response of thin film ZnO gas sensor to ethanol vapour. *Thin Solid Films*, ***373***(1-2), 137–140.

Mitra, P., Chatterjee, A. P., & Maiti, H. S. (1998). Zno thin film sensor. *Materials Letters*, ***35***(1-2), 33–38.

Mitra, P., & Mukhopadhyay, A. K. (2007). ZnO thin film as methane sensor. *Bulletin of the Polish Academy of Sciences: Technical Sciences*, ***55***(3), 281–285.

Mostafa, A. M., & Mwafy, E. A. (2020). Synthesis of ZnO and Au@ ZnO core/shell nano-catalysts by pulsed laser ablation in different liquid media. *Journal of Materials Research and Technology*, ***9***(3), 3241–3248.

Mridha, S., & Basak, D. (2007). Aluminium doped ZnO films: electrical, optical and photoresponse studies. *Journal of Physics D: Applied Physics*, ***40***(22), 6902.

Mun, Y., Park, S., An, S., Lee, C., & Kim, H. W. (2013). NO_2 gas sensing properties of Au-functionalized porous ZnO nanosheets enhanced by UV irradiation. *Ceramics International*, ***39***(8), 8615–8622.

Nakahara, K. N. K., Tanabe, T. T. T., Takasu, H. T. H., Fons, P. F. P., Iwata, K. I. K., Yamada, A. Y. A., ... Niki, S. N. S. (2001). Growth of undoped ZnO films

with improved electrical properties by radical source molecular beam epitaxy. *Japanese Journal of Applied Physics*, ***40***(1R), 250.

Nanto, H., Minami, T., & Takata, S. (1986). Zinc-oxide thin-film ammonia gas sensors with high sensitivity and excellent selectivity. *Journal of Applied Physics*, ***60***(2), 482–484.

Özgür, Ü., Alivov, Y. I., Liu, C., Teke, A., Reshchikov, M., Doğan, S., ... H (2005). A comprehensive review of ZnO materials and devices. *Journal of applied physics*, ***98***(4), 11.

Poloju, M., Jayababu, N., & Reddy, M. R. (2018). Improved gas sensing performance of Al doped ZnO/CuO nanocomposite based ammonia gas sensor. *Materials Science and Engineering: B*, ***227***, 61–67.

Prajapati, C., & Sahay, P. (2013). Influence of In doping on the structural, optical and acetone sensing properties of ZnO nanoparticulate thin films. *Materials science in semiconductor processing*, ***16***(1), 200–210.

Pramod, N., & Pandey, S. (2014). Influence of Sb doping on the structural, optical, electrical and acetone sensing properties of In_2O_3 thin films. *Ceramics International*, ***40***(2), 3461–3468.

Qi, Q., Zhang, T., Liu, L., Zheng, X., Yu, Q., Zeng, Y., & Yang, H. (2008). Selective acetone sensor based on dumbbell-like ZnO with rapid response and recovery. *Sensors and Actuators B: Chemical*, ***134***(1), 166–170.

Qiang, Z., Ma, S., Jiao, H., Jin, W., Wang, T., Jiang, X., & Zhang, Z. (2016). Solvothermal synthesis of 3D leaf-like $\alpha - Fe_2O_3$ and its gas-sensing properties research. *Materials Letters*, ***181***, 29–33.

Radhakrishnan, J., Kumara, M., et al. (2021). Effect of temperature modulation, on the gas sensing characteristics of ZnO nanostructures, for gases O_2, CO and CO_2. *Sensors International*, ***2***, 100059.

Rai, H., Kondal, N., et al. (2022). A review on defect related emissions in undoped ZnO nanostructures. *Materials Today: Proceedings*, ***48***, 1320–1324.

Rambu, A., Nica, V., & Dobromir, M. (2013). Influence of Fe-doping on the optical and electrical properties of ZnO films. *Superlattices and Microstructures*, ***59***, 87–96.

Rayleigh, L. (1892). XLVII. On the interference bands of approximately homogeneous light; in a letter to Prof. A. Michelson. *The London, Edinburgh, and Dublin Philosophical Magazine and Journal of Science*, ***34***(210), 407–411.

Roopa Kishore, K., Balamurugan, D., & Jeyaprakash, B. (2021). CuO nanograins: synthesis and acetone vapour detection. *Journal of Materials Science: Materials in Electronics*, ***32***, 1204–1220.

Sahoo, B., Sankaran, K., Sakthivel, R., Pradhan, S. K., & Behera, D. (2020). Effect of Fe-In co-doping on microstructural, optical, electrical and LPG response properties of spray pyrolytic ZnO thin films. *Superlattices and Microstructures*, ***146***, 106666.

Saito, S., Miyayama, M., Koumoto, K., & Yanagida, H. (1985). Gas sensing characteristics of porous ZnO and Pt/ZnO ceramics. *Journal of the American Ceramic Society*, ***68***(1), 40–43.

Santhaveesuk, T., & Choopun, S. (2013). Ethanol sensing characteristics of Sn-doped ZnO tetrapods sensor. In *Advanced materials research* (Vol. **770**, pp. 185–188).

Santhaveesuk, T., Wongratanaphisan, D., & Choopun, S. (2010). Enhancement of sensor response by TiO_2 mixing and Au coating on ZnO tetrapod sensor. *Sensors and Actuators B: Chemical*, ***147***(2), 502–507.

Saravanavel, G., Honnali, S. K., Lourdes, K. S., John, S., & Gunasekhar, K. (2021). Study on the thermoelectric properties of Al-ZnO thin-film stack fabricated by physical vapour deposition process for temperature sensing. *Sensors and Actuators A: Physical*, ***332***, 113097.

Sawalha, A., Abu-Abdeen, M., & Sedky, A. (2009). Electrical conductivity study in pure and doped ZnO ceramic system. *Physica B: Condensed Matter*, ***404***(8-11), 1316–1320.

Saydi, J., Karimi, M., Mazhdi, M., Seidi, J., & Mazhdi, F. (2014). Synthesis, Characterization, and Gas Sensing Properties of Pure and Mn-doped ZnO Nanocrystalline Particles. *Journal of materials engineering and performance*, ***23***, 3489–3496.

Sberveglieri, G., Nelli, P., Groppelli, S., Quaranta, F., Valentini, A., & Vasanelli, L. (1990). Oxygen gas sensing characteristics at ambient pressure of undoped and lithium-doped ZnO-sputtered thin films. *Materials Science and Engineering: B*, ***7***(1-2), 63–68.

Schmidt-Mende, L., & MacManus-Driscoll, J. L. (2007). ZnO–nanostructures, defects, and devices. *Materials today*, ***10***(5), 40–48.

Seiyama, T., & Kagawa, S. (1966). Study on a Detector for Gaseous Components Using Semiconductive Thin Films. *Analytical chemistry*, ***38***(8), 1069–1073.

Seiyama, T., Kato, A., Fujiishi, K., & Nagatani, M. (1962). A new detector for gaseous components using semiconductive thin films. *Analytical Chemistry*, ***34***(11), 1502–1503.

Shakti, N., & Gupta, P. (2010). Structural and optical properties of sol-gel prepared ZnO thin film. *Applied Physics Research*, ***2***(1), 19.

Shao, F., Fan, J., Hernández-Ramírez, F., Fábrega, C., Andreu, T., Cabot, A., ... others (2016). NH_3 sensing with self-assembled ZnO-nanowire μHP sensors in isothermal and temperature-pulsed mode. *Sensors and Actuators B: Chemical*, ***226***, 110–117.

Shinde, V., Lokhande, C., Mane, R., & Han, S.-H. (2005). Hydrophobic and textured ZnO films deposited by chemical bath deposition: annealing effect. *Applied Surface Science*, ***245***(1-4), 407–413.

Shrestha, S. P., Ghimire, R., Nakarmi, J. J., Kim, Y.-S., Shrestha, S., Park, C.-Y., & Boo, J.-H. (2010). Properties of ZnO: Al films prepared by spin coating of aged precursor solution. *Bulletin of the Korean Chemical Society*, ***31***(1), 112–115.

Srinivasulu, T., Saritha, K., & Reddy, K. R. (2017). Synthesis and characterization of Fe-doped ZnO thin films deposited by chemical spray pyrolysis. *Modern Electronic Materials*, ***3***(2), 76–85.

Sun, H., Chen, S.-C., Wang, C.-H., Lin, Y.-W., Wen, C.-K., Chuang, T.-H., ... Dai, M.-J. (2019). Electrical and magnetic properties of (Al, Co) co-doped ZnO films deposited by RF magnetron sputtering. *Surface and Coatings Technology*, ***359***, 390–395.

Takao, Y., Miyazaki, K., Shimizu, Y., & Egashira, M. (1994). High ammonia sensitive semiconductor gas sensors with double-layer structure and interface electrodes. *Journal of the Electrochemical Society*, ***141***(4), 1028.

Tampo, H., Yamada, A., Fons, P., Shibata, H., Matsubara, K., Iwata, K., ... Takasu, H. (2004). Degenerate layers in epitaxial ZnO films grown on sapphire substrates. *Applied Physics Letters*, ***84***(22), 4412–4414.

Tsay, C.-Y., Cheng, H.-C., Tung, Y.-T., Tuan, W.-H., & Lin, C.-K. (2008). Effect of Sn-doped on microstructural and optical properties of ZnO thin films deposited by sol–gel method. *Thin Solid Films*, ***517***(3), 1032–1036.

Vasudevan, J., Jeyakumar, S. J., Arunkumar, B., Jothibas, M., Muthuvel, A., & Vijayalakshmi, S. (2022). Optical and magnetic investigation of cu doped ZnO nanoparticles synthesized by solid state method. *Materials Today: Proceedings*, ***48***, 438–442.

Vijayakumar, Y., Nagaraju, P., Yaragani, V., Parne, S. R., Awwad, N. S., & Reddy, M. R. (2020). Nanostructured Al and Fe co-doped ZnO thin films for enhanced ammonia detection. *Physica B: Condensed Matter*, ***581***, 411976.

Wagner, C. (1950). The mechanism of the decomposition of nitrous oxide on zinc oxide as catalyst. *The Journal of Chemical Physics*, ***18***(1), 69–71.

Wahyuono, R. A., Schmidt, C., Dellith, A., Dellith, J., Schulz, M., Seyring, M., ... Dietzek, B. (2016). ZnO nanoflowers-based photoanodes: aqueous chemical synthesis, microstructure and optical properties. *Open Chemistry*, ***14***(1), 158–169.

Walker, J. M., Akbar, S. A., & Morris, P. A. (2019). Synergistic effects in gas sensing semiconducting oxide nano-heterostructures: A review. *Sensors and Actuators B: Chemical*, ***286***, 624–640.

Wan, Q., Li, Q., Chen, Y., Wang, T.-H., He, X., Li, J., & Lin, C. (2004). Fabrication and ethanol sensing characteristics of ZnO nanowire gas sensors. *Applied physics letters*, ***84***(18), 3654–3656.

Wang, L., Teleki, A., Pratsinis, S. E., & Gouma, P. (2008). Ferroelectric WO_3 nanoparticles for acetone selective detection. *Chemistry of Materials*, ***20***(15), 4794–4796.

Wang, Z. L. (2009). ZnO nanowire and nanobelt platform for nanotechnology. *Materials Science and Engineering: R: Reports*, ***64***(3-4), 33–71.

Wei, A., Pan, L., & Huang, W. (2011). Recent progress in the ZnO nanostructure-based sensors. *Materials Science and Engineering: B*, ***176***(18), 1409–1421.

Wei, A., Wang, Z., Pan, L., Li, W.-W., Xiong, L., Dong, X.-C., & Huang, W. (2011). Room-temperature NH_3 gas sensor based on hydrothermally grown ZnO nanorods. *Chinese Physics Letters*, ***28***(8), 080702.

Wisz, G., Virt, I., Sagan, P., Potera, P., & Yavorskyi, R. (2017). Structural, optical and electrical properties of zinc oxide layers produced by pulsed laser deposition method. *Nanoscale Research Letters*, ***12***(1), 1–7.

Wongrat, E., Chanlek, N., Chueaiarrom, C., Thupthimchun, W., Samransuksamer, B., & Choopun, S. (2017). Acetone gas sensors based on ZnO nanostructures decorated with Pt and Nb. *Ceramics International*, ***43***, S557–S566.

Xiao, Y., Lu, L., Zhang, A., Zhang, Y., Sun, L., Huo, L., & Li, F. (2012). Highly enhanced acetone sensing performances of porous and single crystalline ZnO nanosheets: high percentage of exposed (100) facets working together with

surface modification with Pd nanoparticles. *ACS applied materials & interfaces*, ***4***(8), 3797–3804.

Xiong, Z., Chen, L., He, C., & Liang, Z. (2011). Ab initio studies of the Sn-doped ZnO transparent conductive oxide. In *Journal of physics: Conference series* (Vol. **276**, p. 012194).

Xu, C., Sun, X., Zhang, X., Ke, L., & Chua, S. (2004). Photoluminescent properties of copper-doped zinc oxide nanowires. *Nanotechnology*, ***15***(7), 856.

Xu, L., & Li, X. (2010). Influence of Fe-doping on the structural and optical properties of ZnO thin films prepared by sol–gel method. *Journal of Crystal Growth*, ***312***(6), 851–855.

Xu, S., & Wang, Z. L. (2011). One-dimensional ZnO nanostructures: solution growth and functional properties. *Nano research*, ***4***, 1013–1098.

Xu, X., Chen, Y., Ma, S., Li, W., & Mao, Y. (2015). Excellent acetone sensor of La-doped ZnO nanofibers with unique bead-like structures. *Sensors and Actuators B: Chemical*, ***213***, 222–233.

Yang, C., Su, X., Xiao, F., Jian, J., & Wang, J. (2011). Gas sensing properties of CuO nanorods synthesized by a microwave-assisted hydrothermal method. *Sensors and Actuators B: Chemical*, ***158***(1), 299–303.

Yang, Z., Huang, Y., Chen, G., Guo, Z., Cheng, S., & Huang, S. (2009). Ethanol gas sensor based on Al-doped ZnO nanomaterial with many gas diffusing channels. *Sensors and Actuators B: Chemical*, ***140***(2), 549–556.

Yi, G.-C., Wang, C., & Park, W. I. (2005). ZnO nanorods: synthesis, characterization and applications. *Semiconductor science and technology*, ***20***(4), S22.

Young, R. A., & Kalin, R. V. (1986). Scanning electron microscopic techniques for characterization of semiconductor materials. ACS Publications.

Yu, A., Qian, J., Pan, H., Cui, Y., Xu, M., Tu, L., ... Zhou, X. (2011). Micro-lotus constructed by Fe-doped ZnO hierarchically porous nanosheets: preparation, characterization and gas sensing property. *Sensors and Actuators B: Chemical*, ***158***(1), 9–16.

Yung, K. C., Liem, H., & Choy, H. (2009). Enhanced redshift of the optical band gap in Sn-doped ZnO free standing films using the sol–gel method. *Journal of Physics D: Applied Physics*, ***42***(18), 185002.

Zhang, H., Zhu, L., Cheng, J., Chen, L., Liu, C., & Yuan, S. (2019). Photoluminescence characteristics of Sn^{2+} and Ce^{3+}-doped Cs_2SnCl_6 double-perovskite crystals. *Materials*, ***12***(9), 1501.

Zhang, W.-H., Zhang, W.-D., & Zhou, J.-F. (2010). Solvent thermal synthesis and gas-sensing properties of Fe-doped ZnO. *Journal of materials science*, ***45***, 209–215.

Zhang, Y., Ram, M. K., Stefanakos, E. K., & Goswami, D. Y. (2012). Synthesis, characterization, and applications of ZnO nanowires. *Journal of Nanomaterials*, ***2012***, 1–22.

Zhang, Y., Wu, L., Li, H., Xu, J., Han, L., Wang, B., . . . Xie, E. (2009). Influence of Fe doping on the optical property of ZnO films. *Journal of alloys and compounds*, ***473***(1-2), 319–322.

Zhang, Y.-H., Liu, C.-Y., Jiu, B.-B., Liu, Y., & Gong, F.-L. (2018). Facile synthesis of Pd-decorated ZnO nanoparticles for acetone sensors with enhanced performance. *Research on Chemical Intermediates*, ***44***, 1569–1578.

Zhao, M., Wang, X., Cheng, J., Zhang, L., Jia, J., & Li, X. (2013). Synthesis and ethanol sensing properties of Al-doped ZnO nanofibers. *Current Applied Physics*, ***13***(2), 403–407.

Zhu, G., Li, Y., Zhou, H., Liu, J., & Yang, W. (2008). FAU-type zeolite membranes synthesized by microwave-assisted in situ crystallization. *Materials Letters*, ***62***(28), 4357–4359.

Zhu, L., Li, Y., & Zeng, W. (2017). Enhanced ethanol sensing and mechanism of Cr-doped ZnO nanorods: Experimental and computational study. *Ceramics International*, ***43***(17), 14873–14879.

Zhu, L., & Zeng, W. (2017). Room-temperature gas sensing of ZnO-based gas sensor: A review. *Sensors and Actuators A: Physical*, ***267***, 242–261.

APPENDIX

Academic Activities

A. Attended courses offered by IoST

In the first semester:

PHS 911, Philosophy of Science (Cr. Hrs. 3)

PHS 912, Research Methodology (Cr. Hrs. 3)

PHS 913, Seminar (Cr. Hrs. 3)

In the second semester:

PHS 951, Advanced Research Methodology (Cr. Hrs. 3)

PHS 952, Seminar (Cr. Hrs. 3)

PHS 956, Advanced Solid State Physics (Cr. Hrs. 3)

B. Paper publications

International

1) Chaudhary, D. K., Ghimire, R., Amatya, S. P., Shrestha, S. P., & Joshi, L. P. (2020, December). Study on influence of Fe doping into ZnO film for ethanol sensing. *Journal of Physics: Conference Series*, **1706**: 012036). IOP Publishing. https://iopscience.iop.org/article/10.1088/1742-6596/1706/1/012036/pdf

2) Chaudhary, D. K., Maharjan, Y. S., Shrestha, S., Maharjan, S., Shrestha, S. P., & Joshi, L. P. (2022). Sensing Performance of a ZnO-based Ammonia Sensor. *Journal of Physical Science*, **33**(1): 97-108. https://doi.org/10.21315/jps2022.33.1.7

3) Joshi, L. P., Khatri, B. V., Gyawali, S., Gajurel, S., & Chaudhary, D. K. (2021). Green Synthesis of Zinc Oxide Nanoparticles Using Ixora Coccinea Leaf Extract for Ethanol Vapour Sensing. *Journal of Physical Science*, **32**(2): 15-26. https://doi.org/10.21315/jps2021.32.2.2

4) Acharya, T. R., Lamichhane, P., Wahab, R., Chaudhary, D. K., Shrestha, B., Joshi, L. P., ... & Choi, E. H. (2021). Study on the Synthesis of ZnO Nanoparticles Using Azadirachta indica Extracts for the Fabrication of a Gas Sensor. *Molecules*, **26**(24): 7685. https://doi.org/10.3390/molecules26247685

C. Publications in national Journals

1) Chaudhary, D. K., Maharjan, Y. S., Amatya, S. P., Shrestha, S. P., Parajuli, R., Shrestha, P., & Joshi, L. P. (2022). Sensing Characteristics of ZnO Nanoparticle

Film towards Acetone. *Journal of Institute of Science and Technology*, **27**(1): 135-140. https://doi.org/10.3126/jist.v27i1.40866

D. Participation

International Conferences

1) Poster presentation entitled "**Influence of Fe doping into ZnO thin film for detection of ethanol vapor**" in the International Meeting on Energy Storage Devices and Academia conclaves (IMESD-2018), held at Department of Physics, Indian Institute of Technology (IIT) Roorkee, Uttarakhand, December 18-20, 2018.

2) Oral presentation entitled "**Study on influence of Fe doping into ZnO film for ethanol sensing**" in First International Conference on Advances in Physical Sciences and Materials (ICAPSM-2020), 13-14, August, 2020, Coimbatore, India.

3) Oral presentation entitled "**Effect of Atmospheric Dielectric Barrier Discharge on Optical, Electrical and Surface Properties of ZnO Film**" in First International Conference on Modern Materials for Engineering and Research (ICMMER-2022), 29-30, September, 2022, Tiruchengoda, Tamilnadu, India.

4) Participated in "**International Symposium on History and Future of Transistors**" organized by The National Academy of Sciences India-Delhi Chapter, Deen Dayal Upadhyay College (University of Delhi) under the aegis of DBT Star College Program, IEEE Electron Device Society (EDS) Delhi Chapter, India, December 30, 2021.

5) Delivered a talk entitled "**Impact of Fe & Sn into ZnO for ethanol sensing**" as an invited speaker in "Sensors Research eConference 2022 (Sensors-eCon2022)" November 21, 2022(London)- November 22, 2022 (Tokyo) Online, organized by The Research Catalyst.
   Organizing Committee:

   (i) Marshal Porterfield Purdue University, USA

   (ii) Jiangguo Jack Wang university of Technology Sydney, Australia

   (iii) Hsiao-Chun Wu Louisiana State University, USA

6) Participated in "**International Energy 2021-Conference On Renewable Energy and Digital Technologies for Development of Africa**" organized by Ministry of Scientific Research and Innovation, Yaoundé, Cameroon during 18-20 November, 2021. This program was supported by International Science Program (ISP), Uppsala University, Sweden.

National Conferences

7) Participated in the "**Training Workshop on Scientific Writing**" program organized by RECAST, Tribhuvan University Kathmandu Nepal, during June 21-25, 2018.

8) Poster presentation entitled "**Optical and Surface Characterization of Thin Films of Semiconductors Tin Sulphide and Zinc Oxide**" in International conference on exploration in Physics (ICEP-2018), 29-31 May, 2018 Kathmandu, Nepal.

9) Poster presentation entitled "**Fe Doped ZnO Thin Film for Ethanol Vapour Detection**" in 4th International Conference Kathmandu Symposia on Advanced Materials (KaSAM-2018) held in Kathmandu, Nepal during October 26 -29, 2018.

10) Oral presentation entitled "**Study of Structural and Optical Properties of Fe Doped ZnO Thin Films Prepared by Spin Coating Method**" in International Conference on Nano-Science and High Energy Physics (ICNHEP-2019), Feb 4-6, 2019, Central Department of Physics, Tribhuvan University, Kathmandu, Nepal.

11) Oral presentation entitled "**Study on Preparation and Properties of Fe doped ZnO as a Vapour Sensor** " in The 8th Asian Conference on Colloid & Interface Science (ACCIS-2019), Sept. 24-27, 2019, Pulchowk Campus, Institute of Engineering, Tribhuvan University, Lalitpur, Kathmandu, Nepal.
At this conference, I was awarded **second best presenter award by Royal Society of Chemistry Books**.

12) Oral presentation entitled "**Study on Ethanol Vapour Sensing Performance of ZnO Prepared by different methods**" in International Conference on Material Science and Characterization Technology (ICMSCT-2021), September 26-28, 2021, organized by Department of Physics, St. Xavier's College, Kathmandu, Nepal.

13) Oral presentation entitled "**Gas Sensing Characteristics of ZnO Film**" in International Conference on Frontiers of Physics (ICFP- 2022, 22-24 Jan, 2022, Kathmandu, Nepal, organized by Nepal Physical Society, Nepal.

14) Oral presentation entitled "**Fe-Al doped ZnO film: A Highly Sensitive Ethanol Sensing**" in "National Conference on Recent Trends in Science, Technology and Innovation (RTSTI-2022), 29-30, May, 2022, Pokhara, Nepal.

15) Oral presentation entitled "**Deposition of Sn-doped ZnO for ethanol sensing**" in "National Conference on Advances in Atmospheric & Material Science, 6-7 November 2022, Amrit Campus, Tribhuvan University, Lainchour, Kathmandu.

Journal of Physical Science, Vol. 33(1), 97–108, 2022

Sensing Performance of a ZnO-based Ammonia Sensor

Dinesh Kumar Chaudhary[1,2], Yogesh Singh Maharjan[1], Sanju Shrestha[2], Surendra Maharjan[3], Shankar Prasad Shrestha[4] and Leela Pradhan Joshi[1*]

[1]Department of Physics, Amrit Campus, Tribhuvan University, Kathmandu 44600, Nepal
[2]Central Department of Physics, Tribhuvan University, Kirtipur, Kathmandu 44618, Nepal
[3]Department of Physics, University of Houston, Houston, TX 77204, USA
[4]Department of Physics, Patan Multiple Campus, Tribhuvan University, Kathmandu 44700, Nepal

[*]Corresponding author: leela.pradhanjoshi@ac.tu.edu.np

Published online: 25 April 2022

To cite this article: Chaudhary, D. K. et al. (2022). Sensing performance of a ZnO-based ammonia sensor. *J. Phys. Sci.*, 33(1), 97–108. https://doi.org/10.21315/jps2022.33.1.7

To link to this article: https://doi.org/10.21315/jps2022.33.1.7

ABSTRACT: *Monitoring and remediation of toxic and flammable gases have become a critical task for the development of a clean society. Among various types of metal oxide semiconductors (MOS), zinc oxide (ZnO) is considered a potential material for gas sensing application because of its high sensitivity, easy synthesis, and high thermal stability behaviours. This research aimed to gain an in-depth understanding of the sensing task of a very stable and porous thin film of spin coated ZnO for detecting toxic ammonia vapour at room temperature. As-prepared ZnO films were characterised by x-ray diffraction (XRD), scanning electron microscopy (SEM), and ultraviolet-visible (UV-vis) analyses. XRD and SEM results revealed the polycrystalline wurtzite ZnO phase with grainy surface morphology. Optical calculations quantify the direct band gap of ZnO as 3.2 eV. The sensitivity measurements showed a good response ratio of 38.5 ± 0.6 with an exposure of 400 ppm of ammonia vapour. The results on sensitivity measurement of several cycles illustrated its stability and sensing performance better than other reported similar works. These findings will be useful to develop a low cost and efficient room temperature MOS gas sensor that can efficiently detect extremely low concentrations as 20 ppm of ammonia vapour which is below the Occupational Safety and Health Administration (OSHA) recommended value.*

Keywords: zinc oxide, sensor, response time, band gap, ammonia

1. INTRODUCTION

Detecting and being aware of the presence of toxic gases in the environment and leakages in occupational places are important and major priorities for safety and wellbeing. Among many other toxic gases, ammonia (NH_3) is one of the widely used in industrial sectors.[1–3] According to the Occupational Safety and Health Administration (OSHA) guidelines, personal exposure of NH_3 with a lower limit of up to 35 ppm for continuous 8 h and an upper limit of up to 50 ppm for 5 min cause severe health hazards. This threshold limit directly influences personal wellbeing as well. Ammonia sensors are highly promising in identifying gas spillage and leakage in a controlled atmosphere at room temperature in various sectors like agriculture, pharmaceutical, automotive, defence and food processing.[4–6] In recent times, experimentalists considered zinc oxide (ZnO) as a promising metal oxide material due to its amazing features like high chemical and thermal stability, wide band gap (3.00 eV–3.24 eV), easy tunability of its structural, optical, electrical, and electronic properties.[7–10] Though ZnO has been utilised for sensing various gases, it has some drawbacks such as high working temperature (>200^{o}C), poor selectivity, and relatively low response.[6] The operation of a metal oxide semiconductors (MOS) gas sensor at high temperatures affects its stability and consumes power.[9] Therefore, the fabrication of a room temperature MOS gas sensor is advantageous for improving long-term stability and low power consumption. A number of research are going on to overcome these problems.[11] In this work, we report the gas sensing efficacies, selectivity, and detection limit of spherical grainy structured spin-coated ZnO thin film-based sensors towards ammonia vapour at room temperature. We also report in-depth sensing characteristics like sensitivity, response and recovery times, and reproducibility of ZnO films.

2. EXPERIMENTAL

2.1 Deposition of ZnO Film

Thin films of ZnO were deposited on glass substrates using a 0.35 M precursor solution of zinc acetate, ethanol, and diethanolamine. The analytical grades of precursor materials were purchased from Merck (China) and used without further purification. The mixture was stirred for 1 h at 70°C until the solution is clear and homogeneous which was subsequently filtered using a Whatman filter paper and left for 24 h at room temperature.[10] The spin coating recipe was set to 30 s of spinning at a rate of 3000 rpm for each layer of deposition. The adherent layer

was then soft-baked at 130°C for 5 min, followed by hard-bake at 400°C for 10 min. Finally, the sample was annealed at 450°C for 1 h inside the muffle furnace.[7]

2.2 Sensor Setup

Figure 1 shows the schematic representation of the gas sensing setup used in this work. It consists of two chambers, a left chamber, where ammonia vapour is created by heating liquid ammonia above its boiling point which interconnects with the right test chamber. A digital temperature controller hot plate (TALBOYS 7X7 CER HP 230 V ADV, by Henry Troemner, LLC, USA) was used to set the temperature hot plate at (120 ± 4) °C. The test chamber has three openings for gas inlet, air inlet, and outlet. The ZnO sensor is retrofitted inside the test chamber to measure its response at exposure to different concentrations of ammonia. The sensitivity of the gas sensor was measured in terms of current measured at two different environments using $R = \frac{I_g}{I_a}$ where I_a and I_g are the currents flowing through the ZnO in air and gas, respectively.[12]

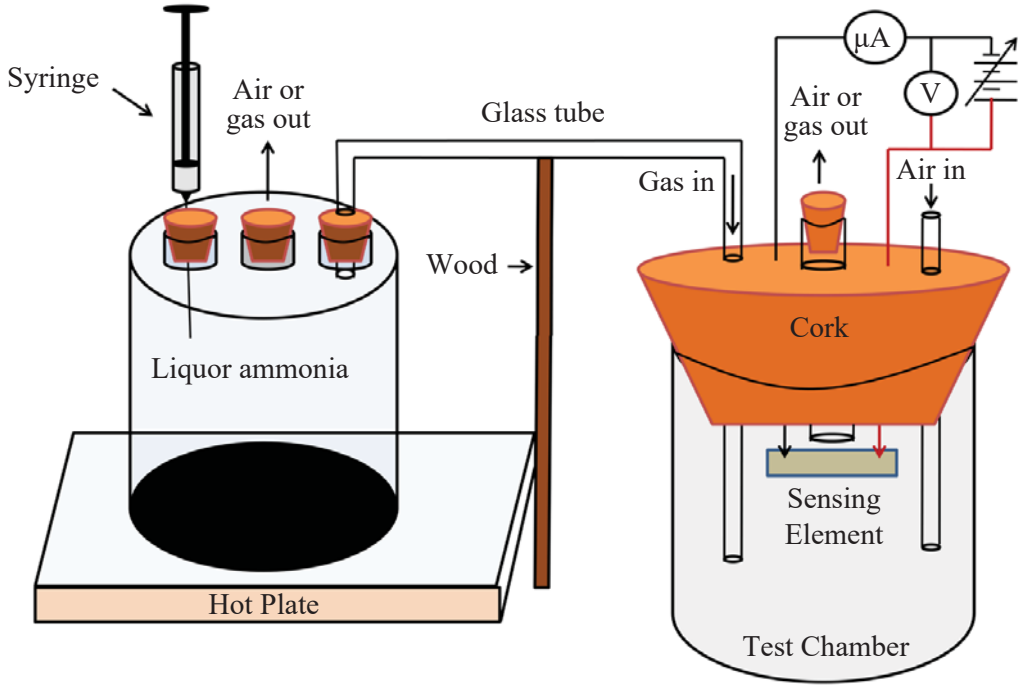

Figure 1: Schematic diagram of a gas sensor setup.

3. RESULTS AND DISCUSSION

3.1 Structural Analysis

Structural examination of ZnO thin films was done using the x-ray diffraction (XRD) technique. Figure 2 shows the XRD of spin coated ZnO in the 2θ from 20°–80° using Cu-K_α radiation of wavelength 1.54056 Å with a Bruker AXS, D2 PHASER A26-X1-A2BOB2A-, Serial No: 207047 diffractometer. The presence of multiple sharp peaks in the XRD pattern of spin-coated ZnO thin film reveals the polycrystalline nature of ZnO film. Major sharp peaks observed at 2θ = 31.8627°, 34.5092°, 36.3202°, 47.5594°, 56.3553°, 62.7889°, 67.8320° and 68.9580° correspond to (100), (002), (101), (102), (110), (103), (112) and (201), respectively, which were found to be consistent with standard values of JCPDS card No., 36-1451.[13] No additional impurity peak was observed which ensures the formation of pure ZnO. The crystallite size (D) was determined using Debye Scherer's formula $D = \frac{0.94\lambda}{\beta \cos\theta}$ where 0.94 is the correction factor, λ is the x-ray, wavelength and β and θ represent the full width at half maximum (FWHM) and diffraction angle, respectively.[14,15] Likewise, the lattice strain (ε) of ZnO film was calculated using the formula, $\varepsilon = \frac{\beta}{4 \tan\theta}$.[9,16] The average D and ε were found to be (27.60 ± 0.86) nm and (3.16 ± 0.28) × 10^{-3}, respectively.

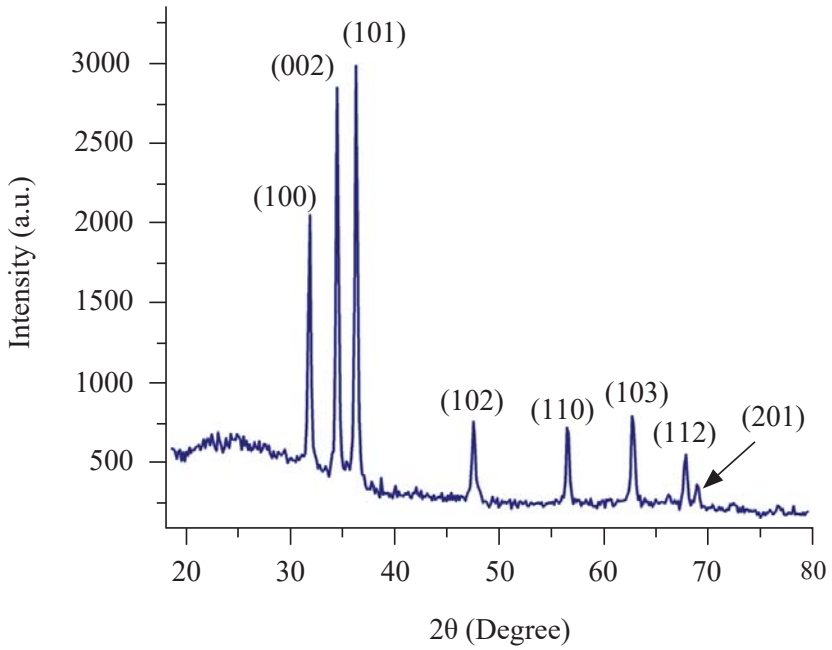

Figure 2: X-ray diffraction pattern of ZnO film.

3.2 Optical Band Gap

Figure 3(a) represents the UV-vis transmission spectrum of the ZnO sample in the wavelength range 300 nm–1000 nm at room temperature captured using a HR4000CG UV-NIR Ocean Optics (Singapore) spectrophotometer. The optical transmittance of ZnO film was more than 80% in the visible region. We notice a sharp decrease in transmittance at shorter wavelengths near the ultraviolet range which is typical in ZnO.[17] The optical band gap was determined from transmittance data using a Tauc plot, described by $(\alpha hv)^2 = A(hv - E_g)$ where α, A, hv and E_g are the absorption coefficient, energy constant, photon energy and optical band gap, respectively. The extrapolation of the linear portion into the x-axis gives the band gap of 3.20 eV [Figure 3(b)] which is consistent with the reported value in the literature.[18]

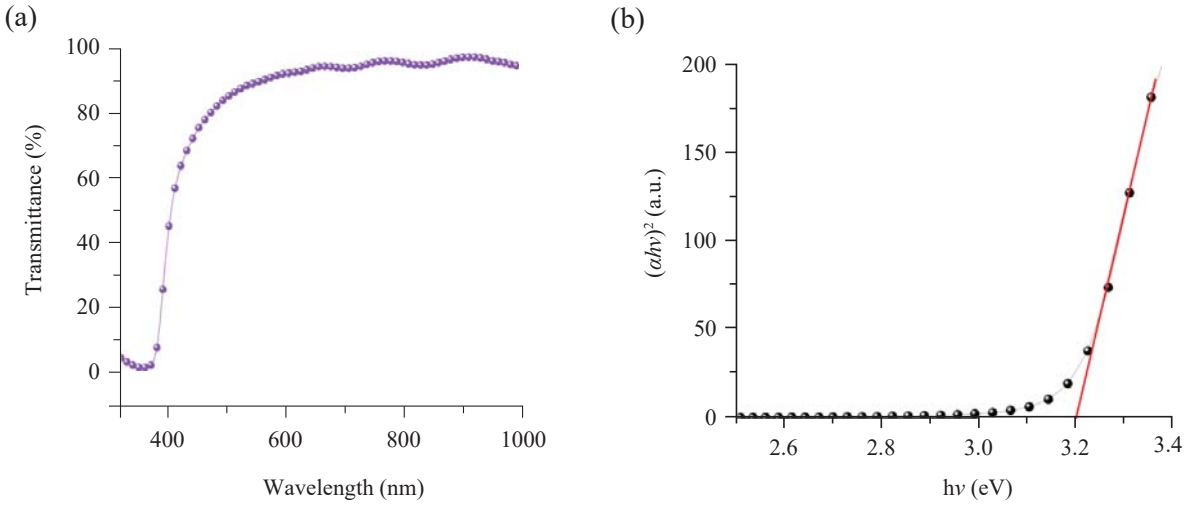

Figure 3: (a) UV-vis transmission spectrum and (b) band gap calculation of ZnO film.

3.3 Surface Morphology

The nature of the sensor surface is a vital factor in determining gas sensitivity towards various gases.[5,19] Figure 4(a) shows the SEM micrograph of porous surface morphology of spin-coated ZnO film consisting of spherical grains. The compositional analysis of this film was performed using the energy dispersive x-ray (EDX) technique. Figure 4(b) reveals the atomic % of Zn and O content to be 52.33% and 47.67%, respectively.

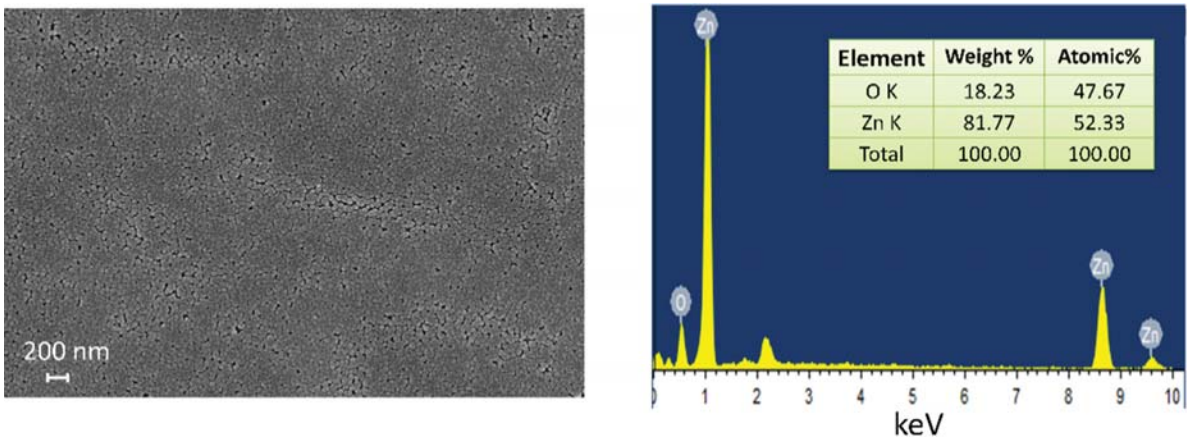

(a) (b)

Figure 4: (a) SEM micrograph and (b) EDX spectrum with Zn and O content in ZnO film.

3.4 Sensor Performance

In the ambient atmosphere, the oxygen molecules are ionosorbed as O_2^- after extracting electrons from the conduction band of ZnO so that there is an increase in the width of the space charge (depletion) region and the height of the potential barrier on the grain boundaries of ZnO.[20] This growth of the depletion layer and barrier height is schematically shown in figure 5(a). The current measured at this state is termed as I_a which is measured by applying a fixed potential difference of 10 V across it. This voltage was kept affixed at 10 V as the baseline for the entire study. In the presence of reducing gas, such as ammonia (NH_3), electrons trapped by oxygen species return to the ZnO which causes the barrier potential height to decrease that concomitantly increasing the conductivity of ZnO. Figure 5(b) shows the liberation of electrons during the interaction of ammonia with O_2^- as $4NH_3 + 3O^-_{2\,(ads)} = 2N_2 + 6H_2O + 6e^-$ and decrease of the depletion layer.[21] The current measured at this instance is denoted as I_g, current in gas. By evaluating the ratios of I_g/I_a, we can find out the sensing performance of ZnO-based gas sensors.[12]

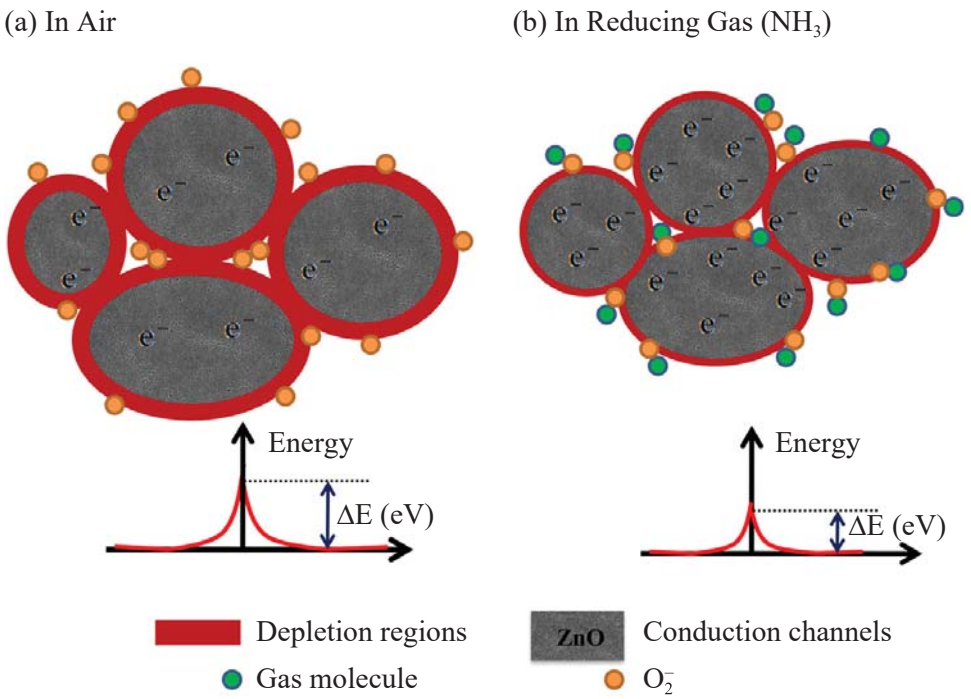

Figure 5: Illustration of the working mechanism of ZnO sensor (a) in the air (b) in reducing gas.

Figure 6(a) shows the response of the ZnO sensor (I_g/I_a~38.5) towards 400 ppm of ammonia vapour for five cycles. Further, we investigated the sensing performance of the sensor towards different concentrations of ammonia vapour. Figure 6(b) shows the variation of gas response plotted against sensing time for various ammonia concentrations. We noticed the reduction in gas response efficacies with decreasing ammonia concentrations. The times needed to acquire 90% and 10% of maximum response after injection and ejection of the gas from the chamber are called response time and recovery times of the sensor, respectively. The response time always depends on the reaction rate of exposed gas with adsorbed oxygen species on sensing material, whereas, the recovery time depends on the rate of desorption of oxygen from the sensor surface after the vapour is ejected.[22] Both response and recovery times may also depend on the sensor geometry. The inset of figure 6(b) shows the determination of response and recovery times of the ZnO sensor upon the exposure of ammonia vapour of 400 ppm. The response and recovery times are found to be 37 s and 90 s, respectively. To test the repeatability and stability of the sensing device, we repeated the same experiment with identical parameters for eight days and discovered the response to be constant at the value of ~38.5, which showed the device to be highly consistent across each measurement [Figure 6(c)]. Figure 6(d) depicts the sensing response of the ZnO sensor towards various vapours including acetone, ethanol, isopropanol, methanol and ammonia. The

ZnO sensor shows prominent selectivity towards ammonia vapour in comparison to other vapours under study. This is attributed to the smaller kinetic diameter and low ionisation energy of ammonia. The ammonia vapour with a small kinetic diameter diffuses easily in the available pores of ZnO and leads to more adsorption sites which consequently increase the gas sensing response.[23,24] For clarity, the molecular weight, kinetic diameter, and ionisation energy of various gas molecules are shown in Table 1.[25,26] The results obtained in this work were compared with the reported sensitivities of ZnO based sensors prepared by different methods and presented in Table 2. The comparison shows that the sensitivity of spin-coated ZnO is better than reported values for similar systems prepared by other methods such as hydrothermal and spray pyrolysis at room temperature.

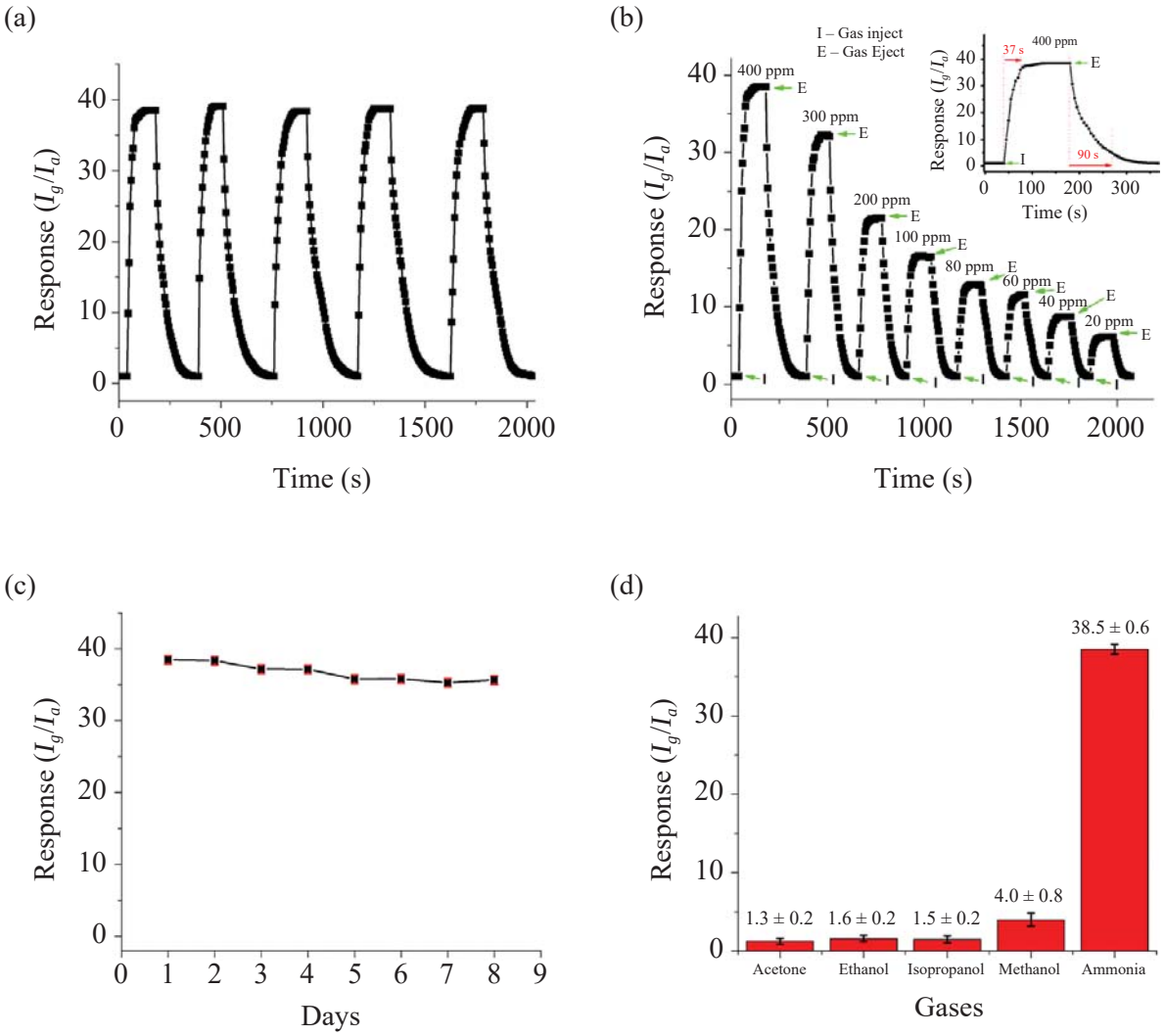

Figure 6: (a) Response curves with 400 ppm of NH_3 for five cycles, (b) response at different concentrations of ammonia (Inset: Calculation of response and recovery time with 400 ppm of NH_3), (c) repeatability, (d) selectivity measured at 400 ppm of various gases of ZnO sensor at room temperature.

Thus, we conclude that the results obtained herein using the spin coated ZnO film can be one of the best sensors for detecting low concentrations of ammonia vapour at room temperature.

Table 1. Kinetic diameter, molecular weight and ionisation energy of different molecules.

Vapour	Molecular weight	Kinetic diameter (nm)	Ionisation energy (eV)
Ammonia	17	0.26	10.18
Methanol	32	0.37	10.5
Ethanol	46	0.45	10.47
Acetone	58.05	0.46	9.69
Isopropanol	60.1	0.46	10.12

Table 2. Comparison of performance of ZnO based ammonia sensor of this work with reported works.

Materials	Method	Operating temperature (°C)	Ammonia (ppm)	Response (R_a/R_g or I_g/I_a)) or sensitivity	Reference
ZnO Nanowire	Hydrothermal	350	200 50 10	4.2 2.3 1.5	[5]
In_2O_3-MgO with Pd- loaded TiO_2 double layer	Thick film	530	300	25	[6]
SnO_2	Spin coating	Room temperature	500	92.1%	[11]
Co-ZnO	Spray pyrolysis	Room temperature	100	3.48	[14]
Ni-ZnO	Spray pyrolysis	Room temperature	100	2.52	[15]
ZnO Nanorod	Hydrothermal	Room temperature	500	8%	[19]
ZnO Nanowire	SILAR	Room temperature	50	80.2	[24]
ZnO Grain	Spin coating	Room temperature	400 20	38.5 ± 0.86 6.1 ± 0.8	This work

4. CONCLUSION

To sum up, the structural characteristics showed the polycrystalline nature of ZnO with an average crystallite size of 27 nm. EDX results confirmed the highest purity of sensing material. SEM image showed porous morphology of ZnO film comprising of spherical grains. The optical band gap was found to be 3.2 eV which is consistent with the reported values. The gas sensing result showed the highest response towards ammonia among all tested gases. The

highest magnitude of the gas response towards 400 ppm of ammonia vapour was ~38.5. This result was compared to similar MOS for consistency and was found to be promising. The response and recovery times at 400 ppm of NH_3 were evaluated to be 37 s and 90 s, respectively. Interestingly, this work concludes that spin-coated ZnO films can be utilised for building a stable and low-cost gas sensor that can efficiently detect extremely low concentrations of ammonia vapour (as low as 20 ppm), which is reasonably below the OSHA recommended lower limit (35 ppm) of health hazard.

5. ACKNOWLEDGEMENTS

The authors would like to acknowledge International Science Program, Uppsala University, Sweden through the NEP-01 grant and University Grants Commission, Nepal for the support on instrumentation and consumables. We would also like to thank the Indian Institute of Technology (IIT), Roorkee, Uttarakhand, India which helped to obtain XRD, SEM and EDX spectra of ZnO thin films.

6. REFERENCES

1. Pearson, J. & Stewart, G. R. (1993). The deposition of atmospheric ammonia and its effects on plants. *New Phytol.*, 125, 283–305. https://doi.org/10.1111/j.1469-8137.1993.tb03882.x
2. Erisman, J. W. et al. (2008). How a century of ammonia synthesis changed the world. *Nat. Geosci.*, 1, 636–639. https://www.nature.com/articles/ngeo325
3. Timmer, B., Olthuis, W. & Berg, A. V. D. (2005). Ammonia sensors and their applications – a review. *Sens. Actuators B. Chem.*, 107(2), 666–677. https://doi.org/10.1016/j.snb.2004.11.054
4. Mani, G. K. & Rayappan, J. B. B. (2013). A highly selective room temperature ammonia sensor using spray deposited zinc oxide thin film. *Sens. Actuators B. Chem.*, 183, 459–466. https://doi.org/10.1016/j.snb.2013.03.132
5. Shao, F. et al. (2016). NH_3 sensing with self-assembled ZnO-nanowire μHP sensors in isothermal and temperature-pulsed mode. *Sens. Actuators B. Chem.*, 226, 110–117. https://doi.org/10.1016/j.snb.2015.11.109
6. Takao, Y. et al. (1994). High ammonia sensitive semi-conductor gas sensors with double-layer structure and interface electrodes. *J. Electrochem. Soc.*, 141, 1028–1034. https://doi.org/10.1149/1.2054836
7. Rambu, A. P., Nica, V. & Dobromir M. (2013). Influence of Fe-doping on the optical and electrical properties of ZnO films. *Superlattices Microstruct.*, 59, 87–96. https://doi.org/10.1016/j.spmi.2013.03.023
8. Hassan, M. M. et al. (2014). Fe dopants enhancing ethanol sensitivity of ZnO thin film deposited by RF magnetron sputtering. *J. Mater. Sci.*, 49, 6248–6256. https://link.springer.com/article/10.1007/s10853-014-8349-2

9. Srinivasulu, T., Saritha, K. & Reddy, K. T. R. (2017). Synthesis and characterization of Fe-doped ZnO thin films deposited by chemical spray pyrolysis. *Mod. Electron. Mater.*, 3(2), 75–85. https://doi.org/10.1016/j.moem.2017.07.001
10. Shrestha, S. P. et al. (2010). Properties of ZnO: Al films prepared by spin coating of aged precursor solution. *Bull. Korean Chem. Soc.*, 31, 112–115. https://doi.org/10.5012/bkcs.2010.31.01.112
11. Beniwal, A., Srivastava, V. & Sunny. (2019). Sol-gel assisted nano-structured SnO_2 sensor for low concentration ammonia detection at room temperature. *Mater. Res. Express*, 6(4), 046421. https://iopscience.iop.org/article/10.1088/2053-1591aafdd8/pdf
12. Jha, R. K. et al. (2018). Enhanced gas sensing properties of liquid-processed semiconducting tungsten chalcogenide (WX_i, X = O and S) based hybrid nanomaterials. *IEEE Sens. J.*, 18(9), 20183494. https://doi.org/10.1109/JSEN.2018.2810811
13. Quan, S. Y., Tian, M. & Yang, L. M. (2009). Characterization of nanostructured ZnO thin films deposited by sol-gel spin coating. *Adv. Mater. Res.*, 79–82, 703–706. https://doi.org/10.4028/www.scientific.net/AMR.79-82.703
14. Mani, G. K. & Rayappan, J. B. B. (2015). A highly selective and wide range ammonia sensor-nanostructured ZnO: Co thin film. *Mater. Sci. Eng. B*, 191, 41–50. https://doi.org/10.1016/j.mseb.2014.10.007
15. Mani, G. K. & Rayappan, J. B. B. (2014). Selective detection of ammonia using spray pyrolysis deposited pure and nickel doped ZnO thin films. *Appl. Surf. Sci.*, 311, 405–412. https://doi.org/10.1016/j.apsusc.2014.05.075
16. Pramod, N. G. & Pandey, S. N. (2014). Influence of Sb doping the structural, optical, electrical and acetone sensing properties of In_2O_3 thin films. *Cearm. Int.*, 40(2), 3461–3468. https://doi.org/10.1016/j.ceramint.2013.09.084
17. Goh, E. G., Xu, X. & McCormick, P. G. (2014). Effect of particle size on the UV absorbance of zinc oxide nanoparticles. *Scripta Mater.*, 78–79, 49–52. https://doi.org/10.1016/j.scriptamat.2014.01.033
18. Nunes, P., Fortunato, E. & Martins, R. (2001). Influence of the post-treatment on the properties of ZnO thin films. *Thin Solid Film.*, 383(1–2), 277–280. https://doi.org/10.1016/S0040-6090(00)01577-7
19. Ang, W. et al. (2011). Room-temperature NH_3 gas sensor based on hydrothermally grown ZnO nanorods. *Chinese Phys. Lett.*, 28(8), 080702. https://doi.org/10.1088/0256-307X/28/8/080702
20. Yu, A. et al. (2011). Micro-lotus constructed by Fe-doped ZnO hierarchically porous nanosheets: preparation, characterization and gas sensing property. *Sens. Actuators B Chem.*, 158, 9–16. https://doi.org/10.1016/j.snb.2011.03.052
21. Dey, A. (2018). Semiconductor metal oxide gas sensors: A review. *Mater. Sci. Eng. B*, 229, 206–217. https://doi.org/10.1016/j.mseb.2017.12.036
22. Hongsith, N. et al. (2010). Sensor response formula for sensor based on ZnO nanostructures. *Sens. Actuators B Chem.*, 144, 67–72. https://doi.org/10.1016/j.snb.2009.10.037

23. Ozawa, K. et al. (2002). Adsorption state and molecular orientation of ammonia on ZnO (studied by photoelectron spectroscopy and near-edge X-ray absorption fine structure spectroscopy. *J. Phys. Chem. B*, 106(36), 9380–9386. https://doi.org/10.1021/jp0205970
24. Anasthasiya, A. N. A. et al. (2018). Adsorption property of volatile molecules on ZnO nanowires: computational and experimental approach. *Bull. Mater. Sci.*, 41(4), 1–7. https:/doi.org/10.1007/s12034-017-1538-2
25. Zhu, G. et al. (2008). FAU-type zeolite membranes synthesized by microwave assisted in situ crystallization. *Mater. Lett.*, 62(28), 4357–4359. https://doi.org/10.1016/j.matlet.2008.07.026
26. Goel, S. et al. (2012). Synthesis and catalytic properties of metal clusters encapsulated within small-pore (SOD, GIS, ANA) zeolites. *J. Am. Chem. Soc.*, 134(42), 17688–17695. https://doi.org/10.1021/ja307370z

Journal of Institute of Science and Technology, 27(1), 135-140 (2022)
ISSN: 2467-9062 (print), e-ISSN: 2467-9240
https://doi.org/10.3126/jist.v27i1.40866

Research Article

SENSING CHARACTERISTICS OF ZnO NANOPARTICLE FILM TOWARDS ACETONE

Dinesh Kumar Chaudhary[1,2], Yogesh Singh Maharjan[1], Sharmila Pradhan Amatya[3], Shankar Prasad Shrestha[4], Rajendra Parajuli[1], Pitamber Shrestha[1], Leela Pradhan Joshi[1]*
[1]Physics Department, Amrit Campus, Tribhuvan University, Kathmandu, Nepal
[2]Central Department of Physics, Tribhuvan University, Kirtipur, Kathmandu, Nepal
[3]Chemistry Department, Amrit Campus, Tribhuvan University, Kathmandu, Nepal
[4]Physics Department, Patan Multiple Campus, Lalitpur, Nepal
Corresponding Author: leela.pradhanjoshi@ac.tu.edu.np
*(**Received**: November 16, 2021; **Revised**: May 16, 2022; **Accepted**: June 30, 2022)*

ABSTRACT
Over the past few decades, nanomaterials of metal oxide such as zinc oxide (ZnO) have been significantly researched for sensing various toxic gases like ethanol, acetone and ammonia. The sensing performance of semiconducting materials depends primarily on their surface structure and the interaction behavior with target gas molecules. The surface quality of ZnO is highly influenced by deposition methods. Although several ZnO surfaces have been rigorously studied for detecting gas leakages, it still possesses drawbacks such as high operating temperature, slow response and recovery times. Henceforth, this investigation was carried out to resolve these issues in the fabrication of future ZnO-based gas sensors. In this work, we report the major findings of the ZnO-based nanoparticle film gas sensor prepared by a doctor blade method to gain insight towards detecting various concentrations of acetone gas at different temperatures. The XRD and FTIR results confirmed the phase purity of ZnO. The results showed the highest response ratio of 25.697 $\pm$0.012 at 285 ^{o}C with an exposure of 800 ppm of acetone along with the quick response and recovery times of 39 sec and 79 sec, respectively. This operating temperature was found to be lower than the reported value for a similar system than that prepared via different methods.

Keywords: Acetone sensor, Operating temperature, Response time, ZnO nanoparticle

INTRODUCTION
Acetone is one of the most common but toxic gases ubiquitously used at many workplaces that include research laboratories, hospitals and chemical manufacturing plants which require immediate attention for its safe remediation. Acetone is also used as an effective biomarker in the diagnosis of type I diabetes. Acetone concentration in a healthy individual should be below 0.8 ppm, while for a diabetic patient it is above 1.8 ppm (Drmosh *et al.,* 2021; Qiang *et al*., 2016). Exposure to acetone can cause severe damage to the liver, lungs, kidney and central nervous system (Li *et al*., 2014). Therefore, it is immensely important to understand and develop effective devices to detect even the low traces of acetone (Kishore *et al*., 2021). Nanomaterials of various metal oxides such as ZnO, Mn-ZnO, Fe_2O_3, ZnO-SnO_2, Au/Ag/Cu doped ZnO, ZnO-TiO_2, etc., have been widely studied to detect toxic and flammable gases because of its interesting electrical, optical and structural properties (Chen *et al*., 2017; Qi *et al*., 2008; Zhu *et al*., 2017). The sensing performance of metal oxide semiconductors is highly dependent on their surface morphology and interfacial structures. ZnO can be prepared using a number of methods such as sol-gel route, electro-spinning and hydrothermal route, phase transport method, solvothermal method etc., (Kashout *et al*., 2010; Cui *et al*., 2016; Hosseini *et al.,* 2015; Xiao *et al.,* 2012). Various efforts have been made to improve gas sensitivity, response and recovery time, reaction rate as well as stability of the ZnO gas sensor. However, these sensors greatly suffer from the inherent drawback of a high operating temperature of more than 300 ^{o}C (Xiao *et al.,* 2012; Chu *et al*., 2012; Al-Hadeethi *et al*., 2017; Wongrat *et al*., 2017). So, it is essential to develop a low cost but effective gas sensor with enhanced sensing performance at lower operating temperatures. To date, ZnO films of various morphologies including nanoparticles, nano rods, nano wires, nano belts, nano sheets and nano fibers have been fabricated (Zhang *et al*., 2018; Zeng *et al*., 2009; Zhang *et al*., 2012; Xi *et al*., 2007; Wang *et al*., 2020; Samanta *et al*., 2015). Among these, ZnO nanoparticles (ZnO NPs) are regarded as a promising metal oxide nanostructures to their large surface area, high chemical, thermal stability, and high yield (Zhao *et al*., 2019; Bhatia *et al.,* 2017; Tang *et al*., 2007).

This work reports the fabrication of a chemical sensor based on ZnO NPs to detect as various concentrations of acetone vapors as possible with improved response ratio, response time and recovery time at operating temperature that is lower than reported values.

EXPERIMENT
Chemicals
Zinc acetate dehydrated, ethanol, sodium hydroxide, stannous chloride dehydrated, concentrated hydrochloric acid were purchased from merk and used without further modifications. Distilled water was used throughout the experiment to prepare the ZnO NPs and their film.

Preparation of ZnO films via doctor blade method

At first, fluorine doped tin oxide layers were deposited on clean glass substrate using the spray pyrolysis method. The prepared layers were found to be transparent and conducting. After then, ZnO films were deposited on these FTO substrates using the paste of ZnO NPs with ethanol and few drops of vinegar as a binder followed by annealing at 550°C for an hour. The prepared film was further aged at room temperature for 7 days to improve the stability before testing (Zhang *et al.*, 2018). Prior to this the ZnO NPs were prepared by reacting the alcoholic solution of zinc acetate with sodium hydroxide via the precipitation method. The residue obtained here were centrifuged at 2500 rpm and filtered very carefully followed by several times washing with distilled water and ethanol to remove organic impurities and dried at a temperature of 550°C inside a programmable muffle furnace (Nabertherm GmbH, LT 3/11/B4 10 Serial No. 36140, Germany) for an hour (Joshi *et al.*, 2021).

The structural investigation of ZnO NPs was completed using X-ray diffractometer (Bruker AXS, D2PHASER A26-X1-A2BOB2A-, Serial No: 207047) with CuKα radiation of wavelength 1.54056 Å. The sensitivity was measured in terms of electrical resistance change before and after gas exposure that was measured using a high-quality digital fluke multimeter in the temperature range of 100–330°C. The base temperature of the chamber was maintained at 150 °C to convert from liquid to vapour phase. The sensor performance of the prepared ZnO NPs film was calculated by taking the resistance ratio, $Response, R = \frac{R_a}{R_g}$ or $Sensitivity, S\,\% = \left(\frac{R_a - R_g}{R_a}\right) x\ 100$ where R_a and R_g are the resistances of the sensing element (ZnO) in the air and gas respectively (Chu *et al.*, 2012).

RESULTS AND DISCUSSION

Structural investigation

The structural properties of as-prepared ZnO NPs were investigated by analyzing its X-ray diffraction pattern. Figure 1(a) depicts the XRD pattern of ZnO using CuK_α radiation of wavelength 1.54056 Å in the 2θ range of 20°−85°. Measuring peak position (2θ) and corresponding full width half maximum (β), the crystallite size (D) of ZnO was calculated using Debye Scherer's formula, $D = \frac{0.94\lambda}{\beta Cos\theta}$ where 0.94 is the correction factor (Bhatia *et al.,* 2017). The observed peaks obtained at 2θ =31.0618, 33.7285, 35.5518, 46.8524, 55.9166, 62.1954, 65.7034, 67.2904, 68.4153, 71.8966, 76.3435 and 80.6931° were indexed as (100), (002), (101), (102), (110), (103), (200), (112), (201), (004), (202) and (104) planes. These observed peaks were indexed with reference to standard JCPDS d-spacing values of pdf # 36-1451(Al-Hardan *et al.*, 2013; Prajapati *et al.*, 2013). The multiple sharp peaks ascertained the polycrystalline nature of ZnO. Considering all the peak values, we calculated the average crystallite size of ZnO which was found to be 20.77 ± 0.90nm. The details of the calculation of average D were shown in table 1. The c/a ratio was found as 1.60 suggested the wurtzite hexagonal phase of ZnO. The average microstrain (4η) and crystallite size (D) were also calculated from the slope of βcosθ against sinθ plot (Figure 1(b)) and Williamson-Hall equation, $\beta\cos\theta = \frac{k\lambda}{D} + 4\eta \sin\theta$ (Hassan *et al.*, 2014). The value of microstrain was found to be 0.0025±0.0012. Using the intercept value, the D was calculated as 24.38 ± 2.16 nm. The absence of impurity phases in the XRD confirmed the purity of prepared material.

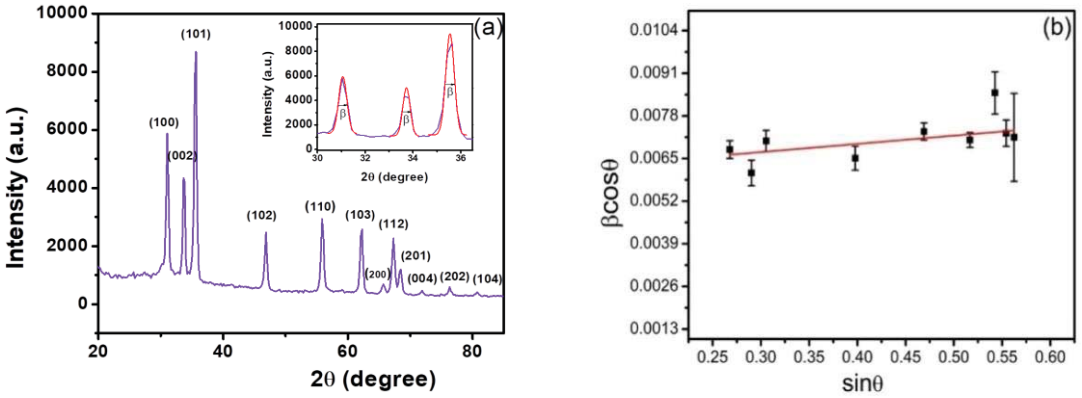

Figure 1. (a) X-ray diffraction pattern (Inset: Determination of β) and (b) W-H plot of as-prepared ZnO NPs

Table 1. Observed 2θ, FWHM, d-spacings and crystallite size (D) of ZnO

(hkl)	2θ (degree)	FWHM (degree)	d-spacing (Å)	d-spacing (Å) JCPDS	D (nm)	Average D (nm)
(100)	31.0618	0.4027	2.8756	2.8143	21.38	
(002)	33.7285	0.3627	2.6541	2.6033	23.89	
(101)	35.5518	0.4232	2.5221	2.4759	20.57	
(102)	46.8524	0.4062	1.9367	1.9111	22.25	
(110)	55.9166	0.4748	1.6424	1.6247	19.78	20.77± 0.90
(103)	62.1954	0.4726	1.4908	1.4771	20.48	
(200)	65.7034	0.5796	1.4194	1.4071	17.03	
(112)	67.2904	0.5002	1.3898	1.3781	19.91	
(201)	68.4153	0.4949	1.3696	1.3582	20.27	
(004)	71.8966	0.4096	1.3116	1.3017	25.02	
(202)	76.3143	0.4277	1.2463	1.2380	24.67	
(104)	80.6983	0.7809	1.1893	1.1816	13.94	

Fourier Transform Infrared Analysis

The bond identification of investigated material was done using a Perkin Elmer -16.10.2 FTIR spectrum version in the range 400 to 4000 cm^{-1}, ATR mode. Fig. 2 shows the FTIR spectrum of so-prepared ZnO NPs which clearly show a large well defined characteristic peak at 524, followed by small peaks at 685, and 872 cm^{-1} due to Zn-O stretching (Sirdeshpande *et al.*, 2018). Weak peak observed at 3489 cm^{-1} attributes for the OH stretching mode of surface hydroxyl groups.

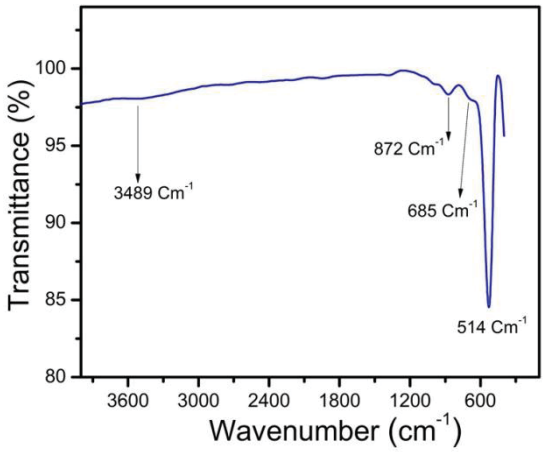

Figure 2. FTIR spectrum of as-prepared ZnO NPs

Sensing Characteristics

The sensing behavior of as-prepared ZnO NPs film towards acetone vapour was investigated in the various temperatures. The ratio of R_a (resistance in the air) and R_g (the resistance in gas) gives the sensor performance. The sensor performance of ZnO depends on the reaction rate of test gas with surface adsorbed oxygen species such as O^-, O^{2-} and O_2^-, that depends on its temperature (Chaudhary *et al.*, 2020, Xu *et al.*, 2015). Hence, to optimize the working temperature, the response characteristics were measured in the temperature range of 100-310 ^oC with an exposure of 800 ppm of acetone. Figure 3(a) showed the measured sensor characteristics at different temperatures. It shows that the highest value of response ratio, 26 at 285^oC. The increase of response ratio with temperature is shown in Figure 3(b). The graph also showed a low response at low temperatures which was attributed to the low reaction rate between the acetone gas molecules with the surface absorbed oxygen species and high activation energy (Hongsith *et al.*, 2010). The enhancement of the sensor response on increasing the operating temperature was due to the increase in thermal energy to overcome the activation energy. Above optimum temperature, desorption of oxygen molecules occurs from the ZnO surface that may ascribe to decrease the gas response (Khayatian *et al.*,2014).

In the gas sensor, response and recovery times are considered as the two important parameters to be known well. The time required to achieve the 90% and 10% of maximum response after injecting and ejecting the test gas are called response and recovery time respectively. Since the carrier concentration of metal oxide semiconductor is a temperature dependent quantity, the response and recovery times are also temperature

dependent. The inset of figure 3(b) shows the graphical calculation of response and recovery times measured with 800 ppm exposure of acetone at 285°C. Figure 3(c) showed that response curves measured with exposure of various concentrations of acetone. The details of calculated response ratio, response and recovery times at 285°C with different concentrations (40-800 ppm) of acetone were shown in table 2. The inset of this figure clearly showed the linear increase of gas response with the concentration of acetone. Figure 3(d) illustrates measured response curves for three cycles with an exposure of 800 ppm of acetone at 285 °C. The result obviously showed good stability of the ZnO sensor.

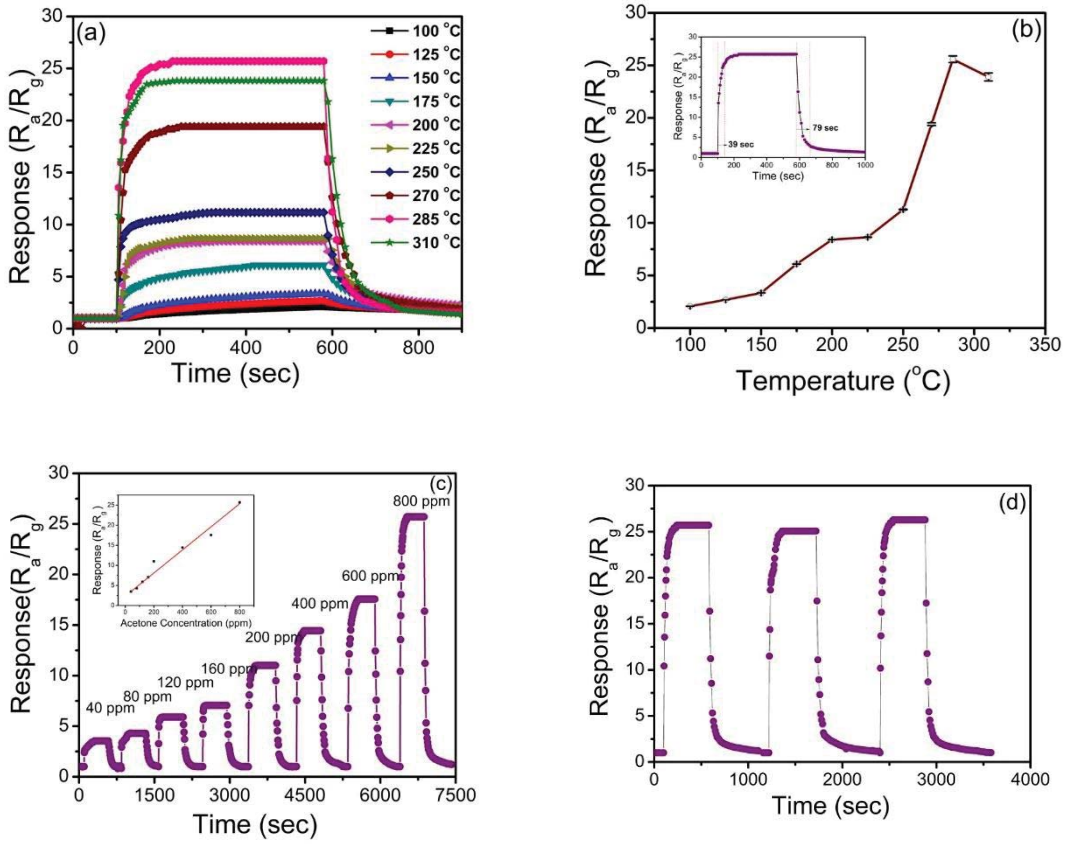

Figure 3. (a) Transient response characteristics at various temperatures (b) Temperature dependent response [inset: response and recovery times at 800 ppm acetone] (c) Response curves at different ppm of acetone [inset: increasing gas response with ppm of acetone] (d) stability curves at 800 ppm

The highest gas response with the higher concentration can be seen clearly which was due to the increase in the surface coverage of acetone molecules on the film that enhanced the interaction rate of gas molecules with the adsorbed oxygen species. The result also showed the changes in response and recovery times with the concentration of acetone. The result showed the response and recovery times for 800 ppm at 285°C were 39 sec and 79 sec respectively. These values were compared with some reported values shown in table 3 for analogous systems but prepared by different methods such as solvothermal, hydrothermal, spray pyrolysis and electro spinning etc.

Table 2. Response ratio, response and recovery times at different concentrations of acetone at 285 °C

Concentration (ppm)	Response (R_a/R_g)	Response time (sec)	Recovery time (sec)
40	3.500 ± 0.002	21	91
80	4.299±0.002	23	101
120	5.899±0.003	21	99
160	7.052 ±0.003	22	100
200	11.009 ±0.006	26	95
400	14.430 ± 0.007	28	97
600	17.562 ± 0.008	31	88
800	25.697 ± 0.012	39	79

Table 3. Comparison of operating temperature, response ratio, response and recovery times with reported works

Sample	Method	Conc. (ppm)	Operating Temperature (°C)	Response/ Sensitivity %	Res/Rec time (sec)	Reference
ZnO nanosheets	Solvothermal	500	420	70	NR	Xiao *et al.*, 2012
La-ZnO	Solvothermal	1000	385 425	1800 1826	16/3 sec	Chu *et al.*, 2012
Ag-ZnO Needle	Facile Hydrothermal	200	370	30.233	10/21	Al-Hadeethi *et al.*, 2017
Pt –ZnO	Thermal Oxidation	400	400	188	NR	Wongrat *et al.*, 2017
ZnO NPs	Chemical	100	370	36	12/14	Zhang *et al.*, 2017
Pd-ZnO NPs	Solution		340	76	8/10	
Cr-ZnO	RF co-sputtering	500	400 300	90	210/70 170/95	Al-Hardan *et al.*, 2013
In-ZnO	Spray Pyrolysis	100	300	96.8	65/24	Prajapati *et al.*, 2014
La-ZnO	Electro Spinning	200	340	68	2/23	Xu *et al.*, 2015
ZnO NPs	Precipitation	800 40	285	26 3.5	39/79 21/91	This work.

CONCLUSIONS

ZnO NPs prepared by the precipitation method were used for the gas sensing task. The XRD results confirmed the polycrystalline ZnO phase with an average crystallite size of 20.77±0.90 nm. Additionally, the chemical bonding of ZnO was studied using the FTIR spectrum. Various concentrations of acetone were tested using ZnO NPs films in temperatures ranging from 100 to 310 °C. The film showed the low and slow response and recovery at low temperatures and high and fast response at higher temperatures. The film showed the highest response of 25.697±0.012 for 800 ppm of acetone vapors at 285 °C with response and recovery time of 39 s and 79 s. The gas sensing results on the exposure of the different concentrations (40-800 ppm) of acetone vapour showed the higher response with an exposure of high concentrations. The highest and lowest values of gas response were found to be ~26 for 800 ppm and ~3.5 for 40 ppm of acetone.

ACKNOWLEDGMENTS

We would like to thank the International Science Program (ISP), Uppsala University, Sweden, under NEP-01 grant for providing financial support for chemicals and design & constructing sensor setup.

AUTHOR CONTRIBUTIONS

Conceptualization, experimental design, data collection and analysis and manuscript preparation were initiated by DKC and LPJ. The FTIR analysis was performed by SPA. YMS, SPS, RP and PS contributed in the data analysis, manuscript writing, review and proof reading.

CONFLICTS OF INTEREST

The authors declare that they have no competing interests.

DATA AVAILABILITY STATEMENT

The data that support the findings of this study are available from the corresponding author, upon reasonable request.

REFERENCES

Al-Hadeethi, Y., Umar, A., Ibrahim, A. A., Al-Heniti, S. H., Kumar, R., Baskoutas, S., & Raffah, B. M. (2017). Synthesis, characterization and acetone gas sensing applications of Ag-doped ZnO nanoneedles. *Ceramics International*, *43*(9), 6765-6770.

Al-Hardan, N. H., Abdullah, M. J., & Aziz, A. A. (2013). Performance of Cr-doped ZnO for acetone sensing. *Applied surface science*, 270, 480-485.

Bhatia, S., Verma, N., & Bedi, R. K. (2017). Ethanol gas sensor based upon ZnO nanoparticles prepared by different techniques. *Results in Physics*, *7*, 801-806.

Chaudhary, D. K., Ghimire, R., Amatya, S. P., Shrestha, S. P., & Joshi, L. P. (2020, December). Study on influence of Fe doping into ZnO film for ethanol sensing. *Journal of Physics: Conference Series* (Vol. 1706, No. 1, p. 012036). IOP Publishing.

Chen, N., Li, Y., Deng, D., Liu, X., Xing, X., Xiao, X., & Wang, Y. (2017). Acetone sensing performances based on nanoporous TiO_2 synthesized by a facile hydrothermal method. *Sensors and Actuators B: Chemical, 238*, 491-500.

Chu, X., Zhu, X., Dong, Y., Ge, X., Zhang, S., & Sun, W. (2012). Acetone Sensors Based on La^{3+} doped ZnO nano-rods prepared by solvothermal method. *Journal of Materials Science & Technology*, *28*(3), 200–204.

Cui, J., Shi, L., Xie, T., Wang, D., & Lin, Y. (2016). UV-light illumination room temperature HCHO gas-sensing mechanism of ZnO with different

nanostructures. *Sensors and Actuators B: Chemical*, *227*, 220-226.

Drmosh, Q. A., Alade, I. O., Qamar, M., & Akabar, S. (2021). Zinc oxide-based acetone gas sensors for breath analysis: A review. *Chemistry: An Asian Journal, 16(12),* 1519-1538.

Hassan, M. M., Khan, W., Naqvi, A. H., Mishra, P., & Islam, S. S. (2014). Fe dopants enhancing ethanol sensitivity of ZnO thin film deposited by RF magnetron sputtering. *Journal of Materials Science*, *49*, 6248–6256.

Hongsith, N., Wongrat, E., Kerdcharoen, T., & Choopun, S. (2010). Sensor response formula for sensor based on ZnO nanostructures. *Sensors and Actuators B: Chemical,144*, 67–72.

Hosseini, Z.S., Irajizad A., & Mortezaali, A. (2015). Room temperature H_2S gas sensor based on rather aligned ZnO nanorods with flower-like structures. *Sensor and Actuators B: Chemical, 207*, 865-871.

Joshi, L. P., Khatri, B. V., Gyawali, S., Gajurel, S., & Chaudhary, D. K. (2021). Green Synthesis of Zinc Oxide Nanoparticles Using Ixora Coccinea Leaf Extract for Ethanol Vapour Sensing. *Journal of Physical Science*, *32*(2), 15–26.

Kashout, A. B., Soliman, H. M. A., Hassan, H. S., & Aousehly, A. M. (2010). Fabrication of ZnO and ZnO:Sb nanoparticles for gas sensor applications, *Journal of Nanomaterials, 2010*.

Khayatian, A., Kashi, M. A., Azimirad, R., & Safa, S. (2014). Enhanced gas-sensing properties of ZnO nanorods encapsulated in an Fe-doped ZnO shell. *Journal of Physics D: Applied Physics*, *47*, 075003.

Kishore, K. R., Balamurugan, D., & Jeyprakash, B. G. (2021). CuO nanograins: synthesis and acetone vapour detection. *Journal of Materials Science: Materials in Electronics*,*32*, 1204–1220.

Li, W. Q., Ma, S. Y., Luo, J., Mao, Y. Z.,Cheng, L.,Gengzang, D. J., Xu, X. L., &Yan, S. H. (2014). Synthesis of hollow SnO_2 nanobelts and their application in acetone sensor, *Materials Letters*, *132*, 338-341.

Prajapati, C. S., & Sahay, P. P. (2013). Influence of In doping on the structural, optical and acetone sensing properties of ZnO nanoparticulate thin films. *Materials science in semiconductor processing*, *16*, 200–210.

Qi, Q., Zhang, T.,Liu, L., Zheng, X., Yu, Q., Zeng, Y., &Yang, H. (2008). Selective acetone sensor based on dumbbell-like ZnO with rapid response and recovery. *Sensors and Actuators B: Chemical, 134*, 166–170.

Qiang, Z., Ma, S. Y., Jiao, H. Y., Jin, W. X., Wang, T. T., Jiang, X. H., & Zhang, Z. Y. (2016). Solvothermal synthesis of 3D leaf-like α-Fe_2O_3 and its gas-sensing properties research. *Materials Letters*, *181*, 29-33.

Samanta, P., Bagchi, S., & Mishra, S. (2015). Synthesis and Sensing characterization of ZnO nanofibers prepared by Electrospinning. *Materials Today: Proceedings*, *2*(9), 4499-4502.

Sirdeshpande, K. D., Sridhar, A., Cholkar, K. M., & Selvaraj, R. (2018). Structural characterization of mesoporous magnetite nanoparticles synthesized using the leaf extract of Calliandra haematocephala and their photocatalytic degradation of malachite green dye. *Applied Nanoscience*, *8*(4), 675-683.

Tang, H., Li, Y., Zheng, C., Ye, J., Hou, X., & Lv, Y. (2007). An ethanol sensor based on cataluminescence on ZnO nanoparticles. *Talanta*, *72*(4), 1593-1597.

Wang, Y., Meng, X. N., & Cao, J. L. (2020). Rapid detection of low concentration CO using Pt-loaded ZnO nanosheets. *Journal of hazardous materials*, *381*, 120944.

Wang, L., Teleki, A., Pratsinis, S. E., & Gouma, P. I. (2008). Ferroelectric WO3 nanoparticles for acetone selective detection. *Chemistry of Materials*, *20(15),* 4794-4796.

Wongrat, E., Chanlek, N., Chueaiarrom, C., Thupthimchun, W., Samransuksamer, B., & Choopun, S. (2017). Acetone gas sensors based on ZnO nanostructures decorated with Pt and Nb. *Ceramics International*, *43*, S557-S566.

Xi, Y., Hu, C. G., Han, X. Y., Xiong, Y. F., Gao, P. X., & Liu, G. B. (2007). Hydrothermal synthesis of ZnO nanobelts and gas sensitivity property. *Solid state communications*, *141*(9), 506-509.

Xiao, Y., Lu, L., Zhang, A., Zhang, Y., Sun, L., Huo, L., & Li, F. (2012). Highly enhanced acetone sensing performances of porous and single crystalline ZnO nanosheets: high percentage of exposed (100) facets working together with surface modification with Pd nanoparticles. *ACS applied materials & interfaces*, *4*(8), 3797-3804.

Xu, X. L., Chen, Y., Ma, S. Y., Li, W. Q., & Mao, Y. Z. (2015). Excellent acetone sensor of La-doped ZnO nanofibers with unique bead-like structures. *Sensors and Actuators B: Chemical*, *213*, 222-233.

Zeng, Y., Zhang, T., Yuan, M., Kang, M., Lu, G., Wang, R., Fan, H., He, Y., & Yang, H. (2009). Growth and selective acetone detection based on ZnO nanorod arrays. *Sensors and Actuators B: Chemical*, *143*(1), 93-98.

Zhang, Y., Ram, M. K., Stefanakos, E. K., & Goswami, D. Y. (2012). Synthesis, characterization, and applications of ZnO nanowires. *Journal of Nanomaterials*, *2012,* 1-22.

Zhang, Y. H., Liu, C. Y., Jiu, B. B., Liu, Y., & Gong, F. L. (2018). Facile synthesis of Pd-decorated ZnO nanoparticles for acetone sensors with enhanced performance. *Research on Chemical Intermediates*, *44*(3), 1569-1578.

Zhao, G., Xuan, J., Liu, X., Jia, F., Sun, Y., Sun, M., Yin, G., & Liu, B. (2019). Low-cost and high-performance ZnO nanoclusters gas sensor based on new-type FTO electrode for the low-concentration H_2S gas detection. *Nanomaterials, 9*, 435-445.

Zhu, L., & Zeng, W. (2017). Room-temperature gas sensing of ZnO-based gas sensor: A review. *Sensors and Actuators A: Physical*, *267*, 242-261.

Study on influence of Fe doping into ZnO film for ethanol sensing

Journal of Physics: Conference Series **1706** (2020) 012036 doi:10.1088/1742-6596/1706/1/012036

Study on influence of Fe doping into ZnO film for ethanol sensing

D K Chaudhary[1,4], R Ghimire[2], S P Amatya[3], S P Shrestha[2] and L P Joshi[1*]

[1]Department of Physics, Amrit Campus, Tribhuvan University, Kathmandu, Nepal
[2]Department of Physics, Patan Multiple Campus, Tribhuvan University, Lalitpur, Nepal
[3]Department of Chemistry, Amrit Campus, Tribhuvan University, Kathmandu, Nepal
[4]Central Department of Physics, Tribhuvan University, Kirtipur, Kathmandu, Nepal

E-mail: leela.pradhan@gmail.com

Abstract. In recent times, the importance of nanostructure of metal oxide semiconductor (MOS) as a gas sensing material is rising tremendously. Among various metal oxide semiconductors ZnO has potential to be used as a sensor for several toxic gases. In this work, we investigated the influence of Fe doping into ZnO to detect various concentrations of ethanol vapour. Pristine and Fe doped ZnO (Fe-ZnO) films were deposited on glass substrates using a spin coating technique wherein the concentration of Fe can be easily controlled. The crystallite size and surface morphology of ZnO samples were characterized by XRD, SEM and EDX techniques. The sensor performance in terms of gas response (R) of ZnO and Fe-ZnO gas sensors towards ethanol vapour were measured in the 100 to 300ºC temperature range using DC electrical resistance. Fe doped ZnO samples showed enhancement in gas response due to increase in specific surface area originated from reducing grain size after doping. The 2% Fe-ZnO sample showed the good response of 40.9 for 400 ppm of ethanol vapour exposure at 260ºC. This was found to be better than reported values for ZnO prepared by different methods.

Key Words: Gas sensor, Ethanol, Fe-ZnO, Sensitivity, Response time.

1. INTRODUCTION

Nano-structured metal oxide semiconductors (MOS) are promising candidates for detecting different types of flammable, hazardous and toxic gases originated at the different sites such as research laboratory, home kitchens, shopping malls, etc [1-2]. The gas sensing properties of MOS materials depend on the following factors; nanostructure and surface morphology, coupling action of gas molecules with MOS surfaces under given conditions, exposed gas quality and concentration and applied sensor geometry [3-5]. By reducing the size from bulk to nano, we improve the specific surface area of the material. This becomes one of the key impetuses in enhancing MOS sensor performance [6]. Currently, various types of MOS such as SnO_2, In_2O_3, Fe_2O_3, TiO_2, CuO, Ce_2O_3, ZnO [7-11] have been used as good sensors to detect several toxic gases. However, we still need to overcome some difficulties such as high operating temperature, low sensitivity percentage or gas response, large response and recovery times in order to advance the use of MOS gas sensors. In this regard, an in-depth and systematic investigation of metal doped ZnO prepared by different methods is an interesting problem because it can bring the changes in crystal structure and underlying electrical and electronic properties of the oxide material [12, 13]. In this work, we investigated the impact of Fe doping into the ZnO to fabricate an economic, low temperature operating, gas sensor. ZnO is an

attractive compound semiconductor which generally exists as an n-type with wide band gap of 3.37eV, a large exciton binding energy of 60 meV at room temperature, and piezoelectric [14-17]. Interestingly, the electrical, electronic and optical properties of ZnO can be tailored effectively in the preparation of its nano material [18-21]. ZnO, a chemically and thermally stable compound, has been extensively studied for various applications from industry to medical field. The quality of thin films of semiconductors always depends on its synthesis route. Though various sophisticated and costly methods are available to prepare thin film of ZnO, the reason for using spin coating was its simplicity and low running cost where the action of metal doping into ZnO can be effectively performed [22]. Preparation, characterization of undoped and 1-4 at.% Fe doped ZnO (Fe-ZnO) samples and its utilization to sense low concentrations of ethanol vapour were investigated herein. The changes in structure, surface topology, electrical and optical properties of films were studied using X-ray diffraction (XRD), scanning electron microscope (SEM), energy dispersive X-ray (EDX) and UV-Vis spectroscopy. The impact of Fe doping into ZnO towards ethanol vapour detection were reported.

2. EXPERIMENTAL

2.1 Film Preparation

ZnO films were deposited on glass substrate using 0.35M ethanol solution of zinc acetate along with diethanolamine. Same molar ferric nitrate tetrahydrate solution was added as a dopant into the zinc acetate precursor solution. All the chemicals used here were of analytical grade. Prior to this, the glass substrates were rinsed systematically with acetone and deionised water in an ultrasonic bath and then dried in the hot air oven at 50ºC for 30 minutes to get free from foreign materials. The undoped and 1-4% Fe-doped ZnO thin films were deposited on glass substrate by using a spin coater with 3000 rpm and spin time of 30 secs which were finally annealed in air at 450ºC for 1 hr. The process is repeated few times to deposit another layer to get desire thickness [23].

2.2 Characterization of ZnO films

The structural investigation of above prepared ZnO thin films were done using X-ray diffraction (XRD) with Cu-K_α radiation (1.54056 Å) in the 2θ range from 20 to 80º. The crystallite size (D) was estimated using Debye-Scherer's equation [24]:

$$D = \frac{K\lambda}{\beta cos\theta} \dots\dots\dots\dots\dots\dots\dots (1)$$

where k (0.94), λ, β and θ are shape factor, x-ray wavelength , full width half maximum and Bragg's angle respectively. The surface morphology, film composition and optical spectra of these films were studied using ZEISS scanning electron microscope, energy dispersive X-ray spectrum and UV-Vis spectrophotometer correspondingly.

2.3 Sensor performance

A gas sensing device consisted of air tight glass chamber having two openings, inlet and outlet, along with a heating device was used to measure change in resistance of film before and after exposing ethanol vapour in the temperature range of 100–300ºC. The operating temperature of heater was controlled by varying the current of heating coil using a variable voltage regulator. The initial temperature inside the chamber was maintained at 100ºC above the boiling point of ethanol to prevent the formation of liquid ethanol. The response (R) of the ZnO films towards ethanol was calculated by using the following formula:

$$R = \frac{R_a}{R_g} \dots\dots\dots\dots\dots\dots\dots (2)$$

where R_a and R_g are the resistances of the sensing element in the air and gas respectively [25]. The

corresponding response time, defined as the time required to change its response by 90% of maxima after injecting test gas from the setup.

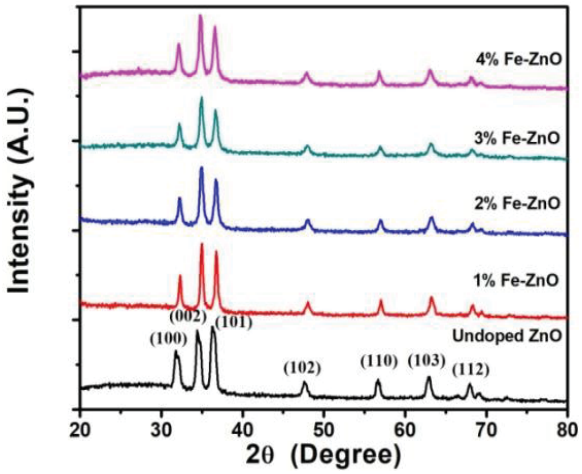

Figure 1. X-ray diffraction pattern of ZnO films

3. RESULTS AND DISCUSSION

3.1. Structural properties

Figure 1 shows the x-ray diffraction pattern of spin coated undoped and 1-4% Fe-ZnO thin films. The pattern showed that the undoped ZnO was of polycrystalline nature with diffraction peaks orientated along (100), (002), (101), (102) (110), (103) and (112). The purity of the film deposited was checked with respect to the standard d-spacing of ZnO from JCPDS card no., 36-1451. Similar XRD patterns with major peak orientations along (100), (002), and (101) but slightly shifting towards larger angle were found for 1-4% Fe-ZnO indicating decrease of d-spacing after Fe doping. This may be due to substitution of Zn^{+2} ions (0.74 Å) by smaller ionic radius Fe^{3+} (0.68 Å). The sharp and intense high intensities of (002) diffraction peaks found in all the Fe-ZnO samples show preferred c-axis orientation. Table 1 below illustrates the measured average crystallite size, D values corresponding to major peaks (100), (002) and (101) of undoped and 1-4% Fe-ZnO films using Debye Scherrer's formula (equation 1). The value of crystallite size of undoped and 1% Fe-ZnO was about 23 nm. For

Table 1. Determination of d-spacing and crystallite size of spin coated ZnO samples

Sample	Plane (hkl)	2θ (degree)	d (Å)	d (Å) JCPDS	Average D (nm)
Undoped	(100)	31.7541	2.8156	2.8143	23
	(002)	34.4202	2.6034	2.6033	
	(101)	36.2394	2.4732	2.4759	
1%Fe-ZnO	(100)	32.2501	2.7735	2.8143	23
	(002)	34.9135	2.5677	2.6033	
	(101)	36.7189	2.4456	2.4759	
2%Fe-ZnO	(100)	32.2106	2.7717	2.8143	19
	(002)	34.8792	2.5659	2.6033	
	(101)	36.6756	2.4444	2.4759	
3%Fe-ZnO	(100)	32.1838	2.7791	2.8143	17
	(002)	34.8766	2.5704	2.6033	
	(101)	36.6371	2.4508	2.4759	
4%Fe-ZnO	(100)	32.0905	2.7869	2.8143	16
	(002)	34.7727	2.5779	2.6033	
	(101)	36.5402	2.4571	2.4759	

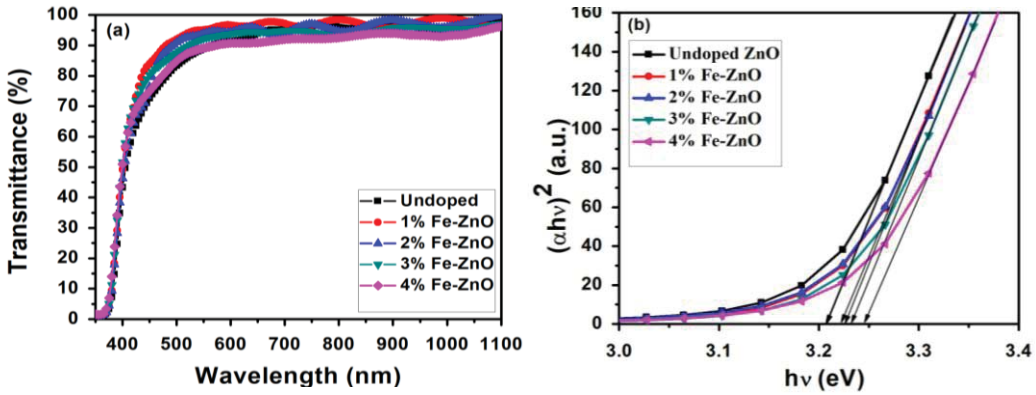

Figure 2. (a) Transmittance and (b) Band gap of undoped and 1-4% Fe-doped ZnO films

increasing Fe concentrations, the value of D continuously decreased from 23nm for 1% Fe-ZnO to 16 nm for 4% Fe-ZnO film. This change in crystallite size produces strains in the film which leads to change in surface morphology of Fe-ZnO films [26].

3.2. Optical properties

Figure 2a shows the optical transmission spectra of undoped and Fe-doped ZnO samples captured in the wavelength range 300-1100 nm at room temperature. The transmittances of as-prepared films were more than 80%. The graph showed sharp decrease of transmittance at short wavelengths near the ultra-violet range but improved in the visible range for Fe-ZnO films. The band gap (E_g) of ZnO films were calculated from the tauc plot (Figure 2b) described by the equation:

$$(\alpha h\nu)^2 = A(h\nu - E_g) \dots\dots\dots\dots\dots\dots (3)$$

where α, A, hν, and E_g are the absorption coefficient, energy constant, photon energy and band gap respectively [27]. The results showed E_g increases from 3.208 eV for undoped to 3.247 eV for 4% Fe doping sample. This increase in E_g due to Fe doping was found to be consistent with the reports on similar system due to decrease in grain size of MOS film [28]. If Fe^{3+} ions substitute the Zn^{2+} ions from their lattice sites, the additional free charge carriers were added which were responsible for shifting the Fermi level into conduction band to increase the band gap of Fe-ZnO films.

3.3 Surface morphology

Surface morphology of as deposited ZnO films was investigated by using Scanning Electron Microscopy (SEM).

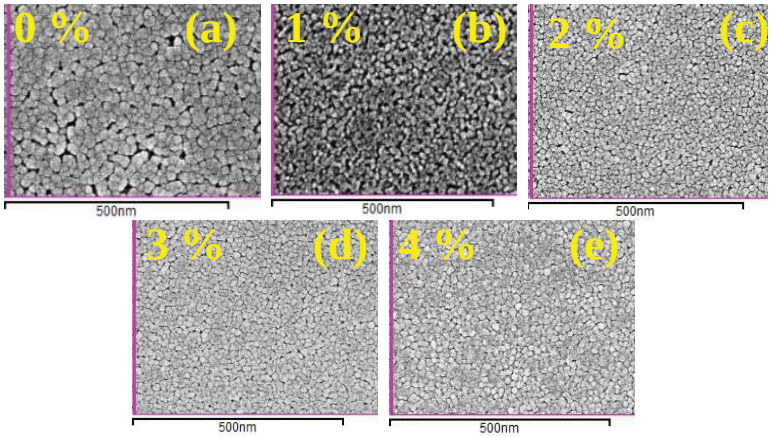

Figure 3. SEM micrographs of undoped and Fe-doped ZnO

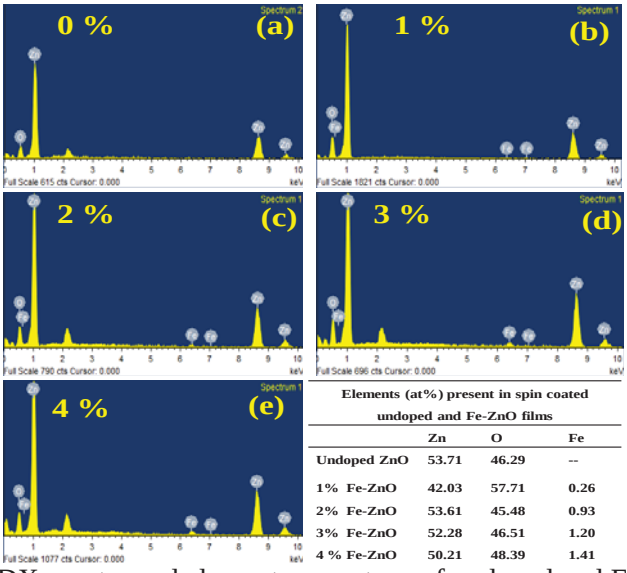

Elements (at%) present in spin coated undoped and Fe-ZnO films

	Zn	O	Fe
Undoped ZnO	53.71	46.29	--
1% Fe-ZnO	42.03	57.71	0.26
2% Fe-ZnO	53.61	45.48	0.93
3% Fe-ZnO	52.28	46.51	1.20
4 % Fe-ZnO	50.21	48.39	1.41

Figure 4. EDX spectra and element percentage of undoped and Fe-doped ZnO

Figure 3(a) through 3(e) shows the SEM images of undoped and 1-4% Fe doped ZnO films respectively. The images clearly showed the agglomeration of ZnO grains with decreasing grain size for increasing doping concentration in the Fe-ZnO films. Compared to undoped and 1% Fe-ZnO films, the 2% Fe-doped ZnO film showed significant decreased grain size. When the grain size decreases, its specific surface area increases and more oxygen molecules are adsorbed which leads to enhance the sensing property of ZnO sensors [29]. Figure 4 shows the energy dispersive X-ray diffraction (EDX) spectra of the undoped and Fe-doped thin films. The EDX patterns reveal the presence of Zn, O and Fe elements, which confirms the purity of products and successful doping of Fe-ions into host ZnO structure. Inset of figure 4 shows the atomic % of elements content in the prepared ZnO samples.

3.4 *Sensing characteristics*

Since the performance or response of the MOS gas sensor at the given temperature is proportional to the reaction rate

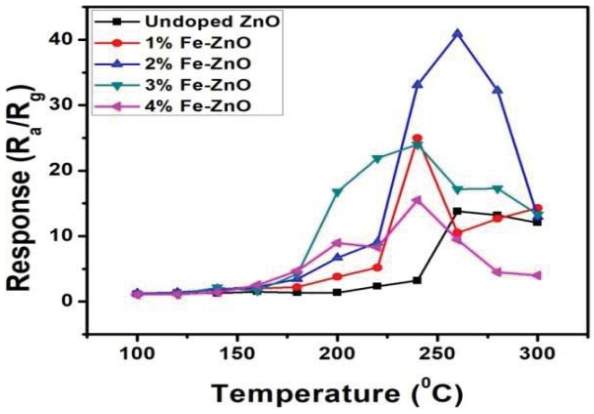

Figure 5. Response of undoped and 1-4% Fe-ZnO films at different temperatures

and activation energy (E_a), the optimization of its working temperature is required prior to measure its sensitivity. The activation energy (E_a) is described by Arrhenius equation [29-31]. During the process, when thermal energy approaches the limit to overcome the activation energy barrier of reaction, charge concentrations significantly increase and a high response results [30, 32]. Above this optimum value desorption of oxygen molecules occurs from the ZnO surface which can reduce response of gas sensor.

In this investigation, the sensor response is measured in terms of resistance change. The resistances of undoped and Fe doped ZnO films were measured in air and in ethanol vapour separately in the temperature range from 100 to 300ºC to optimize the working temperature and the gas response (R) is calculated using equation (2). The response of all the samples increased with temperature till it attains the saturated value after which decreases as shown in figure 5. The working temperature undoped and 1-4% Fe-ZnO samples were found to be 260, 240, 260, 240 and 240ºC correspondingly. The table 2 illustrates the measured values of R of undoped and 2% Fe doped ZnO films. Figure 6(a) illustrates the gas response of undoped and 1-4% Fe-ZnO at their respective working temperatures with various concentrations of ethanol (40-400 ppm). It clearly showed increasing response for increasing ethanol concentration. The result showed highest response of 40.91 for 2% Fe-ZnO at 260 ºC. This enhancement in R of Fe-ZnO samples with respect to undoped ZnO may be due to increase in its specific surface area (surface to volume ratio) and due to increase in carrier concentration after Fe doping in to the ZnO [33]. In Fe-ZnO samples, the substitution of Zn^{2+} ions by Fe ions (Fe^{3+}) surpluses the charge carriers that aids to enhance the reaction rates of exposed gas with adsorbed oxygen species in the measurement of gas response. This may be the primary reason to show higher gas response in Fe-ZnO samples than undoped sample. These results are consistent with the report published by Yu et al, 2011[3]. But, at very higher concentration of Fe doping such as 3 and 4% in our case more scattering atoms may available on the ZnO surface [34] that decreases the surface reaction rate and declines the oxygen capturing sites [35] and hence the response is reduced further. For clarity the graph of response of undoped ZnO and 2% Fe-ZnO along with the calculated value of response and recovery times are shown in figure 6(b). The measured values of gas response, response and recovery times of all ZnO samples are shown in table 3.The response time and recovery time were observed to be 27 sec and 288 sec in 2% Fe-ZnO sample at 400 ppm of ethanol.

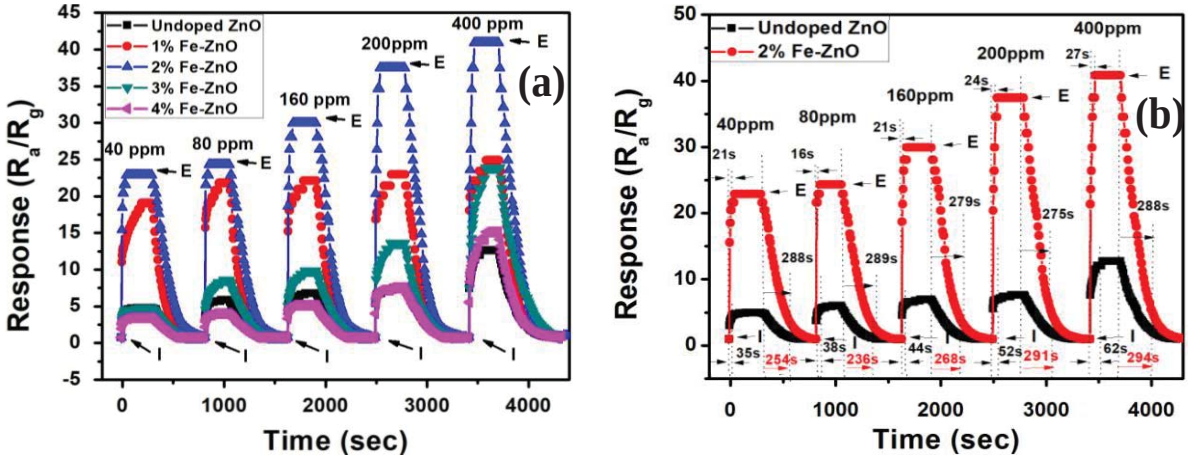

Figure 6. (a) Gas response of undoped and 1-4% Fe-ZnO films at its operating temperatures at various concentrations of ethanol (b) Zoom in response values of undoped and 2%Fe-ZnO along with measured values of response and recovery times.

Table 2. Comparison of performance of ZnO based ethanol sensor in this work with reported work

Materials	Method	Operating Temperature. (°C)	Ethanol (ppm)	Response (R_a/R_g)	Reference
Fe-ZnO	Hydrothermal	400	500	~ 55	[3]
CuO	Micro-wave assisted hydrothermal	210	1000	9.8	[10]
ZnO	Thermal Evaporation	250	50	14.4	[11]
Sn-ZnO	Thermal oxidation reaction method	340	1000	30.4	[12]

Ti-ZnO	Furnace system with hot wire assistance	250	500	2.76	[13]
ZnO	Micro-wave assisted	350	500	250	[20]
Al-ZnO	Sol–gel method.	500	2000	92	[25]
Fe-ZnO	Hydrothermal/dip coating	250	500	19	[30]
Fe-ZnO	RF magnetron sputtering	300	300	2.91	[33]
Ce-ZnO	Dip Coating	320	100	80%	[34]
Fe-ZnO	Spin Coating	260	400 40	40.9 22.9	This work

Table 3. Gas response and response time and recovery time of ZnO and 2% Fe-ZnO at different ppm of ethanol

Ethanol Concentration (ppm)	Undoped ZnO			2% Fe-ZnO		
	Gas Response ($R_a/R_{g)}$	Response time (sec)	Recovery Time (sec)	Gas Response (R_a/R_g)	Response time (sec)	Recovery Time (sec)
40	5	35	254	22.9	21	288
80	6	38	236	24.4	16	289
160	7	44	268	30.0	21	279
200	7.7	52	291	37.5	24	275
400	12.8	62	294	40.9	27	288

4. CONCLUSIONS

In summary, the undoped and various Fe (1, 2, 3 & 4%) doped ZnO thin films were prepared using an economic and effective spin coating technique where doping percentage can be easily controlled. The XRD characterization showed polycrystalline wurtzite structure nature ZnO films along with slight disturbance in microstructure of ZnO due to Fe doping was confirmed by X-ray diffraction pattern. The purity of as-prepared films was confirmed by XRD as well as EDX spectra. The observation of increasing trend of band gap for increasing doping percentage agreed with reported value. The reduced grain size of ZnO after Fe doping shown by SEM images aided in increasing the surface to volume ratio and available more electron transport due substitution of Zn^{2+} ions by Fe^{3+} be the primary reasons to observe enhanced gas response in 2% Fe-ZnO film. The highest response measured with 2% Fe doped ZnO was 40.91 and corresponding response and recovery times were 27 and 288 secs respectively at 400 ppm ethanol. Finally, this work also reports that the fabrication of economic but efficient MOS based gas sensor which can be utilized to detect as small as 40 ppm of ethanol vapour.

ACKNOWLEDGEMENT

The author would like to acknowledge University Grants Commission (UGC), Nepal, and Research Centre, Tribhuvan University, Kirtpur Nepal for providing partial financial support to complete this work. The authors also thank Nepal academy of Science and Technology (NAST), Nepal and Indian Institute of Science (IIT), Roorkee, Uttarakhand, India for completing completing XRD, SEM & EDX experiments.

REFERENCES

[1]. Ansari A, Kaushik A, Solanki P R and Malhotra B D 2008 *Electrochem. Commun*. **10** 1246
[2]. Cui J, Shi L, Xie T, Wang D and Lin Y 2016 *Sens. Actuators B* **227** 220
[3]. Yu A, Qiua J, Pan H, Cui Y, Xu M, Tu L, Chai, Q and Zhou X 2011 *Sens. Actuators B* **158** 9

[4]. Mani G K and Rayappan J B B 2015 *Sens. Actuators B* **223** 343
[5]. Mun Y, Park S, An S, Lee C and Kim H W 2013 *Ceram. Int*. **39** 8615
[6]. Hosseini Z S, Irajizad A and Mortezaali A 2014 *Sens. Actuators B* **207** 865
[7]. Camagni P, Faglia G, Galinetto P, Perego C, Samoggia G and Sberveglieri G 1996 *Sens. Actuators, B* **31** 99
[8]. Comini E, Cristalli A, Faglia G, Sberveglieri G 2000 *Sens. Actuators B* **65** 260
[9]. Neri G, Bonavita A, Galvagno S, Siciliano P and Capone S 2002 *Sens. Actuators B* **82** 40
[10]. Yang C, Su X, Xiao F, Jian J and Wang J 2011 *Sens. Actuators B* **158** 299
[11]. Bhatia S, Verma N and Bedi R K 2017 *Results Phys.* **7** 801
[12]. Santhaveesuk T and Choopun S 2013 *Adv. Mater. Res.***770** 185
[13]. Hsu C L, Gao Y D and Chen Y S 2014 *Sens. Actuators B* **192** 550
[14]. Bandyopadhyay S, Paul G K and Sen S K 2002 *Sol. Energy Mater. Sol. Cells* **71** 103
[15]. Shakti N and Gupta P S 2010 *Appl. Phys. Res.* **2** 19
[16]. Nicholas N J, Franks G V and Ducker W A 2012 *Cryst. Eng. Comm.* **14** 1232
[17]. Ghaffarian H R, Saiedi M, Sayyadnejad M A and Rashidi A M 2012 *Iran. J. Chem. Chem. Eng* **30(1)** 1
[18]. Zhang Y, Wu L, Li J, Han L, Wang B, Tuo Z and Xie E 2009 *J. Alloys Compd.* **473** 319
[19]. Ariyakkani P, Laksmikanthan S and Balakrishana S 2017 *J. Alloys Compd.* **695** 3467
[20]. Hamedani N F, Mahjoub A R, Khodadadi A A and Mortazavi Y 2011 *Sens. Actuators B* **156** 737
[21]. Poloju M, Jayababu N and Reddy M V R *Mater. Sci. Eng. B* **227** 61.
[22]. Shrestha S P, Ghimire R, Nakarmi J J, Kim Y S, Shrestha S, Park C Y and Boo J H 2010 *Bull. Korean Chem. Soc.*, **31** 112.
[23]. Rambu A P, Nica V, and Dobromir M 2013 *Super lattices Micro struct.* **59** 87
[24]. Srinivasulu T, Saritha K and Reddy K T R 2017 *Mod. Electron. Mater.* **3** 76
[25]. Liu X, Pan K, Li W, Hu D, Liu S and Wang Y 2014 *Ceram. Int.* **40** 9931
[26]. Xu L and Li X 2010 *J. Cryst. Growth* **312** 85
[27]. Cheng W and X. Ma 2009 *J. Phys.:Conf. Ser.* **152** 012039.
[28]. Liu C, Meng D, Pang H, Wu X, Xie J, Yu X, Chen L and Liu X 2012 *J. Magn. Magn. Mater.* **324** 3356
[29]. Hongsith N, Wongrat E, Kerdcharoen T and Choopun S 2010 *Sens. Actuators B* **144** 67
[30]. Khayatian A, Safa S, Azimirad R, Kashi M A and Akhtarianfar S F 2016 *Physica E: Low Dimen Syst Nanostruct* **84** 71
[31]. Sawalha A, Abu-Abdeen A and Sedky A 2016 *Physica B,* **404** 1316
[32]. Dey A 2018 *Mater. Sci. Eng. B* **229** 206
[33]. Hassan M M, Khan K, Naqvi A H, Mishra P and Islam S S 2014 *J. Mater. Sci.* **49** 6248
[34]. Ge C, Xie C and Cai S 2007 *Mater. Sci. Eng. B* **137** 53
[35]. Zhang W H, Zhang W D and Zhou J F 2010 *J. Mater. Sci.* **45** 209

Journal of Physical Science, Vol. 32(2), 15–26, 2021

Green Synthesis of Zinc Oxide Nanoparticles Using *Ixora Coccinea* Leaf Extract for Ethanol Vapour Sensing

Leela Pradhan Joshi, Bal Vikram Khatri, Sumana Gyawali, Shiromani Gajurel, and Dinesh Kumar Chaudhary*

Department of Physics, Amrit Campus, Tribhuvan University, Kathmandu, 44600, Nepal

*Corresponding author: dinesh.chaudhary@ac.tu.edu.np

Published online: 25 August 2021

To cite this article: Joshi, L. P. et al. (2021). Green synthesis of zinc oxide nanoparticles using *Ixora Coccinea* leaf extract for ethanol vapour sensing. *J. Phys. Sci*., 32(2), 15–26. https://doi.org/10.21315/jps2021.32.2.2

To link to this article: https://doi.org/10.21315/jps2021.32.2.2

ABSTRACT: *This article reports the effects of natural plant proteins on the morphology of zinc oxide nanoparticles (ZnONPs) prepared via a precipitation method. Green synthesised ZnONPs have a wide range of uses such as biomedical applications, water purification, optical devices and gas sensors. The non-toxic and economical technique described in this article is favourable for large-scale production too. ZnONPs were produced from a zinc acetate precursor with dye extract of Ixora Coccinea (IC) leaves as a capping agent. The as-prepared ZnONPs were characterised by X-ray diffraction (XRD), Fourier transform infrared (FTIR), UV-visible (UV-vis), scanning electron microscopy (SEM) and energy dispersive X-ray (EDX) techniques. The XRD analysis showed an average crystallite size of 23 nm. The SEM analysis revealed a reduction in aggregation of ZnO crystallites due to addition of dye extracts of IC. EDX and UV-vis results confirmed the formation of pure ZnONPs. Finally, the gas sensing properties of ZnO films, prepared by doctor blade method, were used to detect ethanol vapour. The results showed gas response ratios of 28.7 and 5.4 at 800 ppm and 40 ppm exposure, respectively. Furthermore, the response time and recovery time were found to be 24 sec and 47 sec, respectively at 200 ppm exposure of ethanol vapour.*

Keywords: green synthesis, metal oxide semiconductor, nanoparticles, *Ixora Coccinea*, gas response

1. INTRODUCTION

Nanomaterials are classified based on their size. Their size ranges from one to a few hundred nanometers. Materials at this scale show enhanced physical and chemical properties as compared to their bulk size. Nanoparticles of metal and metal oxide semiconductors (MOS) such as silver, iron oxide, tin oxide and zinc oxide are currently being used in several technologies such as photocatalytic dye degradation, biomedical and optoelectronic devices and gas sensing.[1–5] Among various MOS nanoparticles, zinc oxide nanoparticles (ZnONPs) have garnered significant attention for their use in applications such as gas sensors, biosensors, pollution control and piezoelectric devices. This is primarily because of their high mobility and reactivity, biocompatibility and high chemical and thermal stability.[6–7] As such ZnONPs present an opportunity to further develop material science.

ZnO possesses fascinating properties such as a large band gap (3.37 eV) and exciton binding energy (60 meV), high transparency and easy tuning of electrical and optical behaviour. ZnO can be prepared to different morphologies such as nanoflowers, nanoparticles, nanosheets, nanorods, nanowires and hexagonal prismatic crystals using various conventional and new green synthesis methods.[8–11] Many of the available conventional physical and chemical processes used to synthesis metal oxide semiconductor nanoparticles (MOSNPs) are expensive and energy intensive.[9] They also produce substantial quantities of toxic byproducts, prompting concerns for waste storage and removal. On the other hand, the green synthesis method, wherein plant extracts are used to prepare metal and metal oxide nanoparticles, is a cost-effective and alternative route with a reduced toxic waste load.[12–20] Currently, ZnONPs have been synthesised using the extracts of *Aloe barbadensis miller*, *Black tea, Citrus aurantifolia*, *Peltophorumpterocarpum, Cyanometraramiflora* and surfactants such as sodium dodecyl sulfate (SDS), cetyltrimethylammonium bromide (CTAB).[21–26] However, there has been limited work done on the synthesis of ZnONPs using dye extracts of the leaves from *Ixora Coccinea* (IC).[27]

Since the sensing performance of ZnO sensor depends on the interactions of gas molecules with the adsorbed oxygen ions (O_2^- or O^-/O^{2-}) on its surface, the surface morphology of ZnO plays an important role. The surface structure of ZnO can be modified by strategies like metal doping and surface treatment.[28–29]Among them, the addition of proteins and other phytochemicals from the natural plant is considered a significant one as it enhances the stability of the nanoparticles.[19] In this process, the extract's presence not only aids in controlling the growth parameters such as aggregation of crystallites but also forms pure and narrow

particle size distributed materials.[27] The present study describes the preparation of ZnONPs using dye extracts of IC leaves, its characterisation and its utilisation in the detection of ethanol vapour.

2. EXPERIMENTAL

2.1 Materials

IC leaves were collected from Calicut, Kerala, India. The most significant compounds in this plant extract are its hydroxyl and carbonyl groups. The phenolics and alkaloids present in the extract are responsible for capping the ZnO nanoparticles.[27] Zinc acetate dehydrate was used as a metal ion precursor and sodium hydroxide (NaOH) as a precipitating agent.

2.2 Preparation of the Dye Extract

First, fresh leaves of the IC plant were washed several times with distilled water. Then, they were dried and grinded at room temperature. Ten grams of grinded leaves were mixed with 40 ml of distilled water and heated to 60°C for 30 min, followed by filtration to remove the solid extract. Finally, the fine solution of dye extract of IC was preserved in a vessel for further study.

2.3 Preparation of ZnONPs and Film

An aqueous solution of 0.5M zinc acetate dehydrate was mixed with 10 ml of above-prepared dye extract. The 2.0M NaOH was added drop wise to this solution while stirring continuously for 2 h. The pH of the mixture solution was maintained at 12. The precipitate was then washed and left for a day for sedimentation to occur. Afterward, it was separated from the upper supernatant liquid by a simple decantation process followed by centrifuging vigorously four times at 1,500 rpm for 10 min each. Finally, the yield was dried at 100°C in a dry air oven for 16 h. A sample of ZnONPs without the dye extract was also prepared following the same procedure for comparison. Both sets, ZnONPs with IC and ZnONPs without IC, were then deposited on a transparent conducting fluorine-doped tin oxide (FTO) substrate using the conventional doctor blade method. The deposited ZnO films were annealed at 550°C inside the muffle furnace. Finally, the film's sensing performances were tested with various concentrations of ethanol vapour.

3. RESULTS AND DISCUSSION

3.1 X-ray Diffraction (XRD)

The structural properties of ZnONPs prepared by the precipitation method were studied using XRD with Bruker D2 Phaser (Germany) Diffractometer of Cu-K_α radiation of wavelength 1.54184 Å at 30 kV operating voltage and 10 mA current in the 2θ range of 20° to 80° at a scanning rate of 0.33 degree per second at Charotar University of Science & Technology, CHARUSAT-Campus, India. The crystallite size (D) was calculated using Debye Scherrer's formula: $D = \frac{0.9\lambda}{\beta \cos \theta}$ where 0.9 is the correction factor, λ is the wavelength of the X-radiation, β is the full width half maximum (FWHM) measured in radian of the diffraction peak and θ is the Bragg's angle.[14] The XRD powder patterns of ZnONPs prepared with and without IC are shown in Figure 1. The figure illustrated multiple peaks oriented along (100), (002), (101), (102), (110), (103), (200), (112), (201), (004) and (202). All the peaks are indexed concerning the standard JCPDS values of card number 36-1451.[24] The multiple sharp peaks observed in the XRD patterns are characteristics of the polycrystalline nature of ZnO. The calculated values of average crystallite size (D) and lattice parameters of both sets of ZnONPs are shown in Table 1. The result showed the average value of D was 23.80 nm for ZnONPs prepared with IC and 22.02 nm for ZnONPs without IC. The c/a ratio

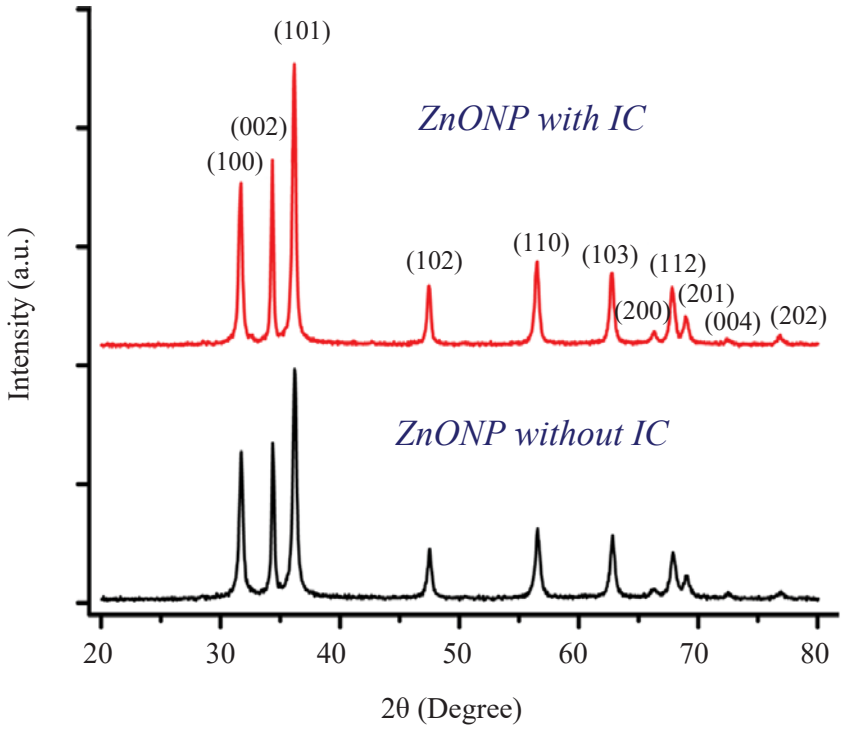

Figure 1: XRD patterns of as-prepared ZnONPs.

for both samples was 1.6 suggesting the wurtzite hexagonal phase of ZnO. There was no observation of other impurity peaks in the XRD pattern, proving that the as-prepared ZnONPs are of high purity.

Table 1: Calculated average crystallite size and lattice parameters of ZnONPs.

Samples	Average crystallite size (nm)	Lattice parameters (Å)	
		a	c
ZnONP with IC	23.08	3.01547	5.2229
ZnONP without IC	22.02	3.25662	5.2150

3.2 Scanning Electron Microscopy (SEM)

Figure 2(a) and 2(b) illustrates the SEM images of ZnONPs prepared without and with dye extract at a resolution of 200 nm. The captured images revealed the aggregated clusters of ZnO crystallites.[24] Figure 2(b) clearly shows the less aggregated morphology of ZnONPs which was due to the presence of IC extract acting as a capping agent.

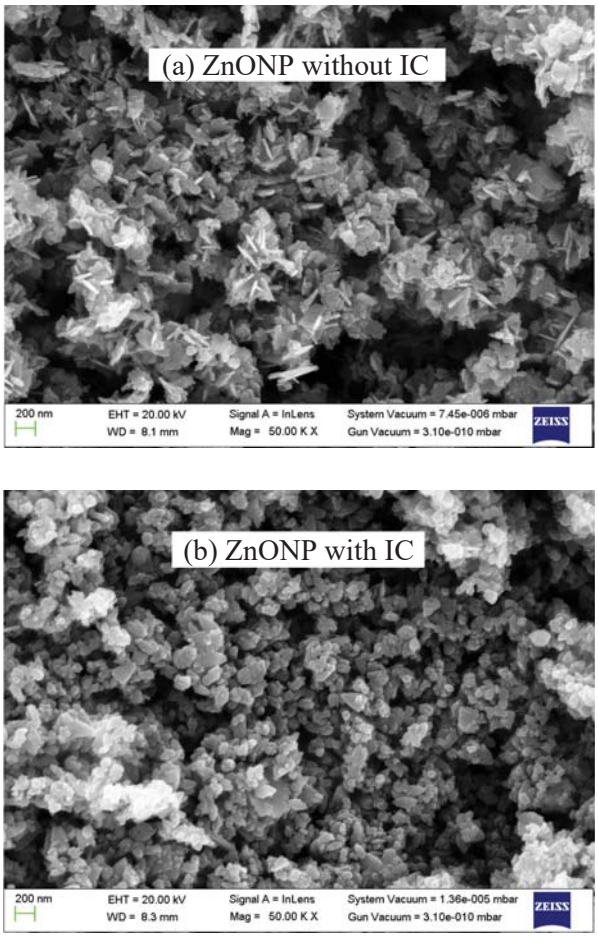

Figure 2: SEM images ZnONPs (a) without IC and (b) with IC.

3.3 Energy Dispersive X-ray (EDX) Analysis

The results of the EDX performed to uncover the elemental composition of the synthesised ZnONPs with and without dye extract, are portrayed in Figure 3. The figure clearly shows two sharp peaks at 1.0 keV and 8.5 keV and a lower one at 0.5 keV, the characteristic features of zinc and oxygen. These results agreed with the reported values.[13] The atomic percentage of the present elements were 55.43% of zinc and 44.57% of oxygen in bare ZnONPs (Figure 3[a]) and 53.80% of zinc and 46.20% of oxygen for ZnONPs prepared with IC (Figure 3[b]). The results confirmed the high purity of as-synthesised ZnONPs.

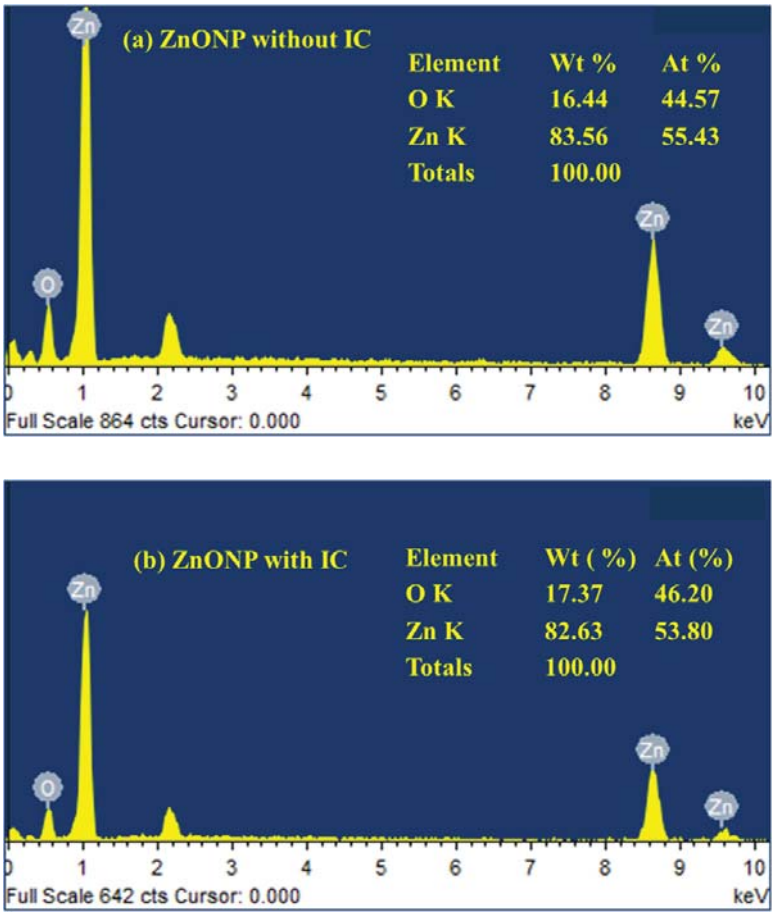

Figure 3: EDX spectra of ZnONPs (a) without IC and (b) with IC.

3.4 Fourier Transforms Infrared (FTIR) and UV-Visible (UV-vis) Spectroscopy

Figure 4(a) depicts the FTIR spectrum of ZnONPs synthesised with IC in the wavenumber range of 400 cm^{-1} to 4,000 cm^{-1}. It clearly shows major bands at 400 cm^{-1}, 574 cm^{-1}, 880 cm^{-1}, 1,407 cm^{-1}, 1,628 cm^{-1} and 3,420 cm^{-1}. The sharp infrared (IR) band extends from 400 cm^{-1}

to 650 cm^{-1} corresponding to metal oxide vibration confirmed the formation of ZnONPs. The peak at 880 cm^{-1} indicated the alkane sp^2 hybridised =C-H bond and the alkane sp^3 hybridised C-H bond bending, respectively.[12] The peaks in the regions 1,407 cm^{-1} and 1,628 cm^{-1} were ascribed to the vibrating, stretching, and bending modes of water molecules present in the sample respectively. Finally, a huge depression peak at 3,420 cm^{-1} showed the presence of hydroxyl group.[13] The UV-vis absorption spectrum was captured using an Ocean Optics spectrophotometer (Model: HR4000CG-UV-NIR, Singapore), to confirm the formation of ZnONPs as depicted in Figure 4(b). The peak observed at 340 nm as certained the formation of ZnONPs.

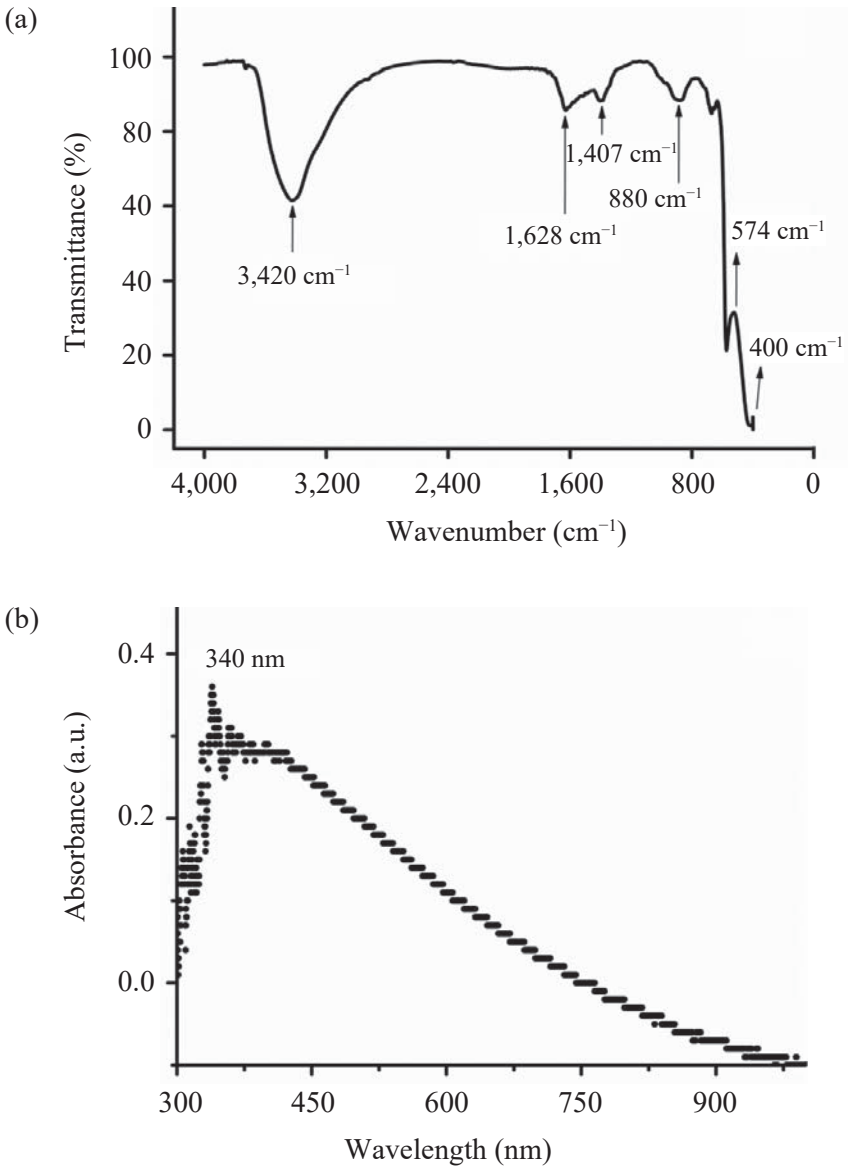

Figure 4: (a) FTIR and (b) absorbance of ZnONPs prepared with dye extract of IC.

3.5 Sensitivity Measurements

The gas response was calculated by measuring the ratio of R_a/R_g, where R_a and R_g are the resistances of ZnO measured in air and gas, respectively. The electrical resistance of MOS is a temperature-sensitive property so its working temperature must be optimised.[29] Figure 5(a) shows the optimised temperature of 285°C for both samples. Figure 5(b) illustrated the linear increment of gas response with increasing gas concentration measured at its optimised temperature. The measured values of gas response, response and recovery times were shown in Table 2. It shows a gas response of 28.7 for ZnO with IC and 37.4 for ZnO without IC at 800 ppm of ethanol exposure. The difference in these values may be due to the change in the morphology of ZnO. The gas response ratios were 5.4 and 3.5 for 40 ppm exposure of ethanol vapour. The inset in Figure 5(b) shows the response and recovery times of ZnO sensors with 200 ppm exposure of ethanol vapour for clarity. The response and recovery times were respectively 24 sec and 47 sec for ZnO with IC, whereas these values were respectively 21 sec and 27 sec for ZnO without IC.

Table 2: Gas response, response and recovery times of the ZnO sensors.

Concentration of ethanol (ppm)	ZnO without IC			ZnO with IC		
	Response R_a/R_g	Response time (sec)	Recovery time (sec)	Response R_a/R_g	Response time (sec)	Recovery time (sec)
40	3.50	15	33	5.47	23	50
80	3.97	21	27	5.56	26	51
120	4.38	23	23	6.22	25	49
160	6.20	23	25	9.94	27	46
200	19.28	21	27	10.23	24	47
400	26.16	24	27	13.63	27	49
800	37.43	19	25	28.76	26	49

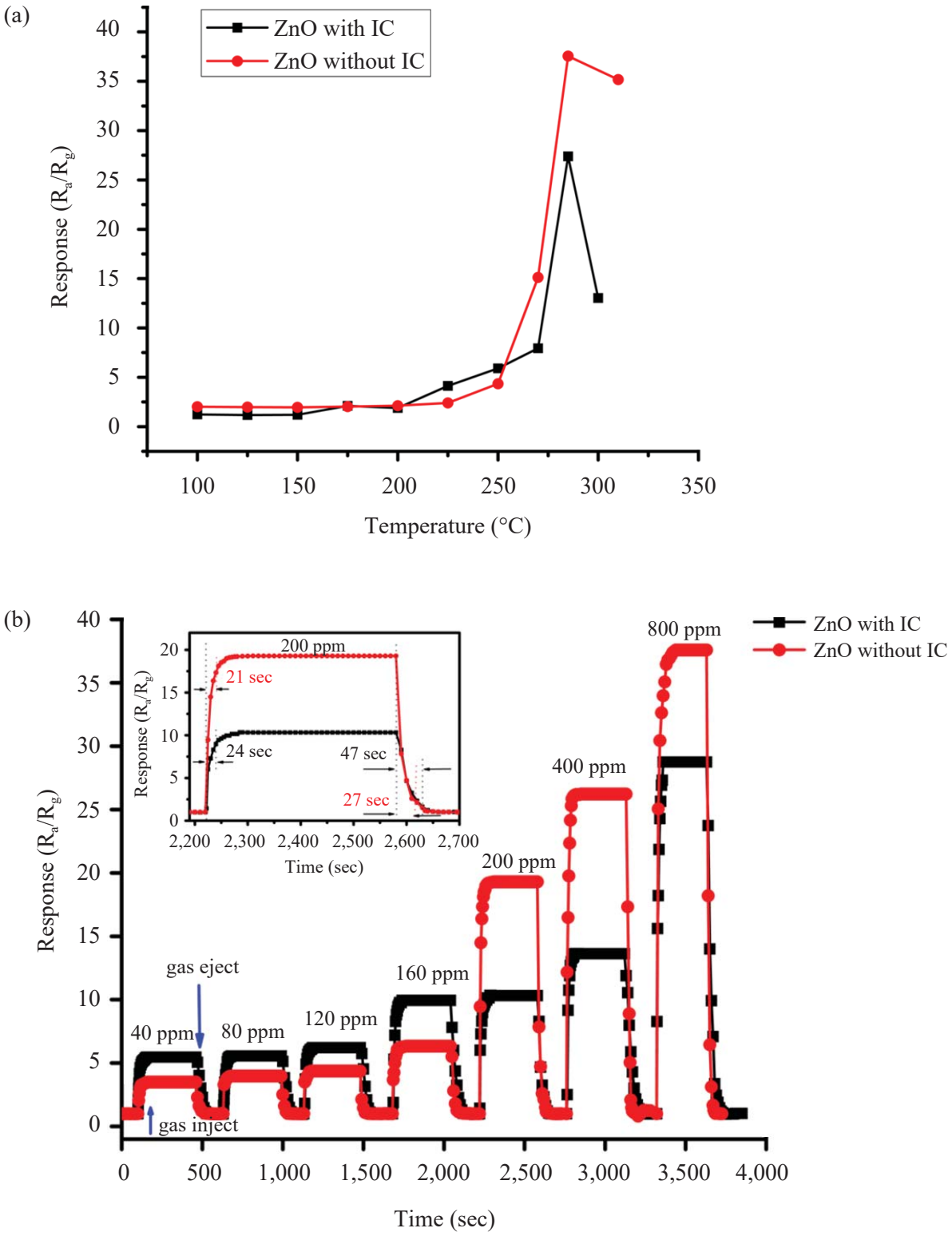

Figure 5: Response characteristics of ZnO film as a function of (a) temperature and (b) gas concentration.

4. CONCLUSION

ZnONPs were successfully fabricated using dye extract of IC leaves as a capping agent by precipitation method. Investigations of morphology, structure and dimension of ZnONPs were performed by SEM, XRD and UV-vis analyses. The average crystallite size of ZnONPs was found to be 23 nm. The SEM investigation illustrated the change in morphology of ZnO from highly clustered to less aggregate clustered of ZnO crystallites after IC dye extract was added. Furthermore, the presence of hydroxyl groups, ZnO bands and the percentage content of zinc and oxygen were established by FTIR and EDX, respectively. The sensitivity results of ZnO film prepared with IC showed a gas response ratio of 28.7 and 5.4 for the exposure of 800 ppm and 40 ppm of ethanol vapour, respectively.

5. ACKNOWLEDGEMENTS

The authors would like to thank the University Grants Commission (UGC), Nepal for providing financial support under FRG-73-74-S & T-09 to complete this research work. The authors would also like to thank Charotar University of Science and Technology CHARUSAT-Campus and the Indian Institute of Technology (IIT), India for the support in conducting FTIR, XRD, SEM and EDX experiments.

6. REFERENCES

1. Vinayagam, R. et al. (2020). Structural characterization of green synthesized α-Fe_2O_3 nanoparticles using the leaf extracts of Spodias dulcis. *Surf. Interface*, 20, 100618. https://doi.org/10.1016/j.surfin.2020.100618
2. Varadavenkatesan, T., Selvaraj, R. & Vinayagam, R. (2020). Green synthesis of silver nanoparticles using Thunbergia gradiflora flower extract and its catalytic action in reduction of Congo red dye. *Mater. Today: Proceeds.*, 23(1), 39–42. https://doi.org/10.1016/j.matpr.2019.05.441
3. Bhatia, S., Verma, N. & Bedi, R. K. (2017). Ethanol gas sensor based upon ZnO nanoparticles prepared by different techniques. *Results in Phys.*, 7, 801–806. https://doi.org/10.1016/j.rinp.2017.02.008
4. Inderan, V. et al. (2019). A comparative study of structural and ethanol gas sensing properties of pure, nickel and palladium doped SnO_2 nanorods synthesized by the hydrothermal method. *J. Phys. Sci.*, 30(1), 127–143. https://doi.org/10.21315/jps2019.30.1.10
5. Hamady, S. O. S. et al. (2019). Development of novel thin film solar cells: Design and numerical optimization. *J. Phys. Sci.*, 30 (Supp.2), 199–205. https://doi.org/10.21315/jps2019.30.s2.17

6. Fardood, S. T. et al. (2020). Facile green synthesis and characterization of zinc oxide nanoparticles using tragacanthgel: Investigation of their photocatalytic performance for dye degradation under visible light irradiation. *Nanochem. Res.,* 5(1), 69–76. https://doi.org/10.22036/ncr.2020.01.007
7. Wang, X. et al. (2006). Piezoelectric field effect transistor and nanoforce sensor based on a single ZnO nanowire. *Nano Lett.* 6(12), 2768-2772. https://doi.org/10.1021/nl061802g
8. Vinayagam, R. et al. (2020). Synthesis, characterization and photocatalytic dye degradation capability of Calliandra haematocephala mediated zinc oxide nanoflowers. *J. Photochem. and Photobiol. B: Biol.*, 203, 111760. https://doi.org/10.1016/j.jphotobiol.2019.111760
9. Liu, X. et al. (2004). Growth mechanism and properties of ZnO nanorods synthesized by plasma-enhanced chemical vapor deposition. *J. Appl. Phys.*, 95(6), 3141–3147. https://doi.org/10.1063/1.1646440
10. Fardood, S. T. et al. (2019). Green synthesis of ZnO nanoparticles via sol-gel method and investigation of its application in solvent-free synthesis of 12-Aryl-tetrahydrobenzo[α] xanthene-11-one derivatives under microwave irradiation. *Chem. Method.,* 3, 632–642. https://doi.org/10.33945/SAMI/CHEMM.2019.6.2
11. Li, S.-M. et al. (2017). Acetone sensing of ZnO nanosheets synthesized using room-temperature precipitation. *Sens. Actuators B: Chemical*, 249, 611–623. http://doi.org/10.1016/j.snb.2017.04.007
12. Vinayagam, R., Varadavenkatesan, T. & Selvaraj, R. (2017.) Green synthesis, structural characterization and catalytic activity of silver nanoparticles stabilized with Bridelia retusa leaf extract. *Green Process Synth*., 7(1), 1–8. https://doi.org/10.1515/gps-2016-0236
13. Sirdeshpande, K. D. et al. (2018). Structural characterization of mesoporous magnetite nanoparticles synthesized using the leaf extract of *Calliandra haematocephala* and their photocatalytic degradation of malachite green dye. *Appl. Nanosci.*, 8(4), 675–683. https://doi.org/10.1007/s13204-018-0698-8
14. Fardood, S. T. et al. (2020). Green synthesis, characterization, and photocatalytic activity of cobalt chromite spinel nanoparticles. *Mater. Res. Express.*, 7, 015086. https://doi.org/10.1088/2053.1591/ab6c8d
15. Gawade, V. V. et al. (2017). Green synthesis of ZnO nanoparticles by using *Calotropis procera* leaves for the photo-degradation of methyl orange. *J. Mater. Sci. Mater. Electron*, 28, 14033–14039.
16. Fardood, S. T. et al. (2019). Biosynthesis of $MgFe_2O_4$ magnetic nanoparticles and their application in photodegradation of malachite green dye and kinetic study. *Nanochem. Res.*, 4(1), 86–93. https://doi.org/10.22036/ncr.2019.01.010
17. Fardood, S. T. et al. (2019). Eco-friendly synthesis and characterization of α-Fe_2O_3 nanoparticles and study of their photocatalytic activity for degradation of Congo red dye. *Nanochem. Res.*, 4(2), 140–147. https://doi.org/10.22036/ncr.2019.02.005

18. Atrak, K., Ramazani, A. & Fardood, S. T. (2019). Green synthesis of $Zn_{0.5}Ni_{0.5}AlFeO_4$ magnetic nanoparticles and investigation of their photocatalytic activity for degradation of reactive blue 21 dye. *Environ. Technol.*, 41(21), 1581841. https://doi.org/10.1080/09593330.2019.1581841
19. Azar, B. E., Fardood S. T. & Morsali, A. (2019). Green synthesis and characterization of $ZnAl_2O_4$@ZnO nanocomposite and its environmental applications in rapid dye degradation. *Optik*, 208, 164129. https://doi.org/10.1016/j.ijleo.2019.164129
20. Vanathi, P. et al. (2014). Biosynthesis and characterization of phyto mediated zinc oxide nanoparticles: A green chemistry approach. *Mater. Lett*, 134, 13–15. https://doi.org/10.1016/j.matlet.2014.07.029
21. Sangeetha, G., Rajeshwari, S. & Venckatesh, R. (2011). Green synthesis of zinc oxide nanoparticles by aloe barbadensis miller leaf extract: Structure and optical properties. *Mater. Res. Bull.*, 46, 2560–2566. https://doi.org/10.1016/j.materresbull.2011.07.046
22. Fardood, S. T., Ramazani, A. & Joo, S. W. (2017). Sol-gel synthesis and characterization of zinc oxide nanoparticles using Black Tea extract. *J. Appl. Chem. Res.*, 11(4), 8–17. http://jacr.kiau.ac.ir/article_536676.html
23. Samat, N. A. & Nor, R. M. (2013). Sol–gel synthesis of zinc oxide nanoparticles using Citrus aurantifolia extracts. *Ceram. Int*., 39, S545–S548. https://doi.org/10.1016/j.ceramint.2012.10.132.
24. Pai, S. et al. (2019). Photocatalytic zinc oxide nanoparticles synthesis using Peltophorum pterocarpum leaf extract and their characterization. *Optik*, 185, 248–255. https://doi.org/10.1016/j.ijleo.2019.03.101
25. Ramimoghadam, D., Hussein, M. Z. B. & Taufiq-Yap, Y. H. (2012). The effect of sodium dodecyl sulfate (SDS) and cetyltrimethylammonium bromide (CTAB) on the properties of ZnO synthesized by hydrothermal method. *Inter. J. Mol. Sci.*, 13, 13275–13293. https://doi.org/10.3390/ijms131013275
26. Varadavenkatesan, T. et al. (2019). Photocatalytic degradation of Rhodamine B by zinc oxide nanoparticles synthesized using the leaf extract of Cyanometra ramiflora. *J. Photochem. & Phtobio. B: Biol.*, 199, 111621. https://doi.org.10.106/j.jphotobiol.2019.111621
27. Yedurkar, S., Maura, C. & Mahanwar, P. (2016). Biosynthesis of zinc oxide nanoparticles using *Ixora Coccinea* leaf extract—a green approach. *Open J. Synth. Theo. Appl.*, 5(1), 1–14. https://doi.org/10.4236/ojsta.2016.51001
28. Paraguay, F. et al. (2000). Influence of Al, In, Cu, Fe and Sn dopants on the response of thin film ZnO gas sensor to ethanol vapor. *Thin Solid Films*, 373, 137–140. https://doi.org/10.1016/S0040-6090(00)01120-2
29. Wei, A., Pan, V. & Huang, W. (2011). Recent progress in the ZnO nanostructure-based sensors. *Mater. Sci. Eng. B*, 176(18), 1409–1421. https://doi.org/10.1016/j.mseb.2011.09.005

molecules

MDPI

Article

Study on the Synthesis of ZnO Nanoparticles Using *Azadirachta indica* Extracts for the Fabrication of a Gas Sensor

Tirtha Raj Acharya [1,2], Pradeep Lamichhane [1], Rizwan Wahab [3], Dinesh Kumar Chaudhary [4], Bhanu Shrestha [5], Leela Pradhan Joshi [4], Nagendra Kumar Kaushik [1,*] and Eun Ha Choi [1,*]

1 Plasma Bioscience Research Center, Applied Plasma Medicine Center, Department of Electrical and Biological Physics, Kwangwoon University, Seoul 01897, Korea; tirtharajacharya2050@gmail.com (T.R.A.); theprodip@gmail.com (P.L.)
2 Department of Physics, Saint Xavier's College, Tribhuvan University, Maitighar, Kathmandu 44600, Nepal
3 Chair for DNA Research, Department of Zoology, College of Science, King Saud University, Riyadh 11451, Saudi Arabia; rwahab@ksu.edu.sa
4 Department of Physics, Amrit Campus, Tribhuvan University, Kathmandu 44600, Nepal; din.2033@gmail.com (D.K.C.); leela.pradhan@gmail.com (L.P.J.)
5 Department of Electronic Engineering, Kwangwoon University, Seoul 01897, Korea; bnu@kw.ac.kr
* Correspondence: kaushik.nagendra@kw.ac.kr (N.K.K.); ehchoi@kw.ac.kr (E.H.C.)

Abstract: This paper compared the effects of *A. indica* plant proteins over chemical methods in the morphology of zinc oxide nanoparticles (ZnO NPs) prepared by a co-precipitation method, and ethanol sensing performance of prepared thin films deposited over a fluorene-doped tin oxide (FTO) bind glass substrate using spray pyrolysis technique. The average crystallite sizes and diameters of the grain-sized cluster ZnO NPs were 25 and (701.79 ± 176.21) nm for an undoped sample and 20 and (489.99 ± 112.96) nm for *A. india* dye-doped sample. The fourier transform infrared spectroscopy (FTIR) analysis confirmed the formation of the Zn–O bond at 450 cm^{-1}, and also showed the presence of plant proteins due to *A. indica* dye extracts. ZnO NPs films exhibited good response (up to 51 and 72% for without and with *A. indica* dye-doped extracts, respectively) toward ethanol vapors with quick response-recovery characteristics at a temperature of 250 °C for undoped and 225 °C for *A. indica* dye-doped ZnO thin films. The interaction of *A. indica* dye extracts helps to decrease the operating temperature and increased the response and recovery rates of the sensor, which may be due to an increase in the specific surface area, resulting in adsorption of more oxygen and hence high response results.

Keywords: ZnO nanoparticles; *Azadirachta indica*; functional group; thin film; ethanol sensor; sensitivity; response and recovery rates

Citation: Acharya, T.R.; Lamichhane, P.; Wahab, R.; Chaudhary, D.K.; Shrestha, B.; Joshi, L.P.; Kaushik, N.K.; Choi, E.H. Study on the Synthesis of ZnO Nanoparticles Using *Azadirachta indica* Extracts for the Fabrication of a Gas Sensor. *Molecules* **2021**, *26*, 7685. https://doi.org/10.3390/molecules26247685

Academic Editor: Mariana Emilia Ghica

Received: 26 November 2021
Accepted: 17 December 2021
Published: 19 December 2021

1. Introduction

Gas tracking devices are becoming increasingly popular for a variety of physical, chemical, and biological purposes. For the detection of harmful pollutant gases, flammable gases, and organic vapors, metal oxide-based chemical sensors have been widely used. Chemical sensors have several benefits, including low cost, compact size, great sensitivity, and minimal power usage [1]. Ethanol is one of the most widely used and distributed alcohols in the fields of food technology, brewing, medicine, clinical research, and biotechnology [2–5]. Excessive ethanol consumption is harmful to living creatures. In humans, ethanol vapor exposure during development can result in ventricular and septal wall thickening [2]. As a result, detecting ethanol fumes is quite important at this time. Different metal oxide semiconductor (MOSs) such as ZnO, TiO_2, WO_3, In_2O_3, MoO_3, SnO_2, and Fe_2O_3, and multi-component oxides, such as $BiFeO_3$, Al_2O_3-ZnO, Cu-TiO_2, Cr-TiO_3, $MgAl_2O_4$, SnO_2-Pd-Pt, $SrTiO_3$, and Nb_2O_5-ZnO, are useful for UV sensing [6–8], solar cells [9], photocatalytic effects [10], and gas sensing applications [11]. Gas sensors based on the nanostructures of MOSs have a high sensitivity with short response and recovery

times [12]. In addition to the chemical properties of MOSs, the surface morphology and surface-to-volume ratio also affect the relative change in resistance of MOS gas sensors [13].

Zinc oxide (ZnO) is a set II–VI *n*-type semiconductor with a vast band gap (3.3 eV) and exceptional assets, such as high exciton binding energy (60 MeV) [14], transparency in the visible region and strong infrared reflectivity [15], excellent audio characteristics and outstanding electronic chattels [16], high electron mobility (100 cm^2 $v^{-1}s^{-1}$) [17], strong room-temperature luminescence, high chemical and thermal stability, abundance in nature, and environmental friendliness [18]. This unique property makes ZnO a proficient semiconducting material in gas sensors. The biological production of ZnO NPs utilizing plant extracts, such as leaves, roots, flowers, and seeds as a bio template, is of particular interest to researchers [12]. This green technique has various advantages, including environmentally friendliness, shorter time, lower-cost precursors, and a higher-purity result; the handling procedure is easy and does not require expensive equipment [13]. Many studies have been conducted on the green synthesis of ZnO NPs by plant leaves such as *Ixora Coccinea*, *Artocarpus gomezianus*, *Coptidis rhizoma*, *Citrus aurantifolia*, *Zingiber officinalis*, *Cyanometraramiflora*, *A. indica*, and others [19,20]. However, only a few studies on the natural synthesis of ZnO NPs using dye extracts from *A. indica* have been conducted. It is reported that the *A. indica* extracts contain approximately 140 chemical compounds [21]. The main composition of *A. indica* leaf includes crude protein (12.40–18.27%), crude fiber (11.40–23.08%), N free extract (43.32–66.60%), ether extract (2.27–6.24%), total ash (7.75–18.37%), calcium (0.89–3.96%), and phosphorus (0.10–0.30%) [22]. Incubation of benzoquinones obtained from *A. indica* leaves promoted activation of quinones, which helped to reduce particle size, according to Mathew et al. [14]. Nicole et al. reported that proteins of both high and low molecular weight play a key role in the both stability and reduction of green produced ZnO NPs [15]. Phytochemicals such as flavones, polyols, terpenoids, and plant proteins found in the *A. indica* leaf contribute functional groups of amines, alcohols, ketones, aldehydes, and carboxylic acid in bio-reduction reactions [16]. Metal compounds are converted to ZnO NPs by phytochemicals and enzymes found in the *A. indica* plant [15]. These metabolites from the *A. indica* leaf have reducing characteristics, allowing zinc ions to be quickly reduced to ZnO NPs.

The interaction of analyte gas molecules with deposited oxygen ions (O_2^- or O^-) on the MOS gas sensors determines its sensing capability, and the surface shape plays a crucial role in oxygen ion adsorption [5]. The addition of *A. indica* plant dye extracts changed the surface shape and enhanced the stability of ZnO NPs. This morphological impact in ZnO NPs is beneficial to gas sensing. A novel idea proposed in this study is the utilization of plant dye extracts in ZnO thin films for the manufacture of an ethanol gas sensor. The current research examines how *A. indica* dye extract is used to generate and analyze ZnO NPs as well as how it functions as a vapor detector.

2. Results and Discussion

2.1. Structural Analysis

The structural analysis of the prepared ZnO NPs with and without *A. indica* dye extracts was performed using X-ray diffraction (XRD). XRD testing was performed using a D_2 Phaser (Bruker, Berlin, Germany) diffractometer with CuK_α radiation (wavelength = 1.54184 Å) at an operating voltage of 30 kV and a current of 10 mA. The scanning rate was 0.33 degrees per second in the 2θ range of 20° to 80°. Figure 1 shows the XRD pattern of the as-prepared ZnO NPs. The sharp diffraction peak indicates the good crystallinity of the prepared ZnO NPs [23]. Interplanar spacing (d-spacing) was obtained using Bragg's relation: $2d \sin\theta = n\lambda$ [17], where λ is the X-ray wavelength, n is the order of reflection, and θ is Bragg's angle. The calculated values of 'd' are compared with the standard JCPDS values for indexing the (hkl) planes as demonstrated in Table 1 [24]. There were slight shifts in the 2θ values with those of the JCPDS card number 36-1451. This may be due to the strain. The comparison of the 'd' values of both samples shows only a slight decrease in 'd' values, which may be due to the doping of the parent solution with *A. indica* dye [25].

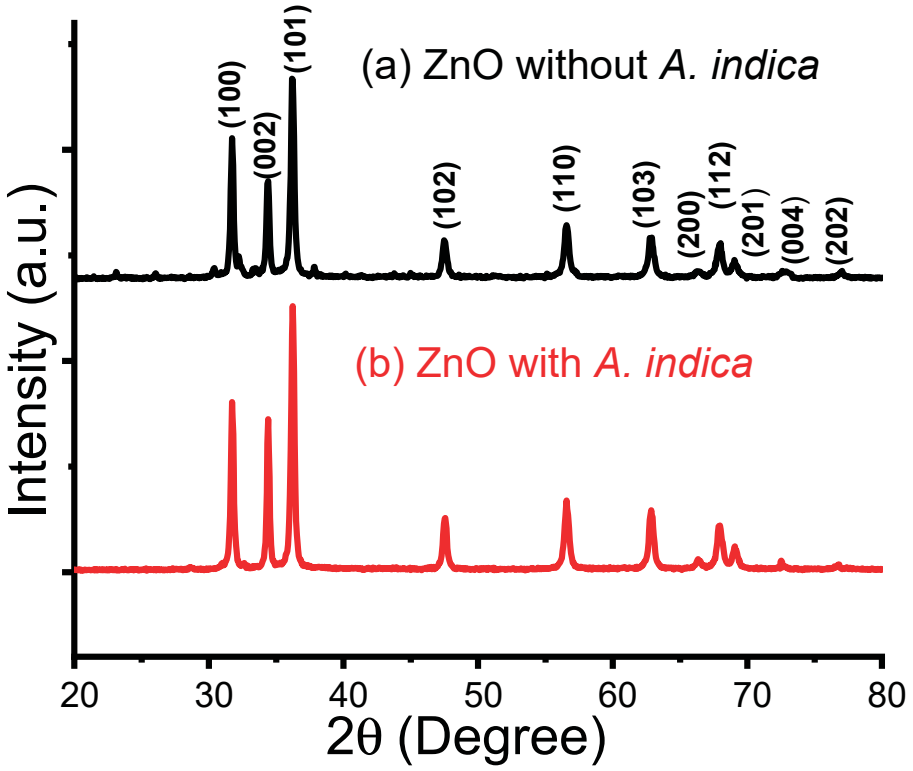

Figure 1. X-ray diffraction pattern of ZnO NPs prepared (**a**) without plant dye extracts and (**b**) with *A. indica* dye extracts.

Table 1. Calculation of d-spacing and crystallite size of prepared ZnO NPs.

Sample	Plane (hkl)	2θ (Degree)	FWHM (β)	d (nm) (Observed)	d (nm) (JCPDS)	Average D (nm)
ZnO NPs Without dye extracts	(100)	31.7279	0.2887	0.2817	0.2814	25 nm
	(002)	34.3859	0.2932	0.2605	0.2603	
	(101)	36.2159	0.3331	0.2478	0.2475	
	(102)	47.5432	0.4110	0.1911	0.1911	
	(110)	56.5770	0.4579	0.1625	0.1624	
	(103)	62.8518	0.5127	0.1477	0.1477	
	(200)	66.1982	0.3328	0.1410	0.1407	
	(112)	67.8183	0.4489	0.1380	0.1378	
	(201)	69.0333	0.4476	0.1359	0.1358	
	(004)	72.5773	0.3236	0.1301	0.1301	
	(202)	77.0325	0.3832	0.1236	0.1238	
Sample	**Plane (hkl)**	**2θ (degree)**	**FWHM (β)**	**d (nm) (Observed)**	**d (nm) (JCPDS)**	**Average D (nm)**
ZnO NPs with *A. indica* dye extracts	(100)	31.6753	0.3976	0.2823	0.2814	20 nm
	(002)	34.3385	0.2745	0.2609	0.2603	
	(101)	36.1626	0.3991	0.2482	0.2475	
	(102)	47.4574	0.3885	0.1914	0.1911	
	(110)	56.4965	0.3885	0.1627	0.1624	
	(103)	62.7772	0.4705	0.1478	0.1477	
	(200)	66.1345	0.4451	0.1411	0.1407	
	(112)	67.8529	0.5553	0.1380	0.1378	
	(201)	69.1237	0.5764	0.1357	0.1358	
	(004)	72.4312	0.6522	0.1303	0.1301	
	(202)	77.1056	0.6822	0.1235	0.1238	

The average crystallite size was estimated by measuring the broadening of the X-ray diffraction peaks observed in the XRD pattern using the Debye–Scherrer formula: $D = \frac{0.9\lambda}{\beta \cos\theta}$ [26], where 0.9 is the Debye constant, λ is the X-ray wavelength of 1.54184 Å, and β is the FWHM of the sharp peak. The average estimated value of the crystallite size of ZnO NPs without and with *A. indica* dye were 25 nm and 20 nm individually. The natural dye of *A. indica* leaf extracts contains different reducing factors, such as phytochemicals and enzymes, which carry out the significant reaction involved in the green synthesis of ZnO NPs. The dye extracts of leaves stabilize the NPs and stop them from aggregating [26].

2.2. Morphological Analysis

The peripheral morphology of ZnO NPs without and with *A. indica* dye extracts stood primarily using the scanning electron microscopy (SEM) (Ipvnano, Pune, India) analysis, and the subsequent images are shown in Figure 2. Using the ImageJ method [27], the diameter of the grain-sized cluster ZnO was estimated. The morphological features of both samples were considerably different based on the observed SEM estimation. The average diameter of the ZnO grain-sized NPs cluster was (701.79 ± 176.21) nm without dye extracts and (489.99 ± 112.96) nm with *A. indica* dye extracts. This finding suggests that the addition of *A. indica* dye extracts affects the morphology of thin films. Furthermore, the ZnO NPs were less aggregated and agglomerated for *the A. indica* dye extracts. This may be due to the strong kinship among them, which results in less accumulation or collection [24]. As a consequence, *A. indica* dye extracts greatly increase NP constancy and collection, and *A. indica* dye extracts lowered the diameter of ZnO NPs [25].

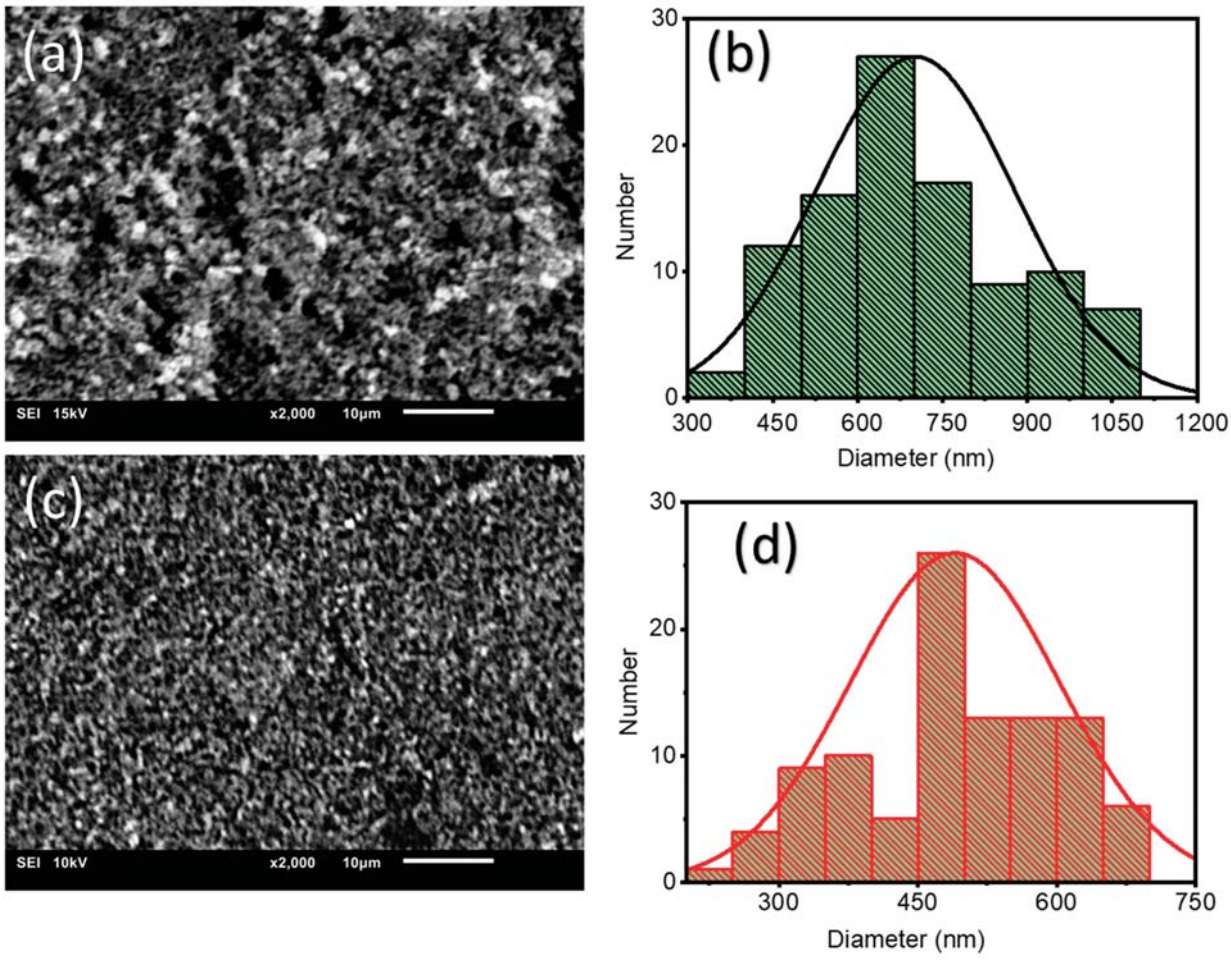

Figure 2. SEM images and cluster size distribution of the ZnO NP cluster at (**a**,**b**) 10 μm scale (without dye extracts) and (**c**,**d**) 10 μm scale (with *A. indica* dye extracts).

2.3. Energy-Dispersive X-ray Analysis

Figure 3 presents the energy-dispersive X-ray (EDX) (Ipvnano, Pune, India) spectra of the ZnO NPs without and with *A. indica* dye extracts. The EDX spectra showed the presence of Zn and O in the synthesized NPs and the purity of the prepared ZnO NPs. The sharp peaks at 1.0, 8.5, and 9.5 keV in the figure indicate the appearance of zinc, and the peak at 0.5 keV reflected the presence of oxygen. The atomic composition of the bare ZnO NPs was 51.37 and 48.63% for zinc and oxygen, respectively. The atomic spreading of the *A. indica* dye extracts was 50.03% for zinc and 49.97% for oxygen. The introduction of *A. indica* dye helped to increase the oxygen ratio slightly to the prepared ZnO NPs, which may be due to the presence of water-soluble proteins from plant extracts. Thus, from the above configuration results, we can easily confirm that the synthesized ZnO NPs of both samples gained a high degree of purity.

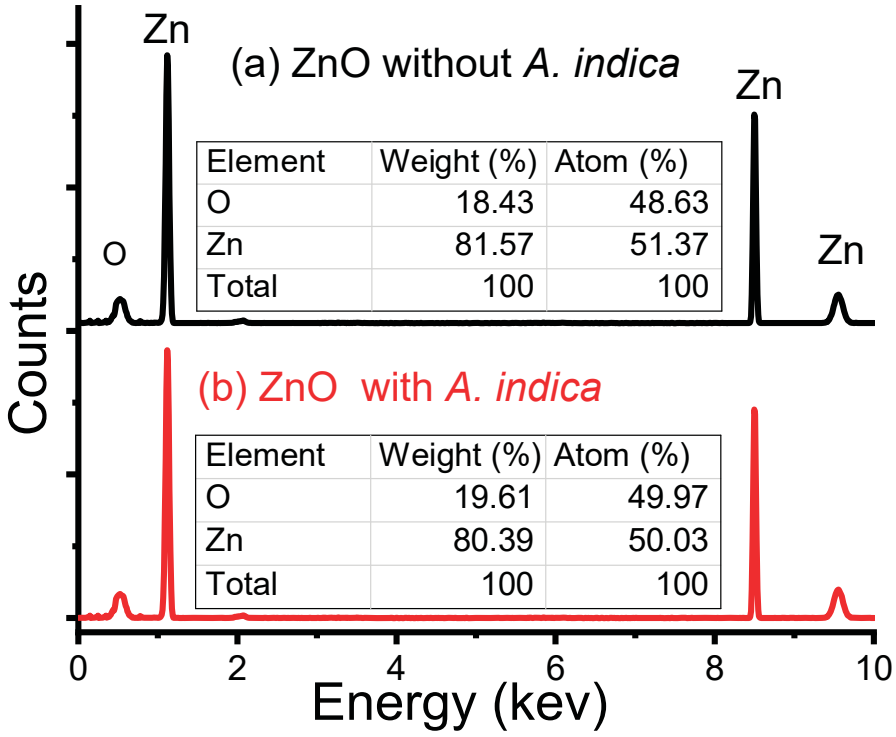

Figure 3. EDX spectra of ZnO NPs (**a**) without *A. indica* dye extracts and (**b**) with *A. indica* dye extracts.

2.4. Fourier Transform Infrared Spectroscopy Analysis

The Fourier transform infrared (FTIR) (Chem Tech Pro, 4100, Gujarat, India) spectrum presented in Figure 4 was applied to examine the cleanliness and arrangement of ZnO NPs without and with *A. indica* dye extracts. For both samples, the peaks at 450 and 527 cm^{-1} are the typical absorption of ZnO [28]. The spectra shown at 630–660 cm^{-1} are attributed to the occurrence of N-H stretching bonds and the peaks between 837 and 850 cm^{-1} are due to C-H stretching of aromatics [29]. The bands at 977 and 1094 cm^{-1} correspond to the C-N stretching of alcohol and phenolic groups, aliphatic amines, and aliphatic and aromatic amides [29]. Similarly, the spectrum bands illustrated between 1105 and 1579 cm^{-1} can be attributed to O-H and C-OH stretching vibration of polyols [30]. The extensive band at 1618 cm^{-1} might likely remain due to the C=C elongation of aromatic rings [30]. The band created at 2912 cm^{-1} likely correlated to the C-H stretching of polyols [31]. In addition, the bands at 3400, 3430, and 3615 cm^{-1} correlated with the O–H widening of the phenolic compounds in the dye extracts [31].

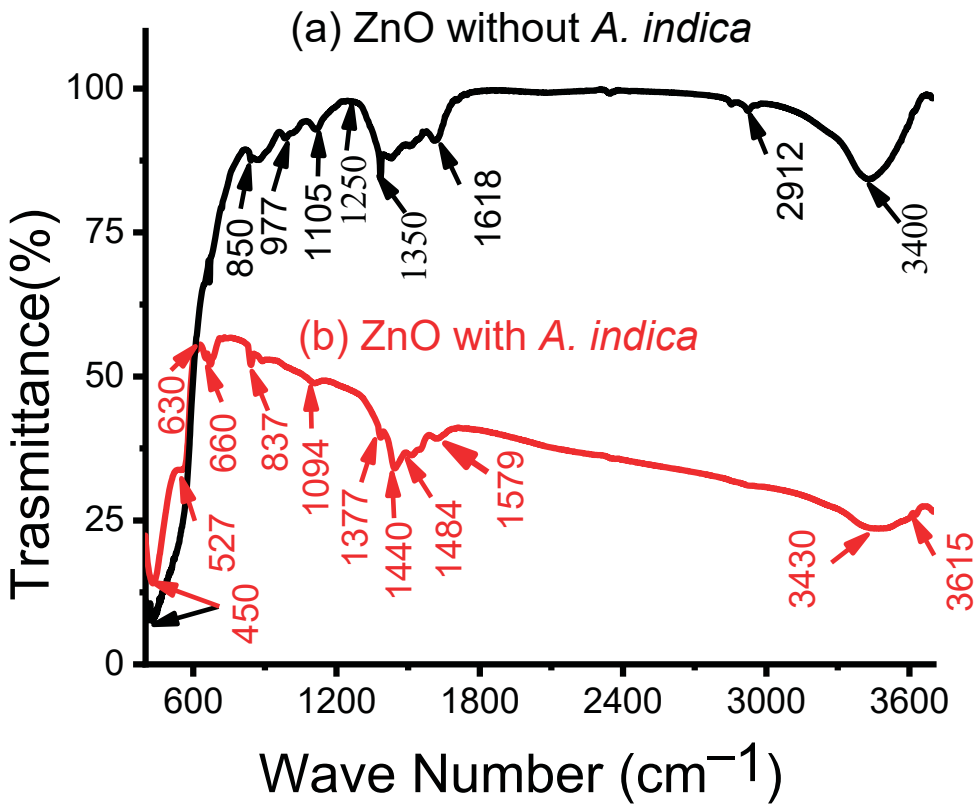

Figure 4. FTIR analysis of ZnO NPs (**a**) without dye extracts, (**b**) with *A. indica* dye extracts.

The peaks viewed in FTIR spectra of ZnO NPs after addition of *A. indica* such as 3615, 3430, 1579, 1484, 1440, 1094, 837, and 660 cm^{-1} show the presence of polyols, terpenoids, and proteins partaking functional groups of amines, alcohols, ketones, and carboxylic acid in bio-reduction responses [26]. Raphael et al. reported that proteins obtained from *A. indica* acted as a green reductant for the synthesis of NPs [32]. Terpenoids, polyols, free amino groups, carboxylic groups, alcohols, and ketones derived from *A. indica* leaf extracts play a significant role in bio-reduction reactions that are responsible for the reduction of zinc ions into ZnO NPs [23]. In addition, the several amide groups of proteins act as capping material that avoids agglomeration and makes ZnO NPs more stable [33]. Thus, the soluble substances present in the dye of *A. indica* could have acted as a capping and stabilizing agent, which averts the accumulation of NPs in the solution and plays an important part in the extracellular forge and shaping of ZnO NPs [34]. Thus, from the above results we may conclude that the soluble substances present in the dye of *A. indica* could have acted as a capping and stabilizing agent, which averts the accumulation of NPs in the solution and plays a significant role in the extracellular forge and shaping of ZnO NPs.

2.5. Sensitivity Analysis

Here, thin films of ZnO without and with *A. indica* dye extracts were coated on FTO substrates. The resistance of the FTO before and after coating the ZnO thin films was measured. The resistance of the FTO increased after the coating of thin films for both samples, confirming the ZnO thin film deposition. In this study, the response of ZnO thin films was measured with respect to the change in resistance before and after the injection of ethanol vapor. The response of an N-type semiconductor of metal oxide thin film gas sensor for reducing gases can be calculated by using Equation (1) [32].

$$R = \frac{R_a - R_g}{R_a} \times 100\% \quad (1)$$

where R is the response of a thin film in terms of change in resistance, R_a is the air resistance, and R_g is the gas resistance. One hundred parts per million of ethanol were injected into the sensing chamber, and the resistance of the ZnO thin film at different temperatures in air and ethanol vapor was measured. The sensing performance of the ZnO films was then studied. The optimization of the operational temperature is mandatory before measuring the response of the ZnO thin film. The response measurements of ZnO films without and with *A. indica* dye extract in the temperature range of 50–325 °C of ethanol vapor are shown in Figure 5. A maximum response of 51.13% and 71.95% were obtained for the ZnO thin film without and with dye extracts at an operating temperature of 250 °C and 225 °C, respectively. The introduction of *A. indica* dye extracts slightly decreased the operating temperature from 250 °C to 225 °C. The decline in operating temperature on the addition of *A. indica* dye extracts may be due to a decrease in activation energy of the reaction in the ZnO thin film [4]. Oxygen vacancies play an important role in varying the conductivity and hence the response of ZnO thin films [35,36]. On increasing the temperature, the response increases; when the thermal energy reaches the boundary to bridge the activation energy barrier of the reaction, the charge volume dramatically increases and causes a high response behavior. After crossing the optimum temperature, desorption of oxygen molecules occurs from the ZnO thin film, which decreases the response [13].

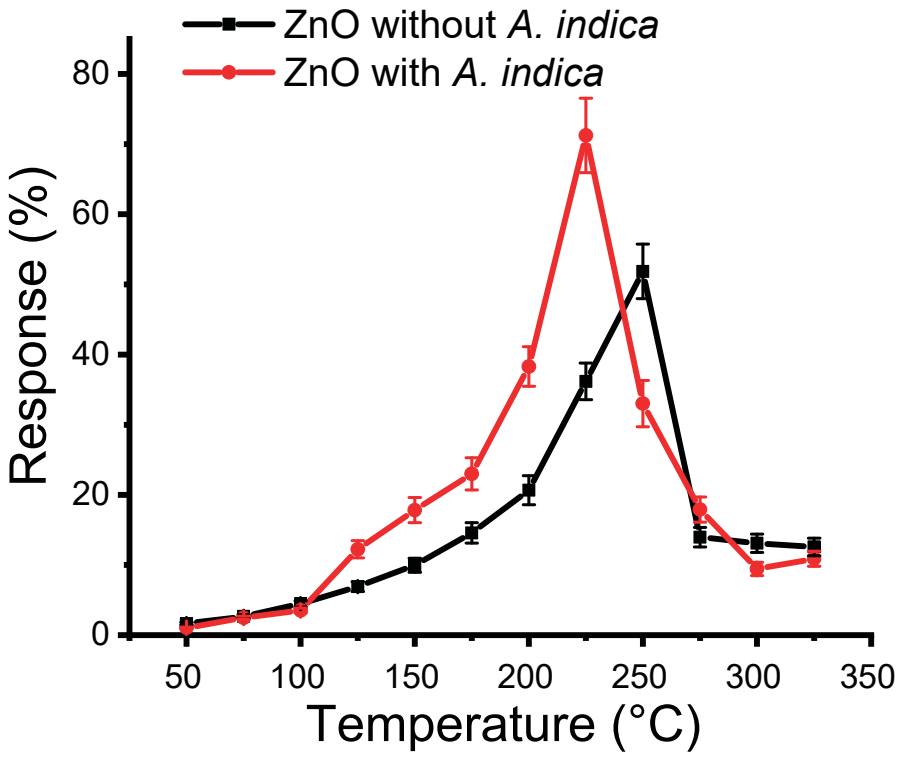

Figure 5. Response measurement as a function of temperature for ZnO thin films without and with *A. indica* dye extracts for ethanol vapor.

The response of an ethanol gas sensor was increased dramatically when *A. indica* dye extract was introduced in ZnO NPs. The natural capping agents present in *A. indica* dye extracts decreased both the grain and crystallite size of ZnO NPs [37]. The decrease in the grain size of ZnO NPs leads to significant increase in the specific surface area, which leads to high activity by adsorbing more oxygen molecules, and helps to enhance the response [38]. Moreover, the geometric dimensions of nanocrystalline and molecular sizes are comparable, which predetermines the difference between the kinetics of chemical transformations in nanocrystalline systems and similar processes in coarsely crystalline materials [39]. These specific features make ZnO thin films very promising for development

of high-sensitivity fast-response gas sensors, in which just surface processes play the key role in the formation of a sensor signal.

The response characteristics of the ZnO NPs films on the exposure of 25, 50, 75, and 100 ppm of ethanol were studied. For the purpose of computing response, each sample was analyzed five times, and the average result for each sample are displayed in Figures 6 and 7. For varying concentrations of ethanol, Figure 6a shows the behavior of the ZnO thin film without and with *A. indica* dye extracts. Clearly, the response increased for higher concentration of ethanol for both cases. At 25, 50, 75, and 100 ppm ethanol, pure ZnO thin films responded with 39.58, 40.71, 40.77, and 51.13%, respectively; however, the response of *A. indica* doped ZnO thin films was 50.52, 56.19, 61.95, and 71.95%, respectively. Figure 6b depicted the curve of sensor resistance against time for ZnO thin films without and with *A. indica* dye extracts at 25, 50, 75, and 100 ppm ethanol concentrations at 250 and 225 °C. The sensor element is exposed to an air-ethanol mixture before being discharged back into the atmosphere. When exposed to air, the sensor's resistance is strong, but it drops dramatically when exposed to ethanol. The ZnO semi-conductor gas sensor exhibited similar behavior [1,40,41]. The response rate and recovery rate are also important parameters in a gas sensor [42]. The measurement process of response and recovery times is shown in Figure 6c. For all ethanol concentrations, the response of *A. indica* dye extracts ZnO thin films is always greater than that of pure ZnO thin films, as shown in Figure 6d.

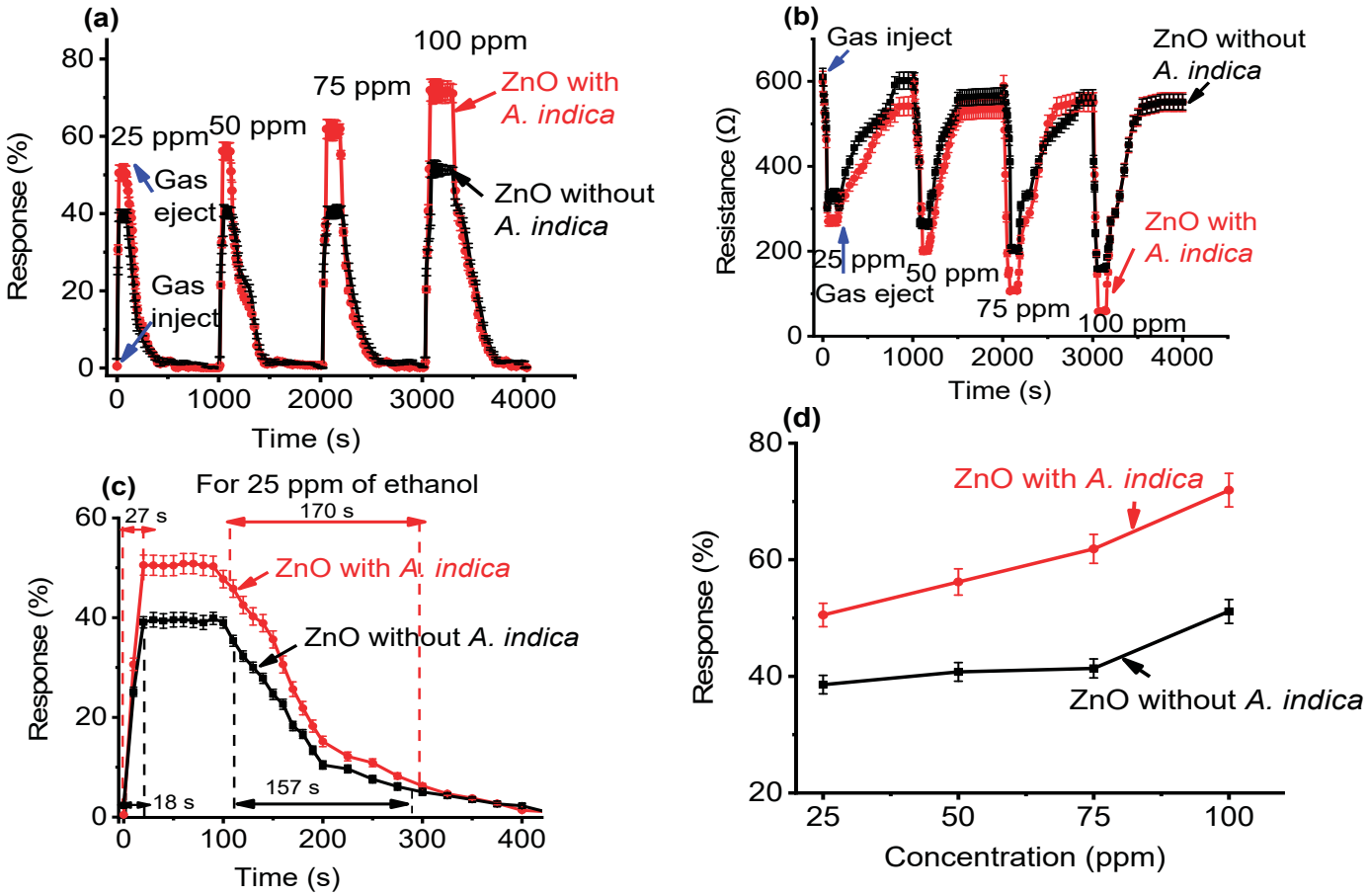

Figure 6. (**a**) Sensitivity measurement of ZnO thin films as a function of time. (**b**) Response curve with time scale and sensor resistance for 25, 50, 75, and 100 ppm ethanol at operating temperature. (**c**) Calculation of the response and recovery time of ZnO thin film for 25 ppm ethanol. (**d**) Sensitivity measurement of ZnO thin films as a function of concentration.

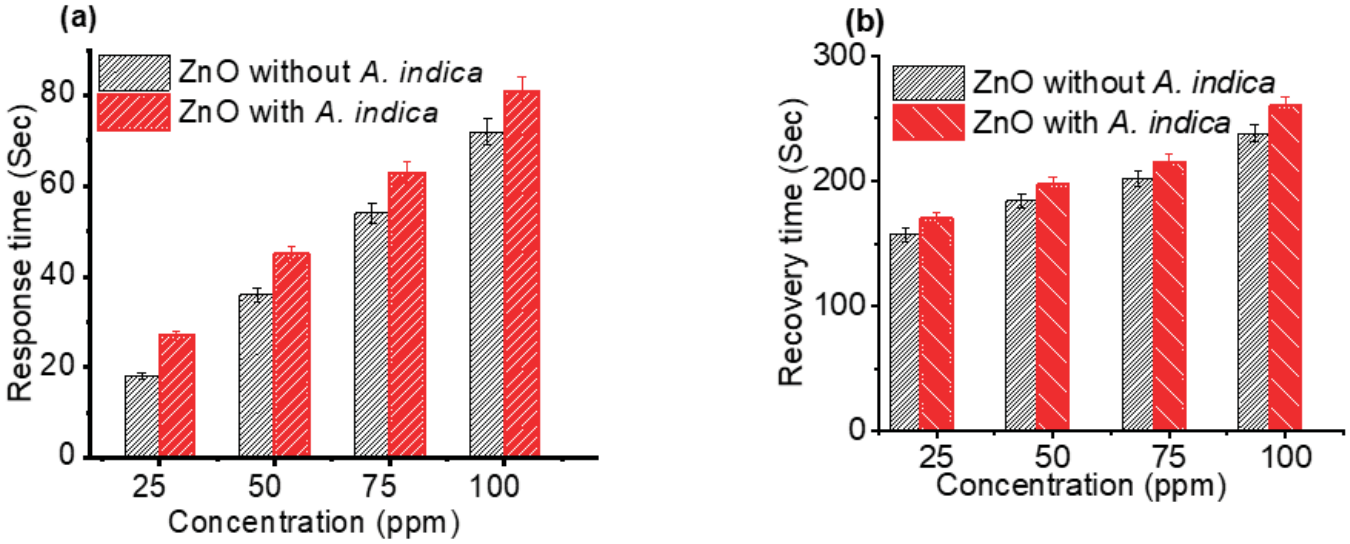

Figure 7. (**a**) Response time of ZnO thin films as a function of concentration and (**b**) recovery time of ZnO thin films as a function of concentration.

Subsequently, response and recovery times as a function of concentration were investigated, as shown in Figure 7. The average response time for bare ZnO thin films with 25, 50, 75, and 100 ppm of ethanol was 18, 36, 54, and 72 s, respectively, whereas the average response time for *A. indica* extracts was 27, 45, 63, and 81 s (Figure 7a). Similarly, the average recovery time for bar ZnO thin films with 25, 50, 75, and 100 ppm of ethanol was 157, 184, 202, and 238 s, respectively, whereas the mean recovery time for *A. indica* extracts was 170, 197, 215, and 260 s (Figure 7b). The response and recovery times of the ZnO thin film increased with the addition of *A. indica* dye extracts at ethanol concentrations ranging from 25 ppm to 100 ppm. This is due to the increased carrier concentration in the ZnO thin film after the *A. indica* dye extract doping. The oxygen adsorption process is the main factor determining the rate of response and recovery cycles [43]. The increasing response and recovery time for ZnO with *A. indica* dye extracts are attributed to the modification of the ZnO surface morphology and increased porosity between the grain- sized ZnO nanostructures, which provide more surface-active sites to promote interaction with ethanol vapor [44].

2.6. Sensing Mechanism

The response features of the ethanol-based gas sensor using ZnO thin films are directly linked to the modification of ZnO NPs. Here, the resistance of the thin film decreased with the supply of ethanol vapor in the sensing device, as shown in Figure 6b. The oxygen present in the atmosphere gets absorbed on the ZnO film as O^{2-} or O^{-}, taking electrons from the conduction band of the ZnO and resulting in a depletion zone on the ZnO thin film [4]. This process increased the resistance of the ZnO thin film significantly. On the exposure of ethanol vapor, the ethanol vapor molecules interact with the absorbed oxygens and reinject the carrier, thereby decreasing the resistance of the ZnO thin film [45]. This effect is relatively higher in ZnO thin films using *A. indica* dye extracts than in thin films without dye. Therefore, the ZnO thin film with *A. indica* extracts shows a large gap in resistance between with ethanol vapor and without ethanol vapor in the sensing device, leading to an increase in the response of the device. The probability of the interaction of ethanol vapor with the ZnO thin film can be explained in Figure 8, as noted in previous literature [46].

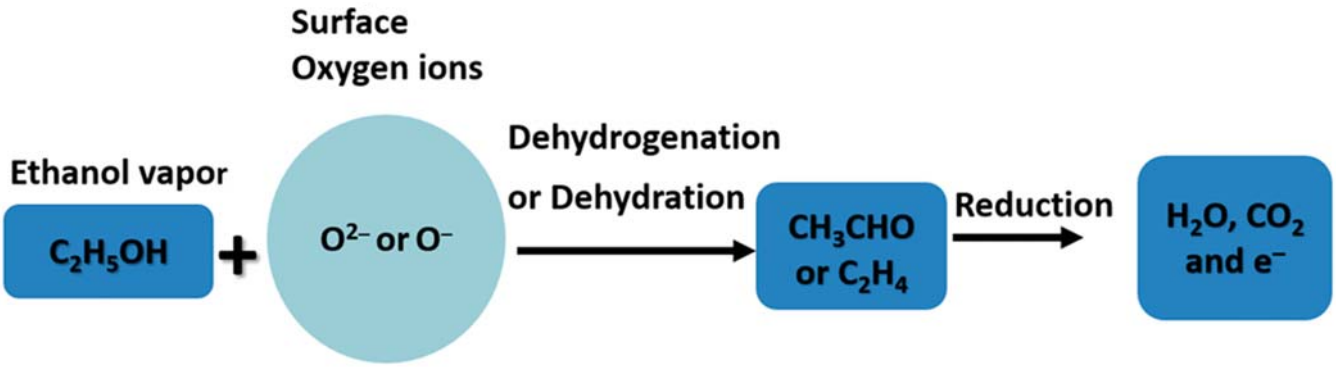

Figure 8. Gas response mechanism of the ZnO thin film based on ethanol vapor.

The approved reactions are initiated by the acid–alkaline behavior of the ZnO thin film. The dehydrogenation procedure mainly occurs on the ZnO thin film with alkaline possessions; however, dehydration is preferred in the acidic region of the ZnO thin film [47]. At determined temperatures (<200 °C), more gaseous elements are adsorbed, depletion area formed on the thin film of ZnO extends intensely, providing a large possibility of interacting ethanol vapor molecules with adsorbed oxygens, thereby generating an improved response [5]. The ZnO thin film with *A. Indica* dye adsorbed more oxygen than that of the pure ZnO thin film because of large specific surface area and desorption of function groups attached with thin film at higher temperatures [48]. This effect caused high possibility of interaction of ethanol vapor molecules with oxygen, resulting in a significant decrease in the resistance of the film, which increased the response. However, at low temperatures, the surface of the ZnO thin film was not perfectly desorbed, which caused a small change in resistance. This slight change in resistance significantly decreased the sensing properties of the ZnO thin film.

3. Materials and Methods

3.1. Synthesis of ZnO NPs without Plant Extracts

ZnO NPs were prepared using the precipitation method. Initially, a 2 M zinc nitrate hexahydrate [Zn $(NO_3)_2.6H_2O$] mixture was prepared in ethanol with continuous stirring using a magnetic stirrer for an hour (h) [49]. Concurrently, a 1 M ethanol solution of sodium hydroxide [$C_2H_7NaO_2$] was prepared with continuous stirring using a magnetic stirrer for 2 h in a different beaker. Likewise, an ethanol solution of sodium hydroxide zinc nitrate solution was added dropwise to the zinc nitrate solution with robust stirring to produce a white precipitate. After total inclusion, the blend was allowed to settle for 1 d. Finally, the resulting precipitate was centrifuged four times at 1000 rpm (centrifuge model 800-B, China), with 10 min (m) each time, for the removal of contaminants. The precipitate was then cleaned three times using distilled water, followed by ethanol. Finally, the filtered white precipitate was dried at 120 °C and then annealed at 500 °C using a muffle furnace (BOECO Muffle Furnace, MF 8/1100, 230 V, 50/60 Hz, Lilienthal, Germany) for 12 h [49].

3.2. Synthesis of ZnO with A. indica Dye Extracts

Fresh leaves of *A. indica* were washed several times using distilled water and dehydrated at room temperature. The leaf extracts were then ground, 10 g of ground leaves were mixed in 40 mL of distilled water, and the mixture of leaves and distilled water was filtered to remove solid extracts. Finally, the fine solution of *A. indica* leaves and distilled water was preserved in a refrigerator at 4 °C. A 2 M zinc nitrate hexahydrate solution was prepared in distilled water under vigorous stirring. After vigorous stirring, 10 mL of aqueous leaf extracts of *A. indica* were introduced into the above solution, and a 1 M ethanol solution of sodium hydroxide was mixed in the above mixture dropwise and stirred thoroughly to obtain a white precipitate. The mixture containing the white precipitate was then stirred using a magnetic stirrer for 2 h. After stirring, the mixture was washed three times with

distilled water and ethanol and then filtered. Finally, the filtered white precipitate was dried at 120 °C and then annealed at 500 °C using a muffle furnace. A schematic of the synthesis of ZnO using the green scheme is illustrated in Figure 9.

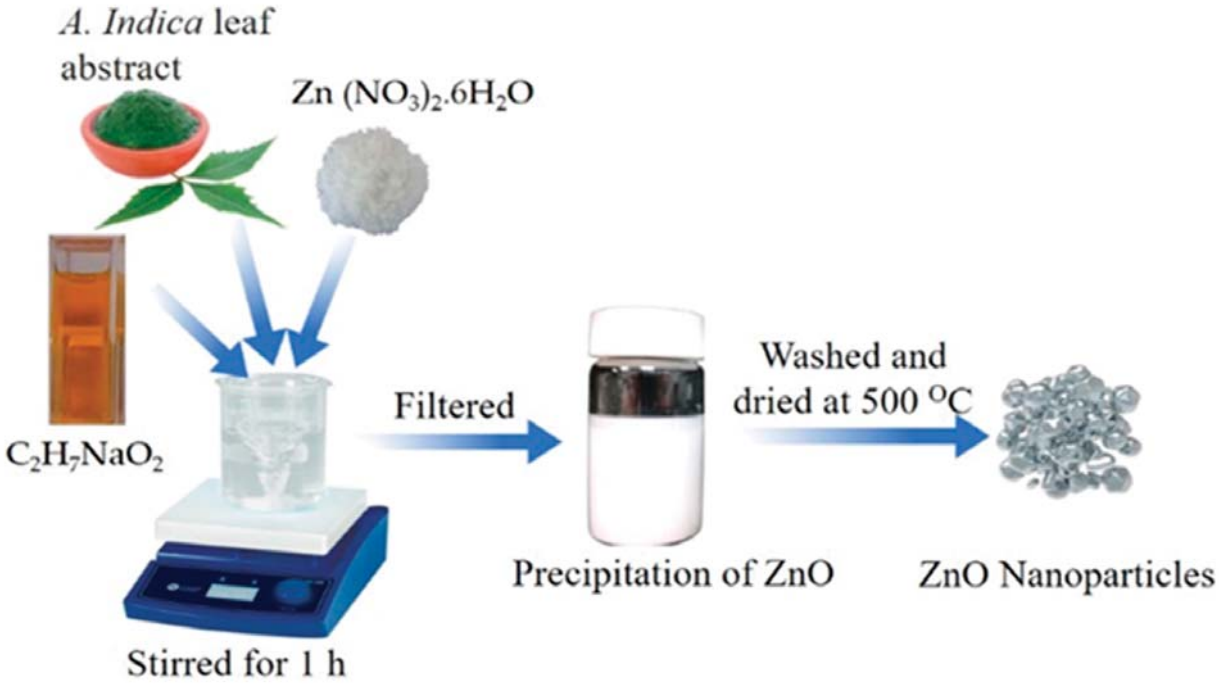

Figure 9. Schematics of the synthesis of ZnO using the green scheme.

3.3. Synthesis of ZnO Thin Films

ZnO thin film was deposited on the FTO coated glass substrate using the spray pyrolysis technique. This method is especially convenient for the settling of ZnO NPs and has been a measurement method for applying a clear electrical conductor of metal oxides to a glass surface [5]. In this process, as shown in Figure 10, the spraying rate remains the same, and the back and forth motions of the machine determine the number of coats, which is digitally controlled. The main benefits of using the spray pyrolysis technique are the spherical surface shape, narrow distribution of atoms or molecules, compilation uniformity, and height controllability of the arrangement of the obtained products and their appropriateness for succeeding refining [50].

A precursor solution was prepared by taking 4.06 g of ZnO in a beaker with 50 mL of ethanol. The solution was mixed using a magnetic stirrer for 1 h at a temperature of 60 °C. The resulting solution was filtered using a filter paper and used to prepare thin films using the spray pyrolysis method. The distance from the nozzle to the glass substrate was 2.0 cm, the diameter of the nozzle was 0.5 cm, and the flow rate was maintained at 8 mL/min. The operating pressure range was maintained between 8 and 16 psi. The spray pyrolysis process included the deposition of ZnO thin films in which the dispersed solution of ZnO NPs prepared with ethanol was sprayed uniformly on the glass substrate over the heated surface at 300 °C. This method yields a very uniform thin film of ZnO owing to the constant spray rate of the nozzle of the spray gun.

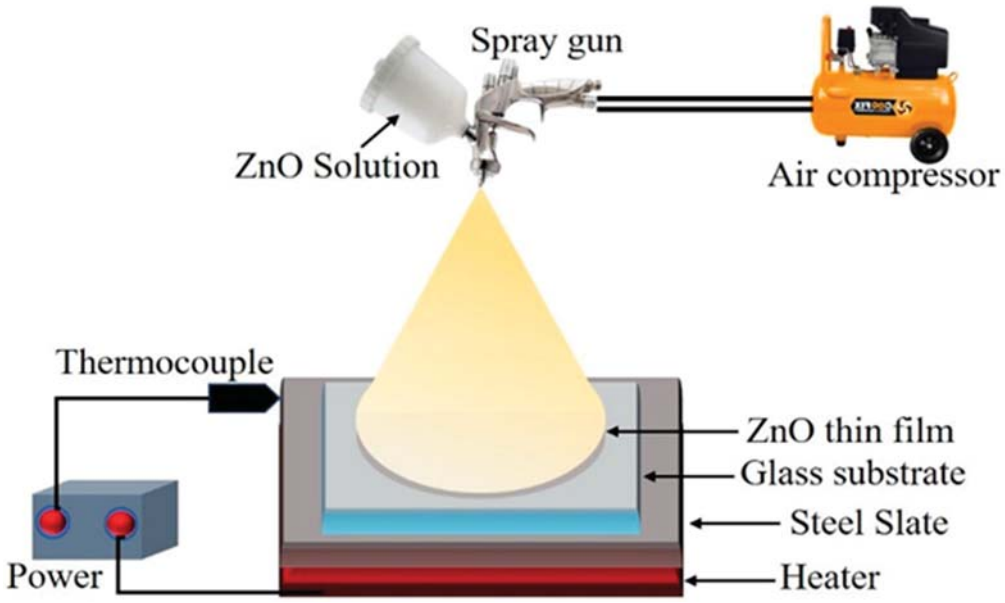

Figure 10. Schematic diagram of the spray pyrolysis method.

3.4. Sensor Application

The response was measured using a custom-made ethanol gas sensor as shown in Figure 11. A nickel-chromium heater was used to heat the sensing element placed just below it, and it could be heated up to 350 °C. A thermocouple was used to monitor the temperature of the sensing element. The temperature controller was set up to maintain the temperature of the glass substrate from 90 °C to 350 °C. The source and drain were fabricated in the ZnO thin film with the help of insulating copper wire using the silver paste and then connected to a fluke multimeter (FLUKE-115, Everett, WA, USA) for resistance measurement. To measure the resistance after injecting the gas, the glass chamber was made airtight. The circuit configuration of the gas sensor was checked by using current-voltage characterization followed by ohmic behavior. The total volume of the sensor chamber is one liter (L). The distance between the base of the sensor chamber and the ZnO thin film is 5 cm. A syringe injects a fixed amount of liquid ethanol (25, 50, 75, or 100 ppm) into the airtight test chamber to achieve the desired concentration. The ethanol concentration calculation method is described in Equations (2)–(4) [51]:

$$V_{ethanol\ gas} = C \times V_s \tag{2}$$

where $V_{ethanol\ gas}$ = volume of gaseous state ethanol, C (ppm) = concentration of the ethanol gas, and V_s = volume of tested chamber with, $PV = nRT$ [51].

$$n_{ethanol} = \frac{PV_{ethanol\ gas}}{RT} = \frac{PCV_s}{RT} \tag{3}$$

where $V = \frac{Mn}{\rho}$.

$$V_{inject} = \frac{Mn_{ethanol}}{\rho} = \frac{MPCV_s}{R\rho T} = (0.69 \times \frac{C}{T})\ \text{mL} \tag{4}$$

The molecular weight of the liquid is M (g/mol), the density is ρ (g/mL), and the average temperature of the test chamber is T (K). The values of M, P, Vs, and R in our work are 46 g/mol, 101,325 Pa, 1 L, 8.31441 J/(mol K), and 0.816 g/cm^3. Equation (4) can be used to compute the ethanol intended concentration.

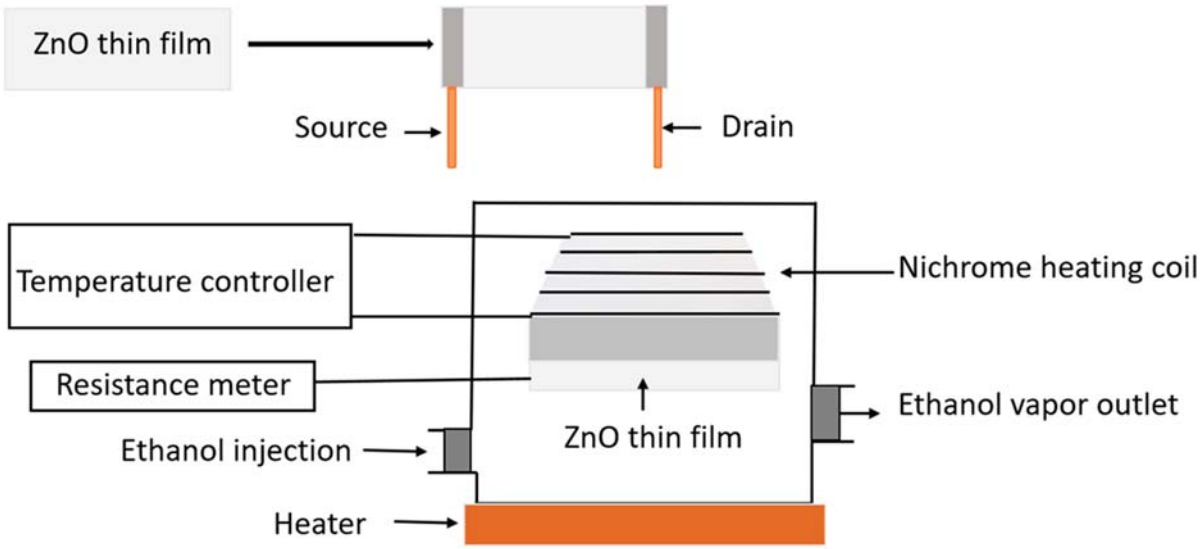

Figure 11. Schematic diagram of the gas sensor.

4. Conclusions

In summary, ZnO NPs were prepared using the precipitation method. The resulting ZnO NPs were coated on glass substrates using the spray pyrolysis method to prepare the thin film. The structural, morphological, and dimensional analyses of the ZnO NPs were performed using XRD, SEM, EDX, and FTIR. The XRD pattern shows that the mean crystallite size of ZnO NPs prepared without dye extracts was 25 nm and that of the *A. indica* dye extracts was 20 nm. The SEM image shows the change in morphology of ZnO NPs from more congregated to less aggregated groups after the addition of *A. indica* dye extracts. The EDX spectra obtained to determine the percentage composition of zinc and oxygen in the synthesized samples also indicated that the prepared ZnO NPs were pure. The FTIR analysis showed the characteristic absorption band of the ZnO bond at 450 cm^{-1} and also revealed the presence of water-soluble proteins such as amines, alcohols, ketones, and carboxylic acid from *A. indica* dye extracts. The results of the sensitivity measurements with the ZnO NPs show high sensitivity toward *A. indica* dye extract thin films with a figure of 71.95% for 100 ppm of ethanol. The ZnO thin film with *A. indica* shows significantly decreased sensor resistance for 25, 50, 75, and 100 ppm of ethanol vapor compared to that of the ZnO thin film without dye extracts. The response and recovery times of the ZnO thin film were higher than those of the bare ZnO thin film between 25 ppm and 100 ppm of ethanol. The sensitivity measurement and calculation of response and recovery for 25 ppm of ethanol concentration suggest that this sensing device can also be used to detect low concentrations of ethanol. To sum up, the addition of *A. indica* dye extracts to ZnO thin films significantly increased the sensing, response, and recovery times of the ethanol-based gas sensor.

Author Contributions: Conceptualization, T.R.A., D.K.C. and L.P.J., validation, L.P.J., R.W., N.K.K. and E.H.C. formal analysis, B.S., L.P.J., R.W., N.K.K. and E.H.C.; investigation, T.R.A., D.K.C., L.P.J. and P.L.; writing—original draft preparation, T.R.A. and P.L.; writing—review and editing, T.R.A., L.P.J., P.L., N.K.K. and E.H.C. All authors have read and agreed to the published version of the manuscript.

Funding: The authors are grateful to University Grants Commission (UGC), Nepal for providing research support under MRS/74_75/S&T-80 for the completion of this research work. This study was also partially supported by the National Research Foundation (NRF) of Korea, funded by the Korean government 2021R1A6A1A03038785, 2021R1F1A1055694 and by the Kwangwoon University in 2021.

Institutional Review Board Statement: Not applicable.

Informed Consent Statement: Not applicable.

Data Availability Statement: The data that support the findings of this study are available from the corresponding author upon reasonable request.

Acknowledgments: The authors would like to thank Vinaya Kumar Jha, Arjun Dhakal, Bishnu Giri, Samir Kattel, Bishnu Pokhrel, Anjila Ghimire, and Amrendra Kumar Singh for their help and support throughout the research process. We are grateful to Department of Physical science, P.D. Patel Institute of Applied Science, Charusat, Gujarat, India allotting time for XRD, SEM, and FTIR measurements.

Conflicts of Interest: The authors declare no conflict of interest.

Sample Availability: Not available.

References

1. Wan, Q.; Li, Q.H.; Chen, Y.J.; Wang, T.-H.; He, X.L.; Li, J.P.; Lin, C.L. Fabrication and Ethanol Sensing Characteristics of ZnO Nanowire Gas Sensors. *Appl. Phys. Lett.* **2004**, *84*, 3654–3656. [CrossRef]
2. Yang, Z.; Huang, Y.; Chen, G.; Guo, Z.; Cheng, S.; Huang, S. Ethanol Gas Sensor Based on Al-Doped ZnO Nanomaterial with Many Gas Diffusing Channels. *Sens. Actuators B Chem.* **2009**, *140*, 549–556. [CrossRef]
3. Arshak, K.; Gaidan, I. Development of a Novel Gas Sensor Based on Oxide Thick Films. *Mater. Sci. Eng. B* **2005**, *118*, 44–49. [CrossRef]
4. Khayatian, A.; Kashi, M.A.; Azimirad, R.; Safa, S. Enhanced Gas-Sensing Properties of ZnO Nanorods Encapsulated in an Fe-Doped ZnO Shell. *J. Phys. D Appl. Phys.* **2014**, *47*, 75003. [CrossRef]
5. Chaudhary, D.K.; Ghimire, R.; Amatya, S.P.; Shrestha, S.P.; Joshi, L.P. Study on Influence of Fe Doping into ZnO Film for Ethanol Sensing. *Proc. J. Phys. Conf. Ser.* **2020**, *1706*, 12036. [CrossRef]
6. Ajmal, H.M.S.; Khan, F.; Huda, N.U.; Lee, S.; Nam, K.; Kim, H.Y.; Eom, T.-H.; Kim, S.D. High-Performance Flexible Ultraviolet Photodetectors with Ni/Cu-Codoped ZnO Nanorods Grown on PET Substrates. *Nanomaterials* **2019**, *9*, 1067. [CrossRef] [PubMed]
7. Ajmal, H.M.S.; Khan, F.; Nam, K.; Kim, H.Y.; Kim, S.D. Ultraviolet Photodetection Based on High-Performance Co-Plus-Ni Doped ZnO Nanorods Grown by Hydrothermal Method on Transparent Plastic Substrate. *Nanomaterials* **2020**, *10*, 1225. [CrossRef]
8. Yedurkar, S.; Maurya, C.; Mahanwar, P. Biosynthesis of Zinc Oxide Nanoparticles Using *Ixora coccinea* Leaf Extract—A Green Approach. *Open J. Synth. Theory Appl.* **2016**, *5*, 1–14. [CrossRef]
9. Kim, S.; Saeed, M.A.; Kim, S.H.; Shim, J.W. Enhanced Hole Selecting Behavior of WO3 Interlayers for Efficient Indoor Organic Photovoltaics with High Fill-Factor. *Appl. Surf. Sci.* **2020**, *527*, 146840. [CrossRef]
10. Lamichhane, P.; Adhikari, B.C.; Nguyen, L.N.; Paneru, R.; Ghimire, B.; Mumtaz, S.; Lim, J.S.; Hong, Y.J.; Choi, E.H. Sustainable Nitrogen Fixation from Synergistic Effect of Photo-Electrochemical Water Splitting and Atmospheric Pressure N2 Plasma. *Plasma Sources Sci. Technol.* **2020**, *29*, 45026. [CrossRef]
11. Tsukazaki, A.; Ohtomo, A.; Onuma, T.; Ohtani, M.; Makino, T.; Sumiya, M.; Ohtani, K.; Chichibu, S.F.; Fuke, S.; Segawa, Y.; et al. Repeated Temperature Modulation Epitaxy for P-Type Doping and Light-Emitting Diode Based on ZnO. *Nat. Mater.* **2005**, *4*, 42–46. [CrossRef]
12. Ramimoghadam, D.; Hussein, M.Z.B.; Taufiq-Yap, Y.H. Hydrothermal Synthesis of Zinc Oxide Nanoparticles Using Rice as Soft Biotemplate. *Chem. Cent. J.* **2013**, *7*, 1–10. [CrossRef]
13. Haripadmam, P.C.; John, H.; Philip, R.; Gopinath, P. Enhanced Optical Limiting in Polystyrene–ZnO Nanotop Composite Films. *Opt. Lett.* **2014**, *39*, 474–477. [CrossRef]
14. Bantz, C.; Koshkina, O.; Lang, T.; Galla, H.-J.; Kirkpatrick, C.J.; Stauber, R.H.; Maskos, M. The Surface Properties of Nanoparticles Determine the Agglomeration State and the Size of the Particles under Physiological Conditions. *Beilstein J. Nanotechnol.* **2014**, *5*, 1774–1786. [CrossRef] [PubMed]
15. Hvolbæk, B.; Janssens, T.V.W.; Clausen, B.S.; Falsig, H.; Christensen, C.H.; Nørskov, J.K. Catalytic Activity of Au Nanoparticles. *Nano Today* **2007**, *2*, 14–18. [CrossRef]
16. Dirmyer, M.R.; Martin, J.; Nolas, G.S.; Sen, A.; Badding, J.V. Thermal and Electrical Conductivity of Size-Tuned Bismuth Telluride Nanoparticles. *Small* **2009**, *5*, 933–937. [CrossRef] [PubMed]
17. Ihsan, K.; Harabbi, K.H. Restriction of Particle Size and Lattice Strain through X-ray Diffraction Peak Broadening Analysis of ZnO Nanoparticles. *Adv. Phys. Theor. Appl.* **2015**, *49*, 638–2225.
18. Sharma, R.; Chandra, B.P.; Bisen, D.P. Thermoluminescence and Optical Absorption Spectra Of Zns: Mn Nanoparticles. *Chalcogenide Lett.* **2009**, *6*, 251–255.
19. Joshi, L.P.; Khatri, B.V.; Gyawali, S.; Gajurel, S.; Chaudhary, D.K. Green Synthesis of Zinc Oxide Nanoparticles Using *Ixora Coccinea* Leaf Extract for Ethanol Vapour Sensing. *J. Phys. Sci.* **2021**, *32*, 15–26. [CrossRef]
20. Basnet, P.; Chanu, T.I.; Samanta, D.; Chatterjee, S. A Review on Bio-Synthesized Zinc Oxide Nanoparticles Using Plant Extracts as Reductants and Stabilizing Agents. *J. Photochem. Photobiol. B Biol.* **2018**, *183*, 201–221. [CrossRef] [PubMed]

21. Basak, S.P.; Chakraborty, D.P. Chemical investigation of *Azadirachta indica* leaf (m azadirachta). *J. Indian Chem. Soc.* **1968**, *45*, 466.
22. Biswas, K.; Chattopadhyay, I.; Banerjee, R.K.; Bandyopadhyay, U. Biological Activities and Medicinal Properties of Neem (*Azadirachta indica*). *Curr. Sci.* **2002**, *82*, 1336–1345.
23. Bhuyan, T.; Mishra, K.; Khanuja, M.; Prasad, R.; Varma, A. Biosynthesis of Zinc Oxide Nanoparticles from *Azadirachta indica* for Antibacterial and Photocatalytic Applications. *Mater. Sci. Semicond. Process.* **2015**, *32*, 55–61. [CrossRef]
24. Nejati, K.; Rezvani, Z.; Pakizevand, R. Synthesis of ZnO Nanoparticles and Investigation of the Ionic Template Effect on Their Size and Shape. *Int. Nano Lett.* **2011**, *1*, 75–81.
25. Mallika, A.N.; Reddy, A.R.; Reddy, K.V. Annealing Effects on the Structural and Optical Properties of ZnO Nanoparticles with PVA and CA as Chelating Agents. *J. Adv. Ceram.* **2015**, *4*, 123–129. [CrossRef]
26. Elumalai, K.; Velmurugan, S. Green Synthesis, Characterization and Antimicrobial Activities of Zinc Oxide Nanoparticles from the Leaf Extract of *Azadirachta indica* (L.). *Appl. Surf. Sci.* **2015**, *345*, 329–336. [CrossRef]
27. Nguyen, L.N.; Kaushik, N.; Lamichhane, P.; Mumtaz, S.; Paneru, R.; Bhartiya, P.; Kwon, J.S.; Mishra, Y.K.; Nguyen, L.Q.; Kaushik, N.K.; et al. In Situ Plasma-Assisted Synthesis of Polydopamine-Functionalized Gold Nanoparticles for Biomedical Applications. *Green Chem.* **2020**, *22*, 6588–6599. [CrossRef]
28. Gayen, R.N.; Sarkar, K.; Hussain, S.; Bhar, R.; Pal, A.K. ZnO Films Prepared by Modified Sol-Gel Technique. *Indian J. Pure Appl. Phys.* **2011**, *49*, 470–477.
29. Xiong, G.; Pal, U.; Serrano, J.G.; Ucer, K.B.; Williams, R.T. Photoluminesence and FTIR Study of ZnO Nanoparticles: The Impurity and Defect Perspective. *Phys. Status Solidi C* **2006**, *3*, 3577–3581. [CrossRef]
30. Bharathi, D.; Bhuvaneshwari, V. Synthesis of Zinc Oxide Nanoparticles (ZnO NPs) Using Pure Bioflavonoid Rutin and Their Biomedical Applications: Antibacterial, Antioxidant and Cytotoxic Activities. *Res. Chem. Intermed.* **2019**, *45*, 2065–2078. [CrossRef]
31. Vafaee, M.; Ghamsari, M.S. Preparation and Characterization of ZnO Nanoparticles by a Novel Sol–Gel Route. *Mater. Lett.* **2007**, *61*, 3265–3268. [CrossRef]
32. Suwanboon, S.; Amornpitoksuk, P.; Sukolrat, A.; Muensit, N. Optical and Photocatalytic Properties of La-Doped ZnO Nanoparticles Prepared via Precipitation and Mechanical Milling Method. *Ceram. Int.* **2013**, *39*, 2811–2819. [CrossRef]
33. Kharissova, O.V.; Dias, H.V.R.; Kharisov, B.I.; Pérez, B.O.; Pérez, V.M.J. The Greener Synthesis of Nanoparticles. *Trends Biotechnol.* **2013**, *31*, 240–248. [CrossRef]
34. Josse, J. Constitutive Inorganic Pyrophosphatase of *Escherichia coli* I. Purification and Catalytic Properties. *J. Biol. Chem.* **1966**, *241*, 1938–1947. [CrossRef]
35. Vaishnav, V.S.; Patel, P.D.; Patel, N.G. Indium Tin Oxide Thin Film Gas Sensors for Detection of Ethanol Vapours. *Thin Solid Film.* **2005**, *490*, 94–100. [CrossRef]
36. Bhasha, S.; Malik, P.; Santosh, S.; Purnima, J. Synthesis and Characterization of Nanocrystalline Zinc Oxide Thin Films for Ethanol Vapor Sensor. *J. Nanomed. Nanotechnol.* **2015**, *6*, 1.
37. Iqbal, Y.; Malik, A.R.; Iqbal, T.; Aziz, M.H.; Ahmed, F.; Abolaban, F.A.; Ali, S.M.; Ullah, H. Green Synthesis of ZnO and Ag-Doped ZnO Nanoparticles Using *Azadirachta indica* Leaves: Characterization and Their Potential Antibacterial, Antidiabetic, and Wound-Healing Activities. *Mater. Lett.* **2021**, *305*, 130671. [CrossRef]
38. Gas' Kov, A.M.; Rumyantseva, M.N. Nature of Gas Sensitivity in Nanocrystalline Metal Oxides. *Russ. J. Appl. Chem.* **2001**, *74*, 440–444. [CrossRef]
39. Henrich, V.E.; Cox, P.A. Fundamentals of Gas-Surface Interactions on Metal Oxides. *Appl. Surf. Sci.* **1993**, *72*, 277–284. [CrossRef]
40. Hongsith, N.; Choopun, S. Effect of Platinum Impregnation on ZnO Tetrapods for Ethanol Sensor. *Adv. Mater. Res.* **2008**, *55*, 289–292.
41. Li, C.C.; Du, Z.F.; Li, L.M.; Yu, H.C.; Wan, Q.; Wang, T.H. Surface-Depletion Controlled Gas Sensing of ZnO Nanorods Grown at Room Temperature. *Appl. Phys. Lett.* **2007**, *91*, 32101. [CrossRef]
42. Korotcenkov, G.; Brinzari, V.; Stetter, J.R.; Blinov, I.; Blaja, V. The Nature of Processes Controlling the Kinetics of Indium Oxide-Based Thin Film Gas Sensor Response. *Sens. Actuators B Chem.* **2007**, *128*, 51–63. [CrossRef]
43. Matsushima, S.; Maekawa, T.; Tamaki, J.; Miura, N.; Yamazoe, N. Role of Additives on Alcohol Sensing by Semiconductor Gas Sensor. *Chem. Lett.* **1989**, *18*, 845–848. [CrossRef]
44. Stambolova, I.; Konstantinov, K.; Vassilev, S.; Peshev, P.; Tsacheva, T. Lanthanum Doped SnO_2 and ZnO Thin Films Sensitive to Ethanol and Humidity. *Mater. Chem. Phys.* **2000**, *63*, 104–108. [CrossRef]
45. Chou, S.M.; Teoh, L.G.; Lai, W.H.; Su, Y.H.; Hon, M.H. ZnO: Al Thin Film Gas Sensor for Detection of Ethanol Vapor. *Sensors* **2006**, *6*, 1420–1427. [CrossRef]
46. Kohl, D. Surface Processes in the Detection of Reducing Gases with SnO_2-Based Devices. *Sens. Actuators* **1989**, *18*, 71–113. [CrossRef]
47. Barzinjy, A.A.; Azeez, H.H. Green Synthesis and Characterization of Zinc Oxide Nanoparticles Using *Eucalyptus globulus* Labill. Leaf Extract and Zinc Nitrate Hexahydrate Salt. *SN Appl. Sci.* **2020**, *2*, 1–14. [CrossRef]
48. Rao, T.P.; Kumar, M.C.S.; Safarulla, A.; Ganesan, V.; Barman, S.R.; Sanjeeviraja, C. Physical Properties of ZnO Thin Films Deposited at Various Substrate Temperatures Using Spray Pyrolysis. *Phys. B Condens. Matter* **2010**, *405*, 2226–2231.
49. Zhang, Y.L.; Yang, Y.; Zhao, J.H.; Tan, R.Q.; Cui, P.; Song, W.J. Preparation of ZnO Nanoparticles by a Surfactant-Assisted Complex Sol–Gel Method Using Zinc Nitrate. *J. Sol-Gel Sci. Technol.* **2009**, *51*, 198–203. [CrossRef]

50. Goyal, A.; Kachhwaha, S. ZnO Thin Films Preparation by Spray Pyrolysis and Electrical Characterization. *Mater. Lett.* **2012**, *68*, 354–356. [CrossRef]
51. Li, X.; Chang, Y.; Long, Y. Influence of Sn Doping on ZnO Sensing Properties for Ethanol and Acetone. *Mater. Sci. Eng. C* **2012**, *32*, 817–821. [CrossRef]

INTERNATIONAL CONFERENCE ON
EXPLORATIONS IN PHYSICS (ICEP-2018)

29-31 May, 2018, Kathmandu, Nepal

Dinesh Kumar Chaudhary

Department of Physics, Amrit Campus, Tribhuvan University, Kathmandu Nepal

Contributed a poster presentation entitled

Optical and Surface Characterization of Thin Film of Semiconductors Tin Sulphide and Zinc Oxide

during the conference

Chief Guest
Prof. Dr. Jiba Raj Pokharel
Vice Chancellor, NAST

Campus Chief
Rajesh Mahaju
Amrit Campus

SOC Chair
Assoc. Prof. Dr. Leela Pradhan Joshi
Amrit Campus

4th International Conference

Kathmandu Symposia on Advanced Materials-2018

(KaSAM-2018), October 26-29, 2018

Certificate

This is herewith certified that
Prof./Dr./Mr./Ms. *Dinesh Chaudhary*
delivered a paper as poster entitled

Fe Doping into ZnO Thin Film for Detection of Ethanol Vapor

in

4th International Conference

Kathmandu Symposia on Advanced Materials-2018

(KaSAM-2018)

held in Kathmandu, Nepal.

R. Adhikari

Prof. Dr. Rameshwar Adhikari
Chairman

Supported by

onyx DÉVELOPPEMENT

IMESD 2018 P-114

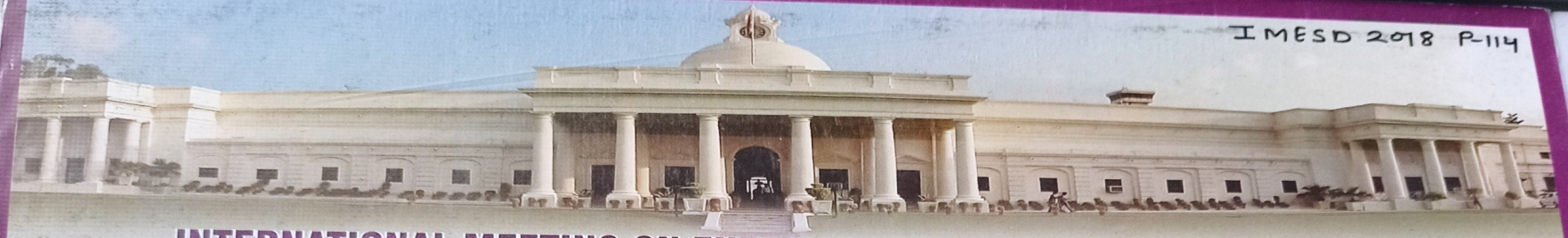

INTERNATIONAL MEETING ON ENERGY STORAGE DEVICES (IMESD) - 2018
&
INDUSTRY-ACADEMIA CONCLAVE (IAC) - 2018

IMESD-2018

December 10 - 12, 2018

CERTIFICATE OF PARTICIPATION

This is to certify that Prof./Dr./Mr./Ms./.....DINESH K. CHAUDHARY.....

from...TRIBHUVAN UNIVERSITY, NEPAL.....*participated and presented a paper (~~Plenary / Keynote / Invited / Oral~~ / Poster) in International Meeting on Energy Storage Devices (IMESD) - 2018 & Industry-Academia Conclave (IAC)-2018, held during December 10-12, 2018 at Department of Physics, Indian Institute of Technology Roorkee.*

Prof. K. L. Yadav
Chair, IMESD-2018
Head of the Department
IIT Roorkee, Roorkee,
Uttarakhand, India

Prof. Yogesh K. Sharma
Convener, IMESD/IAC-2018
IIT Roorkee, Roorkee,
Uttarakhand, India

International Conference on
Nanosciences and High Energy Physics
(ICNHEP-2019)
February 4-6, 2019
Central Department of Physics
Tribhuvan University, Kirtipur, Nepal

Certificate

This is to Certify that Dr./Mr./Ms .Dinesh...Kumar...Chaudhary..... has participated in "ICNHEP-2019" and presented a invited talk/ research paper.

The title of the talk / paper is .Study...of...structural..and...optical..properties of...Fe...doped...ZnO..thin..films...prepared..by...spin..coating...method.

Prof. Dr. Ram Pd. Khatiwada
Dean, IoST, TU, Kirtipur

Dr. Gopi Chandra Kaphle
Convener, ICNHEP-2019

Prof. Dr. Binil Aryal
Head CDP, TU, Kirtipur

ROYAL SOCIETY OF CHEMISTRY | BOOKS

Royal Society of Chemistry Books

This is to certify that

Dinesh Kumar Chaudhary

Has been awarded a Royal Society of Chemistry Book Prize

at

The 8th Asian Conference on Colloid & Interface Science

Kathmandu, Nepal

24 – 27 September 2019

Royal Society of Chemistry Books

www.rsc.org/books/

Registered Charity Number 207890

The 8th Asian Conference on Colloid & Interface Science (ACCIS 2019)

Sept. 24-27, Kathmandu, Nepal

ASCASS

ASIAN SOCIETY FOR COLLOID AND SURFACE SCIENCE

Certificate of Participation

This is to certify that

Dinesh Kumar Chaudhary

has participated and contributed **Poster Presentation** in

The 8th Asian Conference on Colloid & Interface Science (ACCIS 2019) organized by the **Asian Society for Colloid and Surface Science (ASCASS)** held in Pulchowk Campus, Institute of Engineering, Tribhuvan University, Lalitpur, Kathmandu, Nepal.

Dr. Lok Kumar Shrestha
Chairperson (ACCIS 2019)

September 27, 2019

Prof. Dr. Toyoko Imae
President (ASCASS)

St. Xavier's College

Maitighar, Kathmandu, Nepal

Department of Physics

This e-certificate of appreciation is awarded to **Mr. Dinesh Kumar Chaudhary**

of

Central Department of Physics, Kritipur, Nepal

for poster presentation On the title "**Study on ethanol vapor sensing performance of Zno prepared by different methods**"

in the

"International Conference on Material Science and Characterization Technology (ICMSCT)"

held on **September 26-28, 2021**

Mr. Drabindra Pandit Head, Department of Physics	Fr. Dr. Augustine Thomas, S.J. Principal St. Xavier's College	Prof. Dr. Bhim Prasad Subedi Chairperson, University Grants Commission Nepal

SIAS
SPARK INSTITUTE OF ADVANCED SCIENCE

KATHIR COLLEGE OF ENGINEERING
KCE
COIMBATORE - 641 062

CERTIFICATE

of Participation

4 Days Hands on Training on Reference Management Software

This is to certify that Mr./Ms DINESH KUMAR CHAUDHARY

has successfully participated in **4 Days Hands on Training on Reference Management Software - Endnote, Mendeley and Zotero** during **26th December 2021** to **29th December 2021** conducted by Department of Mechanical Engineering, Kathir College of Engineering and SIAS Research Forum.

Zotero

EndNote X9

MENDELEY

HOD.
Department of Mechanical Engineering
Kathir College of Engineering

(Coordinator)
SIAS Research Forum

Principal,
Kathir College of Engineering

Nepal Physical Society

Ghantaghar, Kathmandu, Nepal

International Conference on Frontiers of Physics -2022

(ICFP-2022)

This Certificate of appreciation is awarded to

Dinesh K. Chaudhary

from Amrit Campus, TU, Nepal for his oral presentation on the

"Gas sensing characteristics of ZnO film" in the

International Conference on Frontiers of Physics -2022

held on January 22-24, 2022 via virtual platform.

Prof. Dr. Narayan P. Chapagain

Conference Chair, ICFP-2022

President, Nepal Physical Society

February 1, 2022

2022 First International Conference on

Modern Materials for Engineering and Research (ICMMER 2022)

29 - 30, Septemberl 2022 | Tiruchengode, Tamil Nadu, India | www.icmmer.com

CERTIFICATE

Publication Partner

Scientific.Net

MMER 3027

Peer Reviewed

This certificate is presented to

Dinesh Kumar Chaudhary

Department of Physics, Amrit Campus,
Tribhuvan University, Kathmandu, 44600, Nepal
Central Department of Physics, Tribhuvan University,
Kirtipur, Kathmandu, 44618, Nepal.

for presenting the research paper entitled "**Effect of Atmospheric Dielectric Barrier Discharge on Optical, Electrical and Surface Properties of ZnO Film**" in the First International Conference on Modern Materials for Engineering and Research (ICMMER 2022) held at Hotel Aloft, Coimbatore, Tamil Nadu, India during 29 - 30, September 2022. The conference has been organized by the Department of Mechanical Engineering, Sengunthar Engineering College, Tiruchengode, Tamil Nadu, India.

Prof. A. Baladhandapani, M.A., M.Phill.,
Secretary & Correspondent, SEC

Dr. R. Satish Kumar, M.E., Ph.D.,
Principal, SEC

Dr. T. R. Chinnusamy, M.E., Ph.D.,
Chair, ICMMER 2022

Organized by

SENGUNTHAR ENGINEERING COLLEGE
(An Autonomous Institution)
Approved by AICTE, New Delhi & Affiliated with Anna University, Chennai.
Tiruchengode, Tamil Nadu, India - 637 205

CMS Partner

DILIGENTEC SOLUTIONS

First Edition

SENSORS-eCon 2022

CERTIFICATE

OF PARTICIPATION

PRESENTED TO

Dr. Dinesh Kumar Chaudhary

FOR ATTENDING **SENSORS-ECON2022** AND PRESENTING A TALK TITLED
IMPACT OF FE AND SN DOPING INTO ZNO FOR ETHANOL VAPOUR SENSING

Sensors-eCon2022 THE RESEARCH CATALYST

ORGANIZING COMMITTE

MARSHALL PORTERFIELD
PURDUE UNIVERSITY, USA

JIANGUO JACK WANG
UNIVERSITY OF TECHNOLOGY SYDNEY, AUSTRALIA

HSIAO-CHUN WU
LOUISIANA STATE UNIVERSITY, USA

The Research Catalyst

National Conference on Recent Trends in Science, Technology and Innovation

RTSTI-2022 | Pokhara, Nepal

Certificate of Participation

This is to certify that Mr./Mrs. **DINESH KUMAR CHAUDHARY** has participated as an **ORAL PRESENTER**

entitled **Fe-Al doped ZnO Films: A highly Sensitive Ethanol Sensing (PHO-05)**

in the **National Conference on Recent Trends in Science, Technology and Innovation, RTSTI-2022**

organized by Research Management Unit, Pashchimanchal Campus, Pokhara on 29th - 30th May, 2022.

Asst. Prof. Nirmal Prasad Baral
Chairman, Organizing Committee, RTSTI
Pashchimanchal Campus, Pokhara

Assoc. Prof. Dr. Krishna Raj Adhikari
Chairman, Technical Committee, RTSTI
Pashchimanchal Campus, Pokhara

Prof. Dr. Ganesh Man Gurung
Chief Guest
Chancellor, Gandaki University

Organizer
Research Management Unit, RMU
Pashchimanchal Campus
Pokhara-16, Lamachaur

Co-organizer
Gandaki Province Academy of Science and Technology (GPAST), Pokhara, Nepal

In association with

पोखरा विश्वविद्यालय POKHARA UNIVERSITY · Gandaki University गण्डकी विश्वविद्यालय · PRITHVI NARAYAN CAMPUS पृथ्वीनारायण क्याम्पस · Tribhuvan University Institute of Forestry POKHARA CAMPUS · Tribhuvan University Institute of Medicine POKHARA NURSING CAMPUS · COLLEGE OF NATURAL RESOURCE MANAGEMENT · GANDAKI COLLEGE OF ENGINEERING AND SCIENCE

Certificate of Paper Presentation

This is to certify that

Mr. Dinesh Kumar Chaudhary

has successfully presented the paper titled

Deposition of Sn-doped ZnO for ethanol sensing

at the

National Conference on Advances in Atmospheric and Material Science

held on Nov. 6-7, 2022 at

the Department of Physics, Amrit Campus, Tribhuvan University, Kathmandu, Nepal.

Prof. Dr. Lok Narayan Jha
Chief Guest

Prof Dr. Leela Pradhan Joshi
Head, Department of Physics
Amrit Campus, TU

Dr. Lok Bahadur Baral
Campus Chief
Amrit Campus, TU

Organized by:

Department of Physics
Amrit Campus
Tribhuvan University
Nepal

Supported by:

International Science Programme
Uppsala University
Sweden

In collaboration with:

IEEE ELECTRON DEVICES SOCIETY

SALNet
South Asian Lightning Network